



Journal of  
*Development Biology*

# Scientific Papers by Developmental Biologists in Japan

---

Edited by  
Hideyo Ohuchi and Tsutomu Nohno  
Printed Edition of the Special Issue Published in  
*Journal of Developmental Biology*

# **Scientific Papers by Developmental Biologists in Japan**



# Scientific Papers by Developmental Biologists in Japan

Editors

**Hideyo Ohuchi**

**Tsutomu Nohno**

MDPI • Basel • Beijing • Wuhan • Barcelona • Belgrade • Manchester • Tokyo • Cluj • Tianjin



*Editors*

Hideyo Ohuchi  
Department of Cytology  
and Histology  
Okayama University  
Okayama City  
Japan

Tsutomu Nohno  
Department of Cytology  
and Histology  
Okayama University  
Medical School  
Okayama City  
Japan

*Editorial Office*

MDPI  
St. Alban-Anlage 66  
4052 Basel, Switzerland

This is a reprint of articles from the Special Issue published online in the open access journal *Journal of Developmental Biology* (ISSN 2221-3759) (available at: [www.mdpi.com/journal/jdb/special\\_issues/Developmental\\_Biology\\_Japan](http://www.mdpi.com/journal/jdb/special_issues/Developmental_Biology_Japan)).

For citation purposes, cite each article independently as indicated on the article page online and as indicated below:

LastName, A.A.; LastName, B.B.; LastName, C.C. Article Title. <i>Journal Name</i> <b>Year</b> , Volume Number, Page Range.
--

**ISBN 978-3-0365-7361-8 (Hbk)**

**ISBN 978-3-0365-7360-1 (PDF)**

© 2023 by the authors. Articles in this book are Open Access and distributed under the Creative Commons Attribution (CC BY) license, which allows users to download, copy and build upon published articles, as long as the author and publisher are properly credited, which ensures maximum dissemination and a wider impact of our publications.

The book as a whole is distributed by MDPI under the terms and conditions of the Creative Commons license CC BY-NC-ND.

# Contents

<b>About the Editors</b> . . . . .	vii
<b>Preface to “Scientific Papers by Developmental Biologists in Japan”</b> . . . . .	ix
<b>Hideyo Ohuchi and Tsutomu Nohno</b> Scientific Papers by Developmental Biologists in Japan Reprinted from: <i>J. Dev. Biol.</i> <b>2023</b> , <i>11</i> , 11, doi:10.3390/jdb11010011 . . . . .	1
<b>Yuri Nishiya, Kohei Kawaguchi, Kosuke Kudo, Takuya Kawaguchi, Juma Obayashi and Kunihide Tanaka et al.</b> The Expression of Transcription Factors in Fetal Lamb Kidney Reprinted from: <i>J. Dev. Biol.</i> <b>2021</b> , <i>9</i> , 22, doi:10.3390/jdb9020022 . . . . .	5
<b>Wataru Nakajima, Soya Nakanishi, Ryosuke Hosoya, Toshiaki Uemoto, Shiro Ohgo and Naoyuki Wada</b> Regenerative Polarity of the Fin Ray in Zebrafish Caudal Fin and Related Tissue Formation on the Cut Surface Reprinted from: <i>J. Dev. Biol.</i> <b>2021</b> , <i>9</i> , 50, doi:10.3390/jdb9040050 . . . . .	15
<b>Toshiyuki Goto, Shuhei Torii, Aoi Kondo, Kazumasa Kanda, Junji Kawakami and Yosky Kataoka et al.</b> Actin Filament in the First Cell Cycle Contributes to the Determination of the Anteroposterior Axis in Ascidian Development Reprinted from: <i>J. Dev. Biol.</i> <b>2022</b> , <i>10</i> , 10, doi:10.3390/jdb10010010 . . . . .	31
<b>Toshiki Kinuhata, Keita Sato, Tetsuya Bando, Taro Mito, Satoru Miyaishi and Tsutomu Nohno et al.</b> Involvement of a Basic Helix-Loop-Helix Gene <i>BHLHE40</i> in Specification of Chicken Retinal Pigment Epithelium Reprinted from: <i>J. Dev. Biol.</i> <b>2022</b> , <i>10</i> , 45, doi:10.3390/jdb10040045 . . . . .	45
<b>Taisei Shiraki, Takuma Hayashi, Jotaro Ozue and Minoru Watanabe</b> Appropriate Amounts and Activity of the Wilms’ Tumor Suppressor Gene, <i>wt1</i> , Are Required for Normal Pronephros Development of <i>Xenopus</i> Embryos Reprinted from: <i>J. Dev. Biol.</i> <b>2022</b> , <i>10</i> , 46, doi:10.3390/jdb10040046 . . . . .	59
<b>Koji Oishi, Kazunori Nakajima and Jun Motoyama</b> Activation of Sonic Hedgehog Signaling Promotes Differentiation of Cortical Layer 4 Neurons via Regulation of Their Cell Positioning Reprinted from: <i>J. Dev. Biol.</i> <b>2022</b> , <i>10</i> , 50, doi:10.3390/jdb10040050 . . . . .	71
<b>Mikiko Kudo and Kunimasa Ohta</b> Regulation of the Brain Neural Niche by Soluble Molecule Akhirin Reprinted from: <i>J. Dev. Biol.</i> <b>2021</b> , <i>9</i> , 29, doi:10.3390/jdb9030029 . . . . .	83
<b>Takuma Shinozuka and Shinji Takada</b> Morphological and Functional Changes of Roof Plate Cells in Spinal Cord Development Reprinted from: <i>J. Dev. Biol.</i> <b>2021</b> , <i>9</i> , 30, doi:10.3390/jdb9030030 . . . . .	93
<b>Noriko Funato</b> Craniofacial Phenotypes and Genetics of DiGeorge Syndrome Reprinted from: <i>J. Dev. Biol.</i> <b>2022</b> , <i>10</i> , 18, doi:10.3390/jdb10020018 . . . . .	105

**Hiroshi Yomogita, Naoyuki Miyasaka and Masami Kanai-Azuma**

A Review of Delayed Delivery Models and the Analysis Method in Mice

Reprinted from: *J. Dev. Biol.* **2022**, *10*, 20, doi:10.3390/jdb10020020 . . . . . **123**

# About the Editors

## **Hideyo Ohuchi**

Hideyo Ohuchi is a professor in the Department of Cytology and Histology, Faculty of Medicine, Dentistry and Pharmaceutical Sciences, Okayama University. Her research interests include cellular and molecular mechanisms of organogenesis and regeneration, and identifying cellular or animal models of human retinal disease.

## **Tsutomu Nohno**

Tsutomu Nohno is a visiting researcher in the Department of Cytology and Histology, Okayama University Medical School, and a guest researcher in the Department of Public Health, Kawasaki Medical School. He has a broad background in molecular and developmental biology, having served as a professor of molecular and developmental biology at Kawasaki Medical School.





# Preface to “Scientific Papers by Developmental Biologists in Japan”

We are excited to present this Special Issue of the *Journal of Developmental Biology* featuring intriguing manuscripts submitted by developmental biologists in Japan. These manuscripts showcase a range of cutting-edge research in the field of developmental biology, and we believe that they will be a valuable contribution to this field.

Within this Special Issue, you will find six research articles and four reviews, each offering unique insights and perspectives on various aspects of developmental and regenerative processes. We hope that these articles will not only inform readers, but also inspire new ideas and ways of thinking about these important topics.

We would like to express our sincere gratitude to all the authors who contributed their work to this Special Issue, as well as to the reviewers who provided invaluable feedback and guidance throughout the editorial process.

We hope that you will find these articles as fascinating and thought-provoking as we do, and that they will inspire further research and exploration in the field of developmental biology. We would also like to recommend the *Journal of Developmental Biology* as a journal that offers excellent publishing opportunities for developmental biologists.



**Hideyo Ohuchi and Tsutomu Nohno**

*Editors*



Editorial

# Scientific Papers by Developmental Biologists in Japan

Hideyo Ohuchi <sup>1,\*</sup>  and Tsutomu Nohno <sup>2,3,\*</sup> 

<sup>1</sup> Department of Cytology and Histology, Okayama University Faculty of Medicine, Dentistry and Pharmaceutical Sciences, 2-5-1 Shikata-cho, Kita-ku, Okayama 700-8558, Japan

<sup>2</sup> Department of Cytology and Histology, Okayama University Medical School, 2-5-1 Shikata-cho, Kita-ku, Okayama 700-8558, Japan

<sup>3</sup> Department of Public Health, Kawasaki Medical School, 577 Matsushima, Kurashiki 701-0192, Japan

\* Correspondence: ohuchi-hideyo@okayama-u.ac.jp (H.O.); tnohno@gmail.com (T.N.)

We have assembled ten interesting manuscripts submitted by developmental biologists in Japan. We believe that these manuscripts represent a valuable contribution to the specific field of developmental biology. This Special Issue contains six research articles [1–6] and four reviews [7–10].

In the first article [1], Nishiya et al. investigated the period and location of expression of transcription factors in fetal lamb and adult ewe kidneys. They reported the expression patterns in the developing kidney for herbivorous mammals in reference to the omnivorous rodent, showing that WT1 is involved in nephron development, and that Pax2, Pax8, and HNF1 $\beta$  are involved in nephron maturation and collecting duct formation.

Nakajima et al. [2] examined the regeneration polarity of the fin ray during zebrafish caudal fin regeneration. Although the fin rays always regenerated from the proximal margin toward the distal margin, the regeneration-related genes were expressed at both the proximal and distal edges of the hole in the early stage of regeneration, suggesting that the regenerative response occurs at the distal edge. The difference between the proximal and distal margins is a sheet-like tissue that is formed on the apical side of the regenerated tissue at the proximal margin but not at the distal edge. By separating the distal margin from the proximal margin with manipulation, they showed that the sheet-like tissue was formed at the distal margin and that regeneration of the fin ray was also induced. The regenerated fin rays from the distal margin protruded laterally from the caudal fin and then bent distally, and both ends showed the same characteristics as those of the normal fin rays. The authors concluded that fin rays have the ability to regenerate in both directions, although regeneration is restricted to the proximal margin under normal conditions because of preferential formation of the sheet-like tissue on the apical side of the regenerating tissue from the proximal margin.

Goto et al. [3] reported the body axis determination in ascidian early development through the relocalization of maternal determinants, organelles, or unique cell populations in a cytoskeleton-dependent manner. In the ascidian first cell cycle, the myoplasm, including mitochondria, endoplasmic reticulum, and maternal mRNAs move to the future posterior side concomitantly. This translocation consists of first and second phases depending on the actin and microtubule, respectively. To determine the process of transition from the first to the second phase, the authors analyzed the relationship between the cytoskeletons and myoplasmic components during the first cell cycle with an inhibitor. They showed unexpected F-actin accumulation at the vegetal pole during this transition period. The microtubule structure was strongly affected after F-actin depolymerization, and the myoplasmic components were mislocalized, resulting in disordered anteroposterior axis formation. The authors suggest the importance of F-actin during the first cell cycle and the existence of interactions between microfilaments and microtubules, implying the enigmatic mechanisms of ooplasmic segregation.

**Citation:** Ohuchi, H.; Nohno, T. Scientific Papers by Developmental Biologists in Japan. *J. Dev. Biol.* **2023**, *11*, 11. <https://doi.org/10.3390/jdb11010011>

Received: 7 March 2023

Accepted: 8 March 2023

Published: 10 March 2023



**Copyright:** © 2023 by the authors. Licensee MDPI, Basel, Switzerland. This article is an open access article distributed under the terms and conditions of the Creative Commons Attribution (CC BY) license (<https://creativecommons.org/licenses/by/4.0/>).

Kinuhata et al. [4] studied the role of a basic helix-loop-helix (bHLH) transcription factor, *Bhlhe40*, in chicken eye development, focusing on the stage of optic vesicle morphogenesis, when two retinal domains, the neural retina (NR) and retinal pigment epithelium (RPE), emerge to separate. They reported that *Bhlhe40* is expressed in the prospective and definitive RPE and that its overexpression represses an NR gene, *Vsx2*, while maintaining an RPE gene, *Otx2*. Their attempts to obtain morphological change after expressing dominant negative forms of *Bhlhe40* were not successful, possibly because there are many bHLH factors that could dimerize with *Bhlhe40* and modify its function. Although it was not demonstrated how the cell behavior in the optic cup was changed after *Bhlhe40* overexpression, this study implicates that *Bhlhe40* is a conserved RPE gene functioning like a node for RPE specification.

Shiraki et al. [5] investigated the role of *wt1* in pronephros development in *Xenopus* embryos, with CRISPR/Cas9 mutation of *wt1*, resulting in reduced expression of pronephros marker genes. WT1 activated transcription of the luciferase reporter gene, and the injection of wild-type or artificially altered transcriptional active *wt1* mRNA disrupted the expression of pronephros marker genes in the embryos. Their results suggest that the appropriate amounts and activity of WT1 protein are required for normal pronephros development in *Xenopus* embryos.

Oishi et al. [6] reported important findings on the role of sonic hedgehog (Shh) in glutamatergic cortical subtype specification. They found that E14.5-born neurons with elevated Shh expression frequently differentiated into layer 4 subtypes as judged by the cell positioning and molecular identity, and that this effect was achieved indirectly through the regulation of cell positioning rather than the direct activation of layer 4 differentiation programs. They provided evidence that Shh as an extrinsic factor plays an important role in the specification of cortical superficial layer subtypes.

Kudo and Ohta [7] discussed the role of an extracellular secreted protein, Akhirin, as a niche molecule during mouse brain formation. Akhirin is structurally related to vitrin and cochlin, and supposedly involved in neural stem cell niche regulation in the central nervous system through heterophilic cell adhesion activity.

Shinozuka and Takada [8] reviewed the most dorsal region of neural tube, the roof plate, as the dorsal organizing center of the developing spinal cord. The dorsal half of the spinal cord is separated by a glial structure called the dorsal median septum. Roof plate cells have been shown to dramatically stretch along the dorsoventral axis with reduction of the spinal cord lumen. During this stretching process, the tips of roof plate cells maintain contact with cells surrounding the shrinking lumen, eventually exposed to the inner surface of the central canal. The authors further discuss the role of Wnt ligands secreted by roof plate cells in morphological changes during spinal cord development.

Funato [9] reviewed DiGeorge syndrome (DGS) and velocardiofacial syndrome (VCFS) caused by a 1.5 to 2.5 Mb hemizygous deletion of chromosome 22q11.2 in humans, focusing on craniofacial anomalies, and summarized the current understanding of the genetic factors that impact DGS/VCFS-related phenotypes. She also reviewed DGS/VCFS mouse models that have been designed to better understand the pathogenic processes of DGS/VCFS.

Yomogita et al. [10] discussed the causes of prolonged post-term delivery in humans in relation to the mouse model, providing a foundation for conducting more systematic research on delayed delivery. The length of the gestation period is controlled not only by the maternal signals, but also by fetal and placental signals. Elucidation of the causes of delayed parturition in humans and animals is essential to understand the mechanisms underlying pregnancy and delivery.

We hope that our readers enjoy these articles, not only for their valuable contributions to the respective fields but also for their introductions to new ideas, new ways of thinking, and experiments on developmental and regenerative processes. We would like to thank all reviewers for their independent evaluations of the submitted articles, and the editorial staff at the *Journal of Developmental Biology* for their efforts in assembling this Special Issue.

**Conflicts of Interest:** Ohuchi and Nohno are coauthors of one of the publications included in the special issue [4].

## References

1. Nishiya, Y.; Kawaguchi, K.; Kudo, K.; Kawaguchi, T.; Obayashi, J.; Tanaka, K.; Ohyama, K.; Nagae, H.; Furuta, S.; Seki, Y.; et al. The expression of transcription factors in fetal lamb kidney. *J. Dev. Biol.* **2021**, *9*, 22. [CrossRef] [PubMed]
2. Nakajima, W.; Nakanishi, S.; Hosoya, R.; Uemoto, T.; Ohgo, S.; Wada, N. Regenerative polarity of the fin ray in zebrafish caudal fin and related tissue formation on the cut surface. *J. Dev. Biol.* **2021**, *9*, 50. [CrossRef] [PubMed]
3. Goto, T.; Torii, S.; Kondo, A.; Kanda, K.; Kawakami, J.; Kataoka, Y.; Nishikata, T. Actin filament in the first cell cycle contributes to the determination of the anteroposterior axis in ascidian development. *J. Dev. Biol.* **2022**, *10*, 10. [CrossRef] [PubMed]
4. Kinuhata, T.; Sato, K.; Bando, T.; Mito, T.; Miyaishi, S.; Nohno, T.; Ohuchi, H. Involvement of a basic helix-loop-helix gene *BHLHE40* in specification of chicken retinal pigment epithelium. *J. Dev. Biol.* **2022**, *10*, 45. [CrossRef] [PubMed]
5. Shiraki, T.; Hayashi, T.; Ozue, J.; Watanabe, M. Appropriate amounts and activity of the Wilms' tumor suppressor gene, *wt1*, are required for normal pronephros development of *Xenopus* embryos. *J. Dev. Biol.* **2022**, *10*, 46. [CrossRef] [PubMed]
6. Oishi, K.; Nakajima, K.; Motoyama, J. Activation of sonic hedgehog signaling promotes differentiation of cortical layer 4 neurons via regulation of their cell positioning. *J. Dev. Biol.* **2022**, *10*, 50. [CrossRef] [PubMed]
7. Kudo, M.; Ohta, K. Regulation of the brain neural niche by soluble molecule akhirin. *J. Dev. Biol.* **2021**, *9*, 29. [CrossRef] [PubMed]
8. Shinozuka, T.; Takada, S. Morphological and functional changes of roof plate cells in spinal cord development. *J. Dev. Biol.* **2021**, *9*, 30. [CrossRef] [PubMed]
9. Funato, N. Craniofacial phenotypes and genetics of DiGeorge syndrome. *J. Dev. Biol.* **2022**, *10*, 18. [CrossRef] [PubMed]
10. Yomogita, H.; Miyasaka, N.; Kanai-Azuma, M. A review of delayed delivery models and the analysis method in mice. *J. Dev. Biol.* **2022**, *10*, 20. [CrossRef] [PubMed]

**Disclaimer/Publisher's Note:** The statements, opinions and data contained in all publications are solely those of the individual author(s) and contributor(s) and not of MDPI and/or the editor(s). MDPI and/or the editor(s) disclaim responsibility for any injury to people or property resulting from any ideas, methods, instructions or products referred to in the content.



Article

# The Expression of Transcription Factors in Fetal Lamb Kidney

Yuri Nishiya <sup>1</sup>, Kohei Kawaguchi <sup>1</sup>, Kosuke Kudo <sup>1</sup>, Takuya Kawaguchi <sup>1</sup>, Juma Obayashi <sup>1</sup>, Kunihide Tanaka <sup>1</sup>, Kei Ohyama <sup>1</sup>, Hideki Nagae <sup>1</sup>, Shigeyuki Furuta <sup>1</sup>, Yasuji Seki <sup>1</sup>, Junki Koike <sup>2</sup>, Kevin C. Pringle <sup>3</sup> and Hiroaki Kitagawa <sup>1,\*</sup>

- <sup>1</sup> Division of Pediatric Surgery, School of Medicine, St. Marianna University, 2-16-1, Sugao, Kawasaki 216-8511, Kanagawa, Japan; yuri.nishiya@marianna-u.ac.jp (Y.N.); k3kawaguchi@marianna-u.ac.jp (K.K.); kosuke.kudo@marianna-u.ac.jp (K.K.); t2kawaguchi@marianna-u.ac.jp (T.K.); j2obayashi@marianna-u.ac.jp (J.O.); k3tanaka@marianna-u.ac.jp (K.T.); k2oyama@marianna-u.ac.jp (K.O.); hi-naga@marianna-u.ac.jp (H.N.); its0408@marianna-u.ac.jp (S.F.); skchldrnshp@gol.com (Y.S.)
- <sup>2</sup> Department of Pathology, School of Medicine, St. Marianna University, Kawasaki 216-8511, Kanagawa, Japan; j2koike@marianna-u.ac.jp
- <sup>3</sup> Department of Obstetrics and Gynecology, School of Medicine & Health Science, University of Otago, North Dunedin, Dunedin 9016, New Zealand; kevin.pringle@otago.ac.nz
- \* Correspondence: h2kita@marianna-u.ac.jp; Tel.: +81-44-977-8111

**Abstract:** (1) Background: Renal development involves frequent expression and loss of transcription factors, resulting in the activation of genes. Wilms' tumor 1 (WT1), hepatocyte nuclear factor-1-beta (HNF1 $\beta$ ), and paired box genes 2 and 8 (Pax2 and Pax8) play an important role in renal development. With this in vivo study, we examined the period and location of expression of these factors in renal development. (2) Methods: Fetal lamb kidneys (50 days from gestation to term) and adult ewe kidneys were evaluated by hematoxylin and eosin staining. Serial sections were subjected to immunohistochemistry for WT1, HNF1 $\beta$ , Pax2, and Pax8. (3) Results: Pax2, Pax8, and HNF1 $\beta$  expression was observed in the ureteric bud and collecting duct epithelial cells. We observed expression of WT1 alone in metanephric mesenchymal cells, glomerular epithelial cells, and interstitial cells in the medullary rays and Pax8 and HNF1 $\beta$  expression in tubular epithelial cells. WT1 was highly expressed in cells more proximal to the medulla in renal vesicles and in C- and S-shaped bodies. Pax2 was expressed in the middle and peripheral regions, and HNF1 $\beta$  in cells in the region in the middle of these. (4) Conclusions: WT1 is involved in nephron development. Pax2, Pax8, and HNF1 $\beta$  are involved in nephron maturation and the formation of peripheral collecting ducts from the Wolffian duct.

**Keywords:** kidney; development; WT1; Pax2; Pax8; HNF1 $\beta$

**Citation:** Nishiya, Y.; Kawaguchi, K.; Kudo, K.; Kawaguchi, T.; Obayashi, J.; Tanaka, K.; Ohyama, K.; Nagae, H.; Furuta, S.; Seki, Y.; et al. The Expression of Transcription Factors in Fetal Lamb Kidney. *J. Dev. Biol.* **2021**, *9*, 22. <https://doi.org/10.3390/jdb9020022>

Academic Editors: Hideyo Ohuchi, Tsutomu Nohno and Simon J. Conway

Received: 30 April 2021

Accepted: 17 June 2021

Published: 19 June 2021

**Publisher's Note:** MDPI stays neutral with regard to jurisdictional claims in published maps and institutional affiliations.



**Copyright:** © 2021 by the authors. Licensee MDPI, Basel, Switzerland. This article is an open access article distributed under the terms and conditions of the Creative Commons Attribution (CC BY) license (<https://creativecommons.org/licenses/by/4.0/>).

## 1. Introduction

The development of the mammalian kidney starts from interactions between the Wolffian duct and the metanephric mesenchyme (MM). In response to signals from the MM, the Wolffian duct forms the ureteric bud, which then invades the MM, branching repeatedly. The ureteric bud's invasion of the MM leads to the aggregation of the metanephric mesenchyme and induces mesenchymal–epithelial transition (MET), which leads to the formation of renal vesicles and C- and S-shaped bodies. S-shaped bodies lead to the formation of proximal tubules, Henle's loop, and distal tubules, resulting in a fusion with the ureteric bud. Capillary endothelial cells and mesangial cells invade the cleft of S-shaped bodies. S-shaped-bodies differentiate into Bowman's capsule, and glomerular epithelial cells form the nephron. As the branching of the UB nears its completion, the terminal ends of the UB branches fuse with the distal ends of the developing nephrons and the UB differentiates into the collecting ducts, which drain into the renal pelvis. This process occurs intermittently during the fetal stage, leading to the formation of a mature kidney [1]. In the above-described renal development, the expression and loss of many transcription factors



lead to the activation of various genes. Recent studies on the induction of human embryonic stem cells (hESCs) and human-induced pluripotent stem cells (hiPSCs) in the renal tissue identified transcription factors that play an important role in renal development [2]. It was reported that: (i) SIX2, SALL1, WT1, and paired box gene 2 (Pax2)-positive nephron progenitor cells (NPCs) are induced by hESCs and hiPSCs through the primitive streak and posterior intermediate mesoderm; and (ii) the NPCs result in pretubular aggregates and paired box gene 8 (Pax8), LHX1, and LAM-positive renal vesicles with the expression of hepatocyte nuclear factor-1-beta (HNF1 $\beta$ ) and BRN1, subsequently inducing the podocytes, proximal tubule, Henle's loop, and distal tubule [3].

In this *in vivo* study, we examined fetal lamb kidneys using immunohistochemistry to determine the location and timing of the expression of transcription factors WT1, HNF1 $\beta$ , Pax2, and Pax8, which have been reported to be involved in renal development.

## 2. Materials and Methods

After approval was obtained from the Animal Ethics Committee of the Wellington School of Medicine and Health Sciences, University of Otago, Wellington, New Zealand (approval numbers WAEC 8-03, W03/07, W02-11, W01-12, AEC4-14, AEC 1-16), pregnant ewes were transported from the farm 24 to 48 h before the operation. They were examined by ultrasound to confirm the pregnancy and to avoid unnecessary operations.

Our preoperative and anesthetic management was reported previously [4]. At 50, 60, 70, 80, 90, 100, and 110 days, and full term (145 days), the ewes were anesthetized, and the fetuses were delivered by cesarean section. The lambs were then sacrificed using pentobarbital injected into the umbilical vein, as we previously described [5]. The lambs' kidneys were then removed and fixed in 10% formalin. The kidneys were divided longitudinally, and samples were taken from the cut surface of the kidney, processed for light microscopy in paraffin blocks, and cut into 3  $\mu$ m slices for light microscopy. Sections were deparaffinized in xylene and rehydrated in a graded series of alcohol followed by H<sub>2</sub>O<sub>2</sub>. The sections were then either stained with hematoxylin and eosin (HE) or immunohistochemistry. For immunohistochemistry, we used WT1 mouse monoclonal antibody, NCL-WT1-562 (Leica, Wetzlar, Germany), 1:20 dilution, 60 min; anti-HNF1 $\beta$  rabbit polyclonal antibody, HPA002083 (Sigma-Aldrich, St. Louis, MO, USA), 1:1500 dilution, 60 min; anti-Pax8 mouse monoclonal antibody, ab53490 (Abcam, Cambridge, UK), 1:10 dilution, 60 min; and anti-Pax2 rabbit monoclonal antibody, ab70389 (Abcam, Cambridge, UK), 1:500 dilution, 60 min.

## 3. Results

### 3.1. Number of Samples

Fetal lamb kidneys at 50 ( $n = 4$ ), 60 ( $n = 5$ ), 70 ( $n = 2$ ), 80 ( $n = 2$ ), 90 ( $n = 4$ ), 100 ( $n = 5$ ), 110 ( $n = 4$ ), and 145 (full term,  $n = 4$ ) days of gestation and adult ewe kidneys ( $n = 3$ ) were included in this study. Because the fetal kidneys at 50, 60, and 70 days of gestation were very small, the largest cut surfaces of both kidneys were used for the evaluation, while slices from the left kidney were used for the evaluation for fetuses at 80, 90, 100, and 110 days and full term.

### 3.2. Morphological Changes in the Kidney in Fetal Lambs

Beneath the renal capsule of the fetal lamb kidneys at 50 days, the nephrogenic zone (NZ), ureteric bud, metanephric mesenchymal cells, and C- and S-shaped bodies were observed. In addition, mature glomeruli and renal tubules were found in the deep cortex and near the medulla (data not shown). The NZ in kidneys was found in fetuses at 50, 60, 70, 80, 90, 100, and 110 days of gestation; the NZ thinned progressively as the gestational age increased. No NZ was found in the kidneys of full-term lambs (Figure 1).

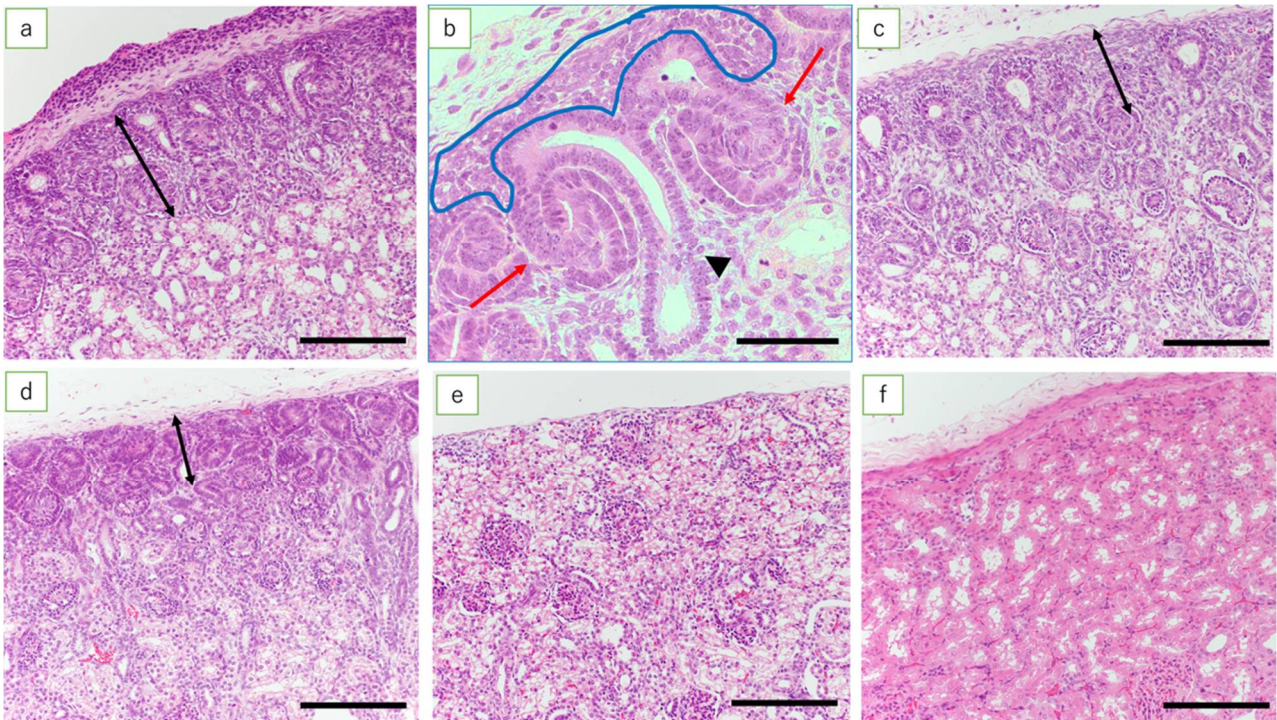


**Figure 1.** Nephrogenic zone (HE). (a) Fetal kidney at 50 days' gestation (HE, scale bar: 200  $\mu$ m); (b) fetal kidney at 50 days' gestation (HE, scale bar: 100  $\mu$ m). Metanephric mesenchymal cells (inside the blue line), ureteric bud (arrowhead), and S-shaped bodies (red arrows); (c) fetal kidney at 70 days' gestation (scale bar: 200  $\mu$ m); (d) fetal kidney at 110 days' gestation (scale bar: 200  $\mu$ m); (e) fetal kidney at term (scale bar: 200  $\mu$ m); and (f) the ewe's kidney (scale bar: 200  $\mu$ m). Fetal kidney at 50 days' gestation has NZ in the renal cortex and the ureteric bud, metanephric mesenchymal cells, and C- and S-shaped bodies. As pregnancy progresses, there is progressive thinning of the NZ, resulting in the loss of NZ at full term. The adult ewe kidney after the development of renal tubules is complete shows well-established tubular epithelial cells and increased inter-glomerular distance (double arrows in (a–d) indicate the extent of the NZ).

### 3.3. Immunohistochemistry

In the adult ewe kidney (control), the expression of WT1 was noted only in the glomerular epithelial cells and epithelial cells of the Bowman's capsule, whereas low expression of Pax2 was found only in the epithelial cells in the collecting duct. Pax8 was expressed in tubular epithelial cells, in the epithelial cells of Bowman's capsule, and in the epithelial cells of the collecting duct. Expression of HNF1 $\beta$  was found in the proximal and distal tubular epithelial cells, in the epithelial cells of Bowman's capsule, and in the epithelial cells in the collecting duct (Figure 2).

In the fetal kidneys at  $\leq 110$  days of gestation where an NZ was observed, the expression of WT1 was found in metanephric mesenchymal cells, C- and S-shaped bodies, glomerular epithelial cells, epithelial cells of Bowman's capsule, the medullary rays, and in interstitial cells in the medulla (Figure 3a). Among these, the expression of WT1 in the renal vesicle and C- and S-shaped bodies was noted mainly in cells closer to the medulla (Figure 4b). In the kidneys of full-term fetuses with no NZ, expression of WT1 was found in glomerular epithelial cells, the epithelial cells of Bowman's capsule, and the interstitial cells in the medullary rays (Figure 5a), in marked contrast with the findings in adult kidneys.

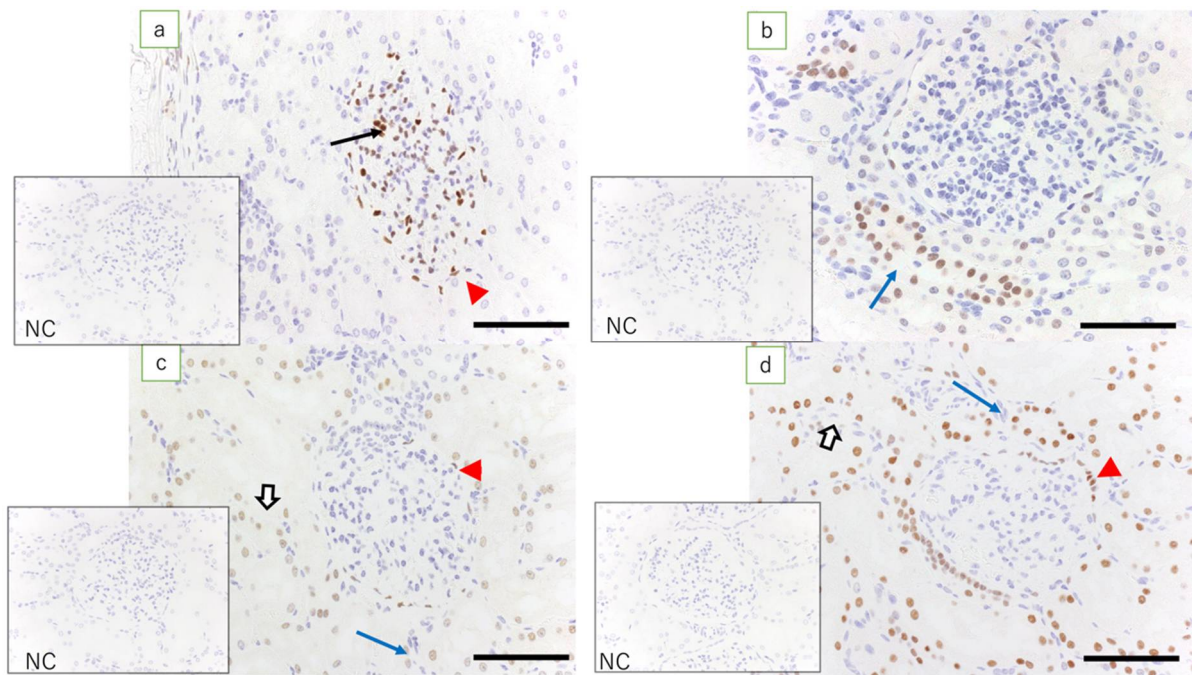


**Figure 2.** Ewe's kidney (immunostaining, scale bar: 100  $\mu$ m). (a) Expression of WT1 is found in glomerular epithelial cells (arrow) and epithelial cells of Bowman's capsule (red arrowhead); (b) low expression of Pax2 is found only in the collecting duct epithelial cells (blue arrow); (c) expression of Pax8 is found in epithelial cells of Bowman's capsule (red arrowhead), tubular epithelial cells (white arrow), and epithelial cells in the collecting duct (blue arrow); and (d) expression of HNF1 $\beta$ , which is equivalent to that in the kidney in term lambs, is found in epithelial cells of Bowman's capsule (red arrowhead), tubular epithelial cells (white arrow), and epithelial cells in the collecting duct (blue arrow); NC: negative control.

Fetal kidneys at  $\leq 110$  days of gestation revealed the expression of Pax2 in the ureteric bud, C- and S-shaped bodies, and epithelial cells in the collecting duct (Figure 3b). In lambs at 90 days' gestation, expression of Pax2 was found in the middle and peripheral regions of the renal vesicle and C-shaped bodies, and in the S-shaped bodies proximal to the medulla (Figure 4c). In the kidneys of full-term fetuses, only epithelial cells in the collecting duct were positive, similar to the findings in the adult kidney (Figure 5b).

Fetal kidneys at  $\leq 110$  days of gestation revealed the expression of Pax8 in the ureteric bud, C- and S-shaped bodies, tubular epithelial cells, epithelial cells of Bowman's capsule, and epithelial cells in the collecting duct (Figure 3c). The expression of Pax8 in renal vesicles and C- and S-shaped bodies did not show obvious polarity. In the kidneys of term fetuses, the expression of Pax8 was found in epithelial cells of Bowman's capsule, tubular epithelial cells, and epithelial cells in the collecting duct (Figure 5c), similar to the findings in the adult kidneys.

In fetal kidneys at  $\leq 110$  days of gestation, the expression of HNF1 $\beta$  was found in C- and S-shaped bodies, tubular epithelial cells, some of the epithelial cells of Bowman's capsule, and epithelial cells in the collecting duct (Figure 3d). In the renal vesicles and C- and S-shaped bodies, high expression of HNF1 $\beta$  was mainly noted, slightly more proximal to the renal capsule than cells expressing WT1 (Figure 4d). In the kidneys of full-term fetuses, the expression of HNF1 $\beta$  was found in the epithelial cells of the Bowman's capsule, tubular epithelial cells, and epithelial cells in the collecting duct (Figure 5d), again similar to the findings in adult kidneys.

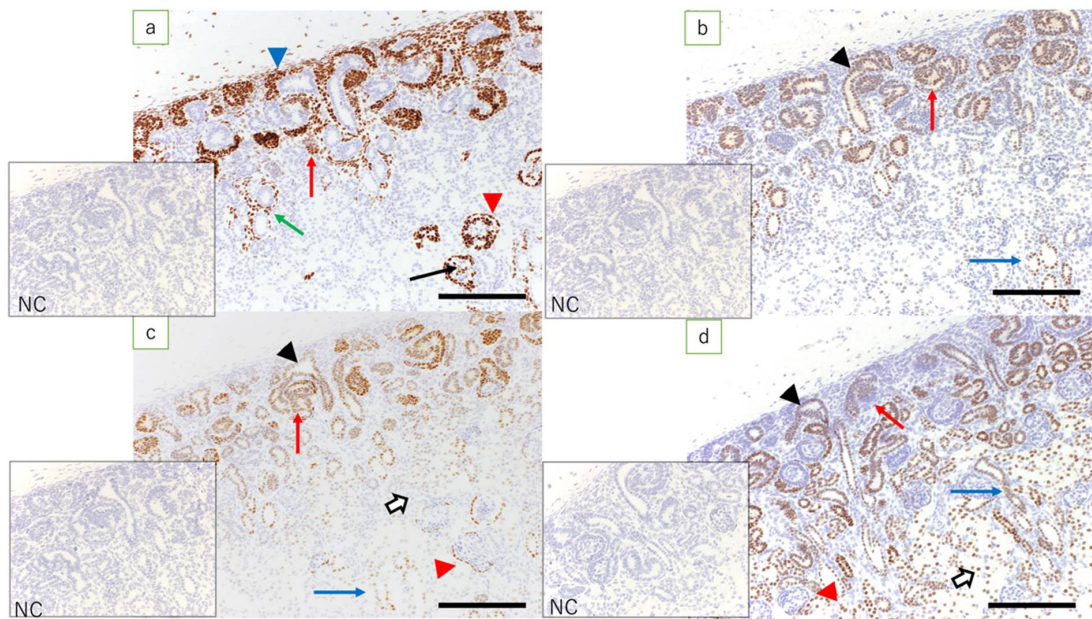


**Figure 3.** Fetal kidney at 90 days' gestation (immunostaining, scale bar: 200  $\mu$ m). (a) Expression of WT1 is found in metanephric mesenchymal cells, C- and S-shaped bodies (red arrow), glomerular epithelial cells (arrow), epithelial cells of Bowman's capsule (red arrowhead), medullary rays (green arrow), and interstitial cells in the medulla (blue arrowhead); (b) expression of Pax2 is found in the ureteric bud (arrowhead), C- and S-shaped bodies (red arrow), and epithelial cells in the collecting duct (blue arrow); (c) expression of Pax8 is found in the ureteric bud (arrowhead), C- and S-shaped bodies (red arrow), tubular epithelial cells (white arrow), epithelial cells of Bowman's capsule (red arrowhead), and epithelial cells in the collecting duct (blue arrow); (d) expression of HNF1 $\beta$  is found in the ureteric bud (arrowhead), C- and S-shaped bodies (red arrow), tubular epithelial cells (white arrow), some of the epithelial cells of Bowman's capsule (red arrowhead), and epithelial cells in the collecting duct (blue arrow); NC: negative control.

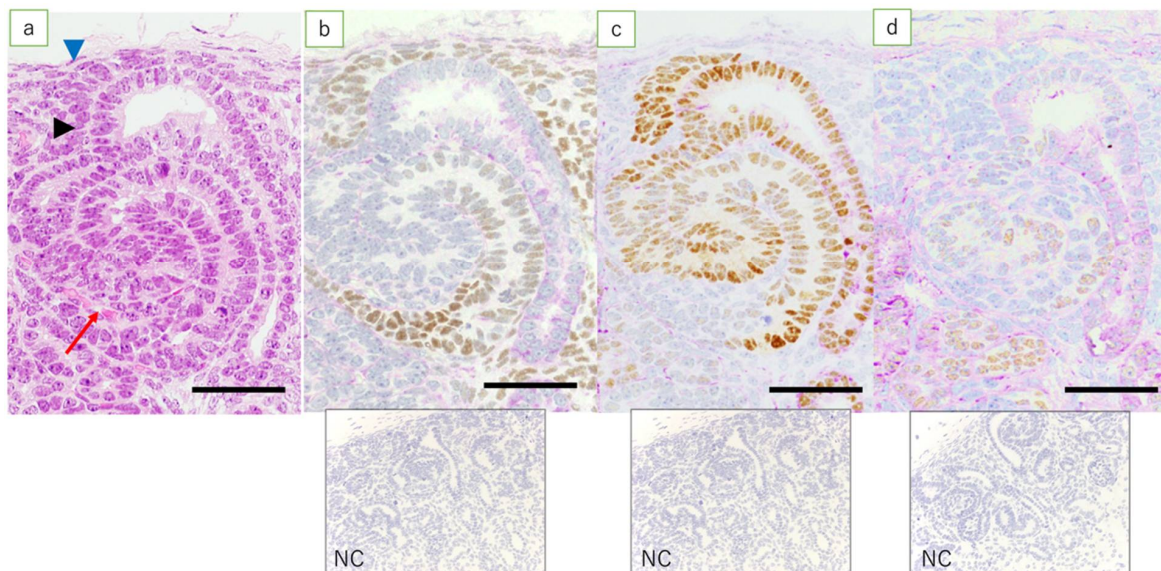


**Figure 4.** NZ in the fetal kidney at 90 days' gestation. (HE, immunostaining, scale bar: 40  $\mu$ m). (a) HE; metanephric mesenchymal cells (blue arrowhead), ureteric bud (arrowhead), S-shaped body (red arrow); (b) expression of WT1 is found in metanephric mesenchymal cells, renal vesicle, and S-shaped body, more proximal to the medulla; (c) expression of Pax2 is mostly found in the ureteric bud, renal vesicle, and S-shaped body; and (d) expression of HNF1 $\beta$  is found in the middle region, more proximal to the cortex in the S-shaped body than cells expressing WT1; NC: negative control.

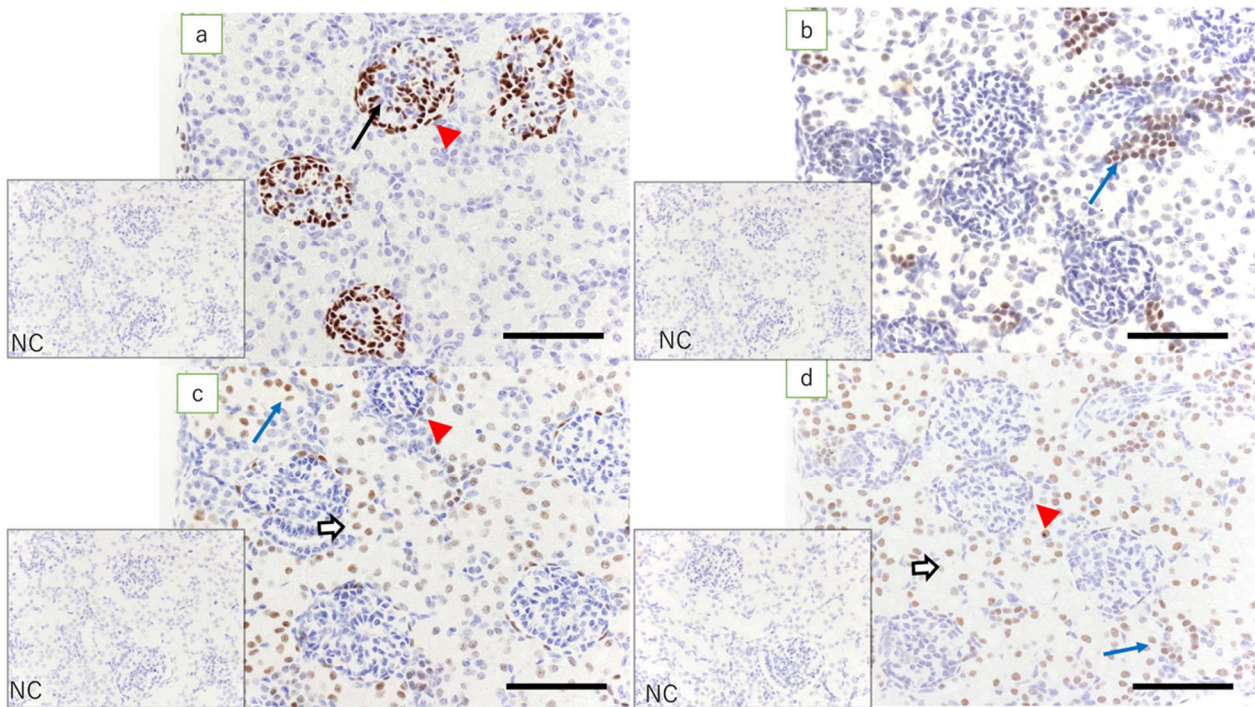


**Figure 5.** Fetal kidney at term (immunostaining, scale bar: 100  $\mu\text{m}$ ). The NZ has been completely lost. (a) Expression of WT1 is found in glomerular epithelial cells (arrow) and epithelial cells of Bowman’s capsule (red arrowhead); (b) expression of Pax2 is found in the epithelial cells in the collecting duct; (c) expression of Pax8 is found in tubular epithelial cells (white arrow), epithelial cells of the Bowman’s capsule (red arrowhead), and epithelial cells in the collecting duct (blue arrow); and (d) expression of HNF1 $\beta$  is found in epithelial cells of Bowman’s capsule (red arrowhead), tubular epithelial cells (white arrow), and epithelial cells in the collecting duct (blue arrow); NC: negative control.

#### 4. Discussion

WT1 was originally reported to be a causative gene in the genesis of nephroblastoma. However, it is mainly involved in the normal development of the kidney, spleen, and gonads. WT1 mutations may lead to nephroblastoma, glomerular sclerosis, gonadal dysgenesis, congenital diaphragmatic hernia, and cardiac disease. Mice with the loss of WT1 do not have kidneys or gonads, exhibit congenital diaphragmatic hernia, and die due to cardiac problems. In renal development, WT1 plays an essential role in MET (the basis of nephron differentiation), which initiates renal development [6]. HNF1 $\beta$  is a transcription factor that modulates the development and function of renal, hepatic, pancreatic, and urogenital epithelial cells. HNF1 $\beta$  is required for the branching of the ureteric bud, onset of kidney development, and nephron differentiation [7]. It was reported that the Pax gene family, consisting of nine genes, is involved in the development of the central nervous system, spine, eyes, and kidneys. It was found that Pax2 and Pax8 mainly contribute to the development of pronephros and mesonephros and that Pax2 and Pax8 double-null mice fail to generate the nephric duct and have renal dysplasia [8].

Recent *in vitro* studies of renal development have produced substantial advances, enabling the efficient creation of kidney-like tissue (kidney organoids) from hESCs and hiPSCs. Morizane et al. [3] found that the development of the nephron starts with the induction of T + TBX6 + (primitive streak) and WT1 + HOXD11 + Pax2 – LHX1 – (the posterior intermediate mesoderm). Although Pax2 and LHX1 are negative in the posterior intermediate mesoderm, they induce NPCs (SIX2 + SALL1 + WT1 + Pax2 +). The NPCs result in pretubular aggregates and Pax8, LHX1, and LAM-positive renal vesicles with the expression of HNF1 $\beta$  and BRN1, leading to the differentiation of epithelial cells [3]. The polarity in renal vesicles and C- and S-shaped bodies has started to be elucidated. In their lower pole, WT1 promotes the proximal differentiation (especially podocytes) by

antagonizing Pax2, leading to the release of signals that attract endothelial cells. HNF1 $\beta$  affects the upper pole of the C-shaped bodies. In the S-shaped bodies, the expression of HNF1 $\beta$  found in the lower pole and middle regions and modulates the expression of notch ligands and Irx1/2, promoting proximal, intermediate, and medial processes [9,10]. In a study of the collecting duct system, Taguchi et al. [11] generated induced Wolffian duct progenitor cells with the expression of Pax2, LHX1, Emx1, Sim1, and Gata3 from pluripotent stem cells. They observed the expression of HNF1 $\beta$ , Wnt9b, and Calb1, which are markers of a mature ureteric bud. In the anterior intermediate mesoderm, the expression of Osr1, Pax2, Lhx1, and Pax8 was noted, leading to the development of the ureteric bud from the Wolffian duct progenitor cells. In the Wolffian duct progenitor cells, due to the loss of expression of markers of the metanephros, such as WT1, the expression of Pax2 mainly affects renal development [11]. HNF1 $\beta$  was found to be involved in the growth and differentiation of the ureteric bud [12].

Previous *in vivo* studies have also shown that WT1, Pax2, Pax8, and HNF1 $\beta$  play important roles in the formation of the posterior kidney, but do not provide a detailed distribution of cells [13–15]. Using immunohistochemistry, we examined the expression of these transcription factors, which play important roles in renal development in lamb fetuses. In kidneys at 60 days of gestation, high expression of WT1 was noted in the mesenchyme around the ureteric bud. The expression of WT1 was also found in glomerular epithelial cells and the epithelial cells of Bowman's capsule. In renal vesicles and C- and S-shaped bodies, high expression of WT1 was observed in the lower pole. These results suggest that the expression of WT1 around the ureteric bud is involved in the development of the metanephric mesenchymal cells into the epithelial cells of Bowman's capsule. The loss of WT1 in the epithelial cells of Bowman's capsule and the surrounding tubular epithelial cells suggests the involvement of WT1 mainly in the development of podocytes in the glomerulus and the parietal epithelium of Bowman's capsule. During early gestation, the expression of Pax2 and Pax8 was observed in the ureteric bud and S-shaped bodies but not in glomerular epithelial cells. In fetal kidneys of all gestational durations, the expression of Pax2 was not observed in Bowman's capsule epithelial cells or tubular epithelial cells, but the expression of Pax8 was detected. The expression of Pax8 was maintained in an adult ewe's kidneys, suggesting that the expression of Pax8 is involved in the function of epithelial cells of the Bowman's capsule and the tubular epithelial cells. In early gestational lamb kidneys, high expression of HNF1 $\beta$  was found in the ureteric bud and S-shaped bodies. At later gestational time points, high expression of HNF1 $\beta$  was noted in the renal tubules and collecting ducts. In renal vesicles and C- and S-shaped bodies, high expression of HNF1 $\beta$  was noted in cells in the upper pole and middle regions, slightly more proximal to the renal capsule than cells expressing WT1. Unlike WT1, this suggests the involvement of HNF1 $\beta$  in the development of the (peripheral) epithelium of the nephron or tubular epithelial cells. In addition, high expression of HNF1 $\beta$  in the collecting duct suggests that HNF1 $\beta$  is involved in the development of the nephron and the collecting duct system.

The above results show that the development of the nephron from metanephric mesenchymal cells to tubular epithelial cells starts with the activation of WT1, leading to its development into glomerular epithelial cells and epithelial cells of the Bowman's capsule. In addition, the activation of HNF1 $\beta$ , Pax2, and Pax8 plays an important role in the differentiation of peripheral tubular epithelial cells. The results of the current study are consistent with previous *in vitro* studies using WT1 as a marker for the differentiation from undifferentiated stem cells into immature nephronal cells in which HNF1 $\beta$ , Pax2, and Pax8 expressed in sequence are used as markers of differentiation into podocytes, epithelial cells of Bowman's capsule, and tubular epithelial cells [10]. Furthermore, our findings suggest that Pax2 and Pax8 may be involved in nephron development and the development of the ureteric bud into the collecting duct system.

The role of the co-expression of Pax2 and Pax8 in the development of the collecting duct system has not yet been elucidated. In early-gestation fetuses, it was found that Pax2 and Pax8 are expressed independently and that Pax2 knock-out mice never develop into the

metanephros, whereas Pax8 knock-out mice show normal kidney development [15]. The postpartum expression of Pax2 persists only in the collecting duct, whereas the expression of Pax8 during early gestation and postpartum is found throughout the entire epithelium from Bowman's capsule to the collecting duct. This suggests that Pax8 modulates selective transporters in the medulla to maintain the salt-water balance even in the postpartum period [16]. Future genetic research should elucidate the morphological features found in the current study of renal development.

In this study, the location of the expression of transcription factors in vivo that have been reported to be involved in renal development in in vitro studies was clarified. However, this study provides a morphological point of view of cells, and genetic studies are required to determine its specific role, which is the limitation of this study. Each of these cells, consisting of the glomerulus, Bowman's capsule, renal tubules, and collecting ducts, in mature kidney tissue may have a specific function, and the abovementioned transcription factors may be involved in the expression of these genes that are responsible for functional expression. Future studies on the relationship between transcription factors and the activation of these genes might help to elucidate the process of renal development.

In the studies of this area, models of the early embryonic period using cultured cells and small animals such as mice and rats have been examined [8,12,17]. However, in this study, the sheep model, which is a large animal, was used, and we compared and examined it with term models and ewes. It is necessary to examine a knock-out model for the study of gene expression, but this could not be done here because the method has not yet been established for sheep.

## 5. Conclusions

Immunohistochemistry for WT1, HNF1 $\beta$ , Pax2, and Pax8 may help with evaluating the transcription factors in renal development. Our findings suggest the possibility that WT1 is mainly involved in development of the nephron, whereas HNF1 $\beta$ , Pax2, and Pax8 are involved in the maturation of the nephron and development of the Wolffian duct that branches to form the peripheral collecting ducts.

**Author Contributions:** Y.N. and J.K. performed experiments, data analysis, and writing. H.K., K.C.P. and Y.S. performed all of the fetal surgery and reviewed and revised the manuscript. K.K. (Kohei Kawaguchi), K.K. (Kosuke Kudo), T.K., J.O., K.T., K.O., H.N. and S.F. reviewed and revised the manuscript. All authors have read and agreed to the published version of the manuscript.

**Funding:** This research received no external funding.

**Institutional Review Board Statement:** The study was conducted according to the guidelines of the Declaration of Helsinki. It was approved by the Animal Ethics Committee of the Wellington School of Medicine and Health Sciences, University of Otago Wellington, New Zealand (approval numbers WAEC 8-03, W03/07, W02-11, W01-12, AEC4-14, and AEC 1-16).

**Informed Consent Statement:** Not applicable.

**Data Availability Statement:** Not applicable.

**Acknowledgments:** Management of the animals in the laboratory was supervised by Rebecca Dyson and Taylor Wilson, animal technicians at the BRU at University of Otago, Wellington. The authors thank Manabu Kubota and the other staff at the Department of Pathology, St. Marianna University School of Medicine for their assistance in processing the histology.

**Conflicts of Interest:** None. This research did not receive any specific grants from funding agencies in the public, commercial, or not-for-profit sectors.

## References

1. Costantini, F.; Kopan, R. Patterning a complex organ: Branching morphogenesis and nephron segmentation in kidney development. *Dev. Cell.* **2010**, *18*, 698–712. [CrossRef]
2. Morizane, R.; Miyoshi, T.; Bonventre, J.V. Concise Review: Kidney Generation with Human Pluripotent Stem Cells. *Stem Cells* **2017**, *35*, 2209–2217. [CrossRef] [PubMed]

3. Morizane, R.; Lam, A.Q.; Freedman, B.S.; Kishi, S.; Valerius, M.T.; Bonventre, J.V. Nephron organoids derived from human pluripotent stem cells model kidney development and injury. *Nat. Biotechnol.* **2015**, *33*, 1193–1200. [CrossRef] [PubMed]
4. Tanaka, K.; Manabe, S.; Ooyama, K.; Seki, Y.; Nagae, H.; Takagi, M.; Kolke, J.; Zuccollo, J.; Pringle, K.C.; Kitagawa, H. Can a pressure-limited V-A shunt for obstructive uropathy really protect the kidney? *J. Pediatr. Surg.* **2014**, *49*, 1831–1834. [CrossRef]
5. Kitagawa, H.; Pringle, K.C.; Koike, J.; Zuccollo, J.; Nakada, K. Different phenotypes of dysplastic kidney in obstructive uropathy in fetal lambs. *J. Pediatr. Surg.* **2001**, *36*, 1698–1703. [CrossRef]
6. Hastie, N.D. Wilms' tumour 1 (WT1) in development, homeostasis and disease. *Development* **2017**, *144*, 2862–2872. [CrossRef] [PubMed]
7. Ferrè, S.; Igarashi, P. New insights into the role of HNF-1 $\beta$  in kidney (patho) physiology. *Pediatr. Nephrol.* **2019**, *34*, 1325–1335. [CrossRef]
8. Narlis, M.; Grote, D.; Gaitan, Y.; Boualia, S.K.; Bouchard, M. Pax2 and pax8 regulate branching morphogenesis and nephron differentiation in the developing kidney. *J. Am. Soc. Nephrol.* **2007**, *18*, 1121–1129. [CrossRef]
9. O'Brien, L.L.; McMahon, A.P. Induction and patterning of the metanephric nephron. *Semin. Cell Dev. Biol.* **2014**, *36*, 31–38. [CrossRef] [PubMed]
10. Hiratsuka, K.; Monkawa, T.; Akiyama, T.; Nakatake, Y.; Oda, M.; Goparaju, S.K.; Kimura, H.; Chikazawa-Nohtomi, N.; Sato, S.; Ishiguro, K.; et al. Induction of human pluripotent stem cells into kidney tissues by synthetic mRNAs encoding transcription factors. *Sci. Rep.* **2019**, *9*, 913. [CrossRef]
11. Taguchi, A.; Nishinakamura, R. Higher-Order Kidney Organogenesis from Pluripotent Stem Cells. *Cell Stem Cell* **2017**, *21*, 730–746.e6. [CrossRef] [PubMed]
12. Lokmane, L.; Heliot, C.; Garcia-Villalba, P.; Fabre, M.; Cereghini, S. vHNF1 functions in distinct regulatory circuits to control ureteric bud branching and early nephrogenesis. *Development* **2010**, *137*, 347–357. [CrossRef] [PubMed]
13. Coffinier, C.; Thépot, D.; Babinet, C.; Yaniv, M.; Barra, J. Essential role for the homeoprotein vHNF1/HNF1beta in visceral endoderm differentiation. *Development* **1999**, *126*, 4785–4794. [CrossRef]
14. Pontoglio, M.; Barra, J.; Hadchouel, M.; Doyen, A.; Kress, C.; Bach, J.P.; Babinet, C.; Yaniv, M. Hepatocyte nuclear factor 1 inactivation results in hepatic dysfunction, phenylketonuria, and renal Fanconi syndrome. *Cell* **1996**, *84*, 575–585. [CrossRef]
15. Bouchard, M.; Souabni, A.; Mandler, M.; Neubüser, A.; Busslinger, M. Nephric lineage specification by Pax2 and Pax8. *Genes Dev.* **2002**, *16*, 2958–2970. [CrossRef] [PubMed]
16. Laszczyk, A.M.; Higashi, A.Y.; Patel, S.R.; Johnson, C.N.; Soofi, A.; Abraham, S.; Dressler, G.R. Pax2 and Pax8 Proteins Regulate Urea Transporters and Aquaporins to Control Urine Concentration in the Adult Kidney. *J. Am. Soc. Nephrol.* **2020**, *31*, 1212–1225. [CrossRef] [PubMed]
17. Kreidberg, J.A.; Sariola, H.; Loring, J.M.; Maeda, M.; Pelletier, J.; Housman, D.; Jaenisch, R. WT-1 is required for early kidney development. *Cell* **1993**, *74*, 679–691. [CrossRef]





## Article

# Regenerative Polarity of the Fin Ray in Zebrafish Caudal Fin and Related Tissue Formation on the Cut Surface

Wataru Nakajima <sup>†</sup>, Soya Nakanishi <sup>†</sup>, Ryosuke Hosoya, Toshiaki Uemoto, Shiro Ohgo <sup>‡</sup> and Naoyuki Wada <sup>\*</sup>

Department of Applied Biological Science, Tokyo University of Science, 2641 Yamazaki, Noda 278-8510, Japan; sobakarute\_sub@yahoo.co.jp (W.N.); nakanishisoya@gmail.com (S.N.); masha-guiter.pc@outlook.com (R.H.); shimashima0401fish@gmail.com (T.U.); ohgo@kitasato-u.ac.jp (S.O.)

\* Correspondence: nwada@rs.tus.ac.jp

<sup>†</sup> These authors contributed equally to this work.

<sup>‡</sup> Present address: College of Liberal Arts and Sciences, Kitasato University, Sagamihara 252-0373, Japan.

**Abstract:** Zebrafish caudal fin rays are used as a model system for regeneration because of their high regenerative ability, but studies on the regeneration polarity of the fin ray are limited. To investigate this regeneration polarity, we made a hole to excise part of the fin ray and analyzed the regeneration process. We confirmed that the fin rays always regenerated from the proximal margin toward the distal margin, as previously reported; however, regeneration-related genes were expressed at both the proximal and distal edges of the hole in the early stage of regeneration, suggesting that the regenerative response also occurs at the distal edge. One difference between the proximal and distal margins is a sheet-like tissue that is formed on the apical side of the regenerated tissue at the proximal margin. This sheet-like tissue was not observed at the distal edge. To investigate whether the distal margin was also capable of forming this sheet-like tissue and subsequent regeneration, we kept the distal margin separated from the proximal margin by manipulation. Consequently, the sheet-like tissue was formed at the distal margin and regeneration of the fin ray was also induced. The regenerated fin rays from the distal margin protruded laterally from the caudal fin and then bent distally, and their ends showed the same characteristics as those of the normal fin rays. These results suggest that fin rays have an ability to regenerate in both directions; however, under normal conditions, regeneration is restricted to the proximal margin because the sheet-like tissue is preferentially formed on the apical side of the regenerating tissue from the proximal margin.

**Citation:** Nakajima, W.; Nakanishi, S.; Hosoya, R.; Uemoto, T.; Ohgo, S.; Wada, N. Regenerative Polarity of the Fin Ray in Zebrafish Caudal Fin and Related Tissue Formation on the Cut Surface. *J. Dev. Biol.* **2021**, *9*, 50. <https://doi.org/10.3390/jdb9040050>

Academic Editors: Simon J. Conway, Tsutomu Nohno and Hideyo Ohuchi

**Keywords:** zebrafish; fin regeneration; tissue polarity; wound epithelium

Received: 13 September 2021

Accepted: 15 November 2021

Published: 19 November 2021

**Publisher's Note:** MDPI stays neutral with regard to jurisdictional claims in published maps and institutional affiliations.



**Copyright:** © 2021 by the authors. Licensee MDPI, Basel, Switzerland. This article is an open access article distributed under the terms and conditions of the Creative Commons Attribution (CC BY) license (<https://creativecommons.org/licenses/by/4.0/>).

## 1. Introduction

Zebrafish have a high regenerative capacity in many organs, including the retina, spinal cord, part of the heart, and fins [1–4]. In particular, the caudal fin is often used as a model system for regeneration studies (for review see [3–9]). The caudal fin skeleton of zebrafish is composed of bony tissues called fin rays, and each fin ray consists of two semicircular structures called hemi-rays. Fin rays are connected by an epithelial sheet with connective tissue, which is called the inter-ray [7,8,10].

Regeneration proceeds in the following three stages: wound healing, blastema formation, and tissue reorganization [8,11]. In the wound healing phase, the cut surface is closed and covered by an epithelial tissue called the wound epithelium [12,13]. Then, the wound epithelium secretes diffusible signaling molecules, and these molecules, in turn, induce the cells beneath the epithelium to dedifferentiate and form the blastema. The blastema is composed of undifferentiated mesenchymal cells beneath the wound epithelium and elongates distally by active proliferation of the mesenchymal cells. In parallel, cells in the proximal region of the blastema begin to re-differentiate into bone and surrounding connective tissue [5,6,9]. Analysis of the gene expression and molecular interactions during the fin regeneration has revealed genes that are selectively expressed in the wound epithelium

or regeneration blastema [6,7,9,14–17]. For example, *fgf24*, its downstream factor *pea3*, and the transcription factor *msxd* are expressed in the wound epithelium from an early stage of regeneration [18–22]. Moreover, expression of genes such as *msxb* and *fgf20a* has been reported in mesenchymal cells, which constitute the blastema [21–24]. The expression of these genes can be considered as an indicator of the formation of each tissue.

Organ regeneration in vertebrates generally proceeds in a unidirectional manner, from the trunk to the distal part of the organ. Studies on the regeneration polarity of fin rays are limited and it has been suggested that their regeneration is also unidirectional from the proximal to the distal part of the fin [3,25]. One of the studies on the regeneration polarity of fin rays involved the partial excision of fin rays and an observation of the direction of the subsequent regeneration. When a part of the caudal fin ray of the zebrafish is excised, the missing part regenerates from the remaining tissue at the proximal margin of the hole, but not in the opposite direction [3,25]. Although the mechanism of polarized regeneration of the fin ray is not well understood, opposite regeneration of the caudal fin has been reported in long fin (*lof*) mutants of zebrafish [26], and the calcineurin signaling pathway has been reported to be involved in the polarity of caudal fin regeneration [26]. These results suggest that opposite directional regeneration of the zebrafish caudal fin only occurs when there are specific genetic mutations present or under pharmacological conditions. In a classical experiment, fin ray regeneration from the distal edge of the hole was observed using goldfish [27]. Therefore, the fin ray of wild-type zebrafish may also have an ability to regenerate in the opposite direction.

In this study, we re-analyzed the polarity of caudal fin ray regeneration in wild-type zebrafish by examining the regeneration of a hole in the fin. Histological observation revealed that fin ray regeneration progressed unidirectionally from the proximal margin to the distal direction, as previously reported. However, genes induced in the early stage of regeneration either in the wound epidermis or blastema were also expressed in cells in the distal margin, suggesting that an early regenerative response is also induced in the distal margin. To elucidate the cause of unidirectional fin ray regeneration, we analyzed the sheet-like region at the apical half of the regenerated tissue on the proximal margin. The expression of several regeneration-related genes was reduced in the region, which distinguished this region from more inner regions and because no similar sheet-like region was observed at the distal margin of the hole, we hypothesized that this tissue was related to the polarity of the fin regeneration and examined the conditions under which this sheet-like region could form at the distal margin. When the distal margin of the hole was kept out of contact with the proximal margin by manipulation, the sheet-like tissue was autonomously formed in the distal margin, and fin ray regeneration also occurred from the distal margin. These results suggest that the zebrafish fin ray has an ability to regenerate distal structures bidirectionally, but regeneration is usually restricted to the proximal margin associated with the preferential formation of the sheet-like tissue on the proximal margin.

## 2. Materials and Methods

### 2.1. Fish

Zebrafish (AB strain) were purchased from a local supplier and were housed in a recirculating system (14 h day/10 h night cycle; 27 °C). Amputation and regeneration experiments of the caudal fin were performed on 6–12-month-old adult zebrafish. All experimental protocols were evaluated and approved by the Regulation for Animal Research at Tokyo University of Science (approval number: 1880).

### 2.2. Fin Ray Excision

Zebrafish were anesthetized with tricaine (Tokyo Kasei, T0941). Then, the caudal fin ray and surrounding soft tissue were hollowed out in a rectangular shape using a fine cutter and fine forceps (Figure 1A). In most experiments, 3–4 segments of a single fin ray that did not include the bifurcation were excised. The fin was left to regenerate until

the desired time and used for subsequent experiments. In all experiments, the fins were fixed in 4% para-formaldehyde (PFA)/PBS and used for subsequent experiments. Each experiment was independently performed at least three times, and almost the same results were obtained.

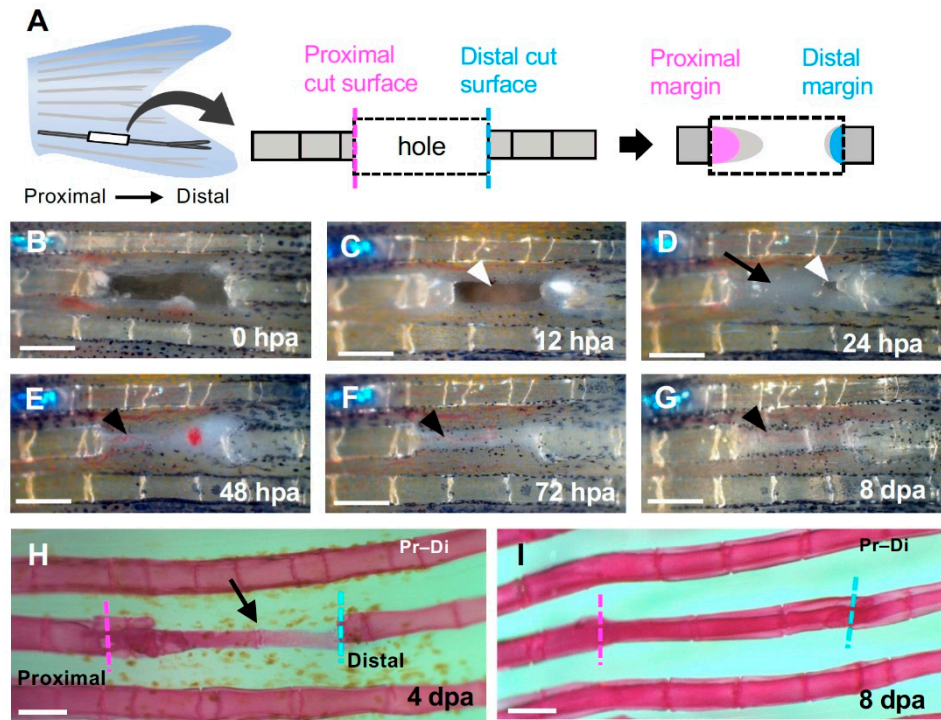


**Figure 1.** Regeneration of the hole induced by partial excision of the fin ray. (A) Schematic diagram of fin ray hollowing. Three to four segments were hollowed out to exclude the branching area (left). The regenerated structures formed from the cells that were distributed on the proximal (magenta) or distal (cyan) surfaces of the hollowed-out hole were investigated (center and right). (B–G) Time course of regeneration in the hole. (B) 0 h post-amputation (hpa); (C) 12 hpa; (D) 24 hpa; (E) 48 hpa; (F) 72 hpa and (G) 8 days post-amputation (dpa). (C) At 12 hpa, the hole remained open (arrowhead). (D) At 24 hpa, the hole was almost covered by epithelium (arrow) except for a small portion near the distal surface (arrowhead). (E–G) At 48 hpa and later, precursor tissue of the fin ray was extended from the proximal side (black arrowheads). (H) At 4 dpa, a fin ray primordium was formed from the proximal to distal edge (black arrow). (I) At 8 dpa, segments were observed and regeneration was complete. Scale bars = 300  $\mu$ m.

To keep the distal edge of the hole separate from the tissues formed in the proximal margin, all epithelium and underlying mesenchyme regenerated from the proximal margin were re-excised at 24 h after the first fin ray excision. This process was repeated two more times so that the distal surface of the hole was kept independent from the proximally derived tissue and allowed to regenerate from distal edge.

### 2.3. Histological Analysis

To analyze the skeletal pattern, the fin ray skeleton was fixed with 4% PFA and dehydrated with methanol. The samples were stained with an alcian blue and alizarin red solution, then cleared with 50% Glycerol-DDW. For the histological sections, the fixed samples were decalcified with EDTA, sectioned with cryostat, and stained with hematoxylin and eosin according to standard procedures.

#### 2.4. Whole Mount in Situ Hybridization

All probes used in this study were synthesized using DIG RNA Labeling Mix (Sigma-Aldrich). *msxb* plasmid was provided by Dr Yano (Jikei Medical School, Japan). The *fgf20a*, *fgf24*, *msxd*, and *pea3* were cloned by PCR. Primers used in the study were as follows:

*fgf20a* forward: 5'-ATGGGTGCAGTCCGGCAGCTGGTGG-3'

*fgf20a* reverse: 5'-TCAGCTGTGACCTAGAACATCCTTG-3'

*fgf24* forward: 5'-ATGICTGTTCTGCCGTC AAGGTICA-3'

*fgf24* reverse: 5'-TCAGTTTGTATTGGGGTTGGGTT-3'

*msxd* forward: 5'-ATGTCGCGTCCGCGAGCCTGAAGG-3'

*msxd* reverse: 5'-TCATGCGAGGTGATACATGCTGTA-3'

*pea3* forward: 5'-ATGGATTATAAGATGGATGGATATC-3'

*pea3* reverse: 5'-TTAGTACATGTAGCCTTTGGAGTAGG-3'

Whole-mount in situ hybridizations were performed according to the method described by Sims et al. [28] with minor modifications.

#### 2.5. Immunohistochemistry

For the immunocytochemistry, we used the following antibodies. As the primary antibodies: anti-p63 (1:200, #ACR163A, BCM, Funakoshi), anti-BrdU (1:200, MS-1058-P0, Thermo SCIENTIFIC, Waltham, MA, USA), anti-active caspase (1:500, R&D systems, AF835), and anti-tubulin (1:250, Sigma, T6793, St. Louis, MO, USA). As the secondary antibodies, Alexa 488 labeled anti-mouse IgG (1:500, Abcam, #AB150109, Cambridge, UK) and Alexa 488 labeled anti rabbit IgG (1:500, ThermoFisher, #A-11008, Waltham, MA, USA) were used. The detailed process of the immunohistochemistry was performed according to the method described in Ohgo et al. [29].

#### 2.6. 3D Reconstruction of the Fin Ray Skeleton

A 3D reconstruction of the regenerated fin ray was performed with the correlative light microscopy and block-face imaging (COMBI) method described in Tajika et al. [30]. Briefly, each alizarin-stained fin ray was embedded in an OCT compound and then sectioned with a cryostat. Each surface of the sectioned plane was photographed, the photo data were stacked, and the image of the fin skeleton was 3D-reconstructed using HOROS (Athens, Greece).

### 3. Results

#### 3.1. Morphological and Histological Analysis of Hole Regeneration

First, to show the polarity of the fin regeneration, we hollowed out 3–4 segments of one fin ray to make a hole and analyzed the time course of the hole closure and fin ray regeneration. We compared the morphology of both the proximal and distal margins, and the tissue structures that formed when each margin was repaired (Figure 1A).

Twelve hours after excision, the entire edges of the excised hole were covered by epithelium (Figure 1C). By 24 h after amputation (hpa), a semi-transparent sheet-like tissue expanded from the proximal edge (Figure 1D, arrow), and almost all of the hole except a small portion near the distal edge was filled by the sheet (Figure 1D, arrowhead). Forty-eight hours later, the hole was completely covered with the sheet, and a subcutaneous cell aggregate extended from the proximal side (Figure 1E, arrowhead). After 72 h, a regenerated fin ray primordium was formed from the proximal side (Figure 1F, arrowhead); after eight days, the regenerated fin ray with segments reached the distal end of the excised fin ray (Figure 1G, arrowhead). We also analyzed the shape of the skeleton during regeneration. Four days later, the regenerated fin ray, which was thinner than the original fin ray, was observed from the proximal margin (Figure 1H, arrow); however, no primordium was observed in the distal margin. Eight days later, the fin ray regenerated with several segments, and the proximal and distal fin ray fused (Figure 1I).

We then performed a histological analysis. At 12 hpa, both the proximal and distal cut ends were covered by epithelium (Figure 2A). The proximal end was covered with thick

epithelium (Figure 2A, arrow), whereas the distal end was covered with thin epithelium (Figure 2A, arrowheads). At 24 hpa, a distally elongated structure was formed on the proximal margin. In the apical part of the structure, the epithelial cell layers formed a somewhat thickened sheet (Figure 2B, arrow), and some mesenchymal cells were also observed beneath the sheet. By contrast, in the distal margin of the hole, the surface was covered with the epithelium, whereas no sheet-like tissue that expanded toward the hole was formed (Figure 2B, arrowheads). At 48 hpa, tissues formed on the proximal and distal margins were connected and no obvious hole-like gap remained (Figure 2C). At the junction of both margins, the remaining epithelial sheet was observed (Figure 2C, arrowheads). At 72 hpa, the proximal and distal edges were fully connected, and regenerated bone tissue was observed from the proximal toward the distal edge (Figure 2D, arrows). In contrast, no bone tissue regeneration toward the proximal edge was observed at the distal edge (Figure 2D, arrowheads).

The distribution of epithelial cells in the apical region of the proximal and distal margins were then examined based on the expression of the p63 protein. At 24 hpa, the apical region of the proximal margin was covered with a p63-positive epithelial cell sheet (Figure 2E, arrow). There were p63-negative mesenchymal cells observed beneath the epithelial sheet near the cut surface, but it was unclear whether mesenchymal cells were distributed in the apical region. In contrast, accumulation of p63-positive epithelial cells was visible in the cut surface of the distal margin, but they did not extend as a sheet-like tissue (Figure 2F).

### 3.2. Expression of Regeneration-Related Genes during Hole Regeneration

Next, we examined the gene expression during the hole regeneration. First, we examined the *fgf20a*, which was expressed in the blastema cells during fin regeneration [23,24]. At 12 hpa, *fgf20a* was observed in both the proximal and distal margins of the hole (Figure 3A). At 24 hpa, the *fgf20a* expression was maintained in the cells of the inner half of the proximal-derived tissue (Figure 3B, arrow), but it was faint in the apical half of the tissue (Figure 3B, bracket). Interestingly, *fgf20a* was also expressed in cells of the distal margin (Figure 3B, arrowhead). At 48 hpa, *fgf20a* was expressed in the tissues elongated from the proximal cut surface (Figure 3C, arrow), and the expression at the distal margin was also maintained (Figure 3C, arrowhead).

We also investigated the expression of *msxb*, which is another blastema marker [21,22]. Expression of *msxb* was detected at 24hpa; strong expression of *msxb* was observed in the inner half of the proximal-derived tissue (Figure 3E, arrow), but faint expression was detected in the apical half of the tissue (Figure 3E, bracket). At the distal margin, *msxb* was also expressed in mesenchymal cells (Figure 3E, arrowhead). The expression was spatially restricted but obvious, which indicated the existence of blastema-like cells in the distal margin. At 48 hpa, *msxb* was maintained in the tissues of both the proximal and distal margins (Figure 3F, arrow and arrowhead).

We then examined the *pea3* expression that is mainly expressed in the wound epidermis and its basal layer [20,23]. At 24 hpa, *pea3* expression was observed in the inner half of the proximal-derived tissue, which is where *fgf20a* and *msxb* were also expressed (Figure 3H, arrow and arrowheads), and a reduced expression in the apical half of the proximal-derived sheet-like tissue was also observed (Figure 3H, bracket). The *pea3* expression sites were similar to those of *msxb* and *fgf20a*, but there was a marked decrease in expression in the apical half of the proximal margin at 24 hpa.

We also analyzed the expression of *msxd* and *fgf24* in the wound epidermis [18–22]. The *msxd* was strongly expressed in the inner half of the regenerating tissue on the proximal margin (Figure 3J, arrow), but it was weakly expressed in the apical half (Figure 3J, bracket). In the distal margin, an apparent signal of *msxd* expression was observed (Figure 3J, arrowhead). The *fgf24* expression was weakly observed throughout the regenerated tissue (Figure 3K, arrow).

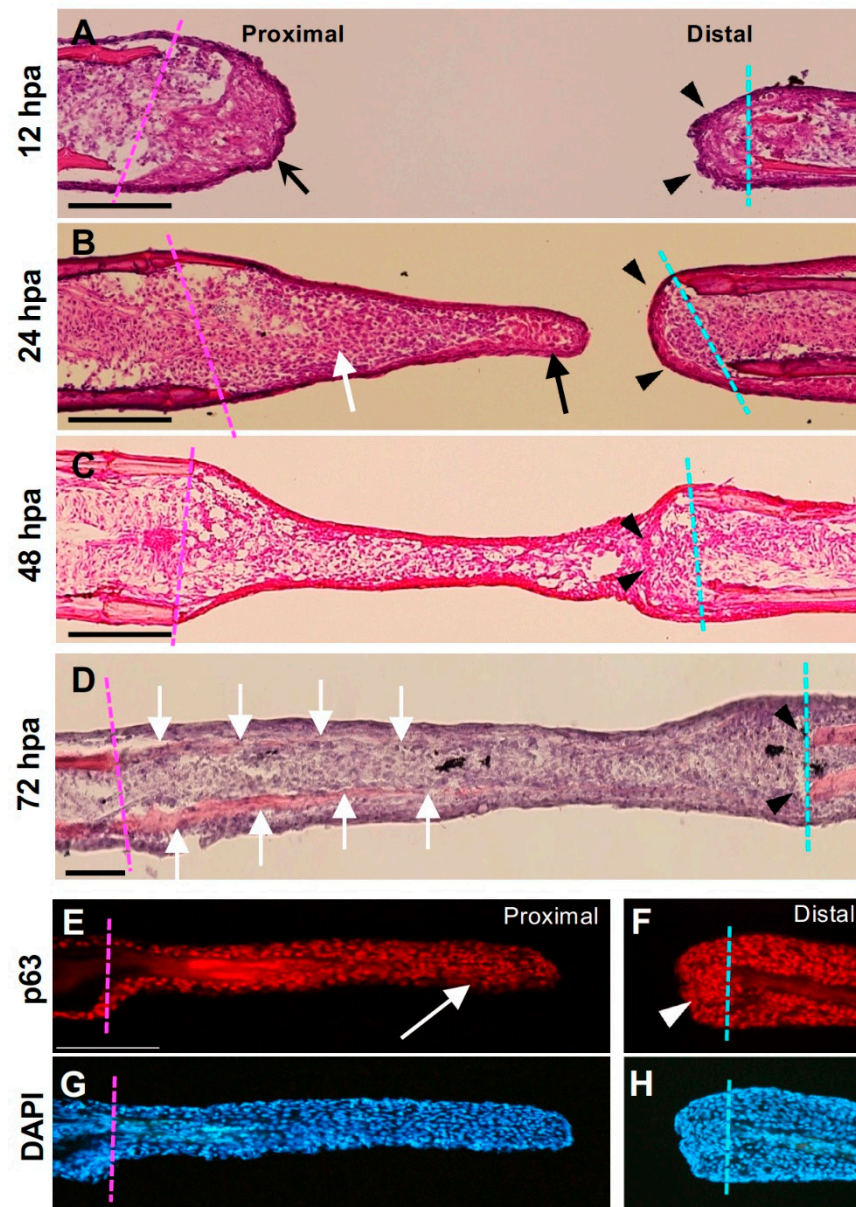


**Figure 2.** Histological analysis of the hole excision site. (A–D) Hematoxylin–eosin–stained images after fin ray hollowing. The magenta dotted line indicates the cut surface of the proximal part, and the cyan dotted line indicates the cut surface of the distal part. (A) At 12 h post-amputation (hpa), the proximal surface of the hole was covered with thick epithelium (arrow), whereas the distal surface was covered with thin epithelium (arrowhead). (B) At 24 hpa, the extended tissue was at the proximal cut surface of the hole. The apical part of the tissue mainly consisted of the epithelial sheet (arrows), and some mesenchymal cells beneath the sheet were also visible. By contrast, the distal cut surface was covered with a thin epithelial sheet and was not elongated (arrowheads). (C) The epithelium and mesenchyme extending from the proximal surface of the hole connected with those in the distal surface. At the junction, epithelial-like cellular fragments derived from the distal surface remained (arrowheads). At this stage, bone formation had not occurred. Scale bars = 300  $\mu$ m. (D) At 72 hpa, newly formed bone tissue was observed from the proximal edge toward the tip (arrows), whereas no regenerated bone was observed from the distal cut surface. (E) Distribution of the p63 protein in regenerated tissue from the proximal margin. In the apical half of the tissue, there was a layer of p63-positive epithelial cells (arrow). (F) Distribution of p63 in the distal margin. Although accumulation of p63-positive cells was visible (arrowhead), they do not extend proximally. (G,H) are DAPI staining views of (E,F), respectively.

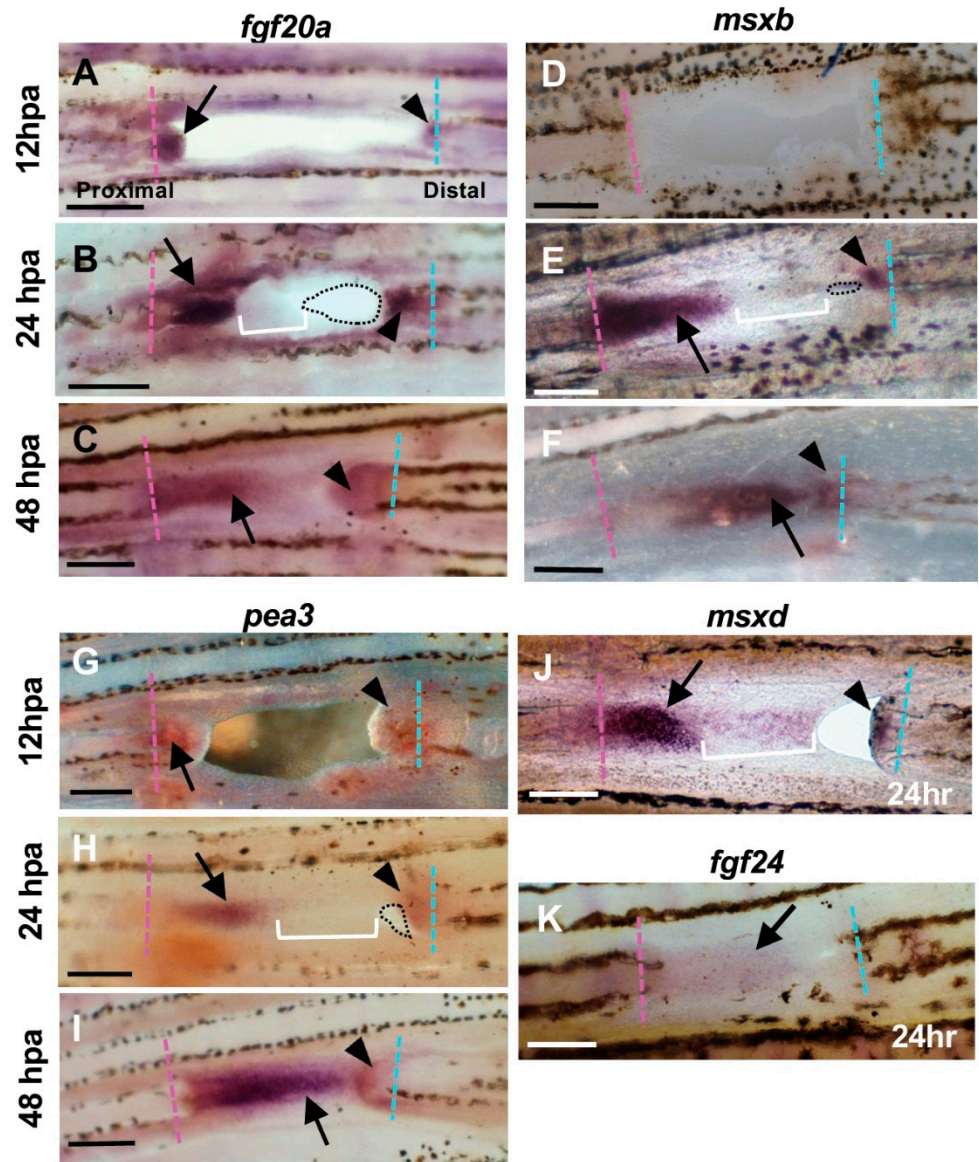


**Figure 3.** Expression of regeneration-related genes during hole closure. (A–C) *fgf20a* expression. (A) At 12 h post-amputation (hpa). The *fgf20a* expression was observed in the cells of the proximal margin (arrow), and distal margin (arrowhead) of the hole. (B) At 24 hpa. In the proximal margin, *fgf20a* was strongly expressed in the cells of the inner half of the regenerated tissue (arrow), whereas the expression was faint in the apical half of the tissue (bracket). In the distal margin, *fgf20a* expression was also observed, but the area of expression was small (arrowhead). Dotted lines show the remaining hole. (C) At 48 hpa. The *fgf20a* expression was maintained in both proximal- and distal-derived tissues (arrow and arrowhead, respectively), and both domains were close together. (D–F) *msxb* expression. (D) At 12 hpa, *msxb* was not expressed. (E) At 24 hpa, in the proximal margin, *msxb* was strongly expressed in the cells near the cut surface of the regenerated tissue (arrow). The expression was faint in the distal half of the tissue that filled the hole (bracket). In the distal margin, *msxb* expression was restricted to a small area (arrowheads). Dotted lines show the remaining hole. (F) At 48 hpa, *msxb* was maintained in both proximal- and distal-derived tissues (arrow and arrowhead, respectively). (G–I) *pea3* expression. (G) At 12 hpa, *pea3* expression was observed in the cells both in the proximal and distal margins of the hole (arrow and arrowhead, respectively). (H) At 24 hpa, *pea3* was expressed in the cells of the inner half of the regenerated tissue in the proximal margin (arrow), whereas the expression was weakened in the apical half of the tissue (brackets). In the distal margin, *pea3* expression was also observed, although the expression domain was small (arrowhead). Dotted



lines show the remaining hole. (I) At 48 hpa, *pea3* expression was maintained in both proximal- and distal-derived tissues (arrow and arrowhead, respectively). (J) *msxd* expression at 24 hpa. In the proximal margin, *msxd* was strongly expressed in the cells of the inner half of the regenerated tissue (arrow), whereas the expression was weakened in the apical half of the tissue (bracket). In the distal margin, *msxd* expression was also observed, but the area of expression was restricted (arrowhead). (K) *fgf24* expression at 24 hpa. The *fgf24* was weakly expressed in the epithelium of the regenerated tissue from the proximal margin (arrow). Expression in the distal margin was unclear. Scale bars = 300  $\mu\text{m}$ .

Overall, the features of regeneration-related gene expression are summarized as follows. In the tissue regenerated from the proximal margin, the expression of regeneration-related genes was apparent in its inner half, whereas the expression in its apical half tended to be faint and this indicates regional differences of the tissue. By contrast, in the tissue of the distal margin, the expression of these genes was also observed despite the failure of subsequent fin ray regeneration.

### 3.3. Cellular Responses during Hole Regeneration

We next investigated the cell proliferation around the hole by detecting cells incorporating BrdU. At 24 hpa, cell proliferation increased in the proximal margin (Figure 4A, arrow), but was low in the distal margin (Figure 4A, arrowhead). This tendency was also maintained at 48 h. At 48 hpa, proliferation was also high in the proximal side (Figure 4B, arrow), but low in the distal side (Figure 4B, arrowhead), which showed that cell proliferation was preferentially enhanced in the proximal margin.

We further investigated the distribution of nerve fibers at the cut surface because nerve fibers have been suggested to have a role in pectoral fin regeneration [23]. At 24 hpa, nerve fibers were distributed to the proximal half of the regenerated tissue, which coincided with the area where expression of regeneration-related genes was apparent (Figure 4C, arrow). By contrast, few nerve fibers were observed in the apical half of the tissue (Figure 4C, arrowhead). At 48 hpa, nerve fibers extended distally and reached the distal cut surface (Figure 4D, arrow). Therefore, it seems that the promoted cell proliferation and nerve fiber distribution are related to the proximal-biased fin ray regeneration.

We also investigated apoptosis in the regenerating surface of the hole (Figure 4E,F). At 24 hpa, apoptotic cells were observed in the tissue near the cut surface of the proximal margin (Figure 4E,E',E'', arrows). By contrast, the apoptotic cells were not obvious in the distal margin (Figure 4E,E',E''). After 48 h, apoptotic cells were observed near the center of the closed hole (Figure 4F,F',F'', arrows), which coincides with the area occupied by the proximal margin-derived cells. Thus, apoptosis may not be a cause for the failure of regeneration from the distal margin.

These results show that gene expression can be induced in the distal margin and in the proximal margins following fin ray excision, whereas cell proliferation and fin ray regeneration do not progress in the distal margin.

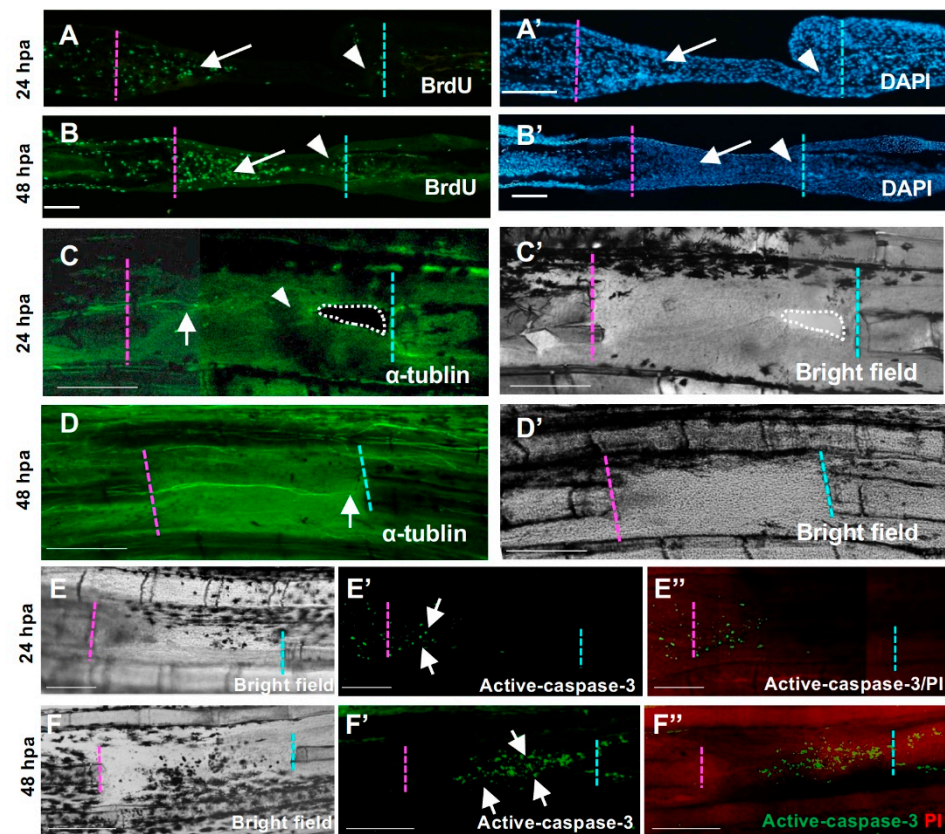


**Figure 4.** Cellular responses during hole regeneration. (A,A',B,B') BrdU-positive cells during hole regeneration. (A) At 24 h post-amputation (hpa), high proliferation of mesenchymal cells was observed in the proximal-derived tissue (arrow), but few cells were observed in the distal side (arrowhead). (B) At 48 hpa, high proliferation of mesenchymal cells was maintained, and proliferation of epithelial cells was also detected. In the distal tissue, some cells were also BrdU-positive (arrowhead). (A') and (B') are DAPI staining of (A,B), respectively. Scale bars = 100  $\mu$ m. (C,C',D,D') Nerve distribution during hole regeneration. (C,C') 24 hpa. (C') is the bright field view of (C). The nerve fiber extended from the proximal end to the regenerative tissue (arrow). By contrast, few nerve fibers were detected in the apical half of the epithelial sheet and the distal cut end (arrowhead). (D,D') 48 hpa. (D') is the bright field view of (D). Several nerve fibers extended from the proximal cut end to the distal cut end (arrow). Scale bars = 300  $\mu$ m. (E,E',F,F') Apoptosis during hole regeneration. (E,F) Bright field. (E',F') Active caspase-3. (E'',F'') Merged images of active caspase-3 and propidium iodide (PI) staining. (E,E',E'') At 24 hpa, apoptosis was only observed in the epithelium covering the blastema formed on the surface of the proximal side (arrow,  $n = 3$ ). (F,F',F'') At 48 hpa, apoptotic cells were observed in the tissue derived from the proximal surface (arrow,  $n = 3$ ). Resection edges (dotted lines). Scale bars = 100  $\mu$ m (A,B), 300  $\mu$ m (C,D).

#### 3.4. Fin Ray Regeneration from the Distal Margin Can Be Induced by Keeping the Margin Independent from the Proximal Margin

The results have so far revealed that the cells in the distal margin of the hole can respond to fin ray excision by retaining the ability to regenerate, although the regeneration from this margin did not occur. We considered that one reason for the lack of regeneration in the distal margin may be a failure to form the sheet-like region in the distal ends. We hypothesized that the formation of the sheet-like tissue at the distal edge might take a longer time than at the proximal edge. To test this, we performed a manual manipulation in which the distal and proximal margins were kept separate so that they did not make contact. We excised the sheet-like region formed on the proximal margin three times. The distal end was left in place during this process. After this, regeneration was promoted

from the distal and proximal margins, and gene expression at the regeneration site and the morphology of the subsequently formed fin rays were analyzed (Figure 5).

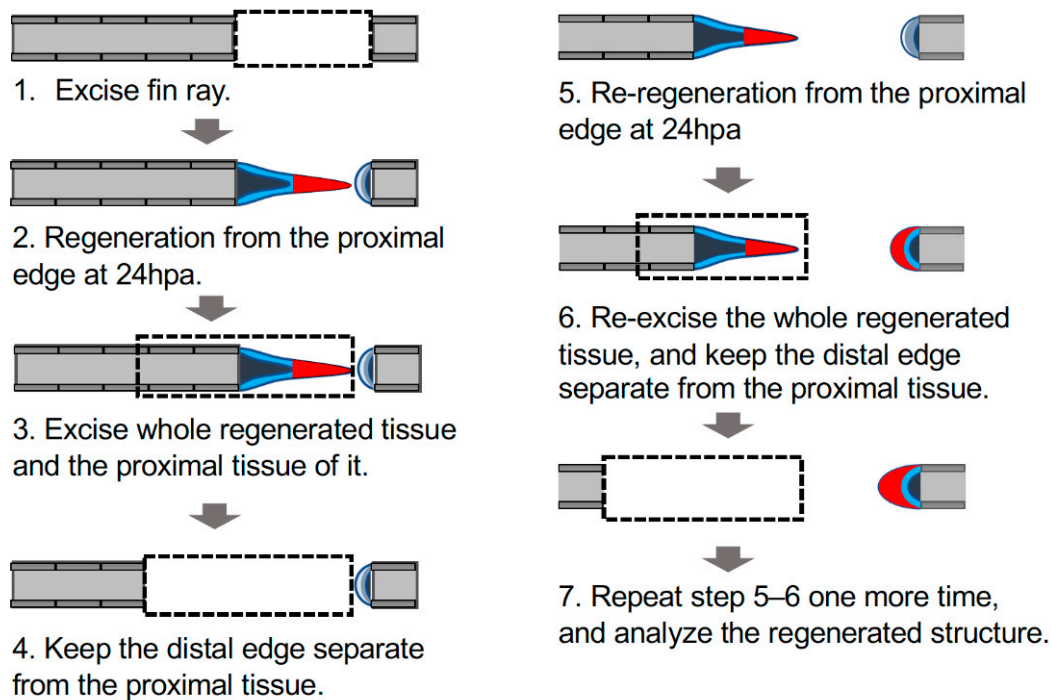


**Figure 5.** Schema of manipulation to investigate autonomous sheet-like tissue formation in the distal margin. Schema of the experimental procedure; the detailed procedure is described in the Materials and Methods section. Dashed rectangles indicate excision sites of the fin ray; gray, fin ray; light blue, epithelium of the cut surface; dark blue, mesenchyme of the cut surface; red, the sheet-like tissue formed on the proximal margin (triangle) or an equivalent structure on the distal margin (crescent shape).

By this repeated excision, the distal margin remained independent and unaffected by the proximal end for 96 h. At 24 h after the final manipulation, *msxb* and *pea3* were expressed at both the proximal and distal ends (Figure 6A,B); in particular, their expression at the distal end was enhanced and extended (Figure 6A,B, arrowheads), compared with the expression observed in the simple hole regeneration. In addition, a new sheet-like region in which there was faint expression of *msxb* and *pea3* was also observed (Figure 6A,B, brackets). The hole was located proximal to the tissue (Figure 6A,B, asterisks), suggesting the sheet-like region was formed from the distal edge and expanded proximally to fill the hole.

We then followed the subsequent regeneration of the fin rays. In the first week, a rod-like fin ray was observed protruding from the corresponding position of the hole (Figure 6C, arrowheads). The protruding rod-like fin rays were elongated distally until they reached the same length as the distal end of the original fin rays in the following two weeks (Figure 6D, arrowheads).

Next, we analyzed the skeletal pattern by comparing the regenerated and original fin ray. In the position where a lateral protrusion of fin ray was observed, extra branching of fin rays was observed (Figure 6D, asterisk). As mentioned later, the branching pattern was categorized into two groups. In the distal end of each regenerated fin ray, alcian blue-positive tissues were observed (Figure 6D, arrowheads), as in the distal end of the original fin rays. By 3D reconstruction of the fin ray with the COMBI method [30], we confirmed that distal-derived fin rays also bifurcated and then bent distally, which was similar to the normal fin rays (Figure 6E, arrowheads).

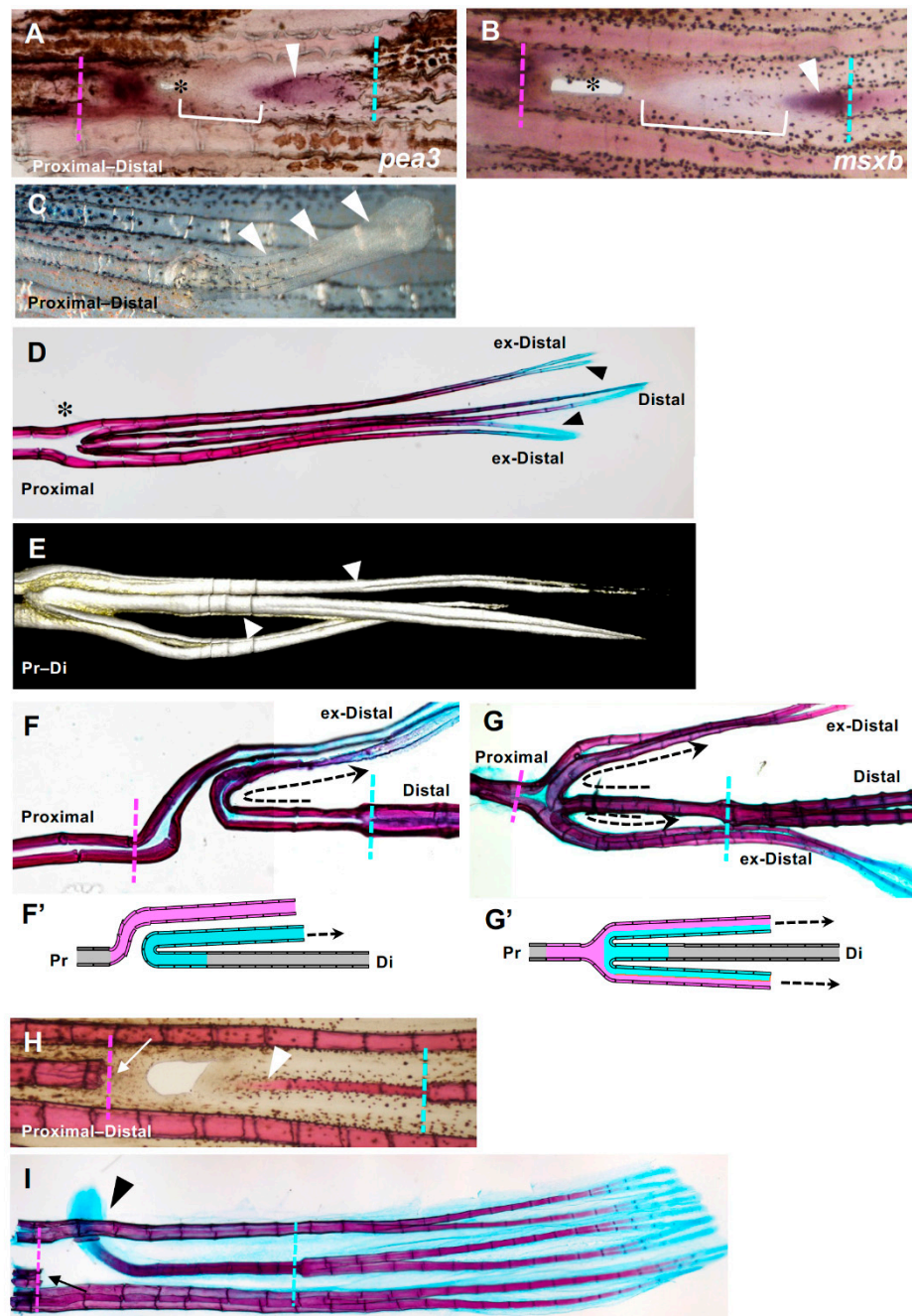


**Figure 6.** Fin ray regeneration of fin ray from the distal margin of the hole. (A,B) Strong expression of both *msxb* and *pea3* was observed at both the proximal and distal sides. Arrowheads indicate gene expression that was extended from the distal side to the proximal side. In addition, a distal margin-derived sheet-like tissue was observed (yellow brackets). (C) Seven days after excision, a rod-like lateral protrusion was formed from the position of the hole closure (arrowheads). (D) An example of the skeletal pattern that was fully regenerated from a hole-excised caudal fin. The original and regenerated fin rays are shown. Regenerated fin rays laterally protruded from the position of the hole with extra branching (asterisk). The distal ends of the regenerated fin rays (indicated as ex-distal) reached the same length as the original fin ray and were stained with alcian blue (arrowheads). (E) A 3D reconstruction of the regenerated extra fin ray shown in (D) using the COMBI method. Bifurcation of the regenerated fin ray was observed (arrows). (F,G) Examples of the skeletal pattern at the branching position of the hole-excised caudal fin. The direction of the regenerated fin ray extending

from the distal margin is indicated with dotted arrows. (F') and (G') are schema that the fin ray patterns shown in (F,G), respectively. In the schema, fin rays regenerated from the distal margin are indicated in blue, and those regenerated from the proximal margin are indicated in pink. In (F) the fin ray that regenerated from the distal margin protruded to either side of the fin at the position where it collided with the fin ray that regenerated from the proximal margin, and then bent distally ( $n = 3/9$ ). In (G) a hemi-ray of the distal-derived fin ray and that of the proximal-derived fin ray merged to form one fin ray and protruded to both sides of the fin ( $n = 6/9$ ). (H,I) A fin ray regenerated from a distal margin after prolonged and repeated excision of tissue at the proximal margin of the hole. (H) After one week, the regenerated fin ray was formed in the same plane of the original fin rays and as a continuous structure of the proximal edge of the original fin ray (arrowhead,  $n = 3$ ). (I) After 2 weeks of regeneration, the distal end of the regenerated fin ray protruded laterally (arrowhead,  $n = 3$ ). The distal end was stained with alcian blue (arrowhead), as was the original fin ray. During the regeneration process from the distal cut edge, regeneration from the proximal margin did not occur because of repeated excision (arrows).

We then investigated the connection between the regenerated fin rays and the original fin rays (Figure 6F,F',G,G'). We categorized the regenerated fin rays into two groups. In the first group, the distal-derived regenerated fin ray first extended proximally but then protruded laterally where the distal-derived fin ray met the proximal-derived fin ray and turned back to extend distally to the caudal fin (Figure 6F,F', arrows). The elongation was often parallel to that of the proximal-derived fin rays. In the second group, each hemi-ray of distal edge-derived fin rays bent toward opposite sides of the fin, and each merged with the hemi-rays of the fin ray from the proximal side; they then formed a single fin ray structure (Figure 6G,G', arrows). In this experiment, the second group was dominantly formed ( $n = 3/9$  for the first group,  $n = 6/9$  for the second group).

These results indicate that fin ray regeneration can also occur from the distal margin, and the "distal end" of the regenerated fin ray from the distal margin of the hole has the same structure as the distal end of the original fin ray; however, it is possible that the proximal tissue still affected the distal tissue and induced regeneration if they made contact after we had excised the tissue three times. Therefore, to eliminate this possibility, we attempted to make the distal margin independent for a longer period by repeated excision of the sheet-like tissue of the proximal margin for another two weeks. Because of the repeated excision, regeneration from the proximal margin did not occur during the experiment (Figure 6I,H, arrows). After one week, a thin but apparent fin ray from the distal margin was formed (Figure 6H, arrowhead,  $n = 3$ ). At this stage, the regenerated fin ray was in the same plane as the original fin rays and there was continuous regeneration of the distal edge of the original fin ray (Figure 6H, arrowhead). After two weeks of regeneration, the distal end of the regenerated fin rays elongated more and protruded laterally (Figure 6I, arrowhead,  $n = 3$ ). The "distal end" of the regenerated fin ray from the distal margin of the hole was stained with alcian blue like the distal end of the original fin ray (Figure 6I, arrowhead). These results show that regeneration of the fin rays from the distal margin of the hole occurs independently of regeneration from the proximal margin, and they also indicate that cells at the distal edge of the hole could regenerate the fin rays but are restricted to the more distal structures.

Taken together, these results indicate that the fin ray has an ability to regenerate bidirectionally, but regeneration is likely to be limited to the proximal margin under normal conditions, because of the preferential formation of a sheet-like tissue on the proximal margin.

#### 4. Discussion

In this study, we investigated the polarity of caudal fin regeneration in zebrafish by focusing on the hole closure following fin ray regeneration. Our findings are as follows. First, even though fin regeneration proceeds in a unidirectional manner from the proximal margin of the hole in normal regeneration, expression of regeneration-related genes was also induced in the distal margin of the hole. Second, a sheet-like tissue was formed in the

proximal margin of the hole, but not in the distal margin. Finally, if the distal margin was kept separate from the proximal margin, the sheet-like tissue was also formed in the distal margin and ectopic regeneration of the fin ray occurred. From these results, we concluded that cells in the distal margin also have an ability to regenerate fin ray autonomously, the same as cells in the proximal margin.

#### *4.1. Fin Regeneration Proceeds Unidirectionally from the Proximal Side, but the Regenerative Response also Occurs in the Distal Side*

Our results indicate that, although fin ray regeneration proceeds in one direction from the proximal margin of the hole to the distal direction, the initial response to regeneration occurs in both the proximal and distal margins. Histological analysis showed that repair of the hole and fin ray regeneration proceeded in a unidirectional manner from the proximal to distal margin, as in previous reports (Figure 1); however, the regeneration marker genes that we investigated were expressed in both the proximal and distal margins (Figure 3). The expressions in the distal margin were restricted to a smaller area than at the proximal margin (Figure 3); thus, the response in the distal margin may be limited compared with the normal response at the proximal margin. In a fracture model of fin rays, bone fracture repair was initiated in both the proximal and distal sides [31], indicating that local tissue or organ repair proceeded from both directions. Cellular and tissue behaviors during the hole regeneration observed in our study may be reflected in these responses.

In contrast to our results, a recent report by Cao et al. [26] on fin hole regeneration did not mention the expression of regeneration-related genes at the distal margin of the hole. This is possibly due to the differences in experimental conditions; in their report, two fin ray rows were excised, but we excised one row. In addition, the length of the hole prepared in our study was longer than that in their experiment [26]. Because the area of gene expression in the distal margin was restricted to a small area in our experiment, as mentioned above, the signals of gene expression may be unclear in other experimental conditions.

Even though a regenerative response was also occurring at the distal margin in terms of the expression of several regeneration-related genes, the fin ray did not regenerate at the distal margin during hole regeneration in the absence of experimental manipulation (Figures 1–3). This result indicates that the cells at the distal margin of the hole maintain their regenerative ability, but under normal regenerative conditions, it is not sufficient to progress the regeneration. During fin regeneration, the proliferation of cells is induced both in the epithelial cells and blastemal cells [12,13,19,32]. In our experiment, less proliferation of cells was induced in the distal margin in contrast to the proximal margin where increasing proliferation was induced (Figure 4A,B). This indicates that that gene expression is not always linked to the induction of cell proliferation and the following regeneration, and again suggests that this sheet-like tissue is necessary for regeneration to proceed (see below).

#### *4.2. Role of the Sheet-like Tissue in Fin Ray Regeneration and Polarity*

Our results in the present study indicate that the formation of sheet-like tissue is important for fin regeneration in hollowed-out holes and is strongly related to regeneration polarity. Previous studies of hole regeneration in the fin mainly described the morphology of regenerating fin ray [3,25], but tissue-level analysis around the hole was not performed. Cao et al. [26] investigated gene expression during the regeneration of excised fin rays but did not mention the expression of regeneration-related genes in the distal edge in wild-type fish [26]. In addition, there has been no mention of the sheet-like region formed on the cut surface; however, Murciano et al. [33] studied inter-ray wound healing and subsequent regeneration, and reported the formation of a membranous, epithelial ‘meniscus-like edge’ where no gene expression was observed [33]. In our study, we focused on the sheet-like tissue formed at the proximal margin, and this may correspond to the membranous structure described in Murciano et al. [33]. Our results and those of Murciano et al. [33] indicate that this sheet-like tissue becomes apparent during the fin regeneration of a confined area along the proximodistal axis.

The formation of this tissue may be associated with wound repair in confined areas; however, as we have shown, the formation of the sheet-like tissue on the distal side of the hole seems to require time; therefore, the sheet-like tissue is not simply formed for wound repair. Rather, our results suggest that its formation is closely related to the regeneration and the polarity of the fin ray. In the usual fin regeneration experiment, in which the distal end of the fin is cut off, a structure that spreads in the regeneration direction, similar to the sheet-like tissue observed in our experiment, is not observed. Instead, the cut surface is covered with a slightly thickened epithelial sheet, the wound epithelium [3,5,7,8]. Its importance in fin regeneration has been previously mentioned [3,5,7,8]. During normal regeneration, it is quite possible that functionally homologous cells or tissues, although not in the form of expanded sheets, arise in the wound epithelium, and that this promotes subsequent regeneration.

#### 4.3. Polarity of Fin Ray Regeneration

We found that cells at the distal margin of the hole could regenerate fin rays when the distal margin was kept independent from the proximal margin (Figure 6). In this case, a sheet-like region was also formed at the distal end, although it took longer (Figure 6). Thus, in wild-type zebrafish, the distal margin was also capable of autonomously regenerating fin rays under specific conditions. This is reasonable because regeneration-related genes were expressed at the distal margin (Figure 3); however, in previous reports [3,25,26], and even in our results (Figure 1), spontaneous regeneration of the hole did not result in regeneration of the fin rays from the distal margin. Taken together, these results suggest that regeneration from the distal margin may be suppressed under spontaneous regeneration. One possible explanation is that cells of the distal margin do not regenerate if the proximal and distal tissues are in a continuous plane or regeneration field. In this case, there may be an inhibitory effect on regeneration from the tissue at the proximal margin toward the distal margin, but the specific mechanism is not known. If such a system exists, it may be useful to prevent excessive regeneration of unnecessary structures from the distal margin during spontaneous regeneration.

In a classic study, regeneration from the distal margin was reported in a fin ray excision experiment of the goldfish tail fin by Nabrit [27]. In the report, four fin rays and six segments in the caudal fin were excised, and the fin rays regenerated from both the distal and proximal margins of the hole. The fin rays that regenerated from the distal margin protruded laterally from the fin to form ectopically elongated fin rays, which corresponded to our observation. Based on our results, Nabrit's [27] results can be interpreted as follows: it required time for the holes in the caudal fin to be closed, resulting in the induction of regeneration from the distal end. Cao et al. [26], however, reported that large holes in the zebrafish tail fin did not induce regeneration from the distal margin. Therefore, there may be some species-specific differences in hole regeneration between zebrafish and goldfish.

#### 4.4. Factors That Influence Regeneration Polarity

Our results show that the unidirectional regeneration of fins reflects the polarity of the sheet-like tissue formation, although the mechanism of polarized formation is unclear. The regeneration of zebrafish pectoral fins involves the distribution of nerve fibers [23]. Hole regeneration in mouse auricles has also been noted to have regeneration polarity along the proximal–distal axis that was suggested to be related to nerve distribution [34–36]. Although the present results do not confirm neural dependency in the early stages of the sheet-like tissue formation, further investigation of the relationship with neural distribution is needed.

A relationship between the unidirectional hole regeneration and calcineurin activity has been suggested [26]; in that report, inhibition of calcineurin activity could induce the regeneration of fin rays from the distal margin in wild-type zebrafish. Although the relationship between calcineurin activity and sheet-like tissue formation is unclear, it is

possible that keeping the distal margin independent reduces the calcineurin activity and leads to sheet-like tissue formation.

#### 4.5. Conclusions

In this study, we showed that regeneration of the zebrafish caudal fin ray proceeds in a unidirectional manner from the proximal margin, and that the sheet-like tissue, which is formed on the proximal margin, must be understood as an initial stage of ray regeneration potential determining the direction of the regeneration. Cells in the distal margin have an ability to regenerate fin rays by forming a sheet-like tissue, but this ability seems to be suppressed during spontaneous regeneration. The formation of this sheet-like tissue is usually unidirectional from the proximal margin and takes time to form at the distal margin. Therefore, studying the formation of this tissue and its function may provide a new perspective on why regeneration proceeds in one direction.

In wound healing and organ regeneration research, understanding tissue polarity is important for promoting stable healing and regeneration. Further studies of fin repair and subsequent regeneration polarity are expected to provide necessary information for elucidating regeneration polarity in other organs.

**Author Contributions:** Conceptualization, T.U. and N.W.; writing—original draft preparation, W.N., S.N., R.H., S.O. and N.W.; writing—review and editing, W.N., S.N., R.H., T.U., S.O. and N.W.; visualization, W.N., S.N., R.H. and N.W.; investigation, W.N., S.N., R.H., T.U., S.O. and N.W.; supervision, N.W.; funding acquisition, S.O. and N.W. All authors have read and agreed to the published version of the manuscript.

**Funding:** This work was supported by Grants-in-Aid for Scientific Research from the Japan Society for the Promotion of Science (KAKENHI), 17K08498, 16H07237. The authors have no conflict of interest to declare.

**Institutional Review Board Statement:** Not applicable.

**Informed Consent Statement:** Not applicable.

**Data Availability Statement:** Not applicable.

**Acknowledgments:** We thank members of the Wada laboratory for their input. We are also grateful to Yuki Tajika (Gunma University, Japan) for instructing us on the COMBI method and providing us with the tools.

**Conflicts of Interest:** The authors have no conflict of interest to declare.

## References


1. Becker, T.; Wullimann, M.F.; Becker, C.G.; Bernhardt, R.; Schachner, M. Axonal regrowth after spinal cord transection in adult zebrafish. *J. Comp. Neurol.* **1997**, *377*, 577–595. [CrossRef]
2. Poss, K.D.; Wilson, L.G.; Keating, M.T. Heart regeneration in zebrafish. *Science* **2002**, *298*, 2188–2190. [CrossRef]
3. Akimenko, M.-A.; Mari-Beffa, M.; Bercera, J.; Géraudie, J. Old questions, new tools, and some answers to the mystery of fin regeneration. *Dev. Dyn.* **2003**, *226*, 190–201. [CrossRef]
4. Fimbel, S.M.; Montgomery, J.E.; Burket, C.T.; Hyde, D.R. Regeneration of inner retinal neurons after intravitreal injection of ouabain in zebrafish. *J. Neurosci.* **2007**, *27*, 1712–1724. [CrossRef] [PubMed]
5. Poss, K.D.; Keating, M.T.; Nechiporuk, A. Tales of Regeneration in Zebrafish. *Dev. Dyn.* **2003**, *226*, 202–210. [CrossRef]
6. Kawakami, A. Stem cell system in tissue regeneration in fish. *Dev. Growth Differ.* **2010**, *52*, 77–87. [CrossRef]
7. Mari-Beffa, M.; Murciano, C. Dermoskeleton morphogenesis in zebrafish fins. *Dev. Dyn.* **2010**, *239*, 2779–2794. [CrossRef] [PubMed]
8. Pfefferli, C.; Jazwinska, A. The art of fin regeneration in zebrafish. *Regeneration* **2015**, *2*, 72–83. [CrossRef]
9. Wehner, D.; Weidinger, G. Signaling networks organizing regenerative growth of the zebrafish fin. *Trends Genet.* **2015**, *31*, 336–343. [CrossRef]
10. Bercera, J.; Montes, G.S.; Bexiga, S.R.; Junqueira, L.C. Structure of the tail fin in teleosts. *Cell Tissue Res.* **1983**, *230*, 127–137. [CrossRef]
11. Poss, K.D. Advances in understanding tissue regenerative capacity and mechanisms in animals. *Nat. Rev. Genet.* **2010**, *11*, 710–722. [CrossRef] [PubMed]



12. Poleo, G.; Brown, C.W.; Laforest, L.; Akimenko, M.A. Cell proliferation and movement during early fin regeneration in zebrafish. *Dev. Dyn.* **2001**, *22*, 380–390. [CrossRef] [PubMed]
13. Santos-Ruiz, L.; Santamaria, J.A.; Ruiz-Sanchez, J.; Becerra, J. Cell proliferation during blastemal formation in the regenerating teleost fin. *Dev. Dyn.* **2002**, *223*, 262–272. [CrossRef]
14. Blum, N.; Begemann, G. Retinoic acid signaling controls the formation, proliferation and survival of the blastemal during adult zebrafish fin regeneration. *Development* **2012**, *139*, 107–116. [CrossRef]
15. Grotek, B.; Wehner, D.; Weidinger, G. Notch signaling coordinates cellular proliferation with differentiation during zebrafish fin regeneration. *Development* **2013**, *140*, 1412–1423. [CrossRef]
16. Stewart, S.; Gomez, A.W.; Armstrong, B.E.; Henner, A.; Stankunas, K. Sequential and opposing activities of Wnt and BMP coordinate zebrafish bone regeneration. *Cell Rep.* **2014**, *6*, 482–498. [CrossRef]
17. Yoshinari, N.; Kawakami, A. Mature and juvenile tissue models of regeneration in small fish species. *Biol. Bull.* **2011**, *221*, 62–78. [CrossRef]
18. Draper, B.W.; Stock, D.W.; Kimmel, C.B. Zebrafish fgf24 functions with fgf8 to promote posterior mesodermal development. *Development* **2003**, *130*, 4639–4654. [CrossRef] [PubMed]
19. Poss, K.D.; Shen, J.; Nechiporuk, A.; McMahon, G.; Thisse, B.; Thisse, C.; Keating, M.T. Roles for Fgf signaling during zebrafish fin regeneration. *Dev. Biol.* **2000**, *222*, 347–358. [CrossRef]
20. Lee, Y.; Hami, D.; De Val, S.; Kagermeier-Schenk, B.; Wills, A.A.; Black, B.L.; Weidinger, G.; Poss, K.D. Maintenance of blastemal proliferation by functionally diverse epidermis in regenerating zebrafish fins. *Dev. Biol.* **2009**, *331*, 270–280. [CrossRef] [PubMed]
21. Akimenko, M.A.; Johnson, S.L.; Westerfield, M.; Ekker, M. Differential induction of four msx homeobox genes during fin development and regeneration in zebrafish. *Development* **1995**, *121*, 347–357. [CrossRef]
22. Murciano, C.; Fernández, T.D.; Durán, I.; Maseda, D.; Ruiz-Sánchez, J.; Becerra, J.; Akimenko, M.A.; Marí-Beffa, M. Ray-interray interactions during fin regeneration of *Danio rerio*. *Dev. Biol.* **2002**, *252*, 214–224. [CrossRef] [PubMed]
23. Simões, M.G.; Anabela Bensimon-Brito, A.; Fonseca, M.; Farinho, A.; Valério, F.; Sousa, S.; Afonso, N.; Kumar, A.; Jacinto, A. Denervation impairs regeneration of amputated zebrafish fins. *BMC Dev. Biol.* **2014**, *14*, 49. [CrossRef] [PubMed]
24. Whitehead, G.G.; Makino, S.; Lien, C.L.; Keating, M.T. fgf20 is essential for initiating zebrafish fin regeneration. *Science* **2005**, *310*, 1957–1960. [CrossRef] [PubMed]
25. Goss, R.J. Regeneration in fishes. In *Principles of Regeneration*; Goss, R.J., Ed.; Academic Press: New York, NY, USA, 1969; pp. 113–139.
26. Cao, Z.; Meng, Y.; Gong, F.; Xu, Z.; Liu, F.; Fang, M.; Zou, L.; Liao, X.; Wang, X.; Luo, L.; et al. Calcineurin controls proximodistal blastema polarity in zebrafish fin regeneration. *Proc. Natl. Acad. Sci. USA* **2021**, *118*, e2009539118. [CrossRef] [PubMed]
27. Nabrit, S.M. The role of the fin rays in the regeneration in the tail fins of fishes (in *Fundulus* and Goldfish). *Biol. Bull.* **1929**, *56*, 235–266. [CrossRef]
28. Sims, K., Jr.; Eble, D.M.; Iovine, M.K. Connexin43 regulates joint location in zebrafish fins. *Dev. Biol.* **2009**, *327*, 410–418. [CrossRef] [PubMed]
29. Ohgo, S.; Ichinose, S.; Yokota, S.; Sato-Maeda, M.; Shoji, W.; Wada, N. Tissue regeneration during lower jaw restoration in zebrafish shows some features of epimorphic regeneration. *Dev. Growth Differ.* **2019**, *61*, 419–430. [CrossRef] [PubMed]
30. Tajika, Y.; Murakami, T.; Iijima, K.; Gotoh, H.; Takahashi-Ikezawa, M.; Ueno, H.; Yoshimoto, Y.; Yorifuji, H. A novel imaging method for correlating 2D light microscopic data and 3D volume data based on block-face imaging. *Sci. Rep.* **2017**, *7*, 3645. [CrossRef] [PubMed]
31. Sousa, S.; Valerio, F.; Jacinto, A. A new zebrafish bone crush injury model. *Biol. Open* **2012**, *1*, 915–921. [CrossRef]
32. Nechiporuk, A.; Keating, M.T. A proliferation gradient between proximal and msxb-expressing distal blastema directs zebrafish fin regeneration. *Development* **2002**, *129*, 2607–2617. [CrossRef] [PubMed]
33. Murciano, C.; Cazorla-Vázquez, S.; Gutiérrez, J.; Hijano, J.A.; Ruiz-Sánchez, J.; Mesa-Almagro, J.; Martín-Reyes, F.; Fernández, T.D.; Marí-Beffa, M. Widening control of fin inter-rays in zebrafish and inferences about actinopterygian fins. *J. Anat.* **2018**, *232*, 783–805. [CrossRef]
34. Buckley, G.; Metcalfe, A.D.; Ferguson, M.W.J. Peripheral nerve regeneration in the MRL/MpJ ear wound model. *J. Anat.* **2011**, *218*, 163–172. [CrossRef] [PubMed]
35. Kumar, A.; Brookes, J.P. Nerve dependence in tissue, organ, and appendage regeneration. *Trends Neurosci.* **2012**, *35*, 691–699. [CrossRef] [PubMed]
36. Seifert, A.W.; Muneoka, K. The blastema and epimorphic regeneration in mammals. *Dev. Biol.* **2018**, *433*, 190–199. [CrossRef] [PubMed]

Article

# Actin Filament in the First Cell Cycle Contributes to the Determination of the Anteroposterior Axis in Ascidian Development

Toshiyuki Goto<sup>1,2</sup>, Shuhei Torii<sup>1</sup>, Aoi Kondo<sup>1</sup>, Kazumasa Kanda<sup>1</sup>, Junji Kawakami<sup>1</sup>, Yosky Kataoka<sup>2,3</sup>   
and Takahito Nishikata<sup>1,\*</sup>

<sup>1</sup> Frontiers of Innovative Research in Science and Technology (FIRST), Konan University, 7-1-20 Minatojima-Minamimachi, Chuo-k, Kobe 650-0047, Japan; d1961001@s.konan-u.ac.jp (T.G.); m2161013@s.konan-u.ac.jp (S.T.); s1891017@s.konan-u.ac.jp (A.K.); kazu186607@gmail.com (K.K.); kawakami@konan-u.ac.jp (J.K.)

<sup>2</sup> Laboratory for Cellular Function Imaging, RIKEN Center for Biosystems Dynamics Research, Kobe 650-0047, Japan; kataokay@riken.jp

<sup>3</sup> RIKEN-JEOL Collaboration Center, Multi-Modal Microstructure Analysis Unit, Kobe 650-0047, Japan

\* Correspondence: nisikata@konan-u.ac.jp; Tel.: +81-78-303-1349

**Abstract:** In many animal species, the body axis is determined by the relocalization of maternal determinants, organelles, or unique cell populations in a cytoskeleton-dependent manner. In the ascidian first cell cycle, the myoplasm, including mitochondria, endoplasmic reticulum (ER), and maternal mRNAs, move to the future posterior side concomitantly (called ooplasmic segregation or cytoplasmic and cortical reorganization). This translocation consists of first and second phases depending on the actin and microtubule, respectively. However, the transition from first to second phase, that is, translocation of myoplasmic components from microfilaments to microtubules, has been poorly investigated. In this study, we analyzed the relationship between these cytoskeletons and myoplasmic components during the first cell cycle and their role in morphogenesis by inhibitor experiments. Owing to our improved visualization techniques, there was unexpected F-actin accumulation at the vegetal pole during this transition period. When this F-actin was depolymerized, the microtubule structure was strongly affected, the myoplasmic components, including maternal mRNA, were mislocalized, and the anteroposterior axis formation was disordered. These results suggested the importance of F-actin during the first cell cycle and the existence of interactions between microfilaments and microtubules, implying the enigmatic mechanism of ooplasmic segregation. Solving this mystery leads us to an improved understanding of ascidian early development.

**Citation:** Goto, T.; Torii, S.; Kondo, A.; Kanda, K.; Kawakami, J.; Kataoka, Y.; Nishikata, T. Actin Filament in the First Cell Cycle Contributes to the Determination of the Anteroposterior Axis in Ascidian Development. *J. Dev. Biol.* **2022**, *10*, 10. <https://doi.org/10.3390/jdb10010010>

Academic Editors: Tsutomu Nohno and Hideyo Ohuchi

Received: 6 December 2021

Accepted: 2 February 2022

Published: 4 February 2022

**Publisher's Note:** MDPI stays neutral with regard to jurisdictional claims in published maps and institutional affiliations.



**Copyright:** © 2022 by the authors. Licensee MDPI, Basel, Switzerland. This article is an open access article distributed under the terms and conditions of the Creative Commons Attribution (CC BY) license (<https://creativecommons.org/licenses/by/4.0/>).

**Keywords:** axis determination; ER; actin; microtubule; maternal mRNA

## 1. Introduction

Maternal mRNA, which is produced from the maternal genome during oogenesis, is indispensable for body planning in many animal species. The localization and translation of maternal mRNA is strictly regulated during early embryogenesis. For the correct localization of maternal mRNA, cytoskeletons play a crucial role in the transport and anchoring of some animal eggs such as flog (cortical rotation) [1,2], teleost fish (cortical rotation) [3], and nematodes (cytoplasmic flow) [4,5].

Ascidian (Chordata) unfertilized eggs have a unique cytoplasm, designated as myoplasm, which consists of mitochondria-rich cytoplasm (MRC), cortical endoplasmic reticulum (cER), and maternal mRNAs called postplasmic/PEM RNAs [6,7]. In the first cell cycle, the myoplasm shows dynamic movement toward the future posterior side (called ooplasmic segregation or cytoplasmic and cortical reorganization) [8], and is important for anteroposterior axis formation [7].

This ooplasmic segregation consists of two phases. In the first phase, fertilization triggers the contraction of cortical actin filaments to the vegetal pole and the concentration of the myoplasm at the vegetal pole [9–11]. This first phase is completed within 5 min postfertilization (mpf). During the second phase, growing sperm aster migrates from the vegetal pole to the posterior side along the egg cortex, and finally, the sperm nucleus enters the center of the egg to fuse with the female nucleus [8]. The myoplasm moves toward the posterior pole following this sperm-aster movement and depends on the microtubules [9–11]. We recently reported the cortical array of microtubules in the posterior-vegetal region (CAMP) during the second phase, suggesting the importance of myoplasm translocation [12,13]. This second phase of ooplasmic segregation occurs roughly from 30 to 45 mpf. Although these two phases of ooplasmic segregations are well-described, the mechanisms of transition between the first and second phases are poorly understood. One of the concerns is how the myoplasm switches its chariot from F-actin to the microtubule.

Previously, cER and postplasmic/PEM mRNAs were thought to move posteriorly together during the second phase [7,8]. However, our recent observations showed that before the second phase, some postplasmic/PEM mRNAs dissociated from dense ER, which corresponds to the cER with a more deeply expanded ER mass [14]. Moreover, they reassembled by the four-cell stage and subsequently inherited in the centrosome attracting body (CAB) [14]. CAB is responsible for unequal cleavage and determines the anteroposterior axis [15,16]. These results strongly suggest the existence of unexpected mechanisms between the first and second phases of ooplasmic segregations and their importance for the anteroposterior axis formation.

In this study, owing to the improvement and refinement of the entire process of visualization techniques, we succeeded in revealing the prolonged F-actin accumulation at the vegetal pole up to 30 mpf. We analyzed the role of actin filaments during the first cell cycle on the segregation of myoplasm, including CAMP formation, translocation of macho-1, dense ER, and mitochondria and axis determination. The importance of the relationship between actin filaments and microtubules will be discussed.

## 2. Materials and Methods

### 2.1. Animal Experiments

Ascidian (*Ciona intestinalis* type A; also called *Ciona robusta*) adults were obtained from the National BioResource Project (NBRP), Tokyo, Japan. Methods for egg and sperm handling, fertilization, and dechoriation were performed as described previously [17,18]. The embryos were reared in filtered seawater at 18 °C. At this temperature, the first and second phase of ooplasmic segregations start immediately after fertilization and from approximately 30 min postfertilization (mpf), respectively. The first cleavage occurs at approximately 60 mpf. In the inhibitor experiments, eggs were treated with 2 µg/mL cytochalasin B (CytB; Sigma-Aldrich, St. Louis, MO, USA), 2.5 µg/mL nocodazole (Noco; Sigma-Aldrich), or the same dilution of solvent (0.1% DMSO) as a control during the desired periods. The eggs were exposed to these inhibitors with 3 mL seawater. Then, eggs were replaced to 10 mL seawater and washed 5 times with fresh seawater. It has been reported that cortical F-actin in CytB-treated culture cells could be recovered within 5 min after washout with this protocol [19].

### 2.2. Whole-Mount Immunofluorescent Staining

For microtubule staining, dechorionated *Ciona* eggs/embryos were fixed with 100% methanol at room temperature (approximately 25 °C) for 1 h. The fixed specimens were treated with ethanol up series (35%, 70%, and 100%) and stored at −30 °C until further use. After washing with phosphate-buffered saline containing 0.05% Tween 20 (PBST), the specimens were treated with G1T0 (4 mol/L urea (MP Biomedicals, Santa Ana, CA, USA), and 1% glycerol in distilled water) for 90 min at 4 °C [12].

For double staining of the ER and microtubules, dechorionated *Ciona* eggs and embryos were fixed with Cold-Fix solution (3.2% formaldehyde in 80% methanol) at −30 °C for

1 h, followed by continued fixation at room temperature for 1 h with gentle shaking every 20 min. Both types of fixed specimens were treated with ethanol up series (35%, 70%, and 100%) and stored at  $-30\text{ }^{\circ}\text{C}$  until further use. After washing with PBST, the specimens were treated with G1T0 for 90 min at  $4\text{ }^{\circ}\text{C}$  and then treated with antigen retrieval solution (modified from Hayashi et al., 2011; 6 M urea and 0.1 M Tris-HCl, pH 9.5) [20] for 30 min at  $80\text{ }^{\circ}\text{C}$ . The specimens were immunostained with the following antibodies: anti- $\alpha$ -tubulin mouse monoclonal antibody (anti-microtubule antibody; clone DM1A; Sigma-Aldrich; 1:100 dilution), anti-glucose-regulated protein 78 (GRP78; also known as Bip) rabbit polyclonal antibody (anti-ER antibody; StressMarq Biosciences, Victoria, BC, Canada; 1:100 dilution), Alexa Fluor 488-conjugated goat anti-mouse IgG antibody (Thermo Fisher Scientific; 1:1000 dilution), and Alexa Fluor Plus 555-conjugated goat anti-rabbit IgG antibody (Thermo Fisher Scientific; 1:1000 dilution). Nuclei were stained with  $5\text{ }\mu\text{g}/\text{mL}$  4',6-diamidino-2-phenylindole dihydrochloride (DAPI). The stained specimens were then mounted with methyl salicylate (Nacalai Tesque, Kyoto, Japan).

### 2.3. Phalloidin Staining

For F-actin staining, dechorionated *Ciona* eggs/embryos were fixed with a 1:1 mixed solution of extraction buffer (2% Triton-X 100, 50 mM  $\text{MgCl}_2$ , 10 mM KCl, 10 mM EGTA, 20% glycerol, 25 mM imidazole) and fixation buffer (0.25% glutaraldehyde (Nacalai Tesque), 3.7% formaldehyde, 100 mM HEPES (pH = 7.0), 50 mM EGTA, 10 mM  $\text{MgSO}_4$ , and 525 mM sucrose) [21] for 15 min at room temperature. This was followed by continued fixation in fixation buffer for 2 h at room temperature. The fixed specimens were washed with PBST and treated with 10 unit/mL Alexa Fluor 488-labeled phalloidin (Molecular Probes, Eugene, OR, USA) for 30 min at room temperature. For clearing without dehydration, stained specimens were treated with 40% fructose (Fujifilm-Wako, Tokyo, Japan) for 30 min at room temperature and then mounted in SeeDB (80.2% wt/wt fructose, 0.5%  $\alpha$ -thioglycerol) [22].

### 2.4. Whole-Mount RNA In Situ Hybridization

Dechorionated *Ciona* eggs/embryos were fixed with a Cold-Fix solution. Fixed specimens were treated with 0.2% Triton-X 100 for 10 min at room temperature and then fixed with paraformaldehyde for 1 h at room temperature. The postfixed specimens were treated with 0.1 M 2,2',2'-nitrilotriethanol (Fujifilm-Wako) and 0.27% acetic anhydride (Nacalai Tesque) for 10 min at room temperature. Then, specimens were treated with G1T0 followed by the mixture of antigen retrieval solution and prehybridization solution containing 3.78 M urea, 0.063 M Tris-HCl (pH = 9.5), 50  $\mu\text{g}/\text{mL}$  heparin, 100  $\mu\text{g}/\text{mL}$  yeast tRNA, and 1% Tween 20. Sense and antisense RNA probes of macho-1 were transcribed from a *Ciona* cDNA clone (cieg016n12: Ghost) [23], using T7 and T3 RNA polymerases (Sigma-Aldrich), respectively, with DIG RNA Labeling Mix (Sigma-Aldrich). The specimens were hybridized with an RNA probe in prehybridization buffer (50% formamide, 50  $\mu\text{g}/\text{mL}$  heparin, 100  $\mu\text{g}/\text{mL}$  yeast tRNA, and 1% Tween 20) for 16 h at  $50\text{ }^{\circ}\text{C}$ . After hybridization, the specimens were washed with SSC ( $5\times$ ,  $2\times$ , and  $0.2\times$ ). For observation of macho-1, DIG probe was detected using an alkaline phosphatase-conjugated anti-DIG Fab fragment (Sigma-Aldrich; 1:1000 dilution). In contrast, when combined with immunofluorescence, specimens were immunostained with the following antibodies: anti-Bip rabbit polyclonal antibody, anti-NN18 mouse monoclonal antibody (antineurofilament antibody; Sigma-Aldrich; 1:100 dilution), horseradish peroxidase-conjugated anti-DIG Fab fragment (Sigma-Aldrich; 1:100 dilution), Alexa Fluor Plus 555-conjugated goat anti-rabbit IgG antibody, and Alexa Fluor 405-conjugated goat anti-mouse IgG antibody (Thermo Fisher Scientific; 1:200 dilution). The NN18 antibody is a good marker of mitochondria that recognizes the F1-ATP synthase  $\alpha$ -subunit in *Ciona* [24]. After immunostaining, the in situ hybridization signals were enhanced using FITC-Tyramide (Akoya Biosciences, Marlborough, MA, USA).

### 2.5. Image Acquisition and Data Analysis

Specimens were observed under LSM700 (Carl Zeiss, Jene, Germany) or A1RHD25 (Nikon, Tokyo, Japan) confocal microscopes using ZEN (Carl Zeiss) or NIS element imaging software (Nikon). Z-projections and the midplane optical sections are displayed with animal pole upward. The animal pole was defined based on the position of the meiotic apparatus, myoplasm configuration, or parallel direction of the CAMP [12]. All analyses were performed using the ImageJ software [25]. Z-projections were displayed as a side view wherein the animal pole was up and posterior side was right, or as a posterior view wherein the animal pole was up. These Z-projections showed the maximum intensity projection of z-stack. To analyze the expansion of the signal area of macho-1 mRNA, the angles between the horizontal and vertical edges of the mRNA signal and the center of the eggs were measured. For the measurement of angles, the side and top views of the Z-projections were used. To analyze the colocalization between the ER and mRNA signals, Z-projections were rendered from five optical sections around the midplane. Then, the dense ER region was extracted using denoising, contrast adjustment, and binarization, followed by a restriction of the object size. The maternal mRNA-positive region was extracted by binarization of the mRNA signals. The ratio of the mRNA-positive regions in the dense ER to the total area of mRNA-positive regions was calculated. The parameters for the extraction of each dense ER or mRNA were fixed for all specimens.

## 3. Results

### 3.1. Prolonged F-Actin Accumulation at the Vegetal Cortex

It has been well-described that the actin cytoskeleton is necessary for the first phase of ooplasmic segregation and results in strong F-actin accumulation in the vegetal cortex [9–11]. However, no report has described how long this accumulation lingered in the vegetal pole. Thus, we improved the phalloidin staining method for detecting F-actin in whole-mount specimens. The main points of this improvement were fixation with permeabilization and treatment with the fructose-based hydrophilic clearing reagent SeeDB [22]. Our methods revealed that vegetal accumulation of F-actin decreased gradually, though it was detected up to at least 30 mpf (Figure 1). The mitotic apparatus was faintly stained at 45 mpf (Figure 1b). As the meiotic spindles beneath the animal cap were not stained, this phalloidin staining of the microtubule structure suggests that the colocalization of actin and tubulin during the second phase of ooplasmic segregation is plausible.

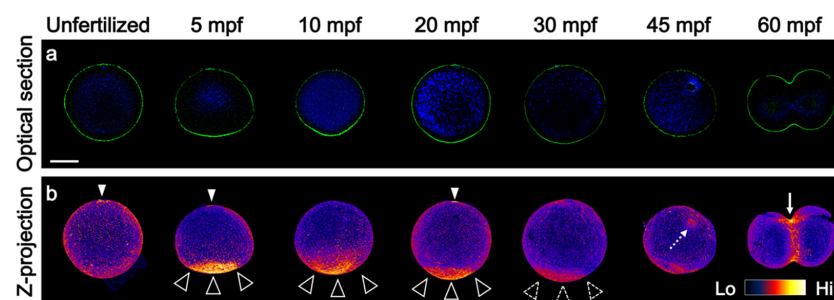


**Figure 1.** Duration of vegetally localized F-actin after fertilization. (a) The embryos during first cell cycle were stained for DNA (blue) and F-actin (green) by using 4',6-diamidino-2-phenylindole dihydrochloride (DAPI) and phalloidin. The optical sections of the midplane are shown except for 60 mpf. At 60 mpf, the frontal view wherein the animal pole is up and right side is right was shown, because the cleavage furrow can be easily observed in this plane. The timings of fixation are indicated on top. The F-actin significantly localized to the vegetal pole at least until 30 mpf. Closed arrowheads in 5 and 20 mpf indicate actin caps of polar body I and II, respectively, suggesting the existence of meiotic spindle beneath them [26]. These observations were repeated four times in each time point using approximately 50 eggs in each experiment. (b) Z-projection models were rendered from single channel of F-actin and represented in fire gradient. The range indicator is shown at the right corner. Arrowheads and dotted arrowheads indicate the strong and weak signals of F-actin at the vegetal pole, respectively. The staining of the other cortical region including 45 mpf was not obvious nor consistent. Mitotic apparatus was slightly stained in 45 mpf (dotted arrow) and contractile ring of cleavage furrow was brightly stained in 60 mpf (arrow). Animal pole (A) is up. Scale bar: 50  $\mu$ m.

### 3.2. Actin Depolymerization Induced Malformation of CAMP

To reveal the functions of prolonged F-actin accumulation at the vegetal cortex during the following events, eggs were treated with CytB at various periods during the first cell cycle; CytB\_01 (0 to 10 mpf), CytB\_02 (0 to 30 mpf), CytB\_03 (10 to 30 mpf), and CytB\_04 (30 to 45 mpf), as shown in Figure 2a. To investigate the effect of CytB treatment on axis formation, we analyzed the second phase of ooplasmic segregation extensively. The effect of CytB treatment was confirmed by phalloidin staining of normal eggs fixed at 10 mpf. In those eggs, no F-actin staining in the vegetal pole could be found (Figure 2b,b'). First, microtubule structures in the eggs of 45 mpf were observed. In the control egg, the CAMP was normally formed, representing a kind of convergence to the midline; thus, microtubule bundles were dense around the midline (Figure 2c). The CAMP formed by CytB\_01 and CytB\_03 treatments were relatively normal, though expanded broadly, and did not show midline accumulation of microtubule bundles (Figure 2d,f). The CytB\_02 treatment gave rise to a widely and randomly distributed microtubule network in the vegetal hemisphere (Figure 2e). In the CytB\_04 treatment, although the microtubule bundles were arrayed in a similar direction and accumulated around the postulated posterior pole, this CAMP-like structure was missing a large portion (Figure 2g). We supposed that the treatment with CytB before the second phase of ooplasmic segregation broadened the CAMP-forming area and made the anteroposterior axis ambiguous, whereas the treatment during the second phase of movement caused a defective CAMP with the postulated anteroposterior axis. Moreover, although several chromosomes detached from spindle microtubules in CytB\_02 (Figure 2j), mitotic apparatus for the first cleavage had bipolar spindles and asters in all CytB-treated eggs (Figure 2h–l). Thus, the effect of CytB treatment mainly affected the microtubules beneath the egg cortex, suggesting a relationship between microfilaments and microtubules beneath the egg cortex.

### 3.3. The Prolonged F-Actin Localization Contributed to the Midline Accumulation of Myoplasm and Maternal mRNA

As the effect of CytB on CAMP formation was different, we first focused on the effect before the second phase of ooplasmic segregation (0 to 30 mpf). The CytB-treated eggs were fixed at 45 mpf and triple-stained for macho-1 mRNA, ER, and mitochondria (Figure 3). In DMSO-treated control embryos, dense ER, MRC, and macho-1 were clearly localized and concentrated at the posterior pole, and both mitochondria and macho-1 were excluded from the dense ER region, as reported in our previous paper (Figure 3a,a',h). When eggs were treated with CytB, the distribution of macho-1 broadly expanded with various phenotypes (Figure 3b–d,b'–d',b''–d''). In CytB\_01, although a large part of macho-1 was localized to the posterior side, some macho-1 were left in anterior side (Figure 3b,b'). Moreover, the localized area of macho-1 was broadened along a left–right axis (Figure 3b''). This result might be due to the retention of macho-1 on almost the entire egg cortex caused by the inhibition of the first phase of ooplasmic segregation. In CytB\_02, macho-1 was broadly localized in the cortical regions of the vegetal hemisphere (Figure 3c,c',c''). This severe phenotype was thought to be the additive effect of CytB\_01 and CytB\_03. In most cases of CytB\_03, macho-1 moved and localized to the posterior pole, similar to those of the normal control (Figure 3d,d'), however, it showed wider distribution along the left–right axis (Figure 3d''). Notably, CytB\_01 and 02 treatments showed scattered distributions of macho-1 signals, while CytB\_03 treatment showed a single lump of macho-1 signal (Figure 3b''–d''). In the quantitative analyses of these results, it was clearly demonstrated that CytB treatments had different effects for the macho-1 distributions along the anteroposterior and left–right axes (Figure 3e–g). To summarize these results, depolymerization of F-actin during the first segregation movement resulted in the scattered and broadened localization of macho-1 along both anteroposterior and left–right axes, while the depolymerization of F-actin during the period between the first and second segregation only broadened the macho-1 localization along the left–right axis. Thus, it was suggested that the actin filaments during the first phase of segregation had the role of lumping macho-1

mRNAs into a single mass in addition to the constriction of the egg cortex into the vegetal pole, and prolonged localization of actin filaments beneath the vegetal pole had the role of the convergence of macho-1 mRNAs to the midline. The MRC resided adjacent to the inner side of dense ER, and macho-1 extruded from dense ER and into the MRC and deeper cytoplasm in all treatments (Figure 3h–k). Although, the macho-1 mRNA was distributed abnormally by CytB treatments, dense ER and MRC were situated close to macho-1, and MRC was always situated next to the dense ER.

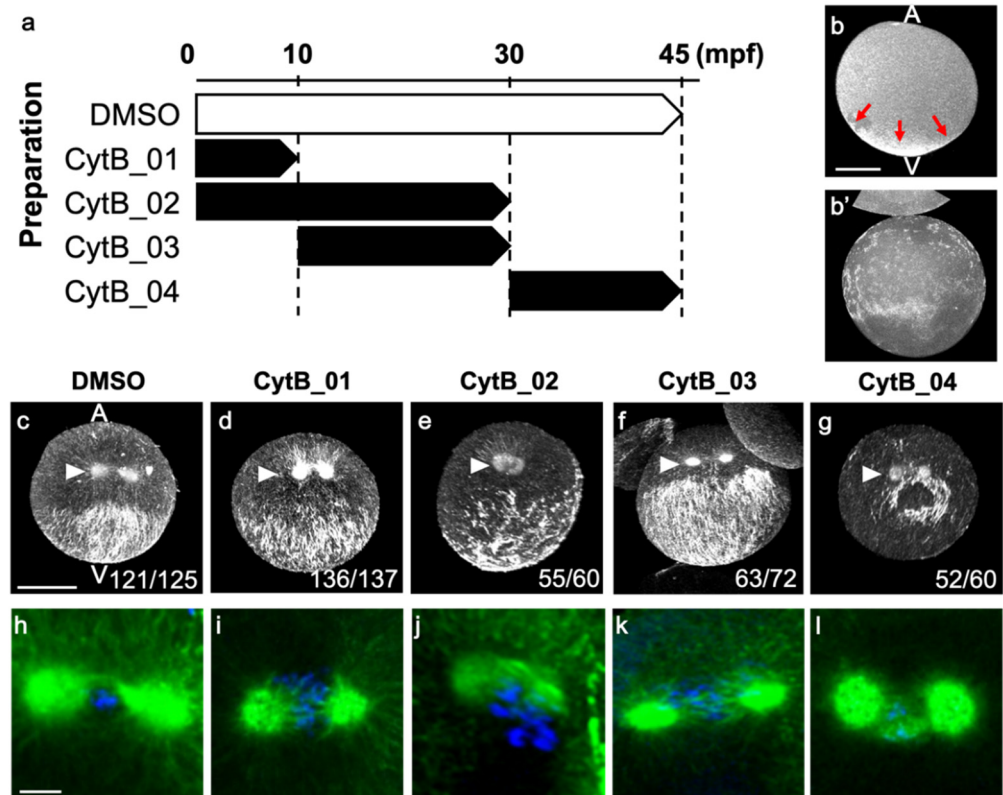


**Figure 2.** The effect of CytB treatment on CAMP formation during first cell cycle. (a) Schematic drawing of sample preparation. The white and black blocks indicate incubation periods with DMSO and 2 µg/mL CytB, respectively. The egg was treated with DMSO as the normal control. (b,b') Normal (b) and CytB-treated eggs (b') were fixed at 10 mpf and stained with phalloidin. CytB-treated eggs did not show F-actin staining in the vegetal pole. The Z-projections of the side view are shown. Animal pole (A) is up. Arrows indicate strong signal at the vegetal pole. Scale bar: 50 µm. (c–g) Eggs were fixed at 45 mpf and immunostained for tubulin. Preparation name of each egg is indicated on the top. Animal pole (A) is up. Posterior views of rendered Z-projection representing various malformations of CAMP. Normal CAMP emerges as a parallel array of microtubules on the posterior-vegetal cortex. Microtubule bundles are relatively dense around the midline (c). Arrowhead indicates mitotic apparatus of first cleavage, representing the midplane is situated in between two centrosomes. It should be noted that, although the progression of the cell cycle was slightly affected (d). The number of embryos represented by the image over the number of embryos examined is indicated at the right corner. Scale bar: 50 µm. (h–l) Enlarged Z-projections rendered from 30 optical sections around the mitotic apparatus in (c–g) are represented. Green and blue indicate microtubule and DNA, respectively. Scale bar: 10 µm.

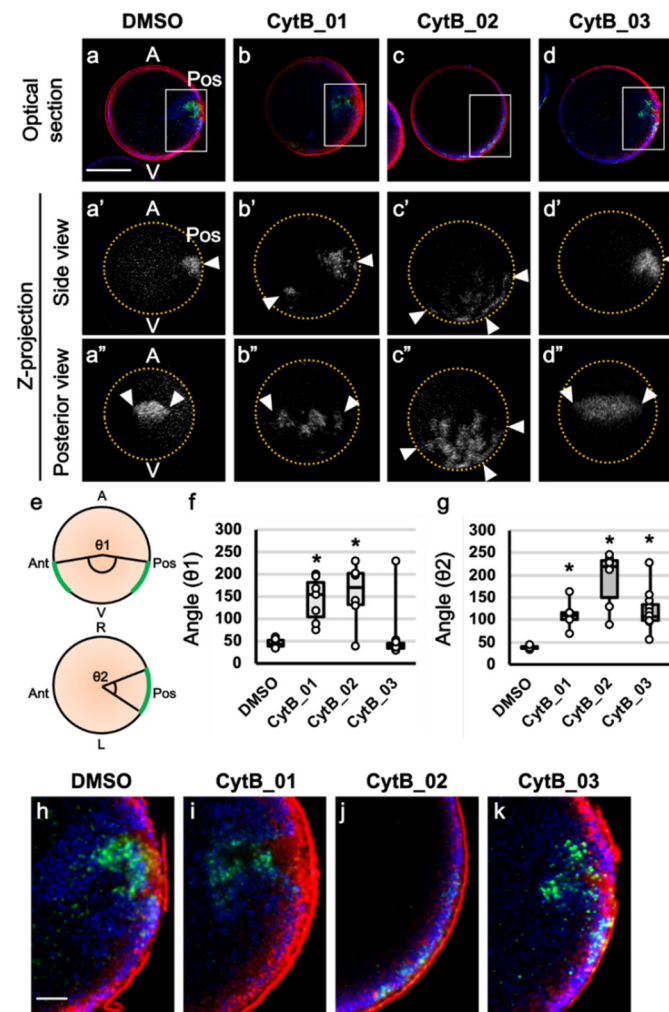


**Figure 3.** The role of prolonged F-actin localization to the vegetal cortex for translocations of organelles and maternal mRNA. ((a–d,a'–d',a''–d'')) The CytB-treated eggs were fixed at 45 mpf. Preparation of each egg is indicated on the top. The double-immunostaining of ER (red) and mitochondria (blue) and in situ hybridization of macho-1 (green) were carried out. Merged images of midplane optical sections ((a–d): optical section) and Z-projections of single channel of macho-1 are shown ((a'–d'): side view, (a''–d''): posterior view). Yellow dotted lines indicate the outline of eggs. Animal pole (A) is up, vegetal pole (V) is down, and posterior pole (Pos) is on the right. Arrowheads indicate mRNA localized region. Scale bar: 50  $\mu$ m. (e) The angles,  $\theta_1$  and  $\theta_2$ , were measured between vertical and horizontal edges of mRNA signal area, respectively, and the center of eggs using Z-projection as shown in the schema. In CytB\_01, macho-1 signals were left in the anterior side, and thus,  $\theta_1$  became relatively large in most cases. (f,g) The central angle of the macho-1-localized region was measured on Z-projection and represented using box plots. Numbers of specimens were 7, 7, 6, and 11 in DMSO, CytB\_01, \_02, and \_03, respectively. These angles represent expansion of macho-1 localization with CytB treatments. Statistical significance was calculated by one-way ANOVA followed by the Dunnett's test (SD in f: DMSO = 9.6, CytB\_01 = 50.2, CytB\_02 = 69.7, CytB\_03 = 58.4; SD in g: DMSO = 3.8, CytB\_01 = 30.9, CytB\_02 = 64.9, CytB\_03 = 43.7). Significant differences versus DMSO are represented by asterisks ( $p < 0.01$ ). (h–k) Enlarged images of white rectangles of (a–d) are represented. In DMSO and CytB\_01, MRC (blue) was adjacent to the inner side of dense ER (red), while in CytB\_02 and \_03, MRC and dense ER were mingled but represented discrete distribution (blue and red signals do not overlapped). Scale bar: 10  $\mu$ m.



### 3.4. The Role of F-Actin during the Second Phase of Ooplasmic Segregation

Eggs treated with CytB\_04 were fixed at 45 mpf and triple-stained for ER, mitochondria, and macho-1 (Figure 4). In normal eggs, dense ER thickened its localized area at the posterior pole region and tended to intrude into the inner cytoplasm by following the movement of sperm aster, and macho-1 was excluded from the ER and intruded into the MRC or even deeper cytoplasm of the posterior pole (Figure 4a,a',c,c'). In the CytB\_04-treated egg, both macho-1 and dense ER were situated on the posterior vegetal cortex (Figure 4b,b'). However, they formed a thin localized area sticking to the cortex, and most of the macho-1 signal colocalized with dense ER (Figure 4d,d'). To examine the role of microtubules in the macho-1 translocation during the second phase of ooplasmic segregation, eggs were treated with 2.5 µg/mL Noco from 30 to 45 mpf (Figure 4e–e'',f–f'''). Noco treatment inhibited the second phase of ooplasmic segregation. Thus, the myoplasm remained in the vegetal pole, and the anteroposterior axis was abolished. Although no microtubule staining was observed in Noco-treated eggs, there was a faint tubulin staining at the vegetal pole (Figure 4e,e'). Dense ER colocalized with this tubulin-staining region, suggesting a close relationship between the ER and microtubules (Figure 4e''). According to the triple-staining result, mutual positioning of the vegetally stained ER and MRC was basically the same as the normal positioning of 30 mpf (Figure 4f,f') and of the CytB\_04 treatment. The MRC resided adjacent to the inner side of dense ER (Figure 4f'''). Although dense ER showed a thin layer beneath the posterior cortex and did not move into the egg cytoplasm in CytB\_04 treatment, Noco treatment did not change dense ER and MRC distribution (Figure 4d,d',f,f',f'''). On the other hand, in Noco treatment, most of the macho-1 signals colocalized with dense ER, similarly to CytB\_04 (Figure 4d,d',f,f',f'''). Quantitative analysis of this abnormality in the translocation of macho-1 revealed a similar effect of both actin and tubulin depolymerizations (Figure 4g,h). As macho-1 dissociated from dense ER by 30 mpf in the normal condition [14], macho-1 went back to dense ER under the condition with each inhibitor. Although, there is a possibility that the depolymerization of microtubules indirectly affects the macho-1 translocation by aborting the movement of the second phase, both F-actin and microtubules were suggested to have some roles in preventing macho-1 being reassociated with dense ER during the second phase of movement.

### 3.5. F-Actin Contributed to the Cleavage Patterning during the First Cell Cycle

The effect of CytB treatment during the first cell cycle to the later cleavage was investigated, focusing on the establishment of the anteroposterior axis. The eggs treated with CytB were fixed at the 32-cell stage and stained for macho-1 (Figure 5). In normal 32-cell stage embryos, macho-1 was localized to the CAB region, which resides equally in the posterior-most vegetal small blastomere pair (B6.3 and B6.3; micromere), and defined the posterior pole (Figure 5a). When the eggs were treated with CytB at various periods of the one-cell stage, they showed various abnormal phenotypes. Two-thirds of the embryos of CytB\_01 treatment gave rise to the embryo with two macho-1-localized spots in the adjacent micromeres, predicting the establishment of the anteroposterior axis, but the sizes of the signal areas and micromeres were unequal (Figure 5b). On the other hand, one-third of CytB\_01-treated embryos had two macho-1 localized spots in two discontinuous blastomeres, which could not define their posterior pole (Figure 5b'). CytB\_02-treated embryos showed the most severe phenotype. Most of the embryos showed delayed and abnormal cleavage with no symmetrical pattern, even in the embryo with two macho-1 signals in neighboring blastomeres (Figure 5c,c'). Three-fourths of them had a single elongated signal situated unevenly in two blastomeres (Figure 5c'). The majority of the CytB\_03-treated embryos had two or three macho-1-localized spots in the equivalent-size blastomeres, and thus could not show the anteroposterior axis (Figure 5d,d'). However, half of the CytB\_04-treated embryos had two macho-1-localized spots with weak left–right symmetry. The other half had only one macho-1-localized spot with no left–right symmetry (Figure 5e,e').

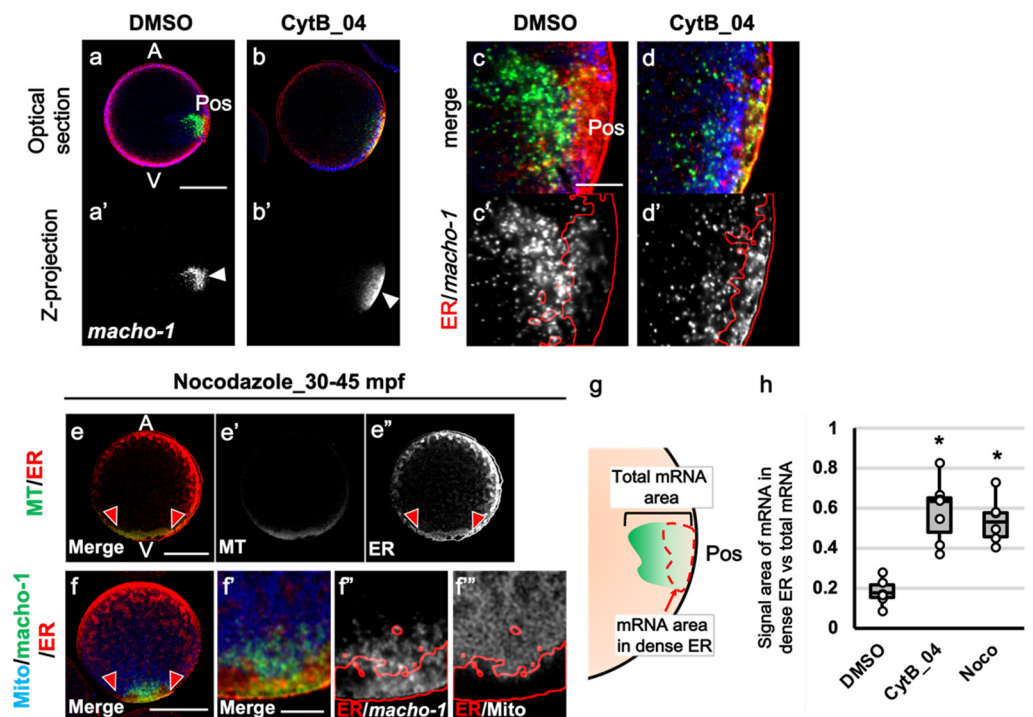


**Figure 4.** The role of F-actin during second phase of movement for the translocation of organelles and maternal mRNA. (a–d, a'–d') The CytB-treated eggs were fixed at 45 mpf and double-immunostaining of ER (red) and mitochondria (blue) and in situ hybridization of *macho-1* (green) were carried out. Preparation of each egg is indicated on the top. Merged images of midplane optical sections ((a,b): optical section) and rendered Z-projections of single channel of *macho-1* signal ((a',b'): Z-projection) are indicated. (c,d) Enlarged merged images of the posterior pole regions of a and b are shown (Merge). (c',d') The outline of dense ER region (red line) was superimposed on single channel of *macho-1* signal of c and d (white). Animal pole (A) is up, vegetal pole (V) is down, and posterior pole (Pos) is on the right. Arrowhead indicates *macho-1*-localized region. (e–e'', f–f'') Noco treatment was carried out during 30–45 mpf and fixed at 45 mpf. Single optical section of the plane including animal–vegetal axis are shown. Regions between two red arrowheads represent dense ER region. Noco-treated eggs were double stained for ER (red) and tubulin (MT; green). Merged images ((e): Merge) and single channel of each signal ((e'); MT, (e''); ER) are represented. Microtubule staining was not present, while faint staining was observed in vegetal pole region, presumably due to the tubulin monomer staining (e'). This tubulin staining was colocalized with dense ER (e,e''). Nocodazole-treated eggs were triple stained for ER (red)/mitochondria-rich cytoplasm (MRC; blue)/*macho-1* (green). Merged images (f: Merge) and enlarged image of vegetal pole region of f ((f'); Merge) are shown. Outlines of the dense ER region (red lines) were superimposed on in situ hybridization signals ((f''); ER/*macho-1*) and MRC signals ((f'''); ER/MRC). Note that the background ER staining of entire cortex of the egg became blotchy. Scale bars: 50  $\mu\text{m}$  (a,e,f) and 10  $\mu\text{m}$  (c,f'). (g) Colocalization between *macho-1* and dense ER was quantitatively evaluated by calculating the ratio of the signal area of the *macho-1* within the dense ER region to the total area of mRNAs, as shown in the schema. (h) The results of ratio of the *macho-1* signal area are represented using box plots. Dissociation of *macho-1* from dense ER was inhibited by both CytB\_04 and Noco treatments. The number of specimens was 6 in all treatments. Statistical significance was calculated by one-way ANOVA followed by the Dunnett's test (SD: DMSO = 0.07, CytB\_04 = 0.15, Noco = 0.11). Significant differences versus DMSO are represented by asterisks ( $p < 0.01$ ).

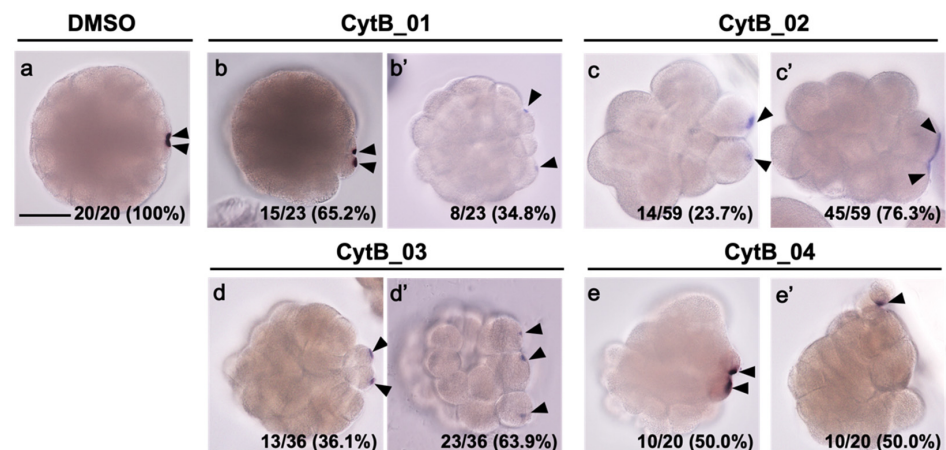


**Figure 5.** The effect of CytB treatment during 1-cell stage on the macho-1 mRNA localization. Preparation name of each egg is indicated on the top. Embryos were fixed at the 32-cell stage (about 3 h after fertilization) and stained for macho-1 by in situ hybridization. (a) The embryo treated with DMSO during 1-cell stage as a normal control exhibited two spots of macho-1 localization, which correspond to the CAB. The CAB is formed bilaterally in the posterior-most blastomeres of vegetal hemisphere, indicating the posterior pole. (b–e, b'–e') The CytB-treated embryos represented cell-cycle retardation and various abnormal phenotypes. They were categorized into two types. In one phenotype, two CABs were formed in two neighboring blastomeres, suggesting the establishment of anteroposterior axis (b–e). The other type included the following phenotypes showing no obvious anteroposterior axis: two CABs were formed in separated blastomeres (b'), elongated CAB was asymmetrically inherited in two blastomeres (c'), three or more CABs were formed in separated blastomeres (d'), and a single CAB was formed in a random position of single blastomere (e'). Arrowheads indicate CABs. The number of embryos represented by the image over the number of embryos examined is indicated in the right corner. Scale bars: 50  $\mu$ m.

These embryos were then stained for macho-1 mRNA, ER, and mitochondria to observe their relative locations (Figure 6). In normal 32-cell stage embryos, macho-1 mRNA colocalized with ER in the micromeres corresponding to CAB formation (Figure 6a, a'). Although CytB-treated embryos showed an abnormal distribution pattern of macho-1 after the second phase of ooplasmic segregation, localized spots of macho-1 in all the treatments were colocalized with ER, suggesting that CAB formation normally occurred (Figure 6b–g, b'–g'). As shown in Figure 5, some of the CABs did not lead to unequal cleavage and posterior pole formation. These CABs suggested a lack of some factors, which is inevitable for exerting the complete function of CAB. Our results suggested that depolymerization of F-actin during the first cell cycle affects the formation of normal CAB.

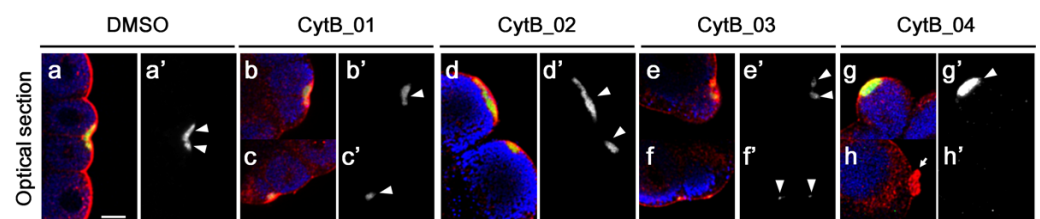


**Figure 6.** Colocalization of macho-1 with ER on the CAB at 32-cell stage. Embryos treated with CytB were fixed at 32-cell stage. The double-immunostaining of ER (red) and mitochondria (blue) and in situ hybridization of macho-1 (green) were performed. (a–h) Single optical section of merged images of CAB region. (a'–h') Single channel of macho-1 in (a–h). Preparation name of each egg is indicated on the top. macho-1 and ER were colocalized at all the CAB regions (arrowheads) despite the CytB treatment. Only the CytB\_04-treated embryo represented small debris of ER, which did not contain macho-1 (arrow). Scale bar: 10  $\mu$ m.

### 3.6. The Disordered Morphogenesis Induced by Cytb Treatment during First-Cell Cycle

Finally, to examine the effect of CytB treatment during the first cell cycle on normal CAB formation, the larval phenotype was examined (Figure 7). Normal larva represented a tadpole shape with a trunk and long tail representing obvious anteroposterior axis (Figure 7a). All of the CytB treatments led to abnormal development and gave rise to two phenotypes (Figure 7b–e, b'–e'). In one phenotype, irregular trunk and abnormal short tail could be identified, suggesting anteroposterior axis formation. In some cases, a pigment granule (thought to be an otolith according to its round shape) was developed (Figure 7b,e). This type of larvae developed approximately 60%, 25%, 45%, and 55% in CytB\_01, CytB\_02, CytB\_03, and CytB\_04, respectively (Figure 7b'–e'). These proportions were close to those of the 32-cell stage embryo with left–right symmetry, as shown in Figure 5. In the other phenotype, although the secretion of tunic suggesting epidermal development and faint rotation symmetry could be observed, it was a type of cell aggregate and we could not define the anteroposterior axis (Figure 7b'–e'). These embryos were thought to be developed from the 32-cell-stage embryo with no anteroposterior axis (Figure 5). This result implied that some CABs could not exert complete functions nor define the anteroposterior axis, suggesting that some important factors were missing from CAB by CytB treatment.

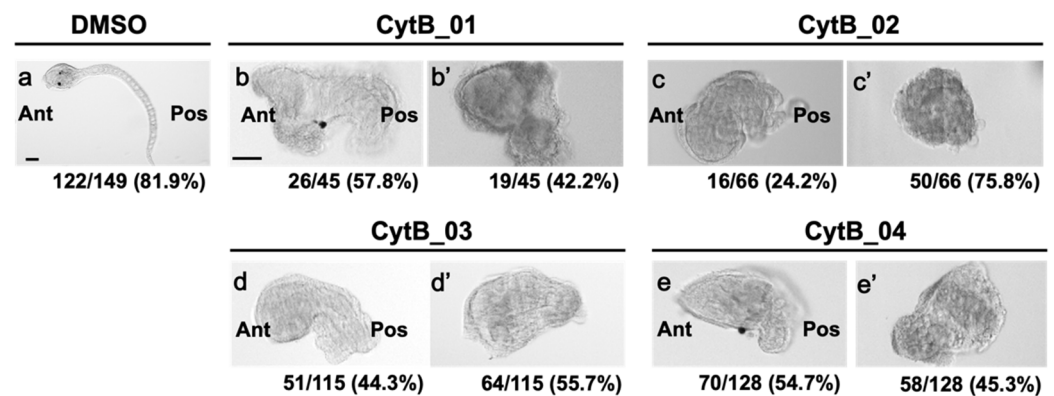


**Figure 7.** The effect of CytB treatment during the 1-cell stage on the larval morphogenesis. Preparation name of each egg is indicated on the top. Embryos were fixed at 20 h postfertilization. (a) The embryo treated with DMSO during 1-cell stage as a normal control exhibited tadpole shape, which has trunk and tail representing anterior (Ant)–posterior (Pos) axis. In addition, two pigment spots (otolith and ocellus) were developed. (b–e, b'–e') The CytB-treated embryos represented various abnormal morphologies. They were categorized into two types. In one type, trunk and tail could be distinguished, suggesting the establishment of anterior–posterior axis. In some cases, otolith-like pigment granules could be observed (b,e). In the other type, embryos became cell aggregates and had no anteroposterior axis. Although they seemed to have tunic on their surface, no other obvious tissue differentiation could be observed (b'–e'). The number of embryos represented by the image over the number of embryos examined is indicated at the right corner. Scale bars: 50  $\mu$ m.

## 4. Discussion

Owing to the methods using unique fixation and hydrophilic clearing reagents, we found prolonged actin localization to the vegetal pole until the start of the second phase. Moreover, we analyzed the role of F-actin during the first cell cycle by describing the colocalization of ER, mitochondria, and mRNA.

When F-actin was depolymerized by CytB at various periods, the cortical microtubule structure, CAMP, showed abnormal shapes according to the period of CytB treatment. The common phenotype of the depolymerization of prolonged vegetal F-actin was the laterally broadened CAMP area, suggesting the inhibition of the convergence of microtubule bundles to the midline. The function and localization of F-actin during the first cell cycle of ascidian early development were reported mainly on the first phase of ooplasmic segregation [9–11], except for a few reports on the existence of cortical F-actin in the posterior–vegetal cortex

during the second phase [27], which we could not confirm in our experiment. Thus, this is the first report that F-actin has some roles, in addition to the first phase of ooplasmic segregation. Specifically, in this report, we found three different roles for maternal mRNA translocation in three different periods, during the first phase of movement, the period between first and second phase, and the second phase of movement. During the first phase, a cortically distributed actin network was suggested to have a role for lumping maternal mRNA in addition to generating contracting force of the first segregation movement. During the period between first and second segregation, prolonged vegetal cortex F-actin was closely located to the vegetally accumulated microtubule fragment [13] and had a role in the convergence of mRNA, mitochondria, and ER to the midline. During the second phase, although we could not detect cortical actin network, depolymerization of F-actin affected the CAMP formation and relocation of maternal mRNA to the dense ER region. The role for keeping maternal mRNAs dissociated from ER was shared by microtubules. These close relationships between microfilaments and microtubules strongly suggest their collaborative mechanisms.

The collaborative role of actin and tubulin in CAMP formation is not an inconceivable event, as it has been reported that actin filaments in somatic cells have various functions in microtubule organization, such as anchoring to the cortex and directional elongation [28]. Moreover, CAMP is suggested to be an acentrosomal microtubule structure. It has been reported that the acentrosomal microtubule structure could be regulated by actin through the spectraplakins (ACF7; crosslinking cytoskeletal protein by binding to both microtubules and F-actin) and the microtubule end-binding proteins (CAMSAP3: calmodulin-regulated spectrin-associated protein 3) [29]. Thus, to reveal the interaction between actin and microtubule in the ascidian egg, analyses of these cytoskeletal-associated molecules are necessary.

The macho-1 dissociation from dense ER during the second phase of ooplasmic segregation was another collaborative mechanism of actin and tubulin. It is well-known that both microtubules and microfilaments have a role in trafficking mRNP granules, complexes of mRNA and ribonucleoproteins (e.g., [30]). In budding yeast, it has been reported that the localization of polysome-interacting protein on the ER is regulated by microtubules [31]. In *Ciona* eggs, one of the RNA binding proteins, Y-box binding protein (YB-1), interacts with *pem-1* mRNA, suggesting the existence of mRNP granule [32]. Type I postplasmic/PEM RNAs associate with ribosomes, which are localized to the cER [33]. From the viewpoint of the collaborative role of different cytoskeletal filaments, an intangible molecular mechanism emerges by combining these reports. In this mechanism, translocation of organelles and mRNA are closely related to translational control. In our results, the importance of excluding mRNA from dense ER is cryptic, whereas the collaborative participation of two different cytoskeletal filaments is a promising mechanism for understanding the translocation of maternal determinants.

On the other hand, the malformation of microtubule structure and the mislocalization of mRNA caused by the depolymerization of microfilaments during the first cell cycle largely affected early development by spoiling the anteroposterior axis. Although most of these damaged embryos had CABs, they could not exert their complete functions, such as determination of the posterior pole and unequal cleavage. This suggested that the components of CABs formed in damaged embryos were insufficient. A considerable number of molecules have been revealed, such as about 40 postplasmic/PEM RNAs and their translational products, Kinesin,  $\beta$ -catenin, YB-1, and regulators of translation initiation [7,16,32,34–37]. Thus, more detailed analyses including these CAB components are required for understanding the relationship between dysfunction of CAB and incomplete translocation of myoplasm. It is well-known that the correct transport of myoplasm and the appropriate distribution of the myoplasmic components through the ooplasmic segregation are important for ascidian development. According to our results, we believe that the precise mechanisms of ooplasmic segregation are more complicated than ever thought. The collaborative role of microfilaments and microtubules is one of these complexities. More

extensive analyses of the mechanisms underlying ooplasmic segregation will contribute to the understanding of the molecular mechanisms of ascidian embryogenesis.

**Author Contributions:** T.G. designed the study, performed the experiments, quantitative analysis, and original draft preparation; S.T., A.K. and K.K. performed the experiments and supported the quantitative analysis; J.K. and Y.K. conceived of this study and participated in interpretation of data; T.N. contributed to the conception of this study and helped to draft the manuscript. All authors have read and agreed to the published version of the manuscript.

**Funding:** This research did not receive any specific grants from funding agencies in the public, commercial, or not-for-profit sectors.

**Institutional Review Board Statement:** Not applicable.

**Informed Consent Statement:** Not applicable.

**Data Availability Statement:** The datasets generated and/or analyzed during the current study are available from the corresponding author upon reasonable request.

**Acknowledgments:** We would like to thank Shirae-Kurabayashi, M. (Nagoya University, Japan) for valuable discussions on immunostaining methods and in situ hybridization. We thank the National BioResource Project for providing *Ciona intestinalis*.

**Conflicts of Interest:** The authors have no conflict of interest directly relevant to the content of this article.





## References

1. Miller, J.R.; Rowning, B.A.; Larabell, C.A.; Yang-Snyder, J.A.; Bates, R.L.; Moon, R.T. Establishment of the Dorsal–Ventral Axis in *Xenopus* Embryos Coincides with the Dorsal Enrichment of Dishevelled that Is Dependent on Cortical Rotation. *J. Cell Biol.* **1999**, *146*, 427–438. [CrossRef]
2. Tao, Q.; Yokota, C.; Puck, H.; Kofron, M.; Birsoy, B.; Yan, D.; Asashima, M.; Wylie, C.C.; Lin, X.; Heasman, J. Maternal Wnt11 Activates the Canonical Wnt Signaling Pathway Required for Axis Formation in *Xenopus* Embryos. *Cell* **2005**, *120*, 857–871. [CrossRef] [PubMed]
3. Tran, L.D.; Hino, H.; Quach, H.; Lim, S.; Shindo, A.; Mimori-Kiyosue, Y.; Mione, M.C.; Ueno, N.; Winkler, C.; Hibi, M.; et al. Dynamic Microtubules at the Vegetal Cortex Predict the Embryonic Axis in Zebrafish. *Development* **2012**, *139*, 3644–3652. [CrossRef] [PubMed]
4. Lyczak, R.; Gomes, J.E.; Bowerman, B. Heads or Tails: Cell Polarity and Axis Formation in the Early *Caenorhabditis Elegans* Embryo. *Dev. Cell* **2002**, *3*, 157–166. [CrossRef]
5. Nance, J.; Zallen, J.A. Elaborating Polarity: PAR Proteins and the Cytoskeleton. *Development* **2011**, *138*, 799–809. [CrossRef] [PubMed]
6. Sardet, C.; Nishida, H.; Prodon, F.; Sawada, K. Maternal mRNAs of PEM and Macho 1, the Ascidian Muscle Determinant, Associate and Move with a Rough Endoplasmic Reticulum Network in the Egg Cortex. *Development* **2003**, *130*, 5839–5849. [CrossRef]
7. Prodon, F.; Yamada, L.; Shirae-Kurabayashi, M.; Nakamura, Y.; Sasakura, Y. Postplasmic/PEM RNAs: A Class of Localized Maternal mRNAs with Multiple Roles in Cell Polarity and Development in Ascidian Embryos. *Dev. Dyn.* **2007**, *236*, 1698–1715. [CrossRef]
8. Sardet, C.; Paix, A.; Prodon, F.; Dru, P.; Chenevert, J. From Oocyte to 16-Cell Stage: Cytoplasmic and Cortical Reorganizations that Pattern the Ascidian Embryo. *Dev. Dyn.* **2007**, *236*, 1716–1731. [CrossRef] [PubMed]
9. Sawada, T.-O.; Schatten, G. Effects of Cytoskeletal Inhibitors on Ooplasmic Segregation and Microtubule Organization during Fertilization and Early Development in the Ascidian *Molgula Occidentalis*. *Dev. Biol.* **1989**, *132*, 331–342. [CrossRef]
10. Chiba, S.; Miki, Y.; Ashida, K.; Wada, M.R.; Tanaka, K.J.; Shibata, Y.; Nakamori, R.; Nishikata, T. Interactions Between Cyto-Skeletal Components during Myoplasm Rearrangement in Ascidian Eggs. *Dev. Growth Differ.* **1999**, *41*, 265–272. [CrossRef]
11. Roegiers, F.; Djediat, C.; Dumollard, R.; Rouviere, C.; Sardet, C. Phases of Cytoplasmic and Cortical Reorganizations of the Ascidian Zygote between Fertilization and First Division. *Development* **1999**, *126*, 3101–3117. [CrossRef] [PubMed]
12. Ishii, H.; Goto, T.; Nishikata, T. Microtubule Array Observed in the Posterior-Vegetal Cortex during Cytoplasmic and Cortical Reorganization of the Ascidian Egg. *Dev. Growth Differ.* **2017**, *59*, 648–656. [CrossRef] [PubMed]
13. Goto, T.; Kanda, K.; Nishikata, T. Non-Centrosomal Microtubule Structures Regulated by Egg Activation Signaling Contribute to Cytoplasmic and Cortical Reorganization in the Ascidian Egg. *Dev. Biol.* **2018**, *448*, 161–172. [CrossRef]
14. Goto, T.; Torii, S.; Kondo, A.; Kawakami, J.; Yagi, H.; Suekane, M.; Kataoka, Y.; Nishikata, T. Dynamic Changes in the Association between Maternal mRNAs and Endoplasmic Reticulum during Ascidian Early Embryogenesis. *Dev. Genes Evol.* **2021**, 1–14. [CrossRef]

15. Hibino, T.; Nishikata, T.; Nishida, H. Centrosome-Attracting Body: A Novel Structure Closely Related to Unequal Cleavages in the Ascidian Embryo. *Dev. Growth Differ.* **1998**, *40*, 85–95. [CrossRef]
16. Nishikata, T.; Hibino, T.; Nishida, H. The Centrosome-Attracting Body, Microtubule System, and Posterior Egg Cytoplasm Are Involved in Positioning of Cleavage Planes in the Ascidian Embryo. *Dev. Biol.* **1999**, *209*, 72–85. [CrossRef]
17. Ishii, H.; Kunihiro, S.; Tanaka, M.; Hatano, K.; Nishikata, T. Cytosolic Subunits of ATP Synthase are Localized to the Cortical Endoplasmic Reticulum-Rich Domain of the Ascidian Egg Myoplasm. *Dev. Growth Differ.* **2012**, *54*, 753–766. [CrossRef] [PubMed]
18. Ishii, H.; Shirai, T.; Makino, C.; Nishikata, T. Mitochondrial Inhibitor Sodium Azide Inhibits the Reorganization of Mitochondria-Rich Cytoplasm and the Establishment of the Anteroposterior Axis in Ascidian Embryo. *Dev. Growth Differ.* **2014**, *56*, 175–188. [CrossRef] [PubMed]
19. Ojima, K.; Lin, Z.X.; Andrade, I.R.; Costa, M.L.; Mermelstein, C. Distinctive Effects of Cytochalasin B in Chick Primary Myoblasts and Fibroblasts. *PLoS ONE* **2016**, *11*, e0154109. [CrossRef]
20. Hayashi, T.; Lewis, A.; Hayashi, E.; Betenbaugh, M.J.; Su, T.P. Antigen Retrieval to Improve the Immunocytochemistry Detection of Sigma-1 Receptors and ER Chaperones. *Histochem. Cell Biol.* **2011**, *135*, 627–637. [CrossRef]
21. Prodon, F.; Hanawa, K.; Nishida, H. Actin Microfilaments Guide the Polarized Transport of Nuclear Pore Complexes and the Cytoplasmic Dispersal of Vasa mRNA during GVBD in the Ascidian *Halocynthia roretzi*. *Dev. Biol.* **2009**, *330*, 377–388. [CrossRef]
22. Ke, M.-T.; Fujimoto, S.; Imai, T. SeeDB: A Simple and Morphology-Preserving Optical Clearing Agent for Neuronal Circuit Reconstruction. *Nat. Neurosci.* **2013**, *16*, 1154–1161. [CrossRef]
23. Satou, Y.; Satoh, N. Cataloging Transcription Factor and Major Signaling Molecule Genes for Functional Genomic Studies in *Ciona intestinalis*. *Dev. Genes Evol.* **2005**, *215*, 580–596. [CrossRef]
24. Chenevert, J.; Pruliere, G.; Ishii, H.; Sardet, C.; Nishikata, T. Purification of Mitochondrial Proteins HSP60 and ATP Synthase from Ascidian Eggs: Implications for Antibody Specificity. *PLoS ONE* **2013**, *8*, e52996. [CrossRef]
25. Schindelin, J.; Arganda-Carreras, I.; Frise, E.; Kaynig, V.; Longair, M.; Pietzsch, T.; Preibisch, S.; Rueden, C.; Saalfeld, S.; Schmid, B.; et al. Fiji: An Open-Source Platform for Biological-Image Analysis. *Nat. Methods* **2012**, *9*, 676–682. [CrossRef] [PubMed]
26. McDougall, A.; Hebras, C.; Pruliere, G.; Burgess, D.; Costache, V.; Dumollard, R.; Chenevert, J. Role of PB1 Midbody Remnant Creating Tethered Polar Bodies during Meiosis II. *Genes* **2020**, *11*, 1394. [CrossRef]
27. Jeffery, W.R.; Meier, S. A Yellow Crescent Cytoskeletal Domain in Ascidian Eggs and its Role in Early Development. *Dev. Biol.* **1983**, *96*, 125–143. [CrossRef]
28. Dogterom, M.; Koenderink, G.H. Actin–Microtubule Crosstalk in Cell Biology. *Nat. Rev. Mol. Cell Biol.* **2018**, *20*, 38–54. [CrossRef]
29. Noordstra, I.; Liu, Q.; Nijenhuis, W.; Hua, S.; Jiang, K.; Baars, M.; Remmelzwaal, S.; Martin, M.; Kapitein, L.C.; Akhmanova, A. Control of Apico-Basal Epithelial Polarity by the Microtubule Minus-End Binding Protein CAMSAP3 and Spectraplakins ACF7. *J. Cell Sci.* **2016**, *129*, 4278–4288. [CrossRef] [PubMed]
30. Koppers, M.; Özkan, N.; Fariás, G.G. Complex Interactions between Membrane-Bound Organelles, Biomolecular Condensates and the Cytoskeleton. *Front. Cell Dev. Biol.* **2020**, *8*, 1661. [CrossRef] [PubMed]
31. Frey, S.; Pool, M.; Seedorf, M. Scp160p, an RNA-Binding, Polysome-Associated Protein, Localizes to the Endoplasmic Reticulum of *Saccharomyces cerevisiae* in a Microtubule-Dependent Manner. *J. Biol. Chem.* **2001**, *276*, 15905–15912. [CrossRef]
32. Tanaka, K.J.; Matsumoto, K.; Tsujimoto, M.; Nishikata, T. CiYB1 Is a Major Component of Storage mRNPs in Ascidian Oocytes: Implications in Translational Regulation of Localized mRNAs. *Dev. Biol.* **2004**, *272*, 217–230. [CrossRef]
33. Paix, A.; Yamada, L.; Dru, P.; Lecordier, H.; Pruliere, G.; Chenevert, J.; Satoh, N.; Sardet, C. Cortical Anchorages and Cell Type Segregations of Maternal Postplasmic/PEM RNAs in Ascidians. *Dev. Biol.* **2009**, *336*, 96–111. [CrossRef] [PubMed]
34. Costache, V.; Hebras, C.; Pruliere, G.; Besnardeau, L.; Failla, M.; Copley, R.R.; Burgess, D.; Chenevert, J.; McDougall, A. Kif2 Localizes to a Subdomain of Cortical Endoplasmic Reticulum that Drives Asymmetric Spindle Position. *Nat. Commun.* **2017**, *8*, 1–13. [CrossRef] [PubMed]
35. Negishi, T.; Takada, T.; Kawai, N.; Nishida, H. Localized PEM mRNA and Protein Are Involved in Cleavage-Plane Orientation and Unequal Cell Divisions in Ascidians. *Curr. Biol.* **2007**, *17*, 1014–1025. [CrossRef] [PubMed]
36. Kumano, G.; Nishida, H. Patterning of an Ascidian Embryo along the Anterior–Posterior Axis through Spatial Regulation of Competence and Induction Ability by Maternally Localized PEM. *Dev. Biol.* **2009**, *331*, 78–88. [CrossRef]
37. Paix, A.; Le Nguyen, P.N.; Sardet, C. Bi-Polarized Translation of Ascidian Maternal mRNA Determinant Pem-1 Associated with Regulators of the Translation Machinery on Cortical Endoplasmic Reticulum (cER). *Dev. Biol.* **2011**, *357*, 211–226. [CrossRef]

Article

# Involvement of a Basic Helix-Loop-Helix Gene *BHLHE40* in Specification of Chicken Retinal Pigment Epithelium

Toshiki Kinuhata <sup>1,†</sup>, Keita Sato <sup>2,†</sup> , Tetsuya Bando <sup>2</sup>, Taro Mito <sup>3</sup> , Satoru Miyaishi <sup>4</sup>, Tsutomu Nohno <sup>5</sup>   
and Hideyo Ohuchi <sup>2,\*</sup> 

<sup>1</sup> Department of Cytology and Histology, Okayama University Graduate School of Medicine, Dentistry and Pharmaceutical Sciences, 2-5-1 Shikata-cho, Kita-ku, Okayama 700-8558, Japan

<sup>2</sup> Department of Cytology and Histology, Okayama University Faculty of Medicine, Dentistry and Pharmaceutical Sciences, 2-5-1 Shikata-cho, Kita-ku, Okayama 700-8558, Japan

<sup>3</sup> Bio-Innovation Research Center, Tokushima University, 2272-2 Ishii, Ishii-cho, Myozai-gun, Tokushima 779-3233, Japan

<sup>4</sup> Department of Legal Medicine, Okayama University Faculty of Medicine, Dentistry and Pharmaceutical Sciences, 2-5-1 Shikata-cho, Kita-ku, Okayama 700-8558, Japan

<sup>5</sup> Department of Cytology and Histology, Okayama University Medical School, 2-5-1 Shikata-cho, Kita-ku, Okayama 700-8558, Japan

\* Correspondence: ohuchi-hideyo@okayama-u.ac.jp

† These authors contributed equally to this work.

**Abstract:** The first event of differentiation and morphogenesis in the optic vesicle (OV) is specification of the neural retina (NR) and retinal pigment epithelium (RPE), separating the inner and outer layers of the optic cup, respectively. Here, we focus on a basic helix-loop-helix gene, *BHLHE40*, which has been shown to be expressed by the developing RPE in mice and zebrafish. Firstly, we examined the expression pattern of *BHLHE40* in the developing chicken eye primordia by in situ hybridization. Secondly, *BHLHE40* overexpression was performed with in ovo electroporation and its effects on optic cup morphology and expression of NR and RPE marker genes were examined. Thirdly, we examined the expression pattern of *BHLHE40* in *LHX1*-overexpressed optic cup. *BHLHE40* expression emerged in a subset of cells of the OV at Hamburger and Hamilton stage 14 and became confined to the outer layer of the OV and the ciliary marginal zone of the retina by stage 17. *BHLHE40* overexpression in the prospective NR resulted in ectopic induction of *OTX2* and repression of *VSX2*. Conversely, *BHLHE40* was repressed in the second NR after *LHX1* overexpression. These results suggest that emergence of *BHLHE40* expression in the OV is involved in initial RPE specification and that *BHLHE40* plays a role in separation of the early OV domains by maintaining *OTX2* expression and antagonizing an NR developmental program.

**Keywords:** basic helix-loop-helix e40; *BHLHE40*; LIM homeobox 1; *LHX1*; chicken; optic vesicle; retinal pigment epithelium; RPE; neural retina

**Citation:** Kinuhata, T.; Sato, K.; Bando, T.; Mito, T.; Miyaishi, S.; Nohno, T.; Ohuchi, H. Involvement of a Basic Helix-Loop-Helix Gene *BHLHE40* in Specification of Chicken Retinal Pigment Epithelium. *J. Dev. Biol.* **2022**, *10*, 45. <https://doi.org/10.3390/jdb10040045>

Academic Editors: Morris F. Maduro and Simon J. Conway

Received: 31 July 2022

Accepted: 24 October 2022

Published: 29 October 2022

**Publisher's Note:** MDPI stays neutral with regard to jurisdictional claims in published maps and institutional affiliations.



**Copyright:** © 2022 by the authors. Licensee MDPI, Basel, Switzerland. This article is an open access article distributed under the terms and conditions of the Creative Commons Attribution (CC BY) license (<https://creativecommons.org/licenses/by/4.0/>).

## 1. Introduction

The eye develops as bilateral optic vesicles from parts of the forebrain. Subsequently, the optic cup develops by invagination of the optic vesicle. The neural retina (NR) and the retinal pigment epithelium (RPE) differentiate from the inner and outer layers of the optic cup, respectively. The NR gives rise to various neuronal cells involved in photoreception (cone and rod cells) and processing of visual information (interneurons, such as amacrine, horizontal and bipolar cells and projection neurons, such as retinal ganglion cells, and Müller glia cells). The RPE is a single layered epithelium that prevents light scattering in the retina and sustains metabolism and maintenance of the photoreceptors. How these two retinal domains are initially specified and develop to mature cell layers consisting of various retinal cell types is a fundamental issue in developmental biology and regenerative medicine to alleviate congenital retinal disorders.



In chicken embryos, FGF1 secreted from the surface ectoderm abutting the optic vesicle can direct the neural retina (NR) domain in the optic vesicle [1]. NR cells are specified by stage 13 (19 pairs of somites), and before this stage, optic vesicle cells can exhibit a dorsal telencephalic character when cultured alone. Then, the NR identity is established by BMP signals from the lens ectoderm [2]. However, another study shows that a high dose of BMP5 is able to reprogram NR into the RPE by inducing the expression of *MITF*, an RPE differentiation transcription factor, when a *Wnt2b* signal is present in the chicken optic cup [3]. This discrepancy is explained by the optic cell behavior depending on the concentration of BMP5 as a low dose of BMP5 induces the expression of *Vsx2*, an NR specification transcription factor, resulting in the conversion of the RPE to the NR [3]. Strikingly, embryonic stem cells from mammals can self-organize to form optic vesicles and develop the layered retina even without surface ectoderm [4,5]. Therefore, it seems likely that the NR and RPE compartments are initially determined by intrinsic factors, but their further development and sustained differentiation require extrinsic factors from the surrounding tissues.

Recent studies in zebrafish have shown that NR development is a default state and specification of RPE in the optic primordia separates the distinct NR and RPE domains in the optic cup [6]. However, differences between species are observed in the development of RPE: Maturation of RPE is fulfilled by cell shape change in zebrafish but in amniotes cell proliferation occurs in that phase [7]. In this study, we focus on an RPE gene, *basic helix-loop-helix e40*, (*BHLHE40*), shown to be expressed in the prospective and definitive RPE cells. In zebrafish, *bhlhe40* expression begins in the optic vesicle, becomes confined to its medial layer, the future RPE, and retains in the RPE throughout embryonic development [8]. Since zebrafish *bhlhe40* could mark the prospective RPE cells from as early as 12-somite stage [9], how the RPE progenitors expand over the optic cup has been visualized [7,9]. In the developing mouse eye, *Bhlhe40* is expressed in the prospective RPE by embryonic day 11.5 (E11.5) and its expression persists in the RPE at later stages [10]. *Bhlhe40*, also known as *DEC1* [11], *Stra13* [12], and *SHARP2* [13], has many physiological and pathological functions, such as in cellular differentiation, circadian rhythm, immunity, and cancer [14–16]. However, roles of *Bhlhe40* in RPE specification has been elusive. As a first step to know the conserved and species-specific systems in early optic vesicle morphogenesis, we examined the expression pattern of *BHLHE40* during chickens' early eye development and the effects of its overexpression in the optic primordia.

## 2. Materials and Methods

### 2.1. Chicken Embryos

Fertilized White Leghorn chicken embryos were obtained from Goto Furanjyo (Gifu, Japan). Eggs were incubated on their sides in a humidified incubator at 38 °C until the desired embryonic stage. All embryos were staged according to Hamburger and Hamilton [17]. All experiments were performed in accordance with the Recombinant DNA Advisory Committee and the Animal Care and Use Committee, Okayama University, in agreement with relevant guidelines in Japan.

### 2.2. Isolation of Chicken cDNAs and Construction of Expression Vectors

Chicken embryonic heads were dissected from 10 embryos at Hamburger and Hamilton (HH) stages 16–17, 21 and 24 in ice-cold PBS, and RNA was extracted using an RNAqueous-Micro Total RNA Isolation Kit (Thermo Fisher Scientific, Waltham, MA, USA). First strand complementary DNA (cDNA) was synthesized using RNA and SuperScript III Reverse Transcriptase (Thermo Fisher Scientific, Waltham, MA, USA) with random primers. Partial cDNAs for chicken *BHLHE40* and other RPE marker genes were isolated using the cDNA and primers listed in Supplementary Table S1 by PCR. The amplified cDNAs were cloned into the pGEM-T Easy (Promega, Madison, WI, USA) or pBluescript II KS (+) (Stratagene, La Jolla, CA, USA) vector and used as templates for *in vitro* transcription. The synthesized RNAs were utilized for *in situ* hybridization probes. For *in ovo* electroporation,

we obtained cDNA containing the entire coding sequence (cds) for chicken *BHLHE40*, which was further cloned into the expression vector pCAGGS [18].

### 2.3. Cryosectioning

Embryonic heads or whole embryos were fixed in 4% paraformaldehyde (PFA) in phosphate-buffered saline (PBS) overnight, washed with PBS, cryoprotected in 20% sucrose/PBS and embedded in OCT compound (Tissue-Tek; Sakura Finetek, Tokyo, Japan) and frozen at  $-80^{\circ}\text{C}$ . Sections were cut at  $15\ \mu\text{m}$  or  $16\ \mu\text{m}$  on a cryostat (Tissue-Tek Polar B; Sakura Finetek Japan, Tokyo, Japan or Leica 1860; Leica Microsystems, Wetzlar, Germany) and mounted on adhesive glass slides (Matsunami Glass, Kishiwada, Japan). The slides were air-dried for 1 h and stored at  $-20^{\circ}\text{C}$  until further analysis.

### 2.4. In Situ Hybridization (ISH)

Whole-mount ISH (WISH) was performed according to Kawau et al. [19] by the use of a semiautomatic ISH machine (HS-5100; Aloka, Tokyo, Japan) (Figure 1A–D', E). The ISH on sections was performed according to Sato et al. [20]. Each RNA probe was used at a concentration of  $0.67\ \mu\text{g}/\text{mL}$  (WISH) or  $0.17\ \mu\text{g}/\text{mL}$  (sections) in hybridization buffer. Fluorescence ISH using HNPP/Fast Red Fluorescent Detection set (Roche #1175888001) was performed basically according to the kit instructions but without proteinase treatment for subsequent immunofluorescence (Figure 2B–D). ISH experiments were performed at least in triplicate (Figure 1) or in duplicate (other data).

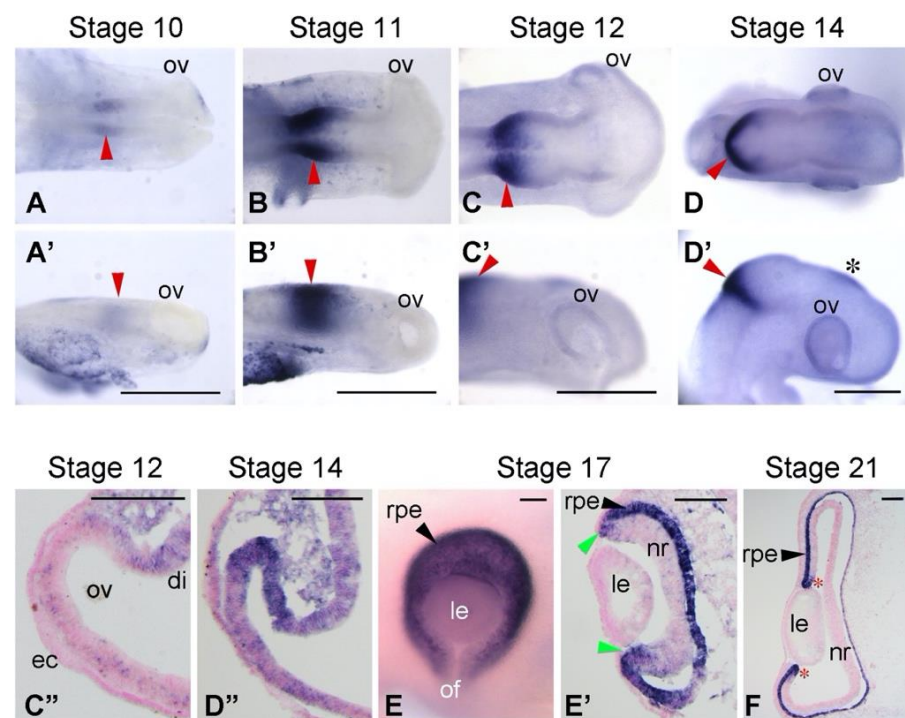


**Figure 1.** Expression pattern of *BHLHE40* in chicken early embryos. (A–D',E) Whole-mount in situ hybridization of chick embryos at Hamburger and Hamilton (HH) stages 10 to 14, and 17. Dorsal views (A–D) and lateral views (A'–D'; to the same scale of A–D, respectively) of embryonic heads or eye (E) are shown. Red arrowheads show the midbrain-hindbrain boundary. Asterisk in (D') shows the developing pineal gland. (C'',D'',E',F) Frontal sections of the optic primordia at stages 12 to 21. Lateral is to the left. Dorsal is to the top. Light green arrowheads in (E') and asterisks in (F) show the ciliary marginal zone. mRNA signals are in dark blue. For sections, cell nuclei were stained with nuclear fast red. di, diencephalon; ec, surface ectoderm; le, lens vesicle; nr, neural retina; of, optic fissure; ov, optic vesicle; rpe, developing RPE. Scale bars: 0.5 mm in (A–D'), 100  $\mu\text{m}$  (C'',D'',E',F).

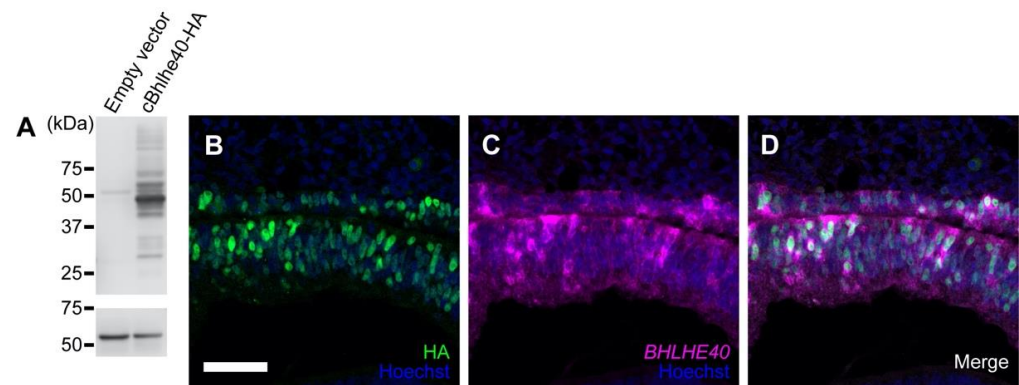


**Figure 2.** Validation of HA-tagged *BHLHE40* expression. (A) Whole cell extracts of HEK293T cells transfected with chicken *BHLHE40-HA*/pCAGGS or empty pCAGGS vector were analyzed by Western blot. HA-tagged proteins were detected by anti-HA antibody. The predicted molecular mass of *BHLHE40* is 44,830 Da. Alpha tubulin from the same samples was detected for loading reference. (B–D) Section of the developing RPE (upper) and NR (lower) layers at 1.5 days post electroporation (*HA*-tagged *BHLHE40* overexpression). (B) Immunofluorescence of *HA*, showing cell nuclei that express *BHLHE40-HA* proteins in both retinal layers. Secondary antibody to anti-*HA* was Alexa Fluor 488-conjugated anti-rat IgG. (C) In situ hybridization of *BHLHE40*, showing cells that express *BHLHE40* mRNA in both retinal layers. Color development was performed with HNPP/FastRed. (D) Merged image of (B) and (C). Cell nuclei were stained with Hoechst 33342. Scale bar: 50  $\mu$ m in (B) for (B–D).

### 2.5. Western Blot Analysis

DNA encoding chicken *BHLHE40* (*cBHLHE40*) tagged with the *HA* epitope (YPYD-VPDYA) at the C-terminus was inserted into the mammalian expression vector pCAGGS. Expression constructs for  $\Delta$ basic *BHLHE40*, and one with acidic extension were similarly tagged with *HA*. The nucleotide sequences were confirmed by Sanger sequencing. The expression of recombinant proteins was assessed by Western blot at least in duplicate as follows. The plasmid DNA was transfected into HEK293T cells (ATCC, Manassas, VA, USA) using polyethyleneimine max (#24765-1; Polysciences, Warrington, PA, USA). An empty pCAGGS vector was also transfected as a negative control. Two days after transfection, the cells were harvested and lysed with RIPA buffer (#08714-04; Nacalai Tesque, Kyoto, Japan) containing 1% SDS. The protein concentration in the lysate was quantified using a Bradford protein assay (5000006JA; Bio-Rad Laboratories, Hercules, CA, USA) after diluting the SDS. The lysate was then mixed with an equal volume of SDS sample buffer (0.1 M Tris-HCl, 2% *w/v* SDS, 20% *w/v* glycerol, 0.02% *w/v* bromophenol blue, 5% *w/v* 2-mercaptoethanol, pH 6.8) and heated at 95  $^{\circ}$ C for 3 min. Ten micrograms of total protein in each sample was separated by SDS-PAGE (12.5% gel) and transferred onto a polyvinylidene difluoride (PVDF) membrane using a wet blotter. Membranes were blocked with Blocking One (#03953-95; Nacalai Tesque, Kyoto, Japan) at RT for 1 h with gentle agitation. The PVDF membrane was then incubated overnight at 4  $^{\circ}$ C with primary antibodies against the *HA* epitope (anti-*HA* High Affinity from rat IgG<sub>1</sub>, 1:2000, #ROAHAHA Roche; Merck, Darmstadt, Germany) or alpha tubulin (alpha Tubulin Monoclonal Antibody DM1A, 1:600, #62204; Thermo Fisher Scientific, Waltham, MA, USA). After washing four times for 10 min with Tris-buffered saline containing 0.1% (*w/v*) Tween 20 (TBST), the membrane was incubated for 90 min at RT with a peroxidase-conjugated anti-rat IgG (1:10,000, #SA00001-15; Proteintech, Rosemont, IL, USA) or anti-mouse IgG (1:5000, #7076; Cell Signaling Technology, Danvers, MA, USA) secondary antibody. Primary and secondary antibodies were diluted in IMMUNO SHOT Reagent 1 and 2 (Cosmo Bio, Tokyo, Japan), respectively. After washing four times for 10 min with TBST, immunoreactive bands were visualized by ImmunoStar LD (FIJIFILM Wako Pure Chemical, Osaka, Japan) for the *HA* epitope or ImmunoStar Zeta (FUJIFILM Wako Pure Chemical, Osaka, Japan) for alpha

tubulin. Images of chemiluminescence were captured with a C-DiGit chemiluminescence Western blot scanner (LI-COR Biosciences, Lincoln, NE, USA).

### 2.6. *In Ovo Electroporation*

*In ovo* electroporation was performed as previously described [21]. Briefly, chicken embryos were incubated for 36–39 h until HH stage 10. Each expression plasmid in the pCAGGS vector [18] (1 µg/µL of *EGFP* and 5 µg/µL of *LHX1* or *BHLHE40*) with Fast Green FCF (0.1%) (FUJIFILM Wako Pure Chemical, Osaka, Japan) was first injected into the right forebrain vesicle using Nanoject II (Drummond Scientific, Broomall, PA, USA) and the injection volume was 64.4 nL for each embryo. Immediately after DNA injection, the embryos were electroporated using a sharpened tungsten needle (CUY614T-200, and CUY615; Nepa Gene, Ichikawa, Japan) as a cathode and a platinum electrode (CUY611P3-1 and CUY580; Nepa Gene, Ichikawa, Japan) as an anode. Twenty-four hours post electroporation, the embryos were observed under a fluorescence dissection microscope (Leica M165 FC; Leica Microsystems, Wetzlar, Germany) to evaluate their embryonic stages, location and extent of ectopic expression by co-electroporated GFP fluorescence, harvested, fixed in 4% PFA/PBS at 4 °C overnight, washed, and stored in 100% ethanol at –20 °C until further analysis.

### 2.7. *Immunofluorescence*

Immunofluorescence (IF) was essentially performed according to Kawaue et al. [19]. Briefly, after blocking with 1% Bovine Serum Albumin in PBS containing 0.1% Triton X-100 and anti-HA (1:200, rat IgG; #ROAHAHA Roche; Merck, Darmstadt, Germany) antibody was applied to the sections and incubated at 4 °C overnight. After washing, the sections were incubated with anti-rat IgG conjugated with Alexa Fluor 488 (1:1000; A-11006; Thermo Fisher Scientific) or Alexa Fluor 568 (1:1000; ab175708; Abcam, Cambridge, UK) and Hoechst 33342 (1 µg/mL) at RT for 60 min. Other antibodies used are listed in Table S2.

### 2.8. *Image Capture and Processing*

The colored embryos after WISH were photographed with a digital camera system (Leica DFC310). Tissue sections were observed with bright-field or differential interference contrast microscopy (Leica DM5000B) and photographed with a CCD camera system (Nikon DS-Fi1; Nikon, Tokyo, Japan). Brightfield images of *in situ* hybridization on tissue sections were also captured with an IDS UI-3290SE-C-HQ camera (Imaging Development Systems, Obersulm, Germany) mounted on a Carl Zeiss Axioplan microscope (Carl Zeiss, Oberkochen, Germany). Fluorescent micrographs (Figure 3K,N; Figure S2K,N) were taken with a Leica upright DM5000B microscope equipped with a Nikon DS-Qi1 CCD camera system. Confocal fluorescence images were collected with a Carl Zeiss LSM 780 laser scanning confocal microscope system with 405, 488, 561 and 633-nm laser lines. Brightness and contrast adjustments were performed for some images, and image manipulation was performed using a ZEN 2012 SP1 black edition. Confocal z-stack images were acquired at 0.606-µm intervals for a total depth of 6.66 µm (Figure 2B–D), at 0.705-µm intervals for a total depth of 9.87 µm (Figure 3A), at 0.705-µm intervals for a total depth of 11.99 µm (Figure 3B–D), at 0.658-µm intervals for a total depth of 12.51 µm (Figure 3E) and at 0.634-µm intervals for a total depth of 12.05 µm (Figure 3F–H). The shown images are maximum intensity projections of these confocal z-series.

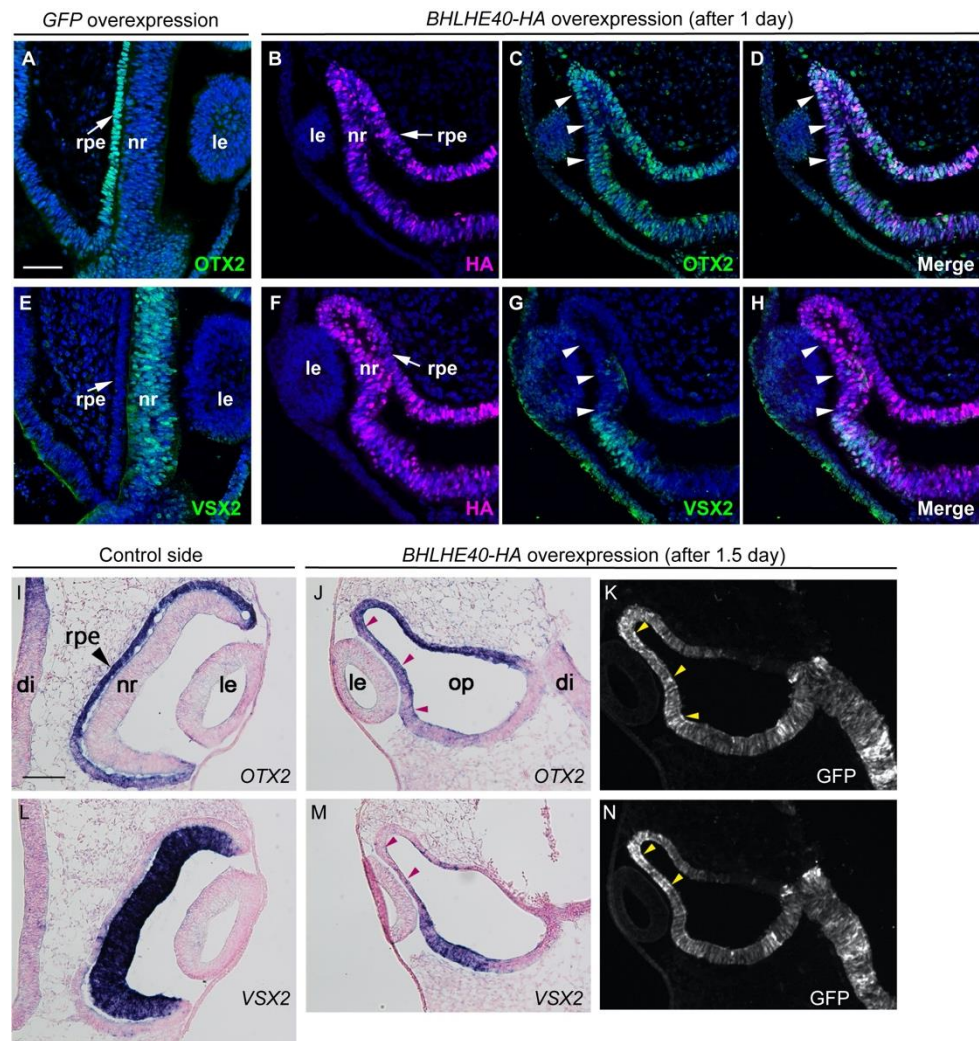


**Figure 3.** Expression pattern of *OTX2* and *VSX2* in the optic cup after *GFP* and *BHLHE40* overexpression. Frontal sections of the optic cup from three embryos (*GFP*#2, *BHLHE40*#14, *BHLHE40*#17) are shown. Dorsal is to the up. (A–H) Optic cups at 1 day post electroporation (for *GFP* alone and HA-tagged *BHLHE40* overexpression). (A,E) Immunofluorescence of *OTX2* (A) and *VSX2* (E) in *GFP* overexpression control (#2). (B–D) Immunofluorescence of HA (B) and *OTX2* (C) in HA-tagged *BHLHE40* overexpression (#14). Secondary antibodies to anti-HA and anti-*OTX2* were Alexa Fluor 568-conjugated anti-rat IgG and Alexa Fluor 647-conjugated anti-rabbit IgG, respectively. (D) Merged image of (B) and (C). (F–H) Immunofluorescence of HA (F) and *VSX2* (G) in HA-tagged *BHLHE40* overexpression. Secondary antibodies to anti-HA and anti-*VSX2* were Alexa Fluor 568-conjugated anti-rat IgG and Alexa Fluor 488-conjugated anti-sheep IgG, respectively. (H) Merged image of (F,G). Cell nuclei were stained with Hoechst 33342 (A–H). Similar data from another embryo (#11) are shown in Supplementary Figure S2A–H. (I–N) Optic cups at 1.5 days post electroporation (HA-tagged *BHLHE40* overexpression, #17). (I,L) Optic cups on the control side are shown. *OTX2* is expressed in the outer layer of the optic cup (I), while *VSX2* is expressed in the inner layer of the optic cup (L). In (K,N), co-electroporated GFP, showing the domain of *BHLHE40* overexpression. Images for GFP were taken before ISH. (J,M) In embryo #17, the inner layer of the optic cup abutting the lens, where *BHLHE40* is ectopically expressed (arrowheads in J), remains thin and expresses *OTX2* (M). In the same domain, *VSX2* expression is downregulated (arrowheads in M). Cell nuclei were stained with nuclear fast red (I–N). di, diencephalon; le, lens vesicle; nr, neural retina; op, optic cup or deformed optic vesicle in (G); rpe, developing RPE. Scale bar: 50  $\mu$ m in (A) for (A–H), 100  $\mu$ m in (I) for (I–N).

### 3. Results

#### 3.1. Expression Patterns of *BHLHE40* in Chickens' Early Eye Development

*Bhlhe40* was reported to be expressed in the developing RPE of mice and zebrafish [8,12], but none of chicken was described. We therefore examined the expression pattern of *BHLHE40* in chicken embryos by in situ hybridization (ISH) (Figure 1). We found that *BHLHE40* mRNA expression emerged in the dorsal portion of the optic vesicle (OV) toward the dorsal diencephalon at stage 12 (Figure 1C',C''). At stage 14, distinct signals of *BHLHE40* were observed in the dorsal region of the OV, the prospective RPE (Figure 1D',D'') [10]. At stage 17, *BHLHE40* was expressed in the outer layer of the optic cup, the nascent RPE and ciliary marginal zone (CMZ) (Figure 1E,E'). At stage 21, *BHLHE40* continued to be expressed in the early-stage RPE and CMZ (Figure 1F). As reported [8], *BHLHE40* was expressed in the midbrain-hindbrain boundary (Figure 1A–D') and developing pineal gland (Figure 1D').

#### 3.2. Overexpression of *BHLHE40* in the OV Drives Early RPE Development

Since *BHLHE40* was expressed in the RPE-lineage of chicken OV, we next examined whether overexpression of *BHLHE40* would drive early RPE development in chicken optic primordia. To discriminate endogenous transcripts for *BHLHE40* from ectopic ones, we constructed an expression plasmid for chicken *BHLHE40* with a human influenza virus hemagglutinin (HA) tag (*cBHLHE40*-HA) at the C-terminus. We confirmed its expression and the protein size as approximately 45 kDa by Western blot analysis using HEK293T cells (Figure 2A), showing the constructed plasmid vector successfully produced full-length *BHLHE40* proteins.

By in ovo electroporation (EP), we overexpressed *cBHLHE40*-HA in the early optic vesicle. At 40 h post EP, the ectopic expression of *BHLHE40*, HA-tagged *BHLHE40* proteins, was verified by immunofluorescence with anti-HA antibody (Figure 2B). Along with a co-electroporated GFP plasmid (Supplementary Figure S1A), cells with ectopic *BHLHE40* proteins were visualized all over the OC (Figure S1B,C). We further verified that *BHLHE40* mRNA was overexpressed in the inner layer of the OC, the prospective NR, after electroporation of the *cBHLHE40*-HA plasmid (Figure 2C,D).

Under these experimental conditions, we examined whether the overexpression of *BHLHE40* could influence the morphology of the optic cup and the expression domains of an RPE specification gene, *OTX2* and an NR specification gene, *VSX2*. After overexpression of GFP alone, *OTX2* proteins were detected in the outer layer of the optic cup, the prospective RPE, while none of *OTX2* was detected in the inner layer, the prospective NR, abutting the lens vesicle (Figure 3A), similar to their normal expression patterns in the optic cup. After *BHLHE40* overexpression, however, *OTX2* was detected in the neuroepithelium abutting the lens vesicle (arrowheads in Figure 3C) and continued to localize to the dorsal and ventral epithelium of the OC. Merged view of HA (Figure 3B) and *OTX2* (Figure 3C) showed (Figure 3D) that *OTX2* protein in the inner layer of the optic cup abutting the lens vesicle was ectopically induced or its early expression in the optic vesicle was maintained under the influence of *BHLHE40* overexpression. Regarding *VSX2*, its expression was downregulated in that portion (arrowheads in Figure 3G,H), while it was observed in the ventral portion of the inner layer of OC (below the arrowheads).

After one and half day post electroporation, as shown by the normal optic cup on the contralateral control side, the outer layer of the OC remains a single layer of *OTX2*-expressing cells (Figure 3I), while the neuroepithelial cells in the inner layer of the OC proliferates to become a thickened NR expressing *VSX2* by this stage (Figure 3L). After *BHLHE40* overexpression, however, the dorsal portion of the neuroepithelium abutting the lens vesicle remained thin (arrowheads in Figure 3J,M), where *BHLHE40* was overexpressed judging from the localization of co-electroporated GFP (Figure 3K,N). At this stage, *OTX2* mRNA was detected in the neuroepithelium abutting the lens vesicle (arrowheads in Figure 3J), while *VSX2* expression was downregulated in that portion (arrowheads in Figure 3M).

In another embryo (#22), the OV development was disrupted and no lens vesicle formation was observed (Figure S2I–N). Although *OTX2* is normally expressed in the dorsal portion of the OV, the prospective RPE, it was expressed in the distal portion of the deformed OV (Figure S2J) where *BHLHE40* was overexpressed, judging from the localization of co-electroporated GFP (Figure S2K). Regarding *VSX2*, its expression was reduced but present partly (Figure S2M). We further examined whether *BHLHE40-HA* overexpression might induce cell death by immunostaining with anti-cleaved caspase 3 antibody. At one day post electroporation, we did not find any positive cells for cleaved caspase 3 in the HA-immunoreactive cells (Figure S3). These data suggest that *BHLHE40* could maintain *OTX2* expression in the optic vesicle, drive early RPE development and repress the developmental program for NR.

### 3.3. Effects of *LHX1* Overexpression on *BHLHE40* Expression

*BHLHE40* lacking a basic region ( $\Delta$ basic *BHLHE40*) is known to act as a dominant negative form of *BHLHE40* [14]. Therefore, we next examined whether overexpression of  $\Delta$ basic *BHLHE40* could alter the morphology of the optic cup, such as lack of RPE development or formation of double NR. We constructed an expression plasmid for  $\Delta$ basic *BHLHE40* with an HA tag, whose calculated molecular mass was 42,877 Da and confirmed its expression by Western blot analysis (Figure S4A). We overexpressed  $\Delta$ basic *BHLHE40* in the early optic vesicle. However, the eye morphology was not altered (Figure S4B and not shown). Additionally, an extension of 12 acidic amino acids in place of the basic region of bHLH transcription factors is known to stabilize heterodimerization between the dominant negative forms and endogenous bHLH proteins [22]. Therefore, we further constructed an acidic extension form of  $\Delta$ basic *BHLHE40* and expressed it in the optic vesicle. However, despite confirmed protein expression for the acidic extension form (39,998 Da with HA) (Figure S4C), overexpression of this construct did not alter the eye morphology, either (Figure S4D and not shown).

We therefore sought to utilize the *LHX1* overexpression. Previously, we found that *LHX1* overexpression in the early chicken OV induced the second NR formation, verified by ectopic expression of NR marker genes, *RX*, *SIX3*, *SOX2*, *SIX6*, and *VSX2*, and called double NR [19]. Recent studies in zebrafish show that the default state of neuroepithelium of the OV is the NR, and expression of RPE specification genes drive the development of RPE and separates the NR and RPE domains [6]. In chicken embryo, however, deducing from overlapping expression domains of the above NR genes and RPE genes, such as *OTX2* and *MITF*, suggests bipotential retinal progenitor cells in the nascent OV. Furthermore, *LHX1* expression in the posterior portion of the chicken OV corresponds to the future central NR domain [23], suggesting its ability to drive NR formation by antagonizing RPE differentiation. Thus, we examined whether *BHLHE40* expression was downregulated in the *LHX1*-overexpressed optic cup. We analyzed it in chicken embryos at 24 h post electroporation of approximately stages 15 to 16, by ISH (Figure 4). After *LHX1* overexpression, protruding regions were observed from the outer layer of the optic cup, where *OTX2* and *MITF*, the RPE genes are repressed [19]. Sectioning of the *LHX1*-overexpressed embryonic heads and ISH on sections revealed that *BHLHE40* expression was downregulated in the portion transforming to NR from the nascent RPE in the outer layer of the OC (arrows in Figure 4C,D and Figure S5C,D,G). Thus, *BHLHE40* expression is negatively regulated by a molecular force of NR formation, *LHX1*.

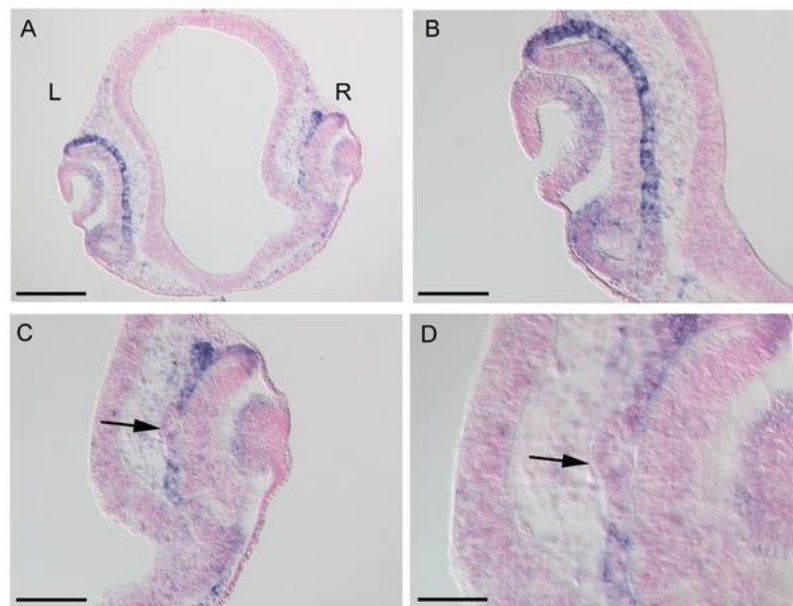


**Figure 4.** *BHLHE40* expression after *LHX1* overexpression. (A) In situ hybridization (ISH) on the frontal section of the chicken embryonic head after 1 day post electroporation (embryo #5). Enlarged view of the left (L) control optic cup (OC) is shown in (B), and that of the right (R) *Lhx1*-overexpressed one is shown in (C,D). *BHLHE40* expression is downregulated in a portion of the outer layer of the OC (arrows in C,D). Cell nuclei were stained with nuclear fast red. Scale bars: 200  $\mu\text{m}$  (A), 100  $\mu\text{m}$  (B,C), 50  $\mu\text{m}$  (D). Similar data from other embryos are shown in Supplementary Figure S5.

#### 4. Discussion

A BHLH transcription factor gene *Bhlhe40* was reported to be expressed in the developing RPE as well as somites and other organ primordia of mice and zebrafish [8,12]. Recently, this gene has been used to visualize the cell behavior during early RPE development [7,9]. Here, we firstly described the early onset of *BHLHE40* expression in the dorsal region of the optic vesicle, the prospective RPE of the chicken [10]. While we focused on the role in RPE development, it has been known that BHLHE40 is involved in circadian rhythm and tumor progression [24]. There is a paralogous gene of *BHLHE40*, *BHLHE41*, which is also expressed in the developing RPE of zebrafish [6], chicken (this study, Figures S6 and S7), and human iPS cell-derived RPE [25]. In human tumor cells, there are functional differences in their roles: BHLHE40 induces apoptosis and epithelial-mesenchymal transition (EMT), whereas BHLHE41 inhibits them [26]. This is considered to be due to their structural differences in which both of BHLHE40/41 have bHLH and Orange domains, but BHLHE41 has an additional alanine/glycine-rich region in the C-terminus [26] (Figure S8). Regarding this, although there are similar upstream regulators for the two paralogs, their downstream effectors and influences are rather opposite. For example, BHLHE40 negatively regulates E-cadherin and Bcl-2, while BHLHE41 negatively regulates Slug (Snail2), Twist1, and caspase-8 [26]. In addition to suppression of these target genes by binding to E-boxes, BHLHE40/41 regulate each other by binding to their E-boxes. Although we have yet to examine the effect of *BHLHE41* overexpression, the involvement of BHLHE41 might be correlated to the result of no phenotypes when dominant negative (DN) forms of *BHLHE40* were overexpressed, as overexpression of the DN forms might induce some compensation by the paralog.

Not a few downstream targets of BHLHE40 have been identified in other contexts [16]. Along with EMT-related genes, BHLHE40 represses Cyclin D1 and STAT1 and upregulates beta-catenin by cooperating with other co-transcription factors. When acting as a repressor, BHLHE40 is known to recruit histone deacetylase, HDAC1. These known target genes represent its multi-functionality and studies on the candidate target genes and transcrip-



tome analysis of *BHLHE40*-overexpressed embryonic eyes will further illuminate detailed molecular aspects of its functions in the chicken eye development.

As we mentioned in the Introduction, *Bhlhe40* was originally isolated as a retinoic acid-inducible gene, *Stra13* [12], and they described that P19 cell clones expressing higher amount of STRA13 died after the passage in culture. In our electroporation method, we did not observe any cell death in *BHLHE40-HA* expressing chicken optic cup cells, as shown in Figure S3. Boudjelal et al. [12] also said that the low expressing cells did not undergo efficient neuronal differentiation, and in this study we could not determine the expression level of *BHLHE40* that robustly altered the morphology and expression of *OTX2* and *VSX2*, which would be our next challenge.

One of the upstream factors of *BHLHE40/41* is hypoxia, which is often molecularly exemplified by HIF1a [26]. RPE cell-specific knockout mice of this pathway genes show that regulation of *Hif1a* in the RPE is required for normal RPE and related ocular development [27]. Therefore, during chicken RPE development, it would be intriguing to know the effect of *HIF1A*-hypoxia pathway genes on the expression *BHLHE40*, which will be researched in the next study. Another important upstream regulator of *BHLHE40/41* in mouse tumor cells is TGF beta [26,27]. It has been reported that TGF beta member activin from the extraocular mesenchyme surrounding the optic primordia patterns the optic vesicle in the chicken [28]. It is therefore conceivable that the expression of *BHLHE40* would be induced by TGF beta family signals from the extraocular mesenchyme at the early phase of optic cup development.

In zebrafish, RPE progenitors expand around the NR in two phases; firstly RPE progenitors are specified with an increase in cell number and then the RPE stretches around the NR with an elongation of RPE progenitor cells [9]. In amniotes (chicken and human), however, in the second phase, the RPE still expands by cell proliferation with a less pronounced cell flatter [7]. Correspondingly, a reported transcriptome analysis has revealed two waves of transcription factor genes regulating the identity of the RPE [6]: Early peaking genes include *tead3b*, *tfap2a*, and *tfap2c*, and representative late peaking genes are *klf5a* and *klf2b* as well as *otx2* and *bhlhe40*. According to this, we cloned the cDNAs and firstly examined the expression patterns of *TEAD3*, *TFAP2A*, *TFAP2C*, *KLF2*, and *KLF5* in chicken embryos, but none of the genes except *TEAD3* were expressed in the developing RPE (Figures S9–S11 and Table S1). Only *TEAD3* was found to be expressed in the developing chicken RPE but its expression domains were not restricted to RPE progenitors as seen for *BHLHE40*. Thus, we suggest that the molecular network regulating RPE specification may not be identical between zebrafish and chicken, except for established RPE genes, such as *OTX2* and *BHLHE40*.

This study showed *BHLHE40* overexpression upregulated *OTX2* expression and down-regulated *VSX2* expression, suggesting *BHLHE40* would drive RPE specification in bipotential retinal progenitor cells of the chicken. Since it was reported that *OTX2* alone could not induce the expression of *MITF*, a melanogenic and differentiation factor for RPE in the chicken embryo [29], *BHLHE40* alone might not proceed with later RPE development in the chicken. In this regard, *MITF* was found to be negatively regulated by *VSX2* in the developing chicken eye [30]. Furthermore, direct repression of *Mitf* by *Vsx2* have been reported in mouse [31]. As *VSX2* was markedly repressed in the optic primordia where *BHLHE40* was ectopically expressed, we think that *BHLHE40* positively regulates *MITF* at least through repression of *VSX2*. Additionally, RNA levels of *Cyclin D1* are significantly decreased in the *Vsx2*-deficient *or<sup>l</sup>* mouse [32]. Since Cyclin D1 is known to promote cell proliferation [33], repression of *Cyclin D1* would have disrupted expansion of the prospective NR layer after *BHLHE40* overexpression and also via downregulation of *VSX2*. In cancer cell lines, *BHLHE40* (*DEC1*) interacts with Cyclin E and stabilizes it, leading to prolonging the S phase and suppressing cell proliferation [34]. Thus, a direct negative effect of *BHLHE40* on the cell cycle of nascent OV cells would be conceivable as well.

We did not succeed in the functional inhibition of *BHLHE40* in the developing chicken eye to see if the presumptive RPE could transdifferentiate into the NR in the stage of

bipotential retinal progenitors. Instead, we utilized *LHX1* overexpression and found that *BHLHE40* is repressed in the transdifferentiating outer layer of the optic cup. Previously, we reported that the second NR formation by *LHX1* overexpression was not mediated by ectopic induction of *FGF8* expression in the early phase [19]. A recent work using fate mapping in chicken embryos has shown that the central NR is defined within the posterior optic vesicle (OV), while the peripheral retina, including future CMZ actually comes from the distal OV [23]. They also showed *LHX1* expression in the posterior portion of the OV corresponds to the future central NR domain. Accordingly, *LHX1* would antagonistically regulate *BHLHE40* in the very early stage of optic vesicle development and determine the central NR domain.

In conclusion, a bHLH gene, *BHLHE40* is expressed in the prospective and definitive RPE cells as well as CMZ of the developing chicken eye. *BHLHE40* can influence the expression of *OTX2* and *VSX2* and its expression can be downregulated by an NR-inducing factor *LHX1*, suggesting its definite role in the NR/RPE developmental programs of the optic vesicle. Conserved expression of *BHLHE40* in the RPE lineage across vertebrates, and its effects on the RPE/NR specification genes verify that this RPE gene belongs to the transcriptional node group among diversified RPE developmental processes.

**Supplementary Materials:** The following supporting information can be downloaded at: <https://www.mdpi.com/article/10.3390/jdb10040045/s1>, Figure S1: data related to Figures 2 and 3; Figure S2: data related to Figure 3; Figure S3: *BHLHE40-HA* expressing cells do not show cell death as revealed by immunofluorescence using anti-cleaved caspase 3; Figure S4: Validation of expression of HA-tagged presumed dominant negative forms of *BHLHE40*; Figure S5: data related to Figure 4; Figure S6: Expression patterns of *BHLHE40* and *BHLHE41* in the developing chicken eye at stage 20; Figure S7: Alignment of coding DNA sequences for chicken *BHLHE40* and *BHLHE41*; Figure S8: Alignment of *BHLHE40* and *BHLHE41* proteins of chicken, human, mouse and zebrafish; Figure S9: Expression patterns of *TEAD3* and *TFAP2A* in the developing chicken eye; Figure S10: Expression patterns of *TFAP2C* and *KLF2* in the developing chicken eye; Figure S11: Expression pattern of *KLF5* in the developing chicken eye; Table S1: PCR primer sequences used in this study; Table S2: Antibodies used in this study.

**Author Contributions:** Conceptualization, T.K., K.S., T.N. and H.O.; methodology, T.K., K.S., T.B., T.M., S.M., T.N. and H.O.; validation, T.K., K.S., T.B., T.N. and H.O.; formal analysis, T.K., K.S., T.B., T.N. and H.O.; investigation, T.K., K.S., T.B. and H.O.; resources, K.S., T.B., T.M. and H.O.; data curation, T.K., K.S. and H.O.; writing—original draft preparation, T.K., K.S. and H.O.; writing—review and editing, T.K., K.S., T.N. and H.O.; visualization, T.K., K.S., T.N. and H.O.; supervision, T.N. and H.O.; project administration, H.O.; funding acquisition, K.S. and H.O. All authors have read and agreed to the published version of the manuscript.

**Funding:** This study was partly supported by academic grants from Pfizer, Astellas, Awa Bank Academic Culture Promotion Foundation (Tokushima, Japan), the Okayama Medical Foundation, a grant from the Takeda Science Foundation, Grants-in-Aid for Scientific Research (20K08885, 20K21655), and a grant from Promotion of Science and Technology in Okayama Prefecture by the Ministry of Education, Culture, Sports, Science and Technology of Japan.

**Institutional Review Board Statement:** All experiments were performed in accordance with the Recombinant DNA Advisory Committee (protocol codes 13044 and 18066 on 24 September 2013 and on 21 June 2018) and the Animal Care and Use Committee, Okayama University, in agreement with relevant guidelines in Japan.

**Informed Consent Statement:** Not applicable.

**Data Availability Statement:** Not applicable.

**Acknowledgments:** We thank Daisuke Daido for initial contribution to this study, Shiori Ikeda for technical assistance and Central Research Laboratory, Okayama University Medical School for confocal laser microscopy.

**Conflicts of Interest:** The authors declare no conflict of interest. The funders had no role in the design of the study; in the collection, analyses, or interpretation of data; in the writing of the manuscript, or in the decision to publish the results.

## References

1. Hyer, J.; Mima, T.; Mikawa, T. FGF1 patterns the optic vesicle by directing the placement of the neural retina domain. *Development* **1998**, *125*, 869–877. [CrossRef] [PubMed]
2. Pandit, T.; Jidigam, V.K.; Patthey, C.; Gunhaga, L. Neural retina identity is specified by lens-derived BMP signals. *Development* **2015**, *142*, 1850–1859. [CrossRef] [PubMed]
3. Steinfeld, J.; Steinfeld, I.; Bausch, A.; Coronato, N.; Hampel, M.-L.; Depner, H.; Layer, P.G.; Vogel-Höpker, A. BMP-induced reprogramming of the retina into RPE requires WNT signalling in the developing chick optic cup. *Biol. Open* **2017**, *6*, 979–992. [CrossRef] [PubMed]
4. Eiraku, M.; Takata, N.; Ishibashi, H.; Kawada, M.; Sakakura, E.; Okuda, S.; Sekiguchi, K.; Adachi, T.; Sasai, Y. Self-organizing optic-cup morphogenesis in three-dimensional culture. *Nature* **2011**, *472*, 51–56. [CrossRef] [PubMed]
5. Nakano, T.; Ando, S.; Takata, N.; Kawada, M.; Muguruma, K.; Sekiguchi, K.; Saito, K.; Yonemura, S.; Eiraku, M.; Sasai, Y. Self-Formation of Optic Cups and Storable Stratified Neural Retina from Human ESCs. *Cell Stem Cell* **2012**, *10*, 771–785. [CrossRef]
6. Buono, L.; Corbacho, J.; Naranjo, S.; Almuedo-Castillo, M.; Moreno-Marmol, T.; de la Cerda, B.; Sanabria-Reinoso, E.; Polvillo, R.; Díaz-Corrales, F.-J.; Bogdanovic, O.; et al. Analysis of gene network bifurcation during optic cup morphogenesis in zebrafish. *Nat. Commun.* **2021**, *12*, 3866. [CrossRef]
7. Moreno-Mármol, T.; Ledesma-Terrón, M.; Tabanera, N.; Martín-Bermejo, M.J.; Cardozo, M.J.; Cavodeassi, F.; Bovolenta, P. Stretching of the retinal pigment epithelium contributes to zebrafish optic cup morphogenesis. *eLife* **2021**, *10*, e63396. [CrossRef]
8. Yao, J.; Wang, L.; Chen, L.; Zhang, S.; Zhao, Q.; Jia, W.; Xue, J. Cloning and developmental expression of the DEC1 ortholog gene in zebrafish. *Gene Expr. Patterns* **2006**, *6*, 919–927. [CrossRef]
9. Cechmanek, P.B.; McFarlane, S. Retinal pigment epithelium expansion around the neural retina occurs in two separate phases with distinct mechanisms. *Dev. Dyn.* **2017**, *246*, 598–609. [CrossRef]
10. Bovolenta, P.; Mallamaci, A.; Briata, P.; Corte, G.; Boncinelli, E. Implication of OTX2 in Pigment Epithelium Determination and Neural Retina Differentiation. *J. Neurosci.* **1997**, *17*, 4243–4252. [CrossRef]
11. Shen, M.; Kawamoto, T.; Yan, W.; Nakamasu, K.; Tamagami, M.; Koyano, Y.; Noshiro, M.; Kato, Y. Molecular Characterization of the Novel Basic Helix–Loop–Helix Protein DEC1 Expressed in Differentiated Human Embryo Chondrocytes. *Biochem. Biophys. Res. Commun.* **1997**, *236*, 294–298. [CrossRef] [PubMed]
12. Boudjelal, M.; Taneja, R.; Matsubara, S.; Bouillet, P.; Dollé, P.; Chambon, P. Overexpression of Stra13, a novel retinoic acid-inducible gene of the basic helix–loop–helix family, inhibits mesodermal and promotes neuronal differentiation of P19 cells. *Genes Dev.* **1997**, *11*, 2052–2065. [CrossRef] [PubMed]
13. Rossner, M.J.; Dörra, J.; Gassb, P.; Schwab, M.H.; Navea, K.A. SHARPs: Mammalian Enhancer-of-Split- and Hairy-Related Proteins Coupled to Neuronal Stimulation. *Mol. Cell. Neurosci.* **1997**, *9*, 460–475. [CrossRef] [PubMed]
14. Sato, F.; Kawamoto, T.; Fujimoto, K.; Noshiro, M.; Honda, K.K.; Honma, S.; Honma, K.-I.; Kato, Y. Functional analysis of the basic helix–loop–helix transcription factor DEC1 in circadian regulation. Interaction with BMAL1. *J. Biol. Inorg. Chem.* **2004**, *271*, 4409–4419. [CrossRef]
15. Cook, M.E.; Jarjour, N.N.; Lin, C.-C.; Edelson, B.T. Transcription Factor Bhlhe40 in Immunity and Autoimmunity. *Trends Immunol.* **2020**, *41*, 1023–1036. [CrossRef]
16. Kiss, Z.; Mudryj, M.; Ghosh, P.M. Non-circadian aspects of BHLHE40 cellular function in cancer. *Genes Cancer* **2020**, *11*, 1–19. [CrossRef]
17. Hamburger, V.; Hamilton, H.L. A series of normal stages in the development of the chick embryo. *J. Morphol.* **1951**, *88*, 49–92. [CrossRef]
18. Niwa, H.; Yamamura, K.-I.; Miyazaki, J.-I. Efficient selection for high-expression transfectants with a novel eukaryotic vector. *Gene* **1991**, *108*, 193–199. [CrossRef]
19. Kawaeue, T.; Okamoto, M.; Matsuyo, A.; Inoue, J.; Ueda, Y.; Tomonari, S.; Noji, S.; Ohuchi, H. Lhx1 in the proximal region of the optic vesicle permits neural retina development in the chicken. *Biol. Open* **2012**, *1*, 1083–1093. [CrossRef]
20. Sato, K.; Nwe, K.N.; Ohuchi, H. The Opsin 3/Teleost multiple tissue opsin system: mRNA localization in the retina and brain of medaka (*Oryzias latipes*). *J. Comp. Neurol.* **2021**, *529*, 2484–2516. [CrossRef]
21. Inoue, J.; Ueda, Y.; Bando, T.; Mito, T.; Noji, S.; Ohuchi, H. The expression of LIM-homeobox genes, *Lhx1* and *Lhx5*, in the forebrain is essential for neural retina differentiation. *Dev. Growth Differ.* **2013**, *55*, 668–675. [CrossRef] [PubMed]
22. Rishi, V.; Vinson, C. Dominant-Negative Mutants of Helix-Loop-Helix Proteins: Transcriptional Inhibition. In *Methods in Enzymology; RNA Polymerases and Associated Factors, Part C*; Academic Press: Cambridge, MA, USA, 2003; Volume 370, pp. 454–466. [CrossRef]
23. Venters, S.J.; Mikawa, T.; Hyer, J. Central and Peripheral Retina Arise through Distinct Developmental Paths. *PLoS ONE* **2013**, *8*, e61422. [CrossRef] [PubMed]

24. Ehata, S.; Hanyu, A.; Hayashi, M.; Aburatani, H.; Kato, Y.; Fujime, M.; Saitoh, M.; Miyazawa, K.; Imamura, T.; Miyazono, K. Transforming growth factor-beta promotes survival of mammary carcinoma cells through induction of antiapoptotic transcription factor DEC1. *Cancer Res.* **2007**, *67*, 9694–9703. [CrossRef] [PubMed]
25. Chuang, J.-H.; Yarmishyn, A.A.; Hwang, D.-K.; Hsu, C.-C.; Wang, M.-L.; Yang, Y.-P.; Chien, K.-H.; Chiou, S.-H.; Peng, C.-H.; Chen, S.-J. Expression profiling of cell-intrinsic regulators in the process of differentiation of human iPSCs into retinal lineages. *Stem Cell Res. Ther.* **2018**, *9*, 140. [CrossRef] [PubMed]
26. Sato, F.; Bhawal, U.K.; Yoshimura, T.; Muragaki, Y. DEC1 and DEC2 Crosstalk between Circadian Rhythm and Tumor Progression. *J. Cancer* **2016**, *7*, 153–159. [CrossRef]
27. Lange, C.A.K.; Luhmann, U.F.O.; Mowat, F.; Georgiadis, A.; West, E.; Abraham, S.; Sayed, H.; Powner, M.B.; Fruttiger, M.; Smith, A.J.; et al. Von Hippel-Lindau protein in the RPE is essential for normal ocular growth and vascular development. *Development* **2012**, *139*, 2340–2350. [CrossRef]
28. Fuhrmann, S.; Levine, E.; Reh, T. Extraocular mesenchyme patterns the optic vesicle during early eye development in the embryonic chick. *Development* **2000**, *127*, 4599–4609. [CrossRef]
29. Westenskow, P.D.; Mckean, J.B.; Kubo, F.; Nakagawa, S.; Fuhrmann, S. Ectopic Mitf in the Embryonic Chick Retina by Co-transfection of  $\beta$ -Catenin and Otx2. *Investig. Ophthalmology Vis. Sci.* **2010**, *51*, 5328–5335. [CrossRef]
30. Rowan, S.; Chen, C.-M.A.; Young, T.L.; Fisher, D.E.; Cepko, C.L. Transdifferentiation of the retina into pigmented cells in ocular retardation mice defines a new function of the homeodomain gene *Chx10*. *Development* **2004**, *131*, 5139–5152. [CrossRef]
31. Zou, C.; Levine, E.M. Vsx2 Controls Eye Organogenesis and Retinal Progenitor Identity via Homeodomain and Non-Homeodomain Residues Required for High Affinity DNA Binding. *PLoS Genet.* **2012**, *8*, e1002924. [CrossRef]
32. Green, E.S.; Stubbs, J.L.; Levine, E. Genetic rescue of cell number in a mouse model of microphthalmia: interactions between *Chx10* and G1-phase cell cycle regulators. *Development* **2003**, *130*, 539–552. [CrossRef] [PubMed]
33. Musgrove, E.A.; Caldon, C.E.; Barraclough, J.; Stone, A.; Sutherland, R.L. Cyclin D as a therapeutic target in cancer. *Nat. Cancer* **2011**, *11*, 558–572. [CrossRef] [PubMed]
34. Bi, H.; Li, S.; Qu, X.; Wang, M.; Bai, X.; Xu, Z.; Ao, X.; Jia, Z.; Jiang, X.; Yang, Y.; et al. DEC1 regulates breast cancer cell proliferation by stabilizing cyclin E protein and delays the progression of cell cycle S phase. *Cell Death Dis.* **2015**, *6*, e1891. [CrossRef] [PubMed]



Communication

# Appropriate Amounts and Activity of the Wilms' Tumor Suppressor Gene, *wt1*, Are Required for Normal Pronephros Development of *Xenopus* Embryos

Taisei Shiraki <sup>1</sup>, Takuma Hayashi <sup>1</sup>, Jotaro Ozue <sup>1</sup> and Minoru Watanabe <sup>1,2,\*</sup>

<sup>1</sup> Graduate School of Sciences and Technology for Innovation, Tokushima University, 1-1 Minamijosanjima-Cho, Tokushima 770-8054, Japan

<sup>2</sup> Institute of Liberal Arts and Sciences, Tokushima University, 1-1 Minamijosanjima-Cho, Tokushima 770-8054, Japan

\* Correspondence: minoru@tokushima-u.ac.jp; Tel.: +81-088-656-7253

**Abstract:** The Wilms' tumor suppressor gene, *wt1*, encodes a zinc finger-containing transcription factor that binds to a GC-rich motif and regulates the transcription of target genes. *wt1* was first identified as a tumor suppressor gene in Wilms' tumor, a pediatric kidney tumor, and has been implicated in normal kidney development. The WT1 protein has transcriptional activation and repression domains and acts as a transcriptional activator or repressor, depending on the target gene and context. In *Xenopus*, an ortholog of *wt1* has been isolated and shown to be expressed in the developing embryonic pronephros. To investigate the role of *wt1* in pronephros development in *Xenopus* embryos, we mutated *wt1* by CRISPR/Cas9 and found that the expression of pronephros marker genes was reduced. In reporter assays in which known WT1 binding sequences were placed upstream of the *luciferase* gene, WT1 activated transcription of the *luciferase* gene. The injection of wild-type or artificially altered transcriptional activity of *wt1* mRNA disrupted the expression of pronephros marker genes in the embryos. These results suggest that the appropriate amounts and activity of WT1 protein are required for normal pronephros development in *Xenopus* embryos.

**Keywords:** CRISPR/Cas9; pronephros; transcription factor; Wilms' tumor; WT1; *Xenopus*

**Citation:** Shiraki, T.; Hayashi, T.; Ozue, J.; Watanabe, M. Appropriate Amounts and Activity of the Wilms' Tumor Suppressor Gene, *wt1*, Are Required for Normal Pronephros Development of *Xenopus* Embryos. *J. Dev. Biol.* **2022**, *10*, 46. <https://doi.org/10.3390/jdb10040046>

Academic Editors: Morris F. Maduro and Simon J. Conway

Received: 17 August 2022

Accepted: 27 October 2022

Published: 29 October 2022

**Publisher's Note:** MDPI stays neutral with regard to jurisdictional claims in published maps and institutional affiliations.



**Copyright:** © 2022 by the authors. Licensee MDPI, Basel, Switzerland. This article is an open access article distributed under the terms and conditions of the Creative Commons Attribution (CC BY) license (<https://creativecommons.org/licenses/by/4.0/>).

## 1. Introduction

*wt1* was identified by positional cloning as a responsible gene for Wilms' tumor, a pediatric kidney tumor that affects 1 in 10,000 children [1–3]. Since deletions or mutations of this gene were found in approximately 15% of Wilms' tumors, this gene has been thought to be a tumor suppressor gene [4]. However, in other Wilms' tumors, *wt1* is expressed at higher levels than normal, suggesting that only a small fraction of Wilms' tumors are caused by loss-of-function of *wt1* [5,6]. Other cancers, such as leukemia and breast cancer, have been shown to overexpress *wt1*, making this gene an oncogene [6,7]. Currently, the functions of *wt1* in cancers are thought to depend on the cell and tissue types. *wt1* is expressed in developing kidneys [8–10], and targeted mutation of *wt1* caused a failure of kidney development in mice embryos [11]. In mouse kidney explant assays, morpholino antisense oligo to *wt1* inhibited kidney development [12]. These results strongly suggest that *wt1* plays an essential role in mammalian kidney development.

*wt1* encodes a protein with four C<sub>2</sub>H<sub>2</sub> zinc finger motifs at its C-terminus, similar to the SP1 family of transcription factors [1–3]. These C<sub>2</sub>H<sub>2</sub> motifs have been shown to bind to the GC-rich motif, suggesting that the WT1 protein acts as a transcription factor [13,14]. Indeed, the transcriptional activity of WT1 has been extensively studied, and the N-terminal region of this protein has been found to contain transcriptional activator and repressor domains that, depending on the target gene and context, act as transcriptional activators in some cases and repressors in others [14,15]. In addition, more than 20 splicing variants exist in

the mammalian *wt1* gene [16]. Among these splicing variants, the insertion of 17 amino acids (17aa) after the activation domain and three amino acids (lysine, threonine, and serine; KTS) between the third and fourth zinc finger domains are conserved in mammals [16]. Interestingly, while KTS insertion has been found in all animals, the 17aa insertion has only been identified in mammals, suggesting an evolutionary significance of the 17aa insertion in mammals [16]. Insertion of the KTS within the zinc finger DNA binding domain results in the reduction of DNA-binding activity, and +KTS variants have been shown to act as RNA-binding factors [17]. This context-dependent transcriptional activity and the many variants with distinct functions make it very difficult to understand the nature of WT1.

The *Xenopus* ortholog of *wt1* has been isolated and shown to be expressed in the developing pronephros, an embryonic kidney of *Xenopus* embryos [18,19]. It has also been found that overexpression of *wt1* in the embryos suppressed pronephros-specific *xlim-1* gene expression, which is essential for normal pronephros development [20,21]. These results indicate that in *Xenopus*, as in mammals, *wt1* plays an essential role in pronephros development. In this research, to investigate the function of *wt1* in pronephros development further, we mutated *wt1* using the CRISPR/Cas9 method. We found that the expression of pronephros marker genes was reduced in these embryos. We also found that in reporter assays in which known WT1 binding sequences were placed upstream of the *luciferase* gene, WT1 activated transcription of the *luciferase* gene. Injection of the *wt1* mRNA of wild-type or artificially altered transcriptional activity disrupted the expression of pronephros marker genes. These results suggest that the appropriate amounts and activity of the WT1 protein are required for normal pronephros development in *Xenopus* embryos.

## 2. Materials and Methods

### 2.1. Embryos and Microinjection

Eggs from female frogs injected with the ovulation-inducing hormone (hCG, human chorionic gonadotropin, 700 units/frog, ASKA Pharmaceutical Co., Ltd. Tokyo, Japan) were artificially fertilized using testis homogenate. They were dejellied with 3% cysteine (pH 7.8) followed by several washes with 0.1 × MMR (1 × MMR: 100 mM NaCl, 2 mM KCl, 2 mM CaCl<sub>2</sub>, 1 mM MgCl<sub>2</sub>, 5 mM HEPES [pH 7.4]), 30 min after fertilization. Embryos were staged, according to Nieuwkoop and Faber [22]. Microinjection was done to both cells anally at the 2-cell stage for *wt1*-sgRNA/Cas9, *tyrosinase*-sgRNA/Cas9 or *luciferase* reporter experiments, with 10 nl volume per injection in 1 × MMR with 3% Ficoll 400. For the *wt1* mRNAs, a single vegetal ventral cell injection on the right side at the 16-cell stage embryos was done to target cells that give rise to pronephros. Microinjection was performed under a microscope with a Mk1 micromanipulator (Singer Instruments, Somerset, UK) and a IM 300 microinjector (Narishige, Tokyo, Japan).

### 2.2. Whole-Mount In Situ Hybridization (WISH)

WISH was performed essentially as described [23], except RNase treatment was omitted, and BM purple (Roche Diagnostics, Tokyo, Japan) was used as a substrate. Antisense *xlim-1* or *pax2* template was linearized with *Xho*I and transcribed with T7 RNA polymerase or *Eco*RI and T3 RNA polymerase, respectively, using digoxigenin-labeled UTP (Roche Diagnostics, Tokyo, Japan).

### 2.3. Beta-Gal Staining

Embryos injected with mRNA encoding nuclear beta-galactosidase (100 pg/embryo) were fixed by MEMFA (0.1 M MOPS (pH 7.4), 2 mM EGTA, 1 mM MgSO<sub>4</sub> and 3.7% formaldehyde) for 15 min, washed by PBS containing 2 mM MgCl<sub>2</sub> and stained in PBS containing 1 mg/mL X-gal, 20 mM K<sub>3</sub>Fe(CN)<sub>6</sub>, 20 mM K<sub>4</sub>Fe(CN)<sub>6</sub>, 2 mM MgCl<sub>2</sub> for 1 h at room temperature.

#### 2.4. CRISPR/Cas9 Knockout of *wt1* and tyrosinase

For the sgRNA target sequence, we selected 20 nucleotides near the N-terminus of the WT1 protein upstream of the PAM sequence (5' NGG 3'), where *wt1.L* and *wt1.S* sequences were identical. The reason for setting the target sequence near the N-terminus of the WT1 protein was the expectation that the frameshift mutation would result in loss of protein function. After selecting target sequences, sgRNA templates were prepared by PCR-based methods. sgRNA plasmid DR274 (Addgene, MA, USA), which was *Dra*I-digested, and 5' TAAT-ACGACTCACTATANNNNNNNNNNNNNNNNNNNNNNNGTTTTAGAGCTAGAAATAGC 3' and 5' AAAAGCACCGACTCGTGCC 3' (T7 promoter sequence in italics, Cas9 protein binding sequence of DR274 in underline, N-stretch is each target sequence) were used to create sgRNA templates by PCR. The resulting PCR products were 117 bp long, including the T7 promoter (17 bp), target sequence (20 bp), and Cas9 protein binding sequence (80 bp), in order from 5' to 3'. These DNAs were subjected to T7 RNA transcriptase reaction to synthesize each sgRNA. The target sequence of the *wt1*-sgRNA was 5' TGGGGGTCTGGGTTCCAGGT 3', which is an antisense strand of *wt1* (Figure 1B). Each embryo was injected with a mixture of 1.3 ng of *wt1*-sgRNA and 6.44 ng of Cas9 protein (EnGen Cas9 NLS, *S. pyogenes*, NEB, MA, USA) to approximately the same molar concentration. The *wt1*-sgRNA/Cas9 was injected in both cells at the 2-cell stage, so half the amount of the sgRNA and Cas9 protein mixture was injected in each cell. Five sgRNA/Cas9 injected embryos (stage 20) were collected in one tube from which DNA was extracted. Therefore, the DNA was a mixture of the five embryos. Genomic DNA containing the target sequence was then PCR amplified by using a pair of primers, 5' TCAGTGGGCTCCAGTC-CTGGACTT 3' and 5' GAACATCCTTGCTTGGCCTGTTGT 3'. Amplified DNAs were subcloned into T-vector (pGEM-T easy, Promega, WI, USA), and nucleotide sequences were determined by Eurofinsgenomics, Inc. (Tokyo, Japan). A total of 22 DNA clones were sequenced, 10 from *wt1.L* and 12 from *wt1.S*. The target sequence of the *tyrosinase*-sgRNA was 5' GGCCCACTGCTCAGAAACCC 3', identical in both *tyrosinase.L* and *S*. Synthesis of *tyrosinase*-sgRNA was essentially identical to that used for *wt1*-sgRNA.

#### 2.5. Plasmid Construction and mRNA Synthesis

*wild-type wt1*: total RNA from a male frog kidney was extracted, and cDNA was synthesized using oligo (dT) primer (Oligo(dT)20 Primer, Toyobo, Osaka, Japan) and reverse transcriptase (PrimeScript Reverse Transcriptase, Takara Bio, Tokyo, Japan). Using this cDNA as a template, WT1.L protein coding sequence was PCR amplified using the following primer sets; 5' GGCTCGAGATGGGATCTGATGTGCGG 3' (the underline represents *Xho*I site for subcloning) and 5' GGGCTAGCCTAAAGGGCCAGATGGAGTT 3' (the underline represents *Nhe*I site for subcloning), and subcloned into the *Xho*I/*Nhe*I digested pCS4-3HA vector. The nucleotide sequence of the resultant plasmid was confirmed by sequencing. This construct was linearized by *Not*I, and mRNA was transcribed by SP6 RNA polymerase (mMESSAGE mMACHINE™ SP6 Transcription Kit, Thermo Fisher Scientific, MA, USA).

*vp16-wt1* and *en-wt1*: the four-zinc finger DNA binding domain sequence from the wild-type *wt1* gene was PCR amplified using the following primer set; 5' GGCTCGAGAGA GGAATTCAAGATGTGAG 3' (the underline represents *Xho*I site for subcloning) and 5' GGGCTAGCCTAAAGGGCCAGCTGGAGAA 3' (the underline represents *Nhe*I site for subcloning). The PCR products were subcloned into *Xho*I/*Nhe*I digested pCS4-HA-VP16 or pCS4-3HA-En vector. Synthesis of mRNA from these constructs was performed in the same manner as described above.



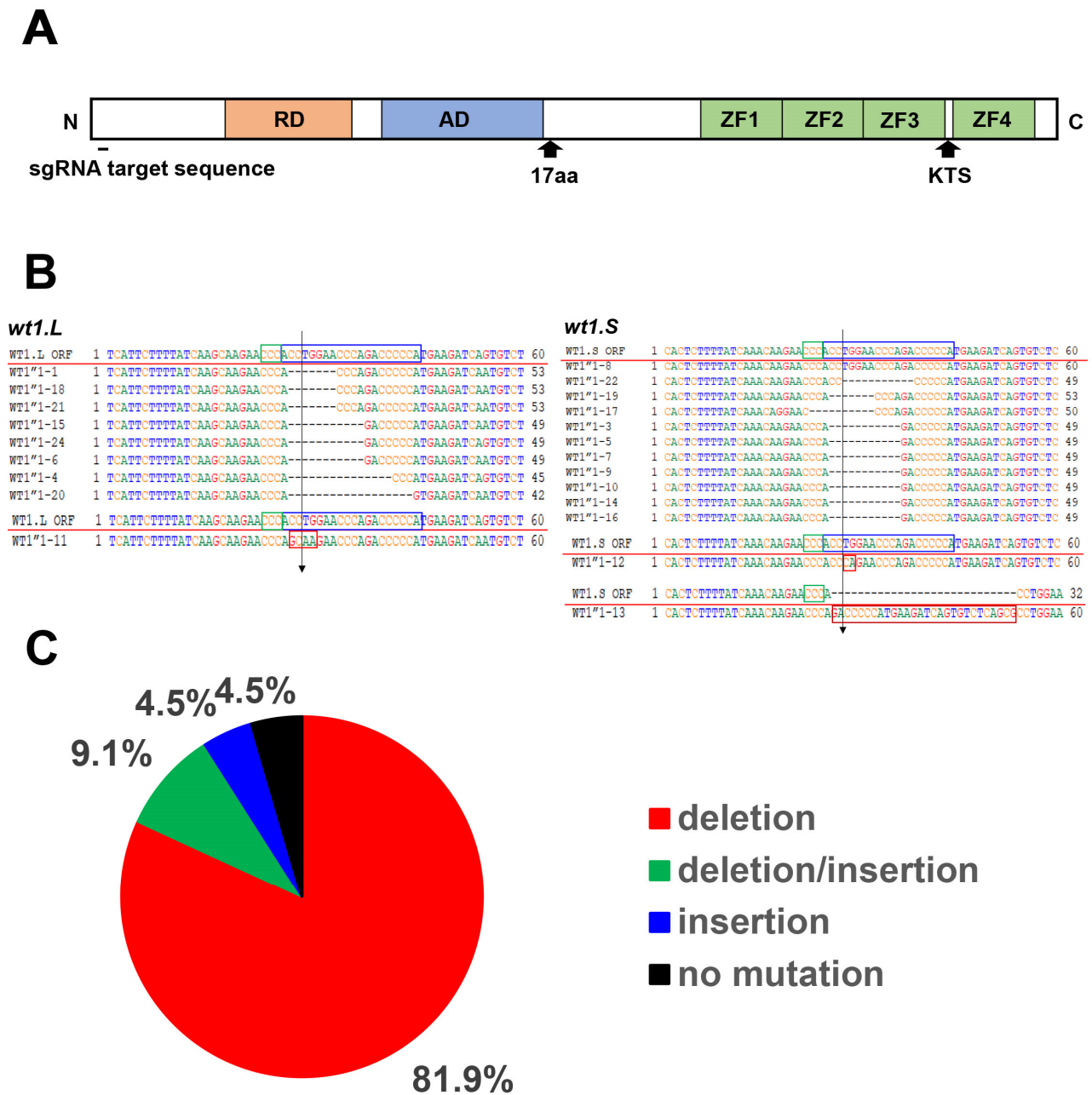


**Figure 1.** Schematic diagram of the WT1 protein and the results of CRISPR/Cas9 knockout of *wt1*. (A) Schematic of the WT1 protein. 17aa and KTS represent splicing variants with or without these insertions (note that 17aa insertion variants are present only in mammals). The target sequence of sgRNA is in the N-terminus. Abbreviations are as follows; RD; transcription repression domain, AD transcription activation domain, ZF; zinc finger DNA binding domain. (B) Details of mutations in *wt1* caused by the injection of *wt1*-sgRNA/Cas9. Mutations in the *wt1.L* gene are shown on the left and in the *wt1.S* gene on the right. The sequence of wild-type *wt1* is shown above the red line. Blue squares indicate sgRNA target sequences, and green squares indicate PAM sequences. Vertical arrows indicate the positions where the Cas9 protein is thought to cleave DNA. Deleted nucleotides are indicated by dots, replaced nucleotides by red squares, and inserted nucleotides by brown square. Each sequence represents an independent DNA clone. (C) Summary of mutations results from CRISPR/Cas9 method. A total of 22 DNA clones were sequenced, 10 from the *wt1.L* gene and 12 from the *wt1.S* gene. The graph summarizes the mutations of both homeologs.

### 2.6. Luciferase Reporter Assay

A canonical WT1 binding sequence and TATA box containing oligonucleotide pair, 5' GATCCGAGTGC~~GGGGG~~CGAGAATTAGGGTATATAATG 3' and 5' AGCTCATTATATAC C~~CTAATTCTCGCCCCCG~~CACTCG 3' (the underlines represent the WT1 binding sequences, and the italics represent TATA box from adenovirus type 5 early region 4 promoter), was annealed and inserted into *Bgl*III/*Hind*III digested *luciferase* vector (pGL3-Basic vector, Promega, WI, USA). The nucleotide sequence of the resultant reporter construct was confirmed by sequencing. Another WT1-binding sequence, 5' GCGTGGGAGT 3', containing *luciferase* reporter was synthesized in the same way. Luciferase reporter (100 pg/embryo) was injected with or without *wt1* mRNA (500 pg/embryo) into 2-cell stage embryos at the animal pole. Four injected embryos were collected in each tube, and 4–5 tubes per injection were prepared. The mean and standard deviation were calculated from the Luciferase activity of these 4–5 tubes. The Luciferase activity was measured using the Luciferase Reporter Assay System (Promega, WI, USA)

## 3. Results

### 3.1. Reduced Expression of the Pronephros Marker Genes in the *wt1* Knockout Embryos by CRISPR/Cas9 Method

To investigate the role of *wt1* in the pronephros development of *Xenopus* embryos, we attempted to knockout *wt1* by the CRISPR/Cas9 method. Because *Xenopus laevis* is an allotetraploid species, most genes have two homeologs, *L* and *S*, and *wt1* had these alleles [24,25]. The sgRNA target sequence of *wt1* which encodes a protein and is identical to the *wt1.L* and *wt1.S* homeologs, was selected, and correspondence sgRNA was synthesized (Figure 1A). The *wt1*-sgRNA was injected into the 2-cell stage embryos together with Cas9 protein, and injected embryos were allowed to develop. When the embryos reached the neurula stage (stage 20), genomic DNAs were extracted, the DNA sequences containing the sgRNA target sequence were amplified by PCR, and the nucleotide sequences were determined after subcloning to a plasmid vector. Mutations were observed in 21 of the 22 clones sequenced (Figure 1B,C). As shown in Figure 1B,C, most of the mutations were deletions (81.1%), while others were insertions (4.5%) or replacements to other sequences (9.1%). Mutations were found in both *wt1.L* ( $n = 10$ ) and *wt1.S* ( $n = 12$ ) genes, suggesting that the identical sgRNA target sequences in both homeologs are efficiently mutated (Figure 1B,C). However, 4 of the 21 mutated sequences were found to be in-frame mutations, which may not affect WT1 protein function (Figure 1B). Nevertheless, these results indicate that the CRISPR/Cas9 method efficiently introduces mutations in *wt1*.

Next, we examined the development of pronephros in *wt1* knockout embryos. To investigate the pronephros development, we examined the expression of the *xlim-1* and *pax2* genes, which are expressed in the developing pronephros and play an essential role in pronephros development [21,26–28]. When *wt1*-sgRNA/Cas9 injected embryos reached stage 34/35, the stage functional pronephros is formed, the expression of the *xlim-1* and *pax2* genes were examined by whole-mount *in situ* hybridization (WISH). As shown in Figure 2A, the *xlim-1* and *pax2* genes were expressed in pronephric tubules (arrows) and ducts (arrowheads) in uninjected embryos. In contrast, expression of *xlim-1* (49%,  $n = 35$ ) or *pax2* (50%,  $n = 36$ ) was reduced in the embryos injected with *wt1*-sgRNA/Cas9 (arrows and arrowheads in Figure 2A). As a control experiment, *tyrosinase*-sgRNA/Cas9 injection was performed. However, no differences in pronephros marker gene expression were observed between control and experimental embryos (Figure 2B). Edema was also observed in some of the injected embryos (Figure 2C). These results suggest that the normal pronephros development in embryos injected with *wt1*-sgRNA/Cas9 was impaired.

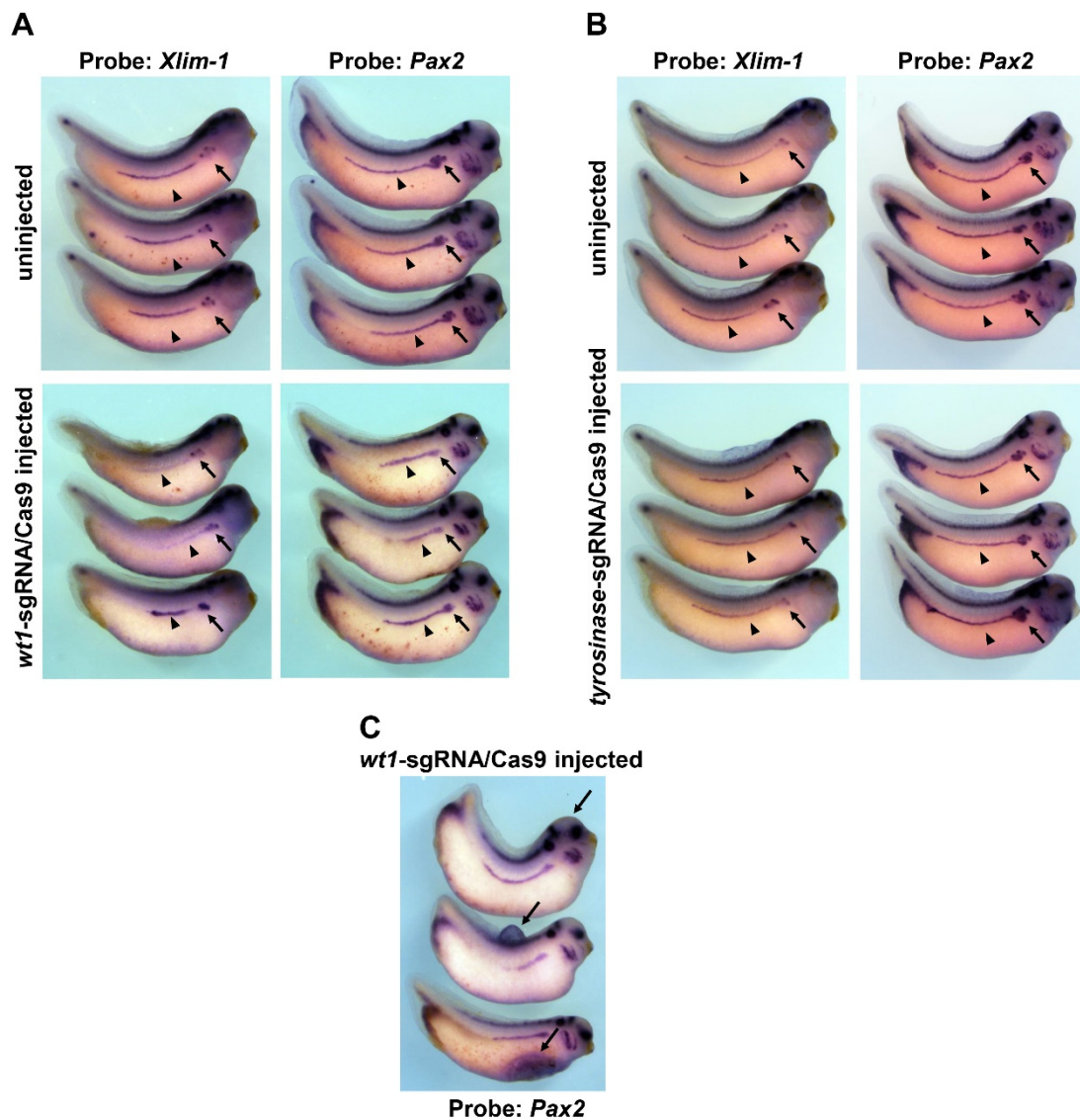


**Figure 2.** Expression of the *xlim-1* and *pax2* genes in embryos injected with *wt1-sgRNA/Cas9*. (A) Expression of the *xlim-1* and *pax2* genes in embryos injected with *wt1-sgRNA/Cas9* are shown with representative embryos and probe combinations of results. Arrows indicate expression in the pronephric tubules, and arrowheads indicate expression in the pronephric ducts. (B) Expression of the *xlim-1* and *pax2* genes in embryos injected with *tyrosinase-sgRNA/Cas9* are shown with representative embryos and probe combinations of results. Arrows and arrowheads indicate the same as in (A). (C) Edema induced in embryos by injection of *wt1-sgRNA/Cas9*. These embryos also show the expression of the *pax2* gene. The top embryo has edema in the head, the middle embryo in the back, and the bottom embryo in the abdomen (the abdominal edema is collapsed). Arrows indicate the regions edema occurred. Note that the morphology of the embryo is altered due to the development of edema.

### 3.2. Transcriptional Activity of the WT1 in *Xenopus* Embryo

Since knockout of *wt1* reduced the expression of pronephros markers, we next wanted to examine the effect of overexpression of this gene in pronephros development. The protein-coding sequence of the *wt1.L* gene was PCR amplified from adult *Xenopus* kidney cDNA, and the nucleotide sequences were determined [24,25]. As previously reported [18,19], two splicing variants were found, one contained the KST sequence between the third and fourth zinc finger DNA binding domains (+KTS), and the other did not (-KTS, See, Figure 1A). A variant with the 17 amino acids (17aa) insertion in N-terminus was not

found in our experiment, as in previous reports [18,19]. This study focused on the -KTS variant since it has higher DNA-binding activity than +KTS [13,17,29]. The WT1 protein has transcriptional activation and repression domains in its N-terminus (see, Figure 1A). It is known that WT1 can activate or repress the expression of target genes. To examine the transcriptional activity in the early *Xenopus* embryos, we made a *luciferase* reporter construct containing canonical WT1-binding sequence, 5' GCGGGGGCG 3' (see, Materials and Method, [13]). This reporter DNA was injected with or without *wt1* mRNA, and Luciferase activity was examined at the gastrula stage (stage 11). As shown in Figure 3A, Luciferase activity was increased when *wt1* mRNA was injected (Figure 3A). We also made another reporter construct containing a WT1-binding sequence, 5' GCGTGGGAGT 3' with a higher binding affinity to the WT1 [29] and examined the transcriptional activity of the WT1. Again, injection of *wt1* mRNA increased Luciferase activity (Figure 3B). These results indicate that, at least in this experimental system, WT1 acts as a transcriptional activator.

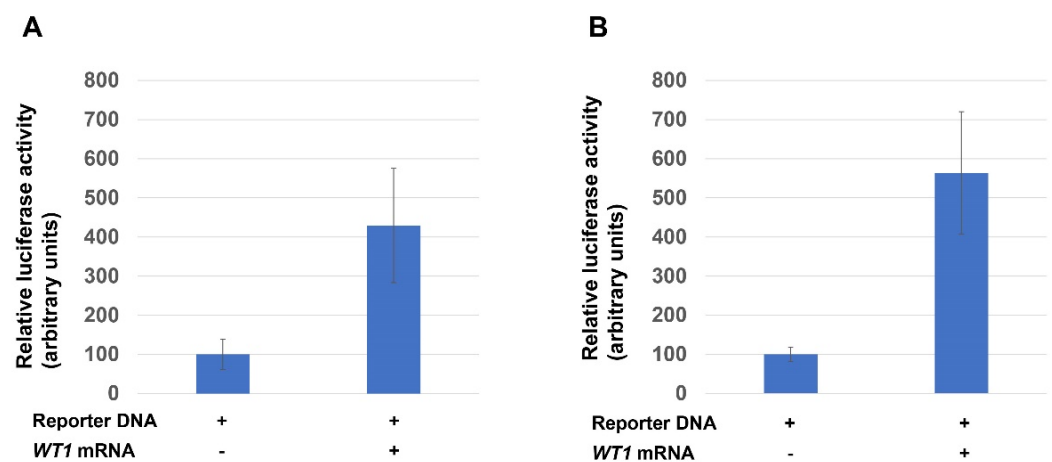


**Figure 3.** Activation of *luciferase* reporter DNA by the WT1. (A) Luciferase activity was examined in embryos by injecting reporter DNA (100 pg/embryos) containing canonical WT1-binding sequence (5' GCGGGGGCG 3') with or without *wt1* mRNA (500 pg/embryos) into the 2-cell stage embryos. The Luciferase activity was examined in the gastrula stage embryos (stage 11). The Luciferase activity of embryos without *wt1* mRNA injection was set at 100, and the Luciferase activity of embryos injected with *wt1* mRNA was expressed as a relative value. Error bars represent the standard deviations. Experiments were repeated at least three times, and the representative result is shown. (B) Another WT1 binding sequence (5' GCGTGGGAGT 3') was injected as in (A), and the representative result is shown.

### 3.3. Pronephric Phenotypes of the *wt1* mRNA Injected Embryos

We next examined the pronephros development of embryos injected with *wt1* mRNA. When wild-type *wt1* mRNA was injected at one cell of the 2-cell stage embryos, injected embryos showed abnormalities such as gastrulation defects and body curvature, which may be non-specific effects due to the overexpression of WT1 (data not shown). To avoid such non-specific effects, the *wt1* mRNA was injected into a single vegetal ventral cell on the right side of the 16-cell stage embryos, which is known to give rise to pronephros at a later stage (Figure 4A, [21,30,31]). To confirm that the injected cell differentiates into pronephros, mRNA encoding nuclear beta-galactosidase (nLacZ) injection was performed as a lineage tracer, and the progenies of the injected cell were visualized at stage 34/35. As shown in Figure 4B, most of the injected embryos (92.5%,  $n = 40$ ) showed nLacZ staining in the region containing pronephros, indicating that the injection was correctly performed (Figure 4B). When such targeted injection of the *wt1* mRNA was performed, non-specific defects were considerably suppressed, although still edema phenotype was observed (data not shown). When injected embryos reached stage 34/35, embryos were harvested, and the expression of the *xlim-1* and *pax2* was studied. As shown in Figure 4C,D, the expression of both markers was reduced on the injected side compared to the uninjected side of the

same embryo (*xlim-1* (52%,  $n = 23$ ) and *pax2* (50%,  $n = 24$ ), red arrows and arrowheads in Figure 4C,D), as previously reported [20]. These results suggest that overexpression of the WT1 inhibits normal pronephros development in the *Xenopus* embryos.

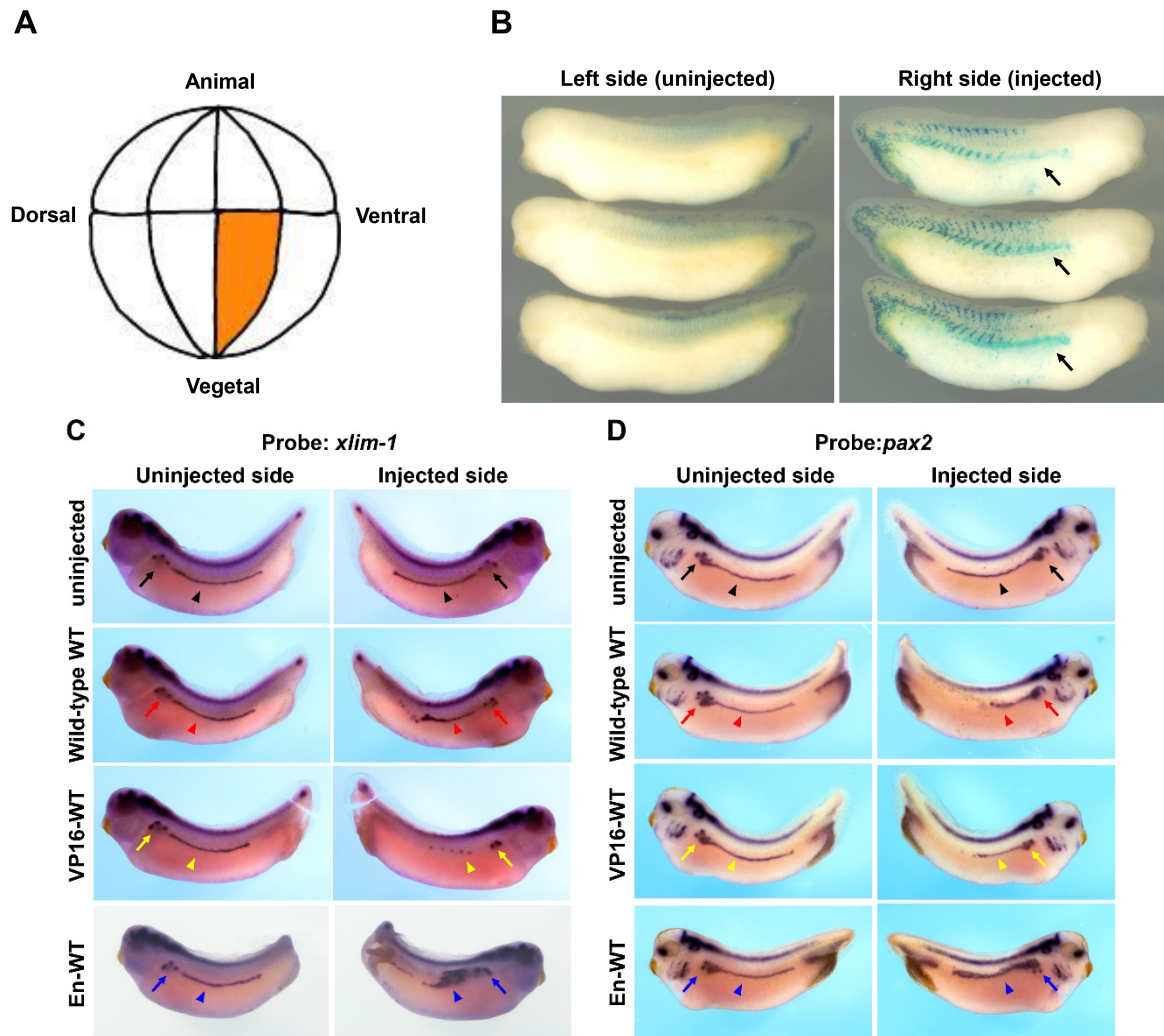


**Figure 4.** The *xlim-1* and *pax2* gene expression in embryos injected with wild-type, activator, or repressor form of *wt1* mRNA. (A) Schematic representation of the right-side view of the 16-cell stage embryo. An injected cell at the vegetal ventral side of the embryo, known to give rise to pronephros at a later stage, was orange-colored. (B) To confirm that the injected cell differentiates into pronephros, mRNA encoding nuclear beta-galactosidase was injected into the cell shown in (A), and the progenies of the injected cell were visualized at stage 34/35. The arrows indicate where the pronephros is formed. (C) Expression of the *xlim-1* gene in *wt1*-mRNA injected embryos. *wt1* mRNA of wild-type (500 pg/embryo), activator (100 pg/embryo), or repressor form (200 pg/embryo) was injected into a single cell at the 16-cell stage embryos as indicated in (A). Arrows indicate expression in the pronephric tubules, and arrowheads indicate expression in the pronephric ducts. (D) Expression of the *pax2* gene was examined as in (C).

Since the WT1 was found to be a transcriptional activator, we attempted to alter the transcriptional activity of the WT1. Therefore, a potent transcriptional activation (VP16) or repression (En) domain was fused to WT1 with endogenous transcription domains removed (see, Figure 1A and Materials and Methods, [32]). These mRNAs were injected into a single vegetal ventral cell at the 16-cell stage embryos as wild-type *wt1* mRNA injection. When injected embryos reached stage34/35, the expression of pronephros marker genes was examined. As shown in Figure 4C,D, *vp16-wt1* mRNA injection reduced the

expression of *xlim-1* (52%,  $n = 25$ ) and *pax2* (50%,  $n = 28$ ), as did wild-type *wt1* mRNA injection (yellow arrows and arrowheads in Figure 4C,D). In some injected embryos, the expression regions were not contiguous but interrupted (data not shown). Injection of the repressor form of WT1, En-WT1, caused disrupted expression of pronephros marker genes. In many cases, the expression of *xlim-1* (72%,  $n = 18$ ) and *pax2* (47%,  $n = 17$ ) were expanded (blue arrows and arrowheads in Figure 4C,D). In some injected embryos, the expression regions were widened, but the length of the regions was shortened (data not shown). These results suggest that altered transcriptional activities of the WT1 inhibit normal pronephros development of *Xenopus* embryos.

#### 4. Discussion

*wt1* was identified as a tumor suppressor gene in Wilms' tumor, and approximately 15% of Wilms' tumors have mutations in *wt1* [1–4]. However, in other Wilms' tumors, *wt1* is expressed normally, sometimes even more [5,6]. In mice, *wt1* is expressed in the developing kidney of the embryos, and targeted knockout of *wt1* resulted in embryonic lethality with failure of kidney development [11]. In addition, morpholino antisense oligo to *wt1* inhibited kidney development in mouse explant assays [12]. These results indicate that *wt1* is required for normal kidney development in mice. Knockout of *Xenopus wt1* with CRISPR/Cas9 also reduced the pronephros marker gene expression (Figure 2A), consistent with the results of mouse experiments. In embryos injected with CRISPR/Cas9, edema was observed (Figure 2C). Since edema is caused by excess fluid retention, pronephros function may be impaired in these embryos [33,34], as evidenced by reduced expression regions of marker genes, although it is caused by reasons other than kidney malfunction. In early *Xenopus* embryos, *wt1* is expressed in the anterior part of the pronephros, glomus anlage, not in tubules or duct anlagen at the tailbud stage [18,28]. CRISPR/Cas9 knockout affected the pronephros marker expression in pronephric tubules and ducts, where *wt1* is not expressed. Since pronephric anlagen are formed from anterior to posterior fashion during embryonic development [20,28,35], *wt1* might be involved in the early pronephros-inducing signaling pathway.

The transcriptional activity of *wt1* has been extensively studied [14–16,36,37]. *wt1* has been shown to repress many target genes, including the *pax2* gene, in mouse kidney development [38]. *wt1* also has been shown to activate the expression of target genes, and both repression and activation domains were mapped in WT1 (see, Figure 1A, [14,15]). Furthermore, chromatin immunoprecipitation (ChIP) analysis using mouse embryonic kidney tissue revealed more than thousands of potential WT1 target genes [12]. We studied the transcriptional activities of the WT1 in early *Xenopus* embryos using a simple *luciferase* reporter system containing WT1-binding sequences; we used two different but related binding sequences [14,29] and found that the WT1 activated the transcription from both sequences (Figure 3A,B). It is important to note that in artificial transcriptional assay systems, including this system, even the choice of expression vectors that drive the transcription of *wt1* may affect the transcriptional activity of the WT1 [39]. Therefore, care should be taken in interpreting the results of the transcriptional activities. However, the expression of pronephros markers in embryos injected with wild-type *wt1* mRNA was similar to those in embryos injected with *vp16-wt1* mRNA, suggesting that the WT1 acted as an activator in *Xenopus* embryos to some extent.

In wild-type *wt1* mRNA-injected embryos, as in our knockout experiments, we observed reduced expression of the *xlim-1* and *pax2* genes (red arrows and arrowheads in Figure 4C,D), as previously reported [20]. Why do overexpression and underexpression of the WT1 result in similar phenotypes? One possibility is that pronephros development in *Xenopus* is sensitive to the amount of WT1 protein and that normal pronephros development requires tight control of the amount of WT1 protein. Therefore, it is thought that changes in the amount of WT1 protein may inhibit normal pronephros development. Consistent with this idea, microinjection of the *strabismus* mRNA, a member of the planar polarity genes, or morpholino antisense oligo into the *Xenopus* embryos resulted in the same trunk

shorting phenotype due to inhibition of planar polarity signaling [40]. In embryos injected with an activator form of WT1 (VP16-WT1), expression of the pronephros marker was reduced (yellow arrows and arrowheads in Figure 4C,D), similar to wild-type *wt1* mRNA injection described above. Conversely, injection of a repressor form (En-WT1) mRNA expanded marker gene expression (blue arrows and arrowheads in Figure 4C,D). These results suggest that some of the WT1 target genes inhibit pronephros development. In other words, VP16-WT1 reduced the pronephros by activating the transcription of genes that inhibit pronephros development, and En-WT1 expanded the pronephros by suppressing the transcription of those genes (Figure 4C,D). In the future, it will be essential to analyze the functions of genes interacting with the WT1 and the WT1 target genes in the embryos to elucidate the molecular mechanism of the WT action in pronephros development.

**Author Contributions:** Conceptualization: M.W.; Methodology: T.S., T.H., J.O. and M.W.; Formal analysis: T.S. and M.W.; Investigation: T.S., T.H., J.O. and M.W.; Supervision: M.W.; Visualization: T.S., T.H. and M.W.; Writing—original draft: M.W. All authors have read and agreed to the published version of the manuscript.

**Funding:** This research received no external funding.

**Acknowledgments:** We thank Chang-Yeol Yeo, and Malcolm Whitman for pCS4-3HA vectors, and Masanori Taira for *xlim-1* and *pax2* cDNAs. Genomic information for *Xenopus laevis* was provided by the Amphibian Research Center at Hiroshima University through the National BioResource Project (NBRP) of the Ministry of Education, Culture, Sports, Science and Technology.

**Conflicts of Interest:** The authors declare no conflict of interest.

## References

1. Bonetta, L.; Kuehn, S.E.; Huang, A.; Law, D.J.; Kalikin, L.M.; Koi, M.; Reeve, A.E.; Brownstein, B.H.; Yeger, H.; Williams, B.R.G.; et al. Wilms Tumor Locus on Lp13 Defined by Multiple CpG Island-Associated Transcripts. *Science* **1990**, *250*, 994–997. [CrossRef] [PubMed]
2. Call, K.M.; Glaser, T.; Ito, C.Y.; Buckler, A.J.; Pelletier, J.; Haber, D.A.; Rose, E.A.; Kral, A.; Yeger, H.; Lewis, W.H.; et al. Isolation and characterization of a zinc finger polypeptide gene at the human chromosome 11 Wilms' tumor locus. *Cell* **1990**, *60*, 509–520. [CrossRef]
3. Gessler, M.; Poustka, A.; Cavenee, W.; Neve, R.L.; Orkin, S.H.; Bruns, G.A. Homozygous deletion in Wilms tumors of a zinc-finger gene identified by chromosome jumping. *Nature* **1990**, *343*, 774–778. [CrossRef] [PubMed]
4. Little, M.; Wells, C. A Clinical Overview of WT1 Gene Mutations. *Hum. Mutat.* **1997**, *9*, 209–225. [CrossRef]
5. Rivera, M.N.; Haber, D.A. Wilms' tumor: Connecting tumorigenesis and organ development in the kidney. *Nat. Rev. Cancer* **2005**, *5*, 699–712. [CrossRef] [PubMed]
6. Yang, L.; Han, Y.; Saiz, F.S.; Minden, M.D. A tumor suppressor and oncogene: The WT1 story. *Leukemia* **2007**, *21*, 868–876. [CrossRef]
7. Huff, V. Wilms' Tumours: About Tumour Suppressor Genes, an Oncogene and a Chameleon Gene. *Nat. Rev. Cancer* **2011**, *11*, 111–121. [CrossRef] [PubMed]
8. Pritchard-Jones, K.; Fleming, S.; Davidson, D.; Bickmore, W.; Porteous, D.; Gosden, C.; Bard, J.; Buckler, A.; Pelletier, J.; Housman, D.; et al. The candidate Wilms' tumor gene is involved in genitourinary development. *Nature* **1990**, *346*, 194–197. [CrossRef]
9. Pelletier, J.; Schalling, M.; Buckler, A.J.; Rogers, A.; Haber, D.A.; Housman, D. Expression of the Wilms' tumor gene WT1 in the murine urogenital system. *Genes Dev.* **1991**, *5*, 1345–1356. [CrossRef] [PubMed]
10. Armstrong, J.F.; Pritchard-Jones, K.; Bickmore, W.A.; Hastie, N.D.; Bard, J.B. The Expression of the Wilms' Tumour Gene, WT1, in the Developing Mammalian Embryo. *Mech. Dev.* **1992**, *40*, 85–97. [CrossRef]
11. Kreidberg, J.A.; Sarioia, H.; Loring, J.M.; Maeda, M.; Pelletier, J.; Housman, D.; Jaenisch, R. WT-1 Is Required for Early Kidney Development. *Cell* **1993**, *74*, 679–691. [CrossRef]
12. Hartwig, S.; Ho, J.; Pandey, P.; Macisaac, K.; Taglienti, M.; Xiang, M.; Alterovitz, G.; Ramoni, M.; Fraenkel, E.; Kreidberg, J.A. Genomic Characterization of Wilms' Tumor Suppressor 1 Targets in Nephron Progenitor Cells during Kidney Development. *Development* **2010**, *137*, 1189–1203. [CrossRef] [PubMed]
13. Rauscher, F.J.; Morris, J.F.; Tournay, O.E.; Cook, D.M.; Curran, T. Binding of the Wilms' tumor locus zinc finger protein to the EGR-1 consensus sequence. *Science* **1990**, *250*, 1259–1262. [CrossRef]
14. Morris, J.F.; Madden, S.L.; Tournay, O.E.; Cook, D.M.; Sukhatme, V.P.; Rauscher, F.J. Characterization of the zinc finger protein encoded by the WT1 Wilms' tumor locus. *Oncogene* **1991**, *6*, 2339–2348. [PubMed]
15. Wangs, Z.Y.; Qius, Q.Q.; Deuel, T.F. Communication the Wilms' Tumor Gene Product WT1 Activates or Suppresses Transcription through Separate Functional Domains. *J. Biol. Chem.* **1993**, *268*, 9172–9175. [CrossRef] [PubMed]

16. Toska, E.; Roberts, S.G.E. Mechanisms of Transcriptional Regulation by WT1 (Wilms' Tumor 1). *Biochem. J.* **2014**, *461*, 15–32. [CrossRef] [PubMed]
17. Hastie, N.D. Life, Sex, and WT1 Isoforms—Three Amino Acids Can Make All the Difference. *Cell* **2001**, *106*, 391–394. [CrossRef]
18. Carroll, T.J.; Vize, P.D. Wilms' Tumor Suppressor Gene Is Involved in the Development of Disparate Kidney Forms: Evidence from Expression in the *Xenopus* Pronephros. *Dev. Dyn.* **1996**, *206*, 131–138. [CrossRef]
19. Semba, K.; Saito-Ueno, R.; Takayama, G.; Kondo, M. cDNA Cloning and Its Pronephros-Specific Expression of the Wilms' Tumor. *Gene* **1996**, *175*, 167–172. [CrossRef]
20. Wallingford, J.B.; Carroll, T.J.; Vize, P.D. Precocious Expression of the Wilms' Tumor Gene XWT1 Inhibits Embryonic Kidney Development in *Xenopus Laevis*. *Dev. Biol.* **1998**, *202*, 103–112. [CrossRef] [PubMed]
21. Delay, B.D.; Corkins, M.E.; Hanania, H.L.; Salanga, M.; Deng, J.M.; Sudou, N.; Taira, M.; Horb, M.E.; Miller, K.M. Tissue-Specific Gene Inactivation in *Xenopus Laevis*: Knockout of Lhx1 in the Kidney with CRISPR/Cas9. *Genetics* **2018**, *208*, 673–686. [CrossRef] [PubMed]
22. Nieuwkoop, P.D.; Faber, J. *Normal Table of Xenopus laevis (Daudin): A systematical and Chronological Survey of the Development from the Fertilized Egg till the End of Metamorphosis*; Garland Publishing, Inc.: New York, NY, USA; London, UK, 1984.
23. Sive, H.L.; Grainger, R.M.; Harland, R.M. *Early Development of Xenopus Laevis: A Laboratory Manual*; Cold Spring Harbor Lab. Press: New York, NY, USA, 2000; pp. 249–274.
24. Session, A.M.; Uno, Y.; Kwon, T.; Chapman, J.A.; Toyoda, A.; Takahashi, S.; Fukui, A.; Hikosaka, A.; Suzuki, A.; Kondo, M.; et al. Genome Evolution in the Allotetraploid Frog *Xenopus Laevis*. *Nature* **2016**, *538*, 336–343. [CrossRef] [PubMed]
25. Fortriede, J.D.; Pells, T.J.; Chu, S.; Chaturvedi, P.; Wang, D.Z.; Fisher, M.E.; James-Zorn, C.; Wang, Y.; Nenni, M.J.; A Burns, K.; et al. Xenbase: Deep integration of GEO & SRA RNA-seq and ChIP-seq data in a model organism database. *Nucleic Acids Res.* **2020**, *48*, D776–D782. [CrossRef] [PubMed]
26. Taira, M.; Otani, H.; Jamrich, M.; Dawid, I.B. Expression of the LIM Class Homeobox Gene Xlim-1 in Pronephros and CNS Cell Lineages of *Xenopus* Embryos Is Affected by Retinoic Acid and Exogastrulation. *Development* **1994**, *120*, 1525–1536. [CrossRef] [PubMed]
27. Heller, N.; Brändli, A.W. *Xenopus* Pax-2 Displays Multiple Splice Forms during Embryogenesis and Pronephric Kidney Development. *Mech. Dev.* **1997**, *69*, 83–104. [CrossRef]
28. Carroll, T.J.; Wallingford, J.B.; Vize, P.D. Dynamic Patterns of Gene Expression in the Developing Pronephros of *Xenopus Laevis*. *Dev. Genet.* **1999**, *207*, 199–207. [CrossRef]
29. Nakagama, H.; Heinrich, G.; Pelletier, J.; Housman, D.E. Sequence and Structural Requirements for High-Affinity DNA Binding by the WT1 Gene Product. *Mol. Cell. Biol.* **1995**, *15*, 1489–1498. [CrossRef]
30. Dale, L.; Slack, J.M.W. Fate Map for the 32-Cell Stage of *Xenopus Laevis*. *Development* **1987**, *551*, 527–551. [CrossRef]
31. Delay, B.D.; Krneta-stankic, V.; Miller, R.K. 2016. Technique to Target Microinjection to the Developing *Xenopus* Kidney. *J. Vis. Exp.* **2016**, *111*, 1–9. [CrossRef]
32. Watanabe, M.; Whitman, M. FAST-1 Is a Key Maternal Effector of Mesoderm Inducers in the Early *Xenopus* Embryo. *Development* **1999**, *126*, 5621–5634. [CrossRef]
33. Li, L.; Wen, L.; Gong, Y.; Mei, G.; Liu, J.; Chen, Y.; Peng, T. *Xenopus* as a Model System for the Study of GOLPH2/GP73 Function: *Xenopus* Golph2 Is Required for Pronephros Development. *PLoS ONE* **2012**, *7*, e38939. [CrossRef] [PubMed]
34. Blackburn, T.M.; Miller, R.K. Modeling Congenital Kidney Diseases in *Xenopus Laevis*. *Dis. Model. Mech.* **2019**, *12*, 038604. [CrossRef] [PubMed]
35. Vize, P.D.; Jones, E.A.; Pfister, R. Development of the *Xenopus* pronephric system. *Dev. Biol.* **1995**, *171*, 531–540. [CrossRef]
36. Madden, S.L.; Cook, D.M.; Morris, J.F.; Gashler, A.; Sukhatme, V.P.; Rauscher, F.J. Transcriptional Repression Mediated by the WT1 Wilms Tumor Gene Product. *Science* **1991**, *253*, 1550–1553. [CrossRef]
37. Roberts, S.G.E. Transcriptional Regulation by WT1 in Development. *Curr. Opin. Genet. Dev.* **2005**, *15*, 542–547. [CrossRef] [PubMed]
38. Ryan, G.; Steele-Perkins, V.; Morris, J.F.; Rauscher, F.J.; Dressler, G.R. Repression of Pax-2 by WT1 during Normal Kidney Development. *Development* **1995**, *875*, 867–875. [CrossRef]
39. Reddy, J.C.; Hosono, S.; Licht, J.D. The Transcriptional Effect of WT1 Is Modulated by Choice of Expression Vector. *J. Biol. Chem.* **1995**, *270*, 29976–29982. [CrossRef] [PubMed]
40. Darken, R.S.; Scola, A.M.; Rakeman, A.S.; Das, G.; Mlodzik, M.; Wilson, P.A. The Planar Polarity Gene Strabismus Regulates Convergent Extension Movements in *Xenopus*. *EMBO J.* **2002**, *21*, 976–985. [CrossRef] [PubMed]





## Article

# Activation of Sonic Hedgehog Signaling Promotes Differentiation of Cortical Layer 4 Neurons via Regulation of Their Cell Positioning

Koji Oishi <sup>1,2,3,\*</sup> , Kazunori Nakajima <sup>3</sup>  and Jun Motoyama <sup>4</sup><sup>1</sup> Graduate School of Pharmaceutical Sciences, The University of Tokyo, Tokyo 113-0033, Japan<sup>2</sup> Organization of Advanced Research and Education, Doshisha University, Kyoto 610-0394, Japan<sup>3</sup> Department of Anatomy, Keio University School of Medicine, Tokyo 160-8582, Japan<sup>4</sup> Laboratory of Developmental Neurobiology, Graduate School of Brain Science, Doshisha University, Kyoto 610-0394, Japan

\* Correspondence: koishi@g.ecc.u-tokyo.ac.jp; Tel.: +81-3-5841-4870

**Abstract:** Neuronal subtypes in the mammalian cerebral cortex are determined by both intrinsic and extrinsic mechanisms during development. However, the extrinsic cues that are involved in this process remain largely unknown. Here, we investigated the role of sonic hedgehog (Shh) in glutamatergic cortical subtype specification. We found that E14.5-born, but not E15.5-born, neurons with elevated Shh expression frequently differentiated into layer 4 subtypes as judged by the cell positioning and molecular identity. We further found that this effect was achieved indirectly through the regulation of cell positioning rather than the direct activation of layer 4 differentiation programs. Together, we provided evidence that Shh, an extrinsic factor, plays an important role in the specification of cortical superficial layer subtypes.

**Keywords:** cerebral cortex; cortical subtype; layer; sonic hedgehog

**Citation:** Oishi, K.; Nakajima, K.; Motoyama, J. Activation of Sonic Hedgehog Signaling Promotes Differentiation of Cortical Layer 4 Neurons via Regulation of Their Cell Positioning. *J. Dev. Biol.* **2022**, *10*, 50. <https://doi.org/10.3390/jdb10040050>

Academic Editors: Hideyo Ohuchi, Tsutomu Nohno and Simon J. Conway

Received: 17 October 2022

Accepted: 23 November 2022

Published: 25 November 2022

**Publisher's Note:** MDPI stays neutral with regard to jurisdictional claims in published maps and institutional affiliations.



**Copyright:** © 2022 by the authors. Licensee MDPI, Basel, Switzerland. This article is an open access article distributed under the terms and conditions of the Creative Commons Attribution (CC BY) license (<https://creativecommons.org/licenses/by/4.0/>).

## 1. Introduction

The mammalian neocortex consists of two major types of neurons according to their usage of neurotransmitters. The majority of them are glutamatergic excitatory neurons derived from the dorsal telencephalon [1,2]. The other population is GABAergic inhibitory interneurons produced by the ventral telencephalon, which consist of 20–30% of all cortical neurons [3,4]. Both excitatory and inhibitory neurons can be further divided into a wider variety of types, which are recognized as neuronal subtypes, according to criteria other than neurotransmitters, such as morphology and gene expression profiles [5,6].

In the dorsal telencephalon, almost all subtypes of glutamatergic neurons are produced by common progenitor cells or neural progenitor/stem cells (NPCs) residing in the dorsal ventricular zone (VZ), which also give rise to glial cells including astrocytes and oligodendrocytes during late embryonic and early postnatal periods [7,8]. In the neurogenic period, NPCs sequentially generate different subtypes of neurons, which ultimately align in the cortical plate from the bottom to top parallelly to the pial surface and form cortical layers comprising anatomically distinguishable 6 layers [9]. Recent studies using unbiased approaches suggested that there are dozens of recognizable subtypes of cortical glutamatergic neurons in the motor area [10].

A plethora of efforts in recent years has provided evidence that determination of cortical subtypes is intrinsically regulated by specific transcription factors, such as *Fezf2* [11–13], *Bcl11b* (aka *Ctip2*) [14], *Rorb* [15,16], *Tbr1* [17], *Brn1/2* [16], and *Satb2* [18,19]. As subtype-specific features are established under the control of these factors, these factors are often called master regulators or subtype determinants. Given that NPCs sequentially generate different subtypes, temporal changes of NPC potentials, such as expression changes of

subtype determinants, which actually occur in *Drosophila* NPCs [20], have been postulated [21]. However, many subtype determinants start to be expressed in postmitotic neurons, although some are also expressed in NPCs [12,22,23], leaving the question of what mechanism regulates the sequential generation of different subtypes from NPCs.

Not only intrinsic factors but also extrinsic factors, such as extracellular environments, play important roles in determining cortical neuronal subtypes. We and others have provided evidence that the specification of L4 neurons is controlled by extracellular environments [24–27]. Moreover, fate regulation by extracellular environments could occur more generally than previously thought [25,28]. However, given that these results were obtained mostly from transplantation experiments, molecular mechanisms that underpin this notion remain to be determined.

As such environmental cues, sonic hedgehog (Shh) is a strong candidate. On top of its role in the patterning formation and resulting specification of ventral structures in the CNS, Shh signaling regulates a wide variety of biological processes [29], such as the proliferation of intermediate progenitor cells [30], induction and expansion of outer radial glial cells that compose the outer SVZ, a progenitor pool commonly observed in the gyrencephalic neocortex [31], and gliogenesis [32–34]. However, the role of Shh signaling in the specification of cortical subtypes has remained unknown; cortical subtype phenotypes observed in Shh signaling mutants are mostly attributable to alteration in dorsoventral patterning and progenitor proliferation [35]. Given that specification of cortical subtypes, especially the L4 subtype, utilizes environmental cues [24–27], we investigated the role of Shh signaling in L4 subtype generation.

## 2. Materials and Methods

### 2.1. Mice

Pregnant ICR mice were purchased from Japan SLC (Shimizu laboratory supplies, Kyoto, Japan). The morning of vaginal plug detection was designated as E0.5. Mice were maintained on a 12 h light/dark cycle with free access to food and water. All experiments were approved by the Doshisha University Animal Experiment Committee and conducted in accordance with guidelines established by the Doshisha University Ethics Review Committee.

### 2.2. In Utero Electroporation

Pregnant mice were deeply anaesthetized, and in utero electroporation was carried out as described previously [36]. In brief, an empty or Shh-encoding plasmid vector together with the pCAGGS vector carrying the enhanced GFP cDNA (1 mg/mL) was injected into the lateral ventricle of the intrauterine embryos, and electronic pulses (33 V, 50 ms, 4 times) were applied using an electroporator (CUY21 EDIT II, BEX, Tokyo, Japan) with a forceps-type electrode (CUY650P5, Nepagene, Chiba, Japan).

For expression of Shh, the gene-encoding, full-length mouse Shh obtained from mouse cDNA was cloned into the plasmid vector pCAGGS or pEF.

### 2.3. Immunohistochemistry

Brains removed from embryos and pups were fixed for 1 h in phosphate-buffered saline (PBS) containing 4% PFA (*w/v*), incubated overnight at 4 °C with 20% sucrose in PBS (*w/v*), embedded in OCT compound (Sakura Finetek, Torrance, CA, USA), and sectioned with a cryostat to obtain 14 µm-thick coronal sections.

For primary antibodies, we used chick antibody to EGFP (Abcam, Cambridge, UK, ab13970), mouse antibody to Rorb (Perseus Proteomics, Tokyo, Japan, N7927), goat antibody to Lhx2 (Santa Cruz, sc-19344), mouse antibody to Brn2 (Santa Cruz, Dallas, TX, USA, sc-393324), and rabbit antibody to Shh (Santa Cruz, c-9024). For some cases, antigen retrieval was performed by incubating the sections for 20 min at 80 °C in 0.01 M sodium citrate buffer (pH 6.0). Because EGFP fluorescence disappeared by the antigen retrieval treatment, EGFP was immunostained with chick antibody against EGFP for revisualization. Immune

complexes were detected with Alexa Flour-conjugated secondary antibodies (Invitrogen, Waltham, MA, USA). For nuclear staining, 1  $\mu\text{g}/\text{mL}$  Hoechst 33,342 (Invitrogen) was used. Images were acquired using a confocal microscope (SP8, Leica, Wetzlar, Germany).

#### 2.4. Quantitative Analysis of the Cell Positioning

To quantify the pattern of migration, the position of each GFP-positive cell relative to the total distance from the bottom of L4 or the subplate to the outer edge of the cortical plate (pial surface) was measured using the Image J software (National Institutes of Health shareware program), followed by sorting into 5 or 10 bins.

#### 2.5. Statistical Analysis

Unless indicated otherwise, data are represented as means  $\pm$  SEM of values from at least three embryos. For quantification of in vivo cell counting, all EGFP-positive cells were counted in the regions where rostrocaudal and mediolateral levels were carefully matched between animals. A representative section per electroporated embryo was quantified. The number of embryos analyzed was indicated in the figure legends. For two-group comparisons with equal variance as determined by the *F*-test, an unpaired Student's *t*-test was used. Welch's correction was used for unpaired *t*-tests of normally distributed data with unequal variance. Differences between groups were considered to be significant at  $p < 0.05$ . Each *p*-value was stated in figures or figure legends.

### 3. Results

According to the previous implication that the specification of L4 neurons may require environmental cues [24–27], we first investigated the role of Shh signaling in L4 subtype generation in mice. We chose to manipulate Shh signaling by introducing a Shh expression vector in NPCs at embryonic day (E) 14.5 by in utero electroporation (IUE) [36] because NPCs at this stage give rise to both L4 and L2/3 neurons. In fact, 55.6% of the EGFP-labeled cells at E14.5 were located in the upper part of L4 at postnatal day (P) P7, while 44.4% of them were located in the lower part of L2/3 in the controls, where only an EGFP vector was introduced (Figure 1A,E). On the other hand, when an Shh expression vector together with an EGFP expression vector was introduced, the electroporated cells were located more in L4 (79.3% in the upper part of L4 and 20.7% in the lower part of L2/3, Figure 1B,E). The expression of ectopic Shh was detected around the EGFP-positive cells, suggesting autocrine action (or short distance effect) of ectopic Shh (Figure 1F,G). Accordingly, we did not observe obvious differences in the overall thickness of L2/3 and L4 (Figures 1 and 2) although we cannot rule out the possibility of a non-cell-autonomous effect.

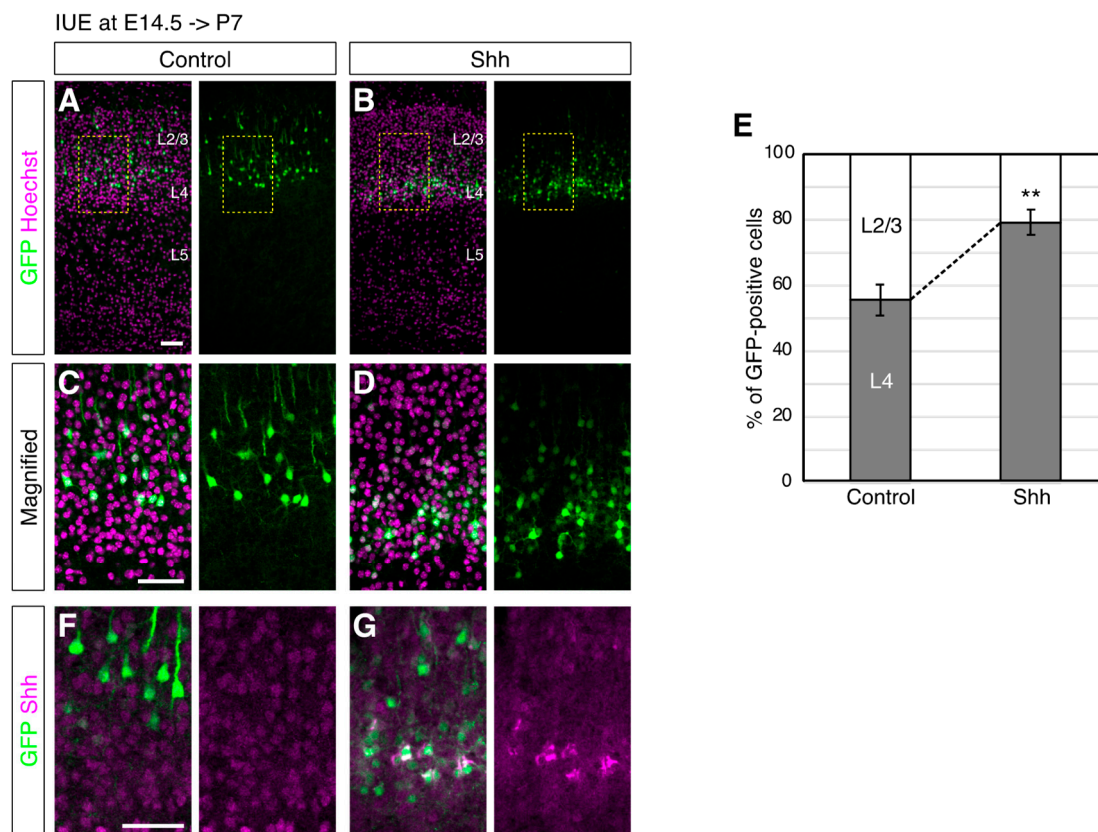


**Figure 1.** Shh overexpression at E14.5 increases the percentage of neurons in L4 at P7. (A,B). Empty (Control, (A)) or Shh expression vector (Shh, (B)) together with a GFP vector was electroporated into E14.5 brains, and then P7 brains were analyzed. The sections were counterstained with Hoechst (magenta). The boxed regions are shown at higher magnification in (C,D). (E). The percentages of the cells in L2/3 and L4 were determined in each condition. Quantitative data are presented ( $n = 3$  for each group).  $** p < 0.01$ . Note that the GFP-positive cells with Shh expression vector are located more in L4 than the control cells. (F,G). Expression of Shh was shown in the neurons treated as in (A,B). (Scale bars: 200  $\mu\text{m}$  in (A,C,F)).

The observed phenotype could be attributable not only to migration or positioning failure but also to cell identity alteration. To distinguish these possibilities, we investigated the neuronal morphology, which often represents subtype-specific features [1,37], upon ectopic Shh expression. Magnified images showed that Shh overexpression decreased the neurons with a pyramidal shape that harbors an apical dendrite, a feature of L2/3 neurons, compared to those with a nonpyramidal shape, a feature of L4 neurons (Figure 1C,D) [15,16], suggesting that elevated Shh signaling modulates not only the positioning of superficial layer neurons but also their fate. These results suggest that elevated Shh signals enhance the generation of L4 neurons.

To further investigate the identity of the neurons with elevated Shh expression, we analyzed the expression of molecular markers that distinguish L4 and L2/3 neurons. An immunohistochemical analysis for *Rorb*, an L4 subtype marker [38,39], revealed that 28.6% of the control cells electroporated at E14.5 differentiated into *Rorb*-positive neurons at P7 (Figure 2A,C). In contrast, 72.3% of the Shh-overexpressing cells became *Rorb*-positive (Figure 2B,C). Moreover, the percentage of neurons that expressed L2/3 markers, such as *Lhx2* [40] and *Brn2* [23,41,42], was decreased by ectopic Shh expression (*Lhx2*, 80.2% in control, 32.7% in Shh overexpressed (Figure 2E,F); *Brn2*, 72.3% in control, 50.2% in Shh overexpressed (Figure 2G–I)). These results suggest that elevated Shh signaling promotes L4 generation, at the expense of L2/3 neurons, at molecular levels. This observation implied a rather surprising scenario, in which high levels of Shh signaling reversed the sequence of

subtype specification of cortical neurons (L6- > L5- > L4- > L2/3) [8,9]; elevated Shh can change the ultimate identity of neurons that are destined to become L2/3 neurons into an L4 fate, an earlier-born subtype than L2/3 subtypes.

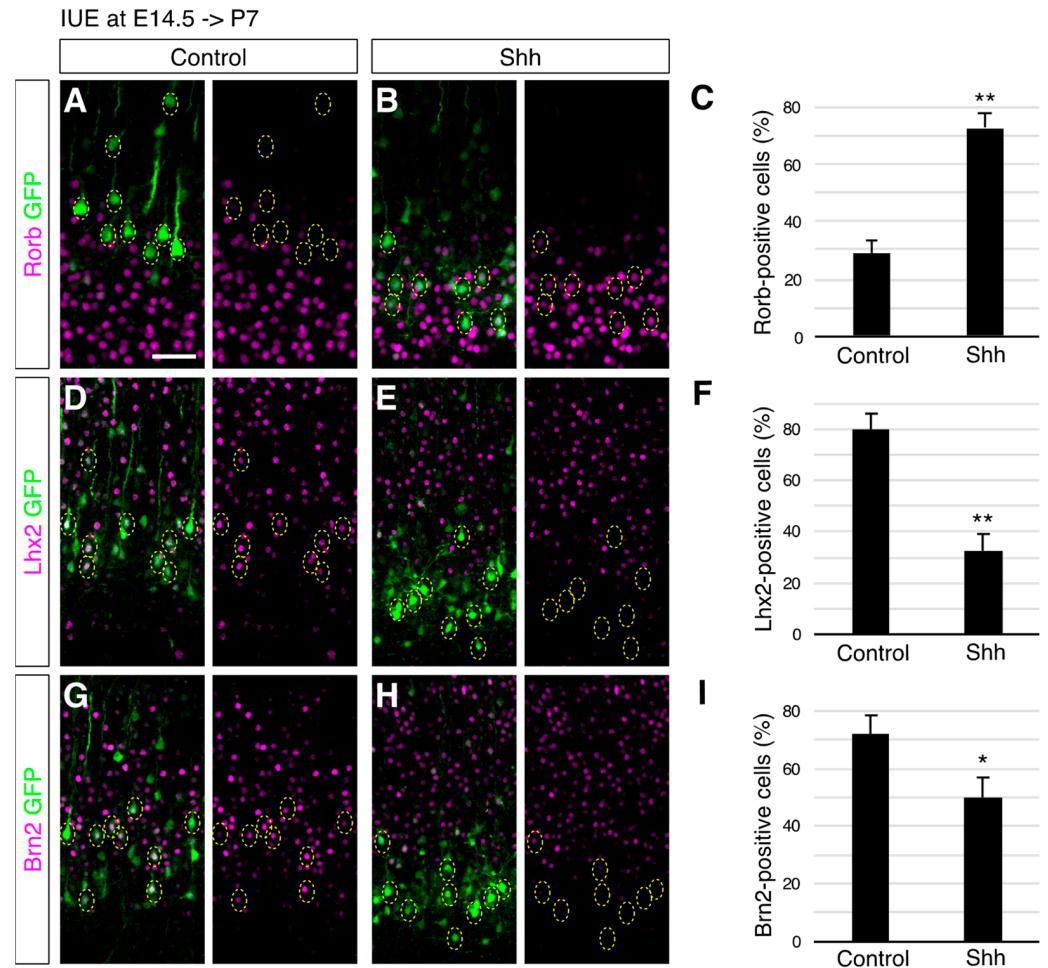


**Figure 2.** Shh-overexpressing cells at E14.5 acquire L4 characteristics. Empty (Control) or Shh expression vector (Shh) together with a GFP vector was electroporated into E14.5 brains, and then P7 brains were analyzed. The sections were immunostained for Rorb (A,B), Lhx2 (D,E), and Brn2 (G,H). The results of quantitative analysis for Rorb (C), Lhx2 (F), and Brn2 (I) are presented ( $n = 3$  for each group). \*\*  $p < 0.01$ , \*  $p < 0.05$ . Note that Shh-overexpressing cells acquired expression of Rorb, but lost expression of Lhx2 and Brn2. (Scale bar: 200  $\mu\text{m}$  in (A)).

To test the possibility of juvenilization of NPCs by high levels of Shh signaling, we overexpressed Shh in later NPCs (IUE at E15.5), which produced predominantly L2/3 neurons and analyzed if they produced earlier-born neurons, such as L4 neurons. Cell positioning analysis showed that Shh overexpression at E15.5 did not change the ultimate positioning of the electroporated cells (Figure 3A–C). In addition, an immunohistochemical analysis for Rorb revealed that only a small fraction of E15.5-electroporated neurons expressed Rorb with or without the ectopic expression of Shh (Figure 3D–F). These results indicate essentially no generation of L4 neurons from E15.5-electroporated cells even in high levels of Shh signaling, suggesting that Shh does not generally regulate the temporal production of different cortical subtypes. In contrast, Shh would play a role in the demarcation of L2/3 and L4 neurons in a rather specific temporal manner.

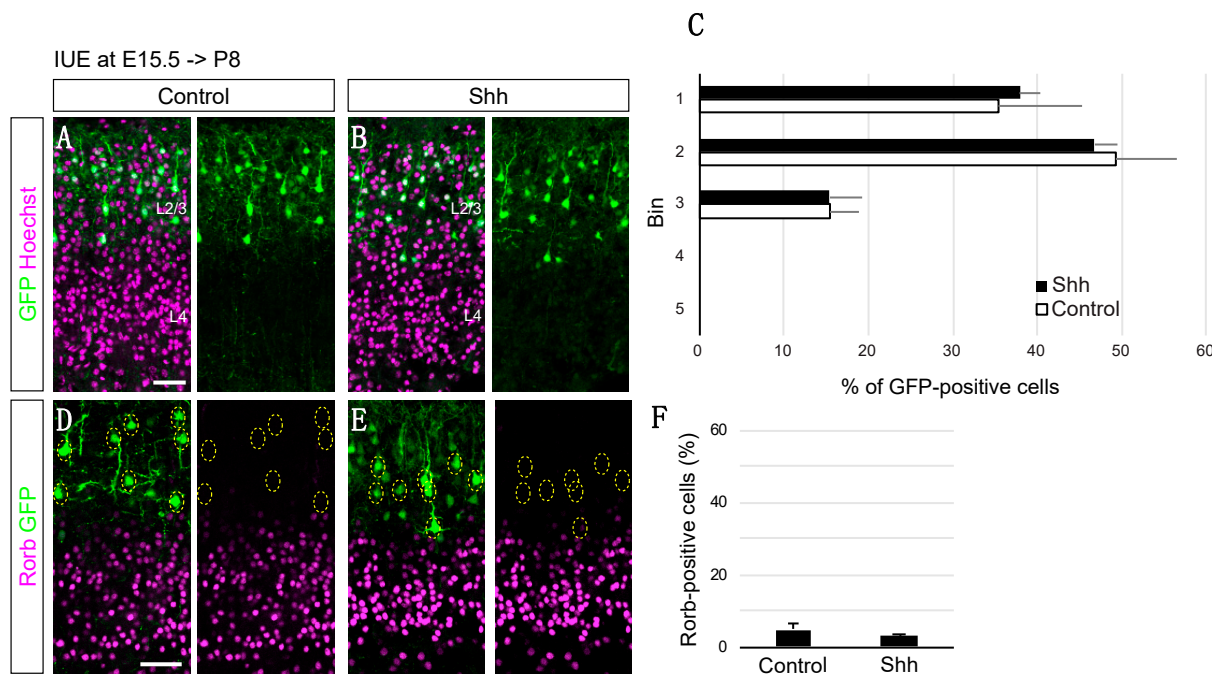


**Figure 3.** Shh overexpression at E15.5 does not alter cell positioning and Rorb expression. Empty (Control) or Shh expression vector (Shh) together with a GFP vector was electroporated into E15.5 brains, and then P8 brains were analyzed. The sections were counterstained with Hoechst (A,B) or immunostained for Rorb (D,E). (C). Quantitative data of cell positioning are presented. The position of each GFP-positive cell relative to the total distance from the bottom of L4 to the outer edge of the cortical plate was measured, followed by sorting into 5 bins (Control,  $n = 3$ ; Shh,  $n = 4$ ). (F). The result of quantitative analysis for Rorb is presented (Control,  $n = 3$ ; Shh,  $n = 4$ ). (Scale bars: 200  $\mu\text{m}$  in (A,D)).

As one of the mechanisms that determines L2/3 and L4 identity, we previously reported a cell position-dependent model, where L2/3 and L4 differentiation occurs along the ultimate positioning of the neurons in the superficial layer despite their birthdates [24]. Therefore, we hypothesized that Shh controls the cell positioning of E14.5-generated neurons. In this scenario, neurons that receive high Shh signals position the lower part of the superficial layer, where further differentiation processes occur.

We then asked if Shh regulates the positioning of neurons before affecting the cell differentiation status. We examined the brains at E18.5, when most of the E14.5-electroporated cells had reached the pial side of the cortical plate and started maturing. We found that Shh-overexpressing cells were located in deeper regions than the control cells at this early time point (Figure 4A–C). Since normal ‘future’ L4 neurons (that are destined to become L4 neurons) reach the pia surface earlier than future L2/3 neurons and later align deeper regions, this observation suggested that cell positioning/migration was already affected at this stage. On the other hand, the expression of Rorb was not detected in the electroporated neurons even with or without the ectopic expression of Shh (Figure 4D,E). These results suggest that upregulated Shh signaling can control the positioning of neurons before affecting their subtype identity.

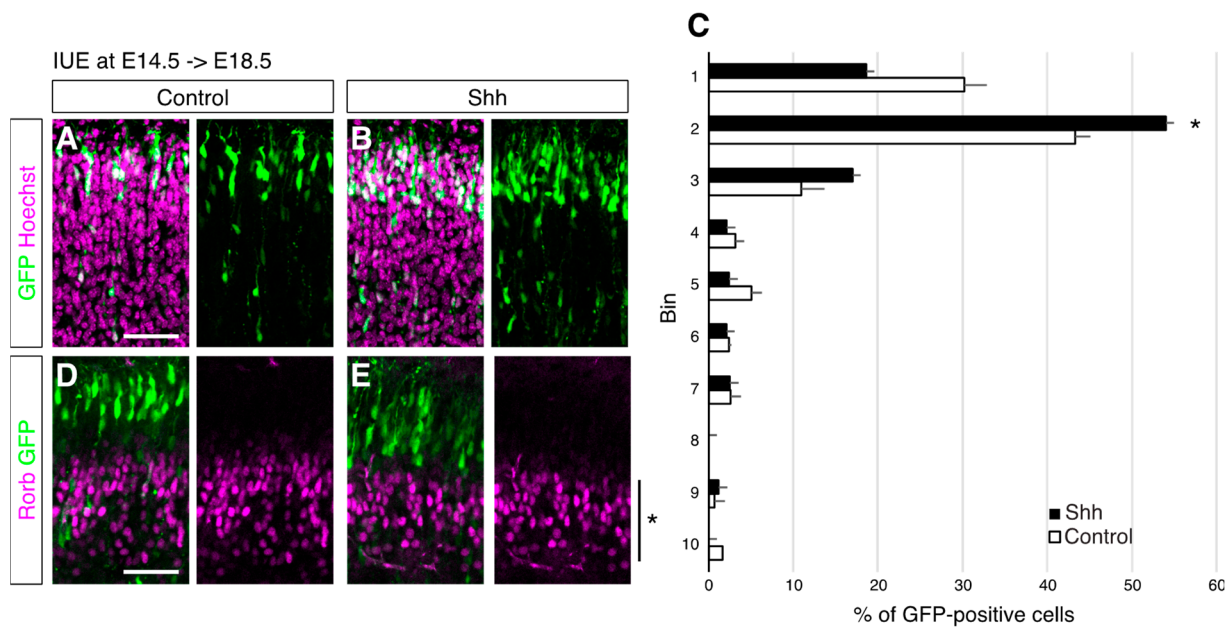


**Figure 4.** Upregulated Shh signaling regulates cell positioning without affecting an L4 marker expression. Empty (Control) or Shh expression vector (Shh) together with a GFP vector was electroporated into E14.5 brains, and then E18.5 brains were analyzed. The sections were counterstained with Hoechst (A,B) or immunostained for Rorb (D,E). The asterisk shows expression of Rorb in developing L5 neurons [16]. (C). Quantitative data of cell positioning are presented. The position of each GFP-positive cell relative to the total distance from the bottom of the subplate to the outer edge of the cortical plate was measured, followed by sorting into 10 bins ( $n = 4$  for each group). \*  $p < 0.05$ . (Scale bars: 200  $\mu\text{m}$  in (A,D)).

The proposed mechanism, in which Shh promotes L4 subtype generation via neuronal positioning, predicts that the neurons that fail to position the lower part of the superficial layer do not differentiate L4 neurons even if they receive high Shh signaling. To directly test this possibility, we tried to reposition the Shh-overexpressing cells back to the upper part of the superficial layer by the knockdown of Pcdh20, which changed the positioning of future L4 neurons into more upper regions without affecting neuronal migration and early subtype specification [24]. We found that Pcdh20 knockdown was able to reposition Shh-overexpressing neurons back to more superficial regions (Figure 5A–C). We then investigated the expression of Rorb in these cells. Rorb staining revealed that 74.6% of Shh-overexpressing neurons were positive for Rorb, but this percentage was reduced to 18.9% by simultaneous Pcdh20 knockdown (Figure 5D–F). These results strongly support the notion that high levels of Shh signaling promote the specification of an L4 subtype via cell positioning.



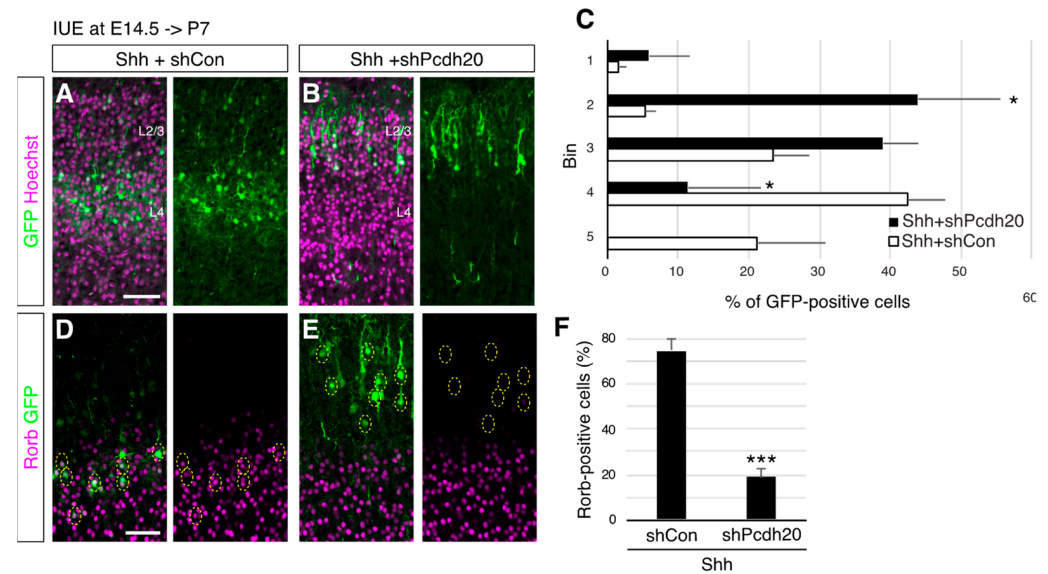


**Figure 5.** Shh overexpression promotes L4 fate acquisition in a cell positioning-dependent manner. Shh expression vector together with a control shRNA (Shh+shCon) or Pcdh20 shRNA vector (Shh+shPcdh20) was electroporated into E14.5 brains, and then P7 brains were analyzed. The sections were counterstained with Hoechst (A,B) or immunostained for Rorb (D,E). (C). Quantitative data of cell positioning are presented. The position of each GFP-positive cell relative to the total distance from the bottom of L4 to the outer edge of the cortical plate was measured, followed by sorting into 5 bins in each condition ( $n = 4$  for each group). (F). The result of quantitative analysis for Rorb is presented ( $n = 4$  for each group). \*  $p < 0.05$ , \*\*\*  $p < 0.001$ . (Scale bars: 200  $\mu\text{m}$  in (A,D)).

#### 4. Discussion

In this study, we found a potential role of Shh signaling in the generation of L4 subtypes of the mouse cortical plate. Shh signaling appeared not to directly activate L4 specification programs but controlled the positioning of a subset of superficial layer neurons, thereby leading to the ultimate specification of L4 subtypes. A similar regulation of cell positioning by Shh signaling was reported previously in the chick optic tectum [43], suggesting a wider role of Shh in cell positioning/distribution.

Shh has been shown to play roles in the proliferation and cell cycle control of progenitor cells in both positive and negative ways during neurogenesis [29]. We previously reported that ectopic expression of Shh in developing NPCs resulted in an increased proliferation of intermediate progenitor cells [30]. As the method used in the current study is similar to that in the previous one, high levels of Shh signaling might have also increased the proliferation rate of intermediate progenitor cells in the present study. However, although increased proliferation may increase the generation of later-born subtypes, altered proliferation did not account for the observed phenotypes that high levels of Shh signaling led to the generation of ‘earlier-born’ subtypes than the control.

What downstream effectors play a role in this type of subtype specification? Upon binding to its receptors, Shh influences a wide variety of signal transduction pathways including the activation of the transcription factor Gli1 [44]. It is well studied that Shh determines an oligodendrocyte fate through Gli1-dependent transcriptional regulation [45,46]. Gli1 directly upregulates Olig2, a master regulator of oligodendrocytes, allowing NPCs to differentiate into oligodendrocytes [45]. Thus, a similar mechanism, by which Shh determines the L4 subtype via direct transcriptional regulation, such as upregulation of L4 fate determinants, is conceivable. However, we are not in favor of this hypothesis due to mainly three reasons. First, we did not observe a premature expression of Rorb in early time points; if Shh directly activated the L4 specification program, the premature induction of downstream targets would be predicted. Second, the repositioning of Shh-overexpressing neurons to the more pial side in the superficial layer canceled the expression of Rorb even in the presence of

Shh. Third, *Gli1* transcriptional activation, a canonical downstream target of the Shh–Ptc1 axis [29,44], was hardly detected in the developing cortical neurons [47]. Accordingly, we did not detect *Gli1* and *Ptc1* mRNAs even in Shh-overexpressing neurons. Instead, another Shh receptor, *Boc*, which activates noncanonical Shh pathways, was strongly expressed [48]. These observations suggest that Shh may indirectly regulate the generation of L4 subtypes.

It remains to be determined what kind of intracellular events Shh signaling regulates to control cell positioning. A possible downstream is calcium signaling [49], which has been shown to play a role in the regulation of neuronal migration [50,51]. In addition, we recently found that Shh can activate calcium signaling (J.M. unpublished observation) [52], leading to a hypothesis that the Shh–calcium axis controls neuronal migration and positioning.

It is also to be determined how Shh specifically regulates L4 development. Shh may act as a limiting factor for immature neurons to be located in the future L4 region (bottom of the superficial layer); the amount of Shh is not abundant so that only a part of E14.5-born cells can receive Shh signaling, which accelerates the positioning of neurons in the future L4 region, where further L4 maturation processes occur. The neurons that do not receive enough Shh are positioned in the more superficial or future L2/3 region and differentiate into L2/3 subtypes. Such endogenous Shh might be provided from the marginal zone of the outermost cortical region, where cortical interneurons are migrating. In fact, interneurons were reported as one of the Shh sources in the developing cortex [53]. Ectopic Shh may have activated the population that normally does not receive Shh signaling, enabling them to be located in the future L4 region. Such differentiation plasticity is probably also regulated temporally in NPCs and/or immature neurons because ectopic Shh expression did not cause any alteration of cell positioning and subtype specification in the E15.5-electroporated cells. As *Boc* is expressed strongly in L4 (formed by mainly E14.0-born neurons) but very weak in L2/3 (formed by E15.5-born neurons), *Boc* expression levels could underlie this differential response to ectopic Shh [48]. In addition, given that E14.5-born neurons can respond to ectopic Shh, one might expect that *Boc*-high neurons exist in layer 2/3, presumably at its bottom. Further studies on the detailed expression pattern of *Boc* will clarify the difference.

Although Reelin, an extracellular protein, is well-known as a factor that controls positioning and/or migration of cortical neurons [54], cortical lamination has been regarded as a relatively intrinsic process, in which new neurons just pile up on the earlier-formed ‘layers’ according to their birthdates. Therefore, the extent to which the lamination process is regulated by extrinsic factors remains obscure [5]. Here, we reported on Shh as an extracellular regulator in the lamination of excitatory cortical neurons. A recent report showing the involvement of *Cxcl12* in the positioning of cortical interneurons [55] would predict further roles of extrinsic cues in the regulation of neuronal migration/positioning and lamination.

**Author Contributions:** Conceptualization, K.O.; methodology, K.O. and K.N.; validation, K.O. and J.M.; formal analysis, K.O.; investigation, K.O.; resources, K.O., K.N., and J.M.; data curation, K.O.; writing—original draft preparation, K.O.; writing—review and editing, K.O., K.N., and J.M.; visualization, K.O.; supervision, J.M.; project administration, K.O.; funding acquisition, K.O. and K.N. All authors have read and agreed to the published version of the manuscript.

**Funding:** This work was supported by the Japan Society for the Promotion of Science (KAKENHI JP21K06381, JP20H05688).

**Institutional Review Board Statement:** All experiments were approved by the Doshisha University Animal Experiment Committee and conducted in accordance with guidelines established by the Doshisha University Ethics Review Committee.

**Informed Consent Statement:** Not applicable.

**Data Availability Statement:** Any data and original materials are available from the corresponding author upon reasonable request.

**Acknowledgments:** We would like to thank H. Hasegawa at Keio University for his expert advice. We thank the members of the Motoyama laboratory and the animal facility of Doshisha university for the discussions and technical assistance.

**Conflicts of Interest:** The authors declare no conflict of interest.

## References

1. Lodato, S.; Arlotta, P. Generating neuronal diversity in the mammalian cerebral cortex. *Annu. Rev. Cell Dev. Biol.* **2015**, *31*, 699–720. [CrossRef] [PubMed]
2. Greig, L.C.; Woodworth, M.; Galazo, M.; Padmanabhan, H.; Macklis, J.D. Molecular logic of neocortical projection neuron specification, development and diversity. *Nat. Rev. Neurosci.* **2013**, *14*, 755–769. [CrossRef] [PubMed]
3. Nakajima, K. Control of tangential/non-radial migration of neurons in the developing cerebral cortex. *Neurochem. Int.* **2007**, *51*, 121–131. [CrossRef]
4. Marin, O.; Rubenstein, J.L.R. A long, remarkable journey: Tangential migration in the telencephalon. *Nat. Rev. Neurosci.* **2001**, *2*, 780–790. [CrossRef] [PubMed]
5. Oishi, K.; Nakajima, K. Subtype Specification of Cerebral Cortical Neurons in Their Immature Stages. *Neurochem. Res.* **2018**, *43*, 238–244. [CrossRef] [PubMed]
6. Miyoshi, G. Elucidating the developmental trajectories of GABAergic cortical interneuron subtypes. *Neurosci. Res.* **2019**, *138*, 26–32. [CrossRef]
7. Tabata, H. Diverse subtypes of astrocytes and their development during corticogenesis. *Front. Neurosci.* **2015**, *9*, 114. [CrossRef]
8. Kwan, K.Y.; Sestan, N.; Anton, E.S. Transcriptional co-regulation of neuronal migration and laminar identity in the neocortex. *Development* **2012**, *139*, 1535–1546. [CrossRef]
9. Takahashi, T.; Goto, T.; Miyama, S.; Nowakowski, R.; Caviness, V.S., Jr. Sequence of neuron origin and neocortical laminar fate: Relation to cell cycle of origin in the developing murine cerebral wall. *J. Neurosci.* **1999**, *19*, 10357–10371. [CrossRef]
10. BRAIN Initiative Cell Census Network (BICCN). A multimodal cell census and atlas of the mammalian primary motor cortex. *Nature* **2021**, *598*, 86–102. [CrossRef]
11. Chen, B.; Schaevitz, L.R.; McConnell, S.K. Fezl regulates the differentiation and axon targeting of layer 5 subcortical projection neurons in cerebral cortex. *Proc. Natl. Acad. Sci. USA* **2005**, *102*, 17184–17189. [CrossRef] [PubMed]
12. Molyneaux, B.J.; Arlotta, P.; Hirata, T.; Hibi, M.; Macklis, J.D. Fezl is required for the birth and specification of corticospinal motor neurons. *Neuron* **2005**, *47*, 817–831. [CrossRef] [PubMed]
13. Chen, J.G.; Rašin, M.-R.; Kwan, K.Y.; Sestan, N. Zfp312 is required for subcortical axonal projections and dendritic morphology of deep-layer pyramidal neurons of the cerebral cortex. *Proc. Natl. Acad. Sci. USA* **2005**, *102*, 17792–17797. [CrossRef]
14. Arlotta, P.; Molyneaux, B.J.; Chen, J.; Inoue, J.; Kominami, R.; Macklis, J.D. Neuronal subtype-specific genes that control corticospinal motor neuron development in vivo. *Neuron* **2005**, *45*, 207–221. [CrossRef] [PubMed]
15. Jabaudon, D.; Shnyder, S.J.; Tischfield, D.; Galazo, M.; Macklis, J.D. ROR $\beta$  induces barrel-like neuronal clusters in the developing neocortex. *Cereb. Cortex* **2012**, *22*, 996–1006. [CrossRef] [PubMed]
16. Oishi, K.; Aramaki, M.; Nakajima, K. Mutually repressive interaction between Brn1/2 and Rorb contributes to the establishment of neocortical layer 2/3 and layer 4. *Proc. Natl. Acad. Sci. USA* **2016**, *113*, 3371–3376. [CrossRef] [PubMed]
17. Hevner, R.F.; Shi, L.; Justice, N.; Hsueh, Y.-P.; Sheng, M.; Smiga, S.; Bulfone, A.; Goffinet, A.M.; Campagnoni, A.T.; Rubenstein, J.L. Tbr1 regulates differentiation of the preplate and layer 6. *Neuron* **2001**, *29*, 353–366. [CrossRef]
18. Alcamo, E.A.; Chirivella, L.; Dautzenberg, M.; Dobрева, G.; Fariñas, I.; Grosschedl, R.; McConnell, S.K. Satb2 regulates callosal projection neuron identity in the developing cerebral cortex. *Neuron* **2008**, *57*, 364–377. [CrossRef]
19. Britanova, O.; de Juan Romero, C.; Cheung, A.; Kwan, K.Y.; Schwark, M.; Gyorgy, A.; Vogel, T.; Akopov, S.; Mitkovski, M.; Agoston, D.; et al. Satb2 is a postmitotic determinant for upper-layer neuron specification in the neocortex. *Neuron* **2008**, *57*, 378–392. [CrossRef]
20. Kohwi, M.; Doe, C.Q. Temporal fate specification and neural progenitor competence during development. *Nat. Rev. Neurosci.* **2013**, *14*, 823–838. [CrossRef]
21. Dehay, C.; Kennedy, H. Cell-cycle control and cortical development. *Nat. Rev. Neurosci.* **2007**, *8*, 438–450. [CrossRef] [PubMed]
22. Hirata, T.; Suda, Y.; Nakao, K.; Narimatsu, M.; Hirano, T.; Hibi, M. Zinc finger gene fez-like functions in the formation of subplate neurons and thalamocortical axons. *Dev. Dyn.* **2004**, *230*, 546–556. [CrossRef] [PubMed]
23. Dominguez, M.H.; Ayoub, A.E.; Rakic, P. POU-III transcription factors (Brn1, Brn2, and Oct6) influence neurogenesis, molecular identity, and migratory destination of upper-layer cells of the cerebral cortex. *Cereb. Cortex* **2013**, *23*, 2632–2643. [CrossRef] [PubMed]
24. Oishi, K.; Nakagawa, N.; Tachikawa, K.; Sasaki, S.; Aramaki, M.; Hirano, S.; Yamamoto, N.; Yoshimura, Y.; Nakajima, K. Identity of neocortical layer 4 neurons is specified through correct positioning into the cortex. *eLife* **2016**, *5*, e10907. [CrossRef] [PubMed]
25. Oberst, P.; Fièvre, S.; Baumann, N.; Concetti, C.; Bartolini, G.; Jabaudon, D. Temporal plasticity of apical progenitors in the developing mouse neocortex. *Nature* **2019**, *573*, 370–374. [CrossRef]
26. Sato, H.; Hatakeyama, J.; Iwasato, T.; Araki, K.; Yamamoto, N.; Shimamura, K. Thalamocortical axons control the cytoarchitecture of neocortical layers by area-specific supply of VGF. *Elife* **2022**, *11*, e67549. [CrossRef]

27. Pouchelon, G.; Gambino, F.; Bellone, C.; Telley, L.; Vitali, I.; Lüscher, C.; Holtmaat, A.; Jabaudon, D. Modality-specific thalamocortical inputs instruct the identity of postsynaptic L4 neurons. *Nature* **2014**, *511*, 471–474. [CrossRef]
28. Desai, A.R.; McConnell, S.K. Progressive restriction in fate potential by neural progenitors during cerebral cortical development. *Development* **2000**, *127*, 2863–2872. [CrossRef]
29. Yabut, O.R.; Pleasure, S.J. Sonic Hedgehog Signaling Rises to the Surface: Emerging Roles in Neocortical Development. *Brain Plast.* **2018**, *3*, 119–128. [CrossRef]
30. Shikata, Y.; Okada, T.; Hashimoto, M.; Ellis, T.; Matsumaru, D.; Shiroishi, T.; Ogawa, M.; Wainwright, B.; Motoyama, J. Ptch1-mediated dosage-dependent action of Shh signaling regulates neural progenitor development at late gestational stages. *Dev. Biol.* **2011**, *349*, 147–159. [CrossRef]
31. Wang, L.; Hou, S.; Han, Y.-G. Hedgehog signaling promotes basal progenitor expansion and the growth and folding of the neocortex. *Nat. Neurosci.* **2016**, *19*, 888–896. [CrossRef] [PubMed]
32. Araújo, G.L.; Araújo, J.A.; Schroeder, T.; Tort, A.B.; Costa, M.R. Sonic hedgehog signaling regulates mode of cell division of early cerebral cortex progenitors and increases astrogliogenesis. *Front. Cell. Neurosci.* **2014**, *8*, 77. [CrossRef] [PubMed]
33. Pozniak, C.D.; Langseth, A.J.; Dijkgraaf, G.J.P.; Choe, Y.; Werb, Z.; Pleasure, S.J. Sox10 directs neural stem cells toward the oligodendrocyte lineage by decreasing Suppressor of Fused expression. *Proc. Natl. Acad. Sci. USA* **2010**, *107*, 21795–21800. [CrossRef] [PubMed]
34. Hill, S.A.; Fu, M.; Garcia, A.D.R. Sonic hedgehog signaling in astrocytes. *Cell Mol. Life Sci.* **2021**, *78*, 1393–1403. [CrossRef]
35. Bertrand, N.; Dahmane, N. Sonic hedgehog signaling in forebrain development and its interactions with pathways that modify its effects. *Trends Cell Biol.* **2006**, *16*, 597–605. [CrossRef]
36. Tabata, H.; Nakajima, K. Efficient in utero gene transfer system to the developing mouse brain using electroporation: Visualization of neuronal migration in the developing cortex. *Neuroscience* **2001**, *103*, 865–872. [CrossRef] [PubMed]
37. Staiger, J.F.; Flagmeyer, I.; Schubert, D.; Zilles, K.; Kötter, R.; Luhmann, H.J. Functional diversity of layer IV spiny neurons in rat somatosensory cortex: Quantitative morphology of electrophysiologically characterized and biocytin labeled cells. *Cereb. Cortex* **2004**, *14*, 690–701. [CrossRef]
38. Nakagawa, Y.; O’Leary, D.D. Dynamic patterned expression of orphan nuclear receptor genes RORalpha and RORbeta in developing mouse forebrain. *Dev. Neurosci.* **2003**, *25*, 234–244. [CrossRef] [PubMed]
39. Schaeren-Wiemers, N.; André, E.; Kapfhammer, J.P.; Becker-André, M. The expression pattern of the orphan nuclear receptor RORbeta in the developing and adult rat nervous system suggests a role in the processing of sensory information and in circadian rhythm. *Eur. J. Neurosci.* **1997**, *9*, 2687–2701. [CrossRef]
40. Nakagawa, Y.; Johnson, J.E.; O’Leary, D.D.M. Graded and areal expression patterns of regulatory genes and cadherins in embryonic neocortex independent of thalamocortical input. *J. Neurosci.* **1999**, *19*, 10877–10885. [CrossRef]
41. McEvilly, R.J.; de Diaz, M.O.; Schonemann, M.D.; Hooshmand, F.; Rosenfeld, M.G. Transcriptional regulation of cortical neuron migration by POU domain factors. *Science* **2002**, *295*, 1528–1532. [CrossRef] [PubMed]
42. Sugitani, Y.; Nakai, S.; Minowa, O.; Nishi, M.; Jishage, K.-I.; Kawano, H.; Mori, K.; Ogawa, M.; Noda, T. Brn-1 and Brn-2 share crucial roles in the production and positioning of mouse neocortical neurons. *Genes Dev.* **2002**, *16*, 1760–1765. [CrossRef] [PubMed]
43. Yang, C.; Li, X.; Li, Q.; Li, H.; Qiao, L.; Guo, Z.; Lin, J. Sonic Hedgehog Regulation of the Neural Precursor Cell Fate During Chicken Optic Tectum Development. *J. Mol. Neurosci.* **2018**, *64*, 287–299. [CrossRef] [PubMed]
44. Huangfu, D.; Anderson, K.V. Signaling from Smo to Ci/Gli: Conservation and divergence of Hedgehog pathways from Drosophila to vertebrates. *Development* **2006**, *133*, 3–14. [CrossRef]
45. Nery, S.V.; Wichterle, H.; Fishell, G. Sonic hedgehog contributes to oligodendrocyte specification in the mammalian forebrain. *Development* **2001**, *128*, 527–540. [CrossRef]
46. Nicolay, D.J.; Doucette, J.R.; Nazarali, A.J. Transcriptional control of oligodendrogenesis. *Glia* **2007**, *55*, 1287–1299. [CrossRef]
47. Garcia, A.D.R.; Petrova, R.; Eng, L.; Joyner, A.L. Sonic hedgehog regulates discrete populations of astrocytes in the adult mouse forebrain. *J. Neurosci.* **2010**, *30*, 13597–13608. [CrossRef]
48. Harwell, C.C.; Parker, P.R.; Gee, S.M.; Okada, A.; McConnell, S.K.; Kreitzer, A.C.; Kriegstein, A.R. Sonic hedgehog expression in corticofugal projection neurons directs cortical microcircuit formation. *Neuron* **2012**, *73*, 1116–1126. [CrossRef]
49. Andhika Rhaditya, P.A.; Oishi, K.; Nishimura, Y.V.; Motoyama, J. [Ca<sup>2+</sup>]<sub>i</sub> fluctuation mediated by T-type Ca<sup>2+</sup> channel is required for the differentiation of cortical neural progenitor cells. *Dev. Biol.* **2022**, *489*, 84–97. [CrossRef]
50. Kamijo, S.; Ishii, Y.; Horigane, S.-I.; Suzuki, K.; Ohkura, M.; Nakai, J.; Fujii, H.; Takemoto-Kimura, S.; Bito, H. A Critical Neurodevelopmental Role for L-Type Voltage-Gated Calcium Channels in Neurite Extension and Radial Migration. *J. Neurosci.* **2018**, *38*, 5551–5566. [CrossRef]
51. Rash, B.G.; Ackman, J.B.; Rakic, P. Bidirectional radial Ca(2+) activity regulates neurogenesis and migration during early cortical column formation. *Sci. Adv.* **2016**, *2*, e1501733. [CrossRef] [PubMed]
52. Teperino, R.; Amann, S.; Bayer, M.; McGee, S.; Loipetzberger, A.; Connor, T.; Jaeger, C.; Kammerer, B.; Winter, L.; Wiche, G.; et al. Hedgehog partial agonism drives Warburg-like metabolism in muscle and brown fat. *Cell* **2012**, *151*, 414–426. [CrossRef] [PubMed]
53. Komada, M.; Saito, H.; Kinboshi, M.; Miura, T.; Shiota, K.; Ishibashi, M. Hedgehog signaling is involved in development of the neocortex. *Development* **2008**, *135*, 2717–2727. [CrossRef] [PubMed]

54. Honda, T.; Kobayashi, K.; Mikoshiba, K.; Nakajima, K. Regulation of cortical neuron migration by the Reelin signaling pathway. *Neurochem. Res.* **2011**, *36*, 1270–1279. [CrossRef]
55. Venkataramanappa, S.; Saaber, F.; Abe, P.; Schütz, D.; Kumar, P.A.; Stumm, R. Cxcr4 and Ackr3 regulate allocation of caudal ganglionic eminence-derived interneurons to superficial cortical layers. *Cell Rep.* **2022**, *40*, 111157. [CrossRef]

Review

# Regulation of the Brain Neural Niche by Soluble Molecule Akhirin

Mikiko Kudo and Kunimasa Ohta \* 

Department of Stem Cell Biology, Faculty of Arts and Science, Kyushu University, 744 Motoooka, Nishi-Ku, Fukuoka 819-0395, Japan; kudo.mikiko.490@s.kyushu-u.ac.jp

\* Correspondence: ohta9203@artsci.kyushu-u.ac.jp

**Abstract:** In the central nervous system (CNS), which comprises the eyes, spinal cord, and brain, neural cells are produced by the repeated division of neural stem cells (NSCs) during the development of the CNS. Contrary to the notion that the CNS is relatively static with a limited cell turnover, cells with stem cell-like properties have been isolated from most neural tissues. The microenvironment, also known as the NSC niche, consists of NSCs/neural progenitor cells, other neurons, glial cells, and blood vessels; this niche is thought to regulate neurogenesis and the differentiation of NSCs into neurons and glia. Although it has been established that neurons, glia, and blood vessels interact with each other in a complex manner to generate neural tissues in the NSC niche, the underlying molecular mechanisms in the CNS niche are unclear. Herein, we would like to introduce the extracellular secreted protein, Akhirin (AKH; Akhi is the Bengali translation for eye). AKH is specifically expressed in the CNS niche—the ciliary body epithelium in the retina, the central canal of the spinal cord, the subventricular zone, and the subgranular zone of the dentate gyrus of the hippocampus—and is supposedly involved in NSC niche regulation. In this review, we discuss the role of AKH as a niche molecule during mouse brain formation.

**Keywords:** Akhirin; neurogenesis; vasculogenesis; LCCL domain; vWF domain; hydrocephalus

**Citation:** Kudo, M.; Ohta, K.

Regulation of the Brain Neural Niche by Soluble Molecule Akhirin. *J. Dev. Biol.* **2021**, *9*, 29. <https://doi.org/10.3390/jdb9030029>

Academic Editors: Tsutomu Nohno, Hideyo Ohuchi and Simon J. Conway

Received: 7 May 2021

Accepted: 20 July 2021

Published: 26 July 2021

**Publisher's Note:** MDPI stays neutral with regard to jurisdictional claims in published maps and institutional affiliations.



**Copyright:** © 2021 by the authors. Licensee MDPI, Basel, Switzerland. This article is an open access article distributed under the terms and conditions of the Creative Commons Attribution (CC BY) license (<https://creativecommons.org/licenses/by/4.0/>).

## 1. Introduction

The central nervous system (CNS; eyes, spinal cord, and brain) acts as a controller that receives, sorts, and organizes information from all over the body and sends the corresponding commands, which is vital for survival. The CNS is formed by the repeated division and proliferation of neural stem cells (NSCs) and neural progenitor cells (NPCs). Dividing immature neurons differentiate into mature neurons. A hallmark of the NSCs/NPCs in the CNS is that they have extremely high proliferation during development; however, once the respective tissues are formed, their rate of cell division reduces dramatically. Therefore, it is important to understand when neuron production is active and how tissue formation progresses during tissue development.

Several studies have identified various cellular sources of NSCs in the adult vertebrate eye [1]. Retinal NSCs are present in the ciliary body epithelium [2,3], iris pigment epithelium [4], peripheral margin of the retina [5], and Müller cells [6,7]. Müller cells are radial glial cells, with morphology and expression of glial markers similar to those of embryonic radial cells, which are used as progenitor cells in the CNS. To date, it is believed that Müller cells are the endogenous NSCs in the retina.

In the spinal cord, several cell types have been identified in the central canal, including cuboidal, tancytic, and radial classes of lumen-contacted ciliated ependymal cells [8]. Numerous studies have indicated that ependymal cells localized in the dorsal central canal, originated from radial glial cells, show NSC activity [9]. Ependymal cells also contribute to the regeneration of oligodendrocytes and remyelination after spinal cord injury [10].

In the adult mouse brain, several studies have indicated two major neurogenic niches: the subventricular zone (SVZ) lining the lateral ventricle and the subgranular zone (SGZ) of the dentate gyrus (DG) of the hippocampus in the CNS [11,12]. In the SVZ, type B stem cells

give rise to type C transit-amplifying cells which, in turn, produce type A neuroblasts [13]. Type B and C cells form a tubular network through which type A neuroblasts migrate into the rostral migratory stream toward the olfactory bulbs. In the SGZ, proliferating radial and nonradial precursors give rise to intermediate progenitors which, in turn, generate neuroblasts. Immature neurons migrate into the inner granule cell layer and differentiate into dentate granule cells in the hippocampus [13].

NSCs/NPCs are constantly maintained in a specific microenvironment (niche) since the time of development processes and throughout adulthood [14]. Typically, equilibrium between cell proliferation and differentiation between the two cell populations, NSCs and NPCs, is important for CNS development. Neurons emerge from a pool of NSCs/NPCs through neurogenesis, which is regulated by many extrinsic and intrinsic factors. The niche in which NSCs are maintained consists of a complex array of other neurons, blood vessels, and other glial cells. The division and self-renewal of NSCs are regulated by specialized niche regulators secreted by these cells. Despite the relevance of the fate of NSCs/NPCs, which is ultimately reflected in the final number of newly generated neurons, the timing and number of divisions of NSCs and their differentiation into neurons are flexible processes; moreover, in several cases, not all types of intermediate progenitors are generated in a clonal lineage [15,16]. Thus, the mechanisms that control their development processes are poorly understood.

Herein, we introduce the secreted protein, Akhirin (AKH; Akhi is the Bengali translation for eye), which was isolated from embryonic day 6 (E6) chick lens using signal sequence trap cDNA screening [17]. We have previously reported extensive expression of AKH in the niches of the CNS. AKH is specifically expressed in the ciliary marginal zone of the retina [18], the middle and ventral central canal of the spinal cord [19], and the SVZ and the DG of the hippocampus in the mouse CNS [20]. As AKH exhibits heterophilic cell adhesion activity, which has been confirmed by cell aggregation analysis [18], it is supposed to function as an extracellular adhesion factor regulating these niches in the CNS. In this review, after summarizing the molecular structure of AKH and its role in the eye and spinal cord, we mainly discuss its role in the brain as a niche regulator in the CNS.

## 2. Possible Roles of the vWF-A and LCCL Domains in AKH

The structure of AKH comprises two von Willebrand factor-A (vWF-A) domains and one Limulus factor C, Coch-5b2 and Lgl1 (LCCL) domain. The chick AKH has an open reading frame of 748 amino acid residues, and the mouse AKH has an open reading frame of 650 amino acid residues (Figure 1A). AKH has relatively high homology to vitrin [21] and cochlin [22]. In mice, AKH can be regarded as a factor almost identical to vitrin, and mouse cochlin is composed of 522 amino acid residues. Based on the two vWF-A domains in AKH, cell aggregation analysis using AKH-expressing transfectants indicated the role of AKH in cell adhesion [18]. As both the control cells and AKH-expressing transfectants adhered to immobilized AKH protein, we concluded that AKH has heterophilic cell adhesion activity [18]. It is one of great interest to identify the molecules that interact with AKH.

The vWF-A domain is involved in blood clotting. In vWF disease, the absence or malfunction of vWF-A results in bleeding which is difficult to control. Most of the vWF-A domains are synthesized in the endothelial cells of blood vessels. The vWF-A domain 1 directly binds to angiogenesis-inducing factors such as vascular endothelial growth factor-A (VEGF-A) and platelet-derived growth factor-BB (PDGF-BB). VEGF and PDGF-BB play an important role in vascularization [23] and neurogenesis, respectively, during early development [24].

Although the interaction of blood vessels with NSCs in the adult brain niche has already been widely reported [25–27], recent reports have shown that the timing of differentiation of NSCs/NPCs into neurons is implicated in the interaction between embryonic vascularization and neurogenesis. For instance, Di Marco et al. showed that nascent periventricular vessels interact with dividing apical neural progenitors by using vascular filopodia induced by the upregulation of VEGF-A in a cell-cycle-dependent manner [23].

They concluded that vascular filopodia helps in fine-tuning NSC behavior for proper brain development. As AKH contains two vWF-A domains, it is interesting to examine the molecular interactions between AKH and VEGF-A and PDGF-BB.

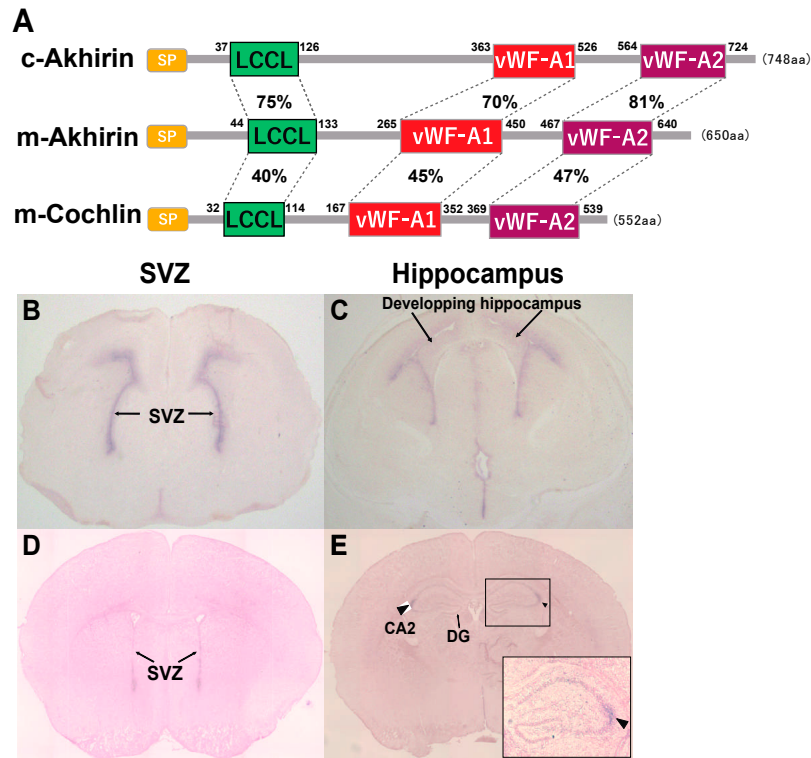


**Figure 1.** (A): A simple schematic diagram of chick and mouse AKH, mouse cochlin protein structure. The amino acid number is presented for each domain. (B–E): The expression of *AKH* mRNA in SVZ (B,D) and the hippocampus region (C,E) of the mouse brain at E17 (B,C) and P20 (D,E). Arrows indicate SVZ niche areas along the LV regions (B,D) and the developing hippocampus (C). Arrowheads indicate the hippocampal CA2 region (E).

The LCCL domain is found in the biodefense factor C of the horseshoe crab, which is a lipopolysaccharide (LPS)-binding protein [28]. LPS is a constituent of the outer membrane of the cell wall of gram-negative bacteria. LPS can bind to Toll-like receptor 4 (TLR4), which is present on the surface of the host cell membrane and works as an endotoxin [29]. TLR family members are involved in the expression of proinflammatory cytokines and play an important role in innate immunity. Recent reports have shown that the LCCL domain is cleaved from the cochlin protein, which sequesters infiltrating bacteria and protects hearing in the organ of Corti [28,30].

Neurons, immune system cells, and blood vessels form a tight network with each other to maintain immune homeostasis in the brain. The LCCL domain binds to LPS and plays a role in immune defense. Infections of bacteria may cause encephalitis, meningitis, and various other diseases in the brain and, occasionally, cause disturbances in the blood-brain barrier (between the neurons and vascular units) and the blood-cerebrospinal fluid barrier (BCSFB; between the cerebrospinal fluid (CSF) and choroid plexus (ChP)) [31]. The ChP is a vascular-rich tissue in the ventricle facing the NSC niche that produces and secretes CSF. Immune system activation following a bacterial infection in a pregnant mother increases the number of activated microglia in the ChP of the fetal brain, which disrupts the intercellular adhesion of ependymal cells, causing the disarrangement of the BCSFB and/or an increase in polarity, which biases the direction of the microglial neurites; this consequently results in abnormal cortical layer formation after birth [32,33]. The progression of layer formation is active during the embryonic and immediate postnatal



periods. The neurons migrate toward the surface of the brain from the ventricular zones, forming the six-layered structure (inside-out). The ventricular zones consist of epithelial tissue, and the cell junctions are rigid. The disrupted regulation of cell junctions on the ventricular surface, especially cadherins, which are calcium ( $\text{Ca}^{2+}$ )-dependent adhesion molecules between epithelial cells, causes abnormal layer formation [34]. In addition, since AKH has heterophilic cell adhesive activity [18], it is highly predictable that the loss of AKH will result in disruption of the tight junctions. Thus, it is likely that there is a mutual relationship between vascularization-neurogenesis and microglia during brain formation; however, the detailed molecular mechanism has not yet been elucidated. Therefore, the activation and neurite polarity of microglia may explain the cause of ventricle expansion in the *AKH*<sup>-/-</sup> mouse brain.

### 3. AKH Localizes in the Niche of the Eye

Different neuronal NSCs/NPCs exist in the vertebrate retina, and their proliferation and differentiation are influenced by a combination of intrinsic and extrinsic factors [35,36]. In chick peripheral retina, both *AKH* mRNA and protein are expressed through the ciliary epithelial layer in the embryonic stage. In the chick embryo, AKH expression is observed in the head ectoderm overlying the lens vesicle at stage 17 and in the retinal pigment epithelial layer at stage 22. Although AKH expression changes during the embryonic stage, AKH accumulates in the presumptive ciliary marginal zone at the postnatal stage where the NSCs/NPCs are localized [18]. As *AKH* mRNA and protein are co-localized in NSCs/NPCs, and AKH exhibits heterophilic cell adhesion activity, we hypothesized that AKH secreted from these cells is associated with other extracellular matrix components on their surface to regulate the niche [18]. Unfortunately, we could not observe the expression of AKH in E14 mouse retina.

### 4. AKH Localizes in the Niche of the Spinal Cord

The spinal cord is the caudal portion of the CNS and transduces information between the brain and the body. NSCs have been isolated from the ependymal zone surrounding the central canal of the spinal cord [37]. A recent study showed that NSCs are the most dorsally located glial fibrillary acid protein (GFAP)-positive cells lying ependymally [38]. AKH expression was observed in the spinal cord of mice on embryonic day 9.5 (E9.5), which disappeared by postnatal day 30 (P30). *AKH*<sup>-/-</sup> mice showed reduced spinal cord size compared to that in wild-type mice (*AKH*<sup>+/+</sup>). The expression patterns of ependymal niche molecules (nestin and GFAP) in *AKH*<sup>-/-</sup> mice were changed when compared with those of *AKH*<sup>+/+</sup> mice in vivo [19]. In vitro culture of the spinal cord neurospheres showed significant reduction in the size of the neurospheres of *AKH*<sup>-/-</sup> mice compared with those of *AKH*<sup>+/+</sup> mice [19]. Interestingly, the distribution of ependymal proliferation factors (Cyclin D2 and vimentin) and proliferation markers (Ki67) in the neurospheres derived from *AKH*<sup>-/-</sup> was disturbed, indicating the involvement of AKH in NSCs/NPCs regulation.

In general, ependymal cells of the spinal cord are normally quiescent in adult mice. However, when the spinal cord is damaged, ependymal cells are rapidly activated and undergo differentiation to form astrocytes at the injured site [8]. Although the expression of AKH in the central canal ependymal cells is very low or not observed in the central canal at P30, AKH expression is rapidly upregulated in ependymal cells after spinal cord injury, suggesting that AKH is involved in post-injury neuronal neogenesis [19]. These observations suggest that AKH plays a crucial role in spinal cord formation in mice by regulating the ependymal niche in the central canal [38].

### 5. AKH Is Exclusively Localized in Brain Neurogenic Niches

The adult mammalian brain contains billions of neurons assembled in defined neural circuits, which are the essential components for mediating the higher functions of the CNS. During the development of the mouse brain, NSCs exist around the ventricles, and the newborn neurons migrate to their destination through various pathways. In the niches,

neurons and glia cells, such as microglia, astrocytes, and oligodendrocytes, emerge; they create a feedback interaction system via numerous secreted and contact-mediated signals for the regulation between quiescence and cell division of NSCs/NPCs. Although NSCs disappear from most parts of the brain after birth, they are still localized at the SVZ on the lateral wall of the LV and the SGZ of the hippocampal DG where they continue to produce neurons throughout life [38,39].

The expression of *AKH* at the SVZ was already observed at E17.5, which then disappeared by P20 (Figure 1B,D). In the hippocampal DG, *AKH* expression was observed in the entire hippocampal region immediately after birth, followed by a specific expression in the hippocampal CA2 region at P20 (Figure 1C,E). Thus, from the embryonic stage, *AKH* is expressed in the brain niche areas and disappears in tandem with the cessation of neurogenesis around P20 when brain formation is approximately complete; this observation suggests the involvement of *AKH* in neurogenesis and neuronal differentiation during early development but not in adult neurogenesis [20].

Newborn neurons migrate to other regions in the brain by forming special chain-like structures, which suggests that the interaction between newborn neurons and the extracellular matrix, such as *AKH*, is important in this process. NSCs are localized in the periventricular region, and nascent neurons migrate to the hippocampal region for hippocampal area formation. One possibility is that *AKH* might be involved in the migration of newborn neurons to the CA2 region because *AKH* secreted by NSCs is supposed to attach to the surface and interacts with the substrate during migration. The CA2 region of the hippocampus is a less well-characterized region than the CA1 and CA3 regions. In recent years, studies have reported the importance of the CA2 region in memory updating—a timeline of memory—and social memory [40–42]. When neuronal migration to the CA2 region is impaired due to the loss of *AKH*, psychiatric disorders, such as autism spectrum disorder, may occur. To examine the effect of *AKH* loss in the CA2 region, we are in the process of preparing a behavioral test battery with *AKH*<sup>-/-</sup> mice.

## 6. Effects of *AKH* Knockout on Neurogenesis and Neuronal Differentiation in the Brain NSC Niche

Self-renewal and differentiation potential of NSCs are dynamically regulated by various niche-derived factors, which relay signals in an autocrine or paracrine manner together with transcription factors that respond to those signals. To investigate whether *AKH* is a niche factor, we compared the brain morphology using *AKH*<sup>-/-</sup> and *AKH*<sup>+/+</sup> mice and found that the ventricles of *AKH*<sup>-/-</sup> mice were widely expanded when compared with those of *AKH*<sup>+/+</sup> mice (Figure 2A,B) [20]. The hippocampal DG region was reduced in *AKH*<sup>-/-</sup> mice when compared to that in *AKH*<sup>+/+</sup> mice (Figure 2D,E) [20]. Furthermore, lower proportion of GFAP, SOX2, and Ki67 trip; e-positive (GFAP<sup>+</sup>/SOX2<sup>+</sup>/Ki67<sup>+</sup>) cells was observed in *AKH*<sup>-/-</sup>, indicating reduced NSC proliferation, but higher population of GFAP and SOX2 double-positive (GFAP<sup>+</sup>/SOX2<sup>+</sup>/Ki67<sup>-</sup>) cells was increased in *AKH*<sup>-/-</sup> mice, indicating increase of quiescent NSCs. Finally, *AKH* deficiency inhibited the differentiation of NSCs into mature neurons and reduced the length of their neurites [20]. These results suggest that the loss of *AKH* causes NSCs to lose their proliferative capacity and become quiescent, resulting in a decrease in neurogenesis from NSCs, leading to the enlargement of the ventricles and reduction of the DG area during early development.

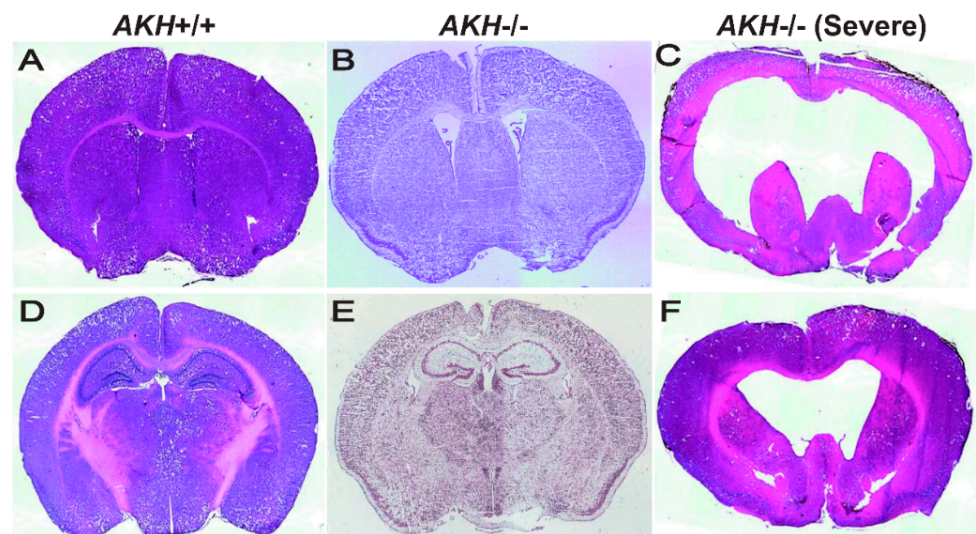


**Figure 2.** Histomorphology of the SVZ (A–C) and the hippocampal regions (D–F) in mouse brain on hematoxylin-eosin (HE) (A,C,D,F) and Nissl (B,E) staining. *AKH*<sup>+/+</sup> (A,D), *AKH*<sup>-/-</sup> (B,E), and *AKH*<sup>-/-</sup> hydrocephalus-like mouse (C,F).

### 7. Relationship between *AKH* and Hydrocephalus

Hydrocephalus is a frequent neurological disorder caused by the expansion of the cerebral ventricles and is associated with high morbidity and mortality rates [43]. Different forms of hydrocephalus have been identified: Noncommunicating hydrocephalus is caused by a blockage in the ventricular system, mainly at the aqueduct level between the third and fourth ventricles. In contrast, the ventricular system is not obstructed in communicating hydrocephalus. Although multiple genes and environmental factors are involved in hydrocephalus development, the molecular mechanisms underlying this condition remain unclear. Due to insufficient knowledge regarding the molecular basis of hydrocephalus, its clinical treatment is limited to invasive methods, with failure rates close to 50%.

Hydrocephalus-like enlargement of the ventricles was observed in the *AKH*<sup>-/-</sup> brain [20]. Interestingly, we found that approximately 3% of *AKH*<sup>-/-</sup> mice showed severely malformed brains that resembled a hydrocephalic brain morphology (Figure 2C,F). We were unable to analyze these fulminant *AKH*<sup>-/-</sup> mice in detail as these mutants died within the first month after birth. These phenotypes of *AKH*<sup>-/-</sup> hydrocephalic mice are similar to those of heterozygous *Nfib* and *Nfix* double mutant mice [44] and *Yap* mutant hydrocephalic mutant mice [45]. Although the ventricles expanded similarly to those in hydrocephalus because of these gene deletions, the molecular mechanisms underlying this condition remain unclear. Therefore, it is plausible to examine the molecular interactions between these genes.

### 8. Conclusions

*AKH* deficiency inhibits the proliferation of NSCs, resulting in a decrease in the total number of neurons in the brain niche area, thereby resulting in ventricular expansion in patients with hydrocephalus. It is of interest to examine the human *AKH* gene sequence in patients with hydrocephalus in the future. At present, the physiological functions of *AKH* remain unclear. While we can predict the important functions of *AKH* during brain formation, such as neurogenesis, vasculogenesis, and immunocompetence, more studies are needed to clarify the functional consequences of the defects in brain formation in *AKH*<sup>-/-</sup> mice. To end this, it is necessary to determine the detailed expression and localization of *AKH* in developed mice brains, etc. Thus, we hope that a more detailed function of *AKH* will be discovered by analyzing the effect of *AKH* deficiency on the interaction between NSCs and blood vessels, and on microglia (Figure 3). To date, research

in the fields of neurogenesis, vasculogenesis, and immunocompetence has been specialized and advanced. We propose that AKH is an interesting molecule that links these three fields and regulates brain formation.

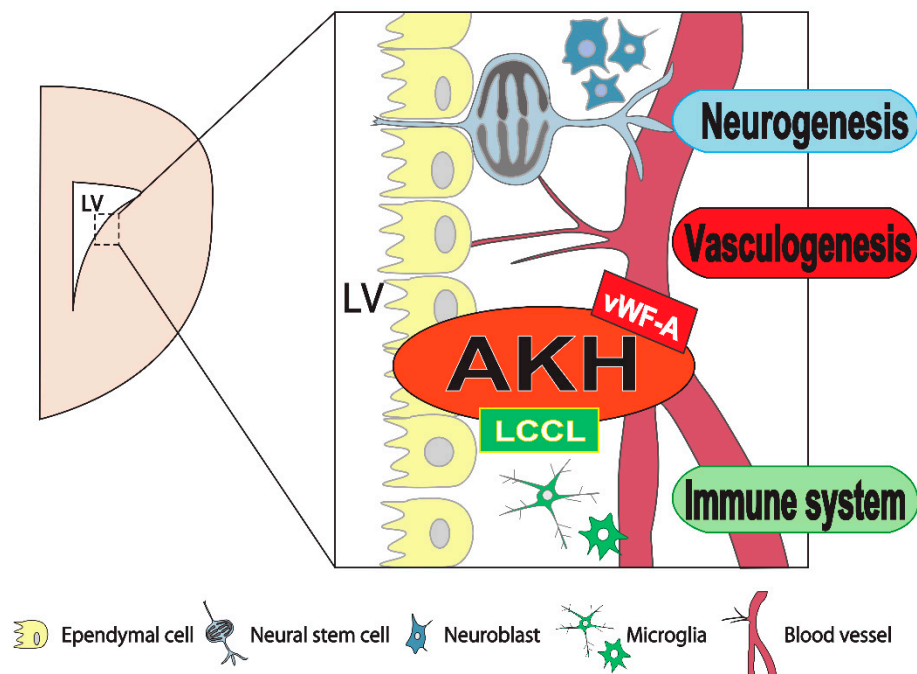


**Figure 3.** AKH is expressed in the neural stem cell niche and acts as a regulator. AKH is involved in the maintenance of neural stem cell proliferation, vasculogenesis, and the immune system during neurogenesis.

**Author Contributions:** M.K. and K.O. conceived the study and wrote the manuscript. All authors have read and agreed to the published version of the manuscript.

**Funding:** This research received no external funding.

**Institutional Review Board Statement:** Not applicable.

**Informed Consent Statement:** Not applicable.

**Data Availability Statement:** Not applicable.

**Acknowledgments:** We gratefully thank Arif Istiaq, Kousei Takashi, Gu Haoxuan, and Fucho Tan for their helpful assistance. This work was supported by Kumamoto University Advanced Research Project Stem Cell-Based Tissue Regeneration Research and Education Unit, the Joint Usage/Research Center for Developmental Medicine, IMEG, Kumamoto University.

**Conflicts of Interest:** The authors declare no conflict of interest.

## References

- Ohta, K.; Ito, A.; Tanaka, H. Neuronal stem/progenitor cells in the vertebrate eye. *Dev. Growth Differ.* **2008**, *50*, 253–259. [CrossRef] [PubMed]
- Ahmad, I.; Tang, L.; Pham, H. Identification of Neural Progenitors in the Adult Mammalian Eye. *Biochem. Biophys. Res. Commun.* **2000**, *270*, 517–521. [CrossRef]
- Tropepe, V.; Coles, B.L.K.; Chiasson, B.J.; Horsford, D.J.; Elia, A.J.; McInnes, R.R.; van der Kooy, D. Retinal Stem Cells in the Adult Mammalian Eye. *Science* **2000**, *287*, 2032–2036. [CrossRef] [PubMed]
- Haruta, M.; Kosaka, M.; Kanegae, Y.; Saito, I.; Inoue, T.; Kageyama, R.; Nishida, A.; Honda, Y.; Takahashi, M. Induction of photoreceptor-specific phenotypes in adult mammalian iris tissue. *Nat. Neurosci.* **2001**, *4*, 1163–1164. [CrossRef] [PubMed]
- Moshiri, A.; Reh, T.A. Persistent Progenitors at the Retinal Margin of ptc+/- Mice. *J. Neurosci.* **2004**, *24*, 229–237. [CrossRef] [PubMed]

6. Fischer, A.J.; Reh, T.A. Müller glia are a potential source of neural regeneration in the postnatal chicken retina. *Nat. Neurosci.* **2001**, *4*, 247–252. [CrossRef] [PubMed]
7. Osakada, F.; Takahashi, M. Neurogenic potential of Mueller glia in the adult mammalian retina. *Inflamm. Regen.* **2007**, *27*, 499–505. [CrossRef]
8. Hamilton, L.; Truong, M.; Bednarczyk, M.; Aumont, A.; Fernandes, K. Cellular organization of the central canal ependymal zone, a niche of latent neural stem cells in the adult mammalian spinal cord. *Neuroscience* **2009**, *164*, 1044–1056. [CrossRef]
9. Namiki, J.; Tator, C.H. Cell proliferation and nestin expression in the ependyma of the adult rat spinal cord after injury. *J. Neuropathol. Exp. Neurol.* **1999**, *58*, 489–498. [CrossRef]
10. Meletis, K.; Barnabé-Heider, F.; Carlen, M.; Evergren, E.; Tomilin, N.; Shupliakov, O.; Frisén, J. Spinal Cord Injury Reveals Multilineage Differentiation of Ependymal Cells. *PLoS Biol.* **2008**, *6*, e182. [CrossRef]
11. Doetsch, F.; Caillé, I.; Lim, D.; García-Verdugo, J.M.; Alvarez-Buylla, A. Subventricular Zone Astrocytes Are Neural Stem Cells in the Adult Mammalian Brain. *Cell* **1999**, *97*, 703–716. [CrossRef]
12. Furutachi, S.; Miya, H.; Watanabe, T.; Kawai, H.; Yamasaki, N.; Harada, Y.; Imayoshi, I.; Nelson, M.; I Nakayama, K.; Hirabayashi, Y.; et al. Slowly dividing neural progenitors are an embryonic origin of adult neural stem cells. *Nat. Neurosci.* **2015**, *18*, 657–665. [CrossRef] [PubMed]
13. Ming, G.-L.; Song, H. Adult Neurogenesis in the Mammalian Brain: Significant Answers and Significant Questions. *Neuron* **2011**, *70*, 687–702. [CrossRef] [PubMed]
14. Eriksson, P.S.; Perfilieva, E.; Björk-Eriksson, T.; Alborn, A.M.; Nordborg, C.; Peterson, D.A.; Gage, F.H. Neurogenesis in the adult human hippocampus. *Nat. Med.* **1998**, *4*, 1313–1317. [CrossRef]
15. Falk, S.; Bugeon, S.; Ninkovic, J.; Pilz, G.-A.; Postiglione, M.P.; Cremer, H.; Knoblich, J.A.; Götz, M. Time-Specific Effects of Spindle Positioning on Embryonic Progenitor Pool Composition and Adult Neural Stem Cell Seeding. *Neuron* **2017**, *93*, 777–791.e3. [CrossRef]
16. Pilz, G.-A.; Shitamukai, A.; Reillo, I.; Pacary, E.; Schwausch, J.; Stahl, R.; Ninkovic, J.; Snippert, H.J.; Clevers, H.; Godinho, L.; et al. Amplification of progenitors in the mammalian telencephalon includes a new radial glial cell type. *Nat. Commun.* **2013**, *4*, 2125. [CrossRef]
17. Mu, H.; Ohta, K.; Kuriyama, S.; Shimada, N.; Tanihara, H.; Yasuda, K.; Tanaka, H. Equarin, a novel soluble molecule expressed with polarity at chick embryonic lens equator, is involved in eye formation. *Mech. Dev.* **2003**, *120*, 143–155. [CrossRef]
18. Ahsan, M.; Ohta, K.; Kuriyama, S.; Tanaka, H. Novel soluble molecule, Akhirin, is expressed in the embryonic chick eyes and exhibits heterophilic cell-adhesion activity. *Dev. Dyn.* **2005**, *233*, 95–104. [CrossRef]
19. Abdhaleem, M.F.A.; Song, X.; Kawano, R.; Uezono, N.; Ito, A.; Ahmed, G.; Hossain, M.; Nakashima, K.; Tanaka, H.; Ohta, K. Akhirin regulates the proliferation and differentiation of neural stem cells in intact and injured mouse spinal cord. *Dev. Neurobiol.* **2014**, *75*, 494–504. [CrossRef]
20. Anam, M.B. Akhirin regulates the proliferation and differentiation of neural stem cells/progenitor cells at neurogenic niches in mouse brain. *Dev. Growth Differ.* **2020**, *62*, 97–107. [CrossRef]
21. Mayne, R.; Ren, Z.X.; Liu, J.; Cook, T.; Carson, M.; Narayana, S. VIT-1: The second member of a new branch of the von willebrand factor A do-main superfamily. *Biochem. Soc. Trans.* **1999**, *27*, 832–835. [CrossRef]
22. Heller, S.; Sheane, C.A.; Javed, Z.; Hudspeth, A.J. Molecular Markers for Cell Types of the Inner Ear and Candidate Genes for Hearing Disorders. 1998. Available online: <https://www.pnas.org/content/95/19/11400> (accessed on 25 July 2021).
23. Di Marco, B.; Crouch, E.E.; Shah, B.; Duman, C.; Paredes, M.F.; de Almodovar, C.R.; Huang, E.J.; Alfonso, J. Reciprocal Interaction between Vascular Filopodia and Neural Stem Cells Shapes Neurogenesis in the Ventral Telencephalon. *Cell Rep.* **2020**, *33*, 108256. [CrossRef]
24. Funa, K.; Sasahara, M. The Roles of PDGF in Development and During Neurogenesis in the Normal and Diseased Nervous System. *J. Neuroimmune Pharmacol.* **2014**, *9*, 168–181. [CrossRef]
25. Mirzadeh, Z.; Merkle, F.; Soriano-Navarro, M.; García-Verdugo, J.M.; Alvarez-Buylla, A. Neural Stem Cells Confer Unique Pinwheel Architecture to the Ventricular Surface in Neurogenic Regions of the Adult Brain. *Cell Stem Cell* **2008**, *3*, 265–278. [CrossRef] [PubMed]
26. Tavazoie, M.; Van der Veken, L.; Silva-Vargas, V.; Louissaint, M.; Colonna, L.; Zaidi, B.; García-Verdugo, J.M.; Doetsch, F. A Specialized Vascular Niche for Adult Neural Stem Cells. *Cell Stem Cell* **2008**, *3*, 279–288. [CrossRef] [PubMed]
27. Shen, Q.; Wang, Y.; Kokovay, E.; Lin, G.; Chuang, S.-M.; Goderie, S.K.; Roysam, B.; Temple, S. Adult SVZ Stem Cells Lie in a Vascular Niche: A Quantitative Analysis of Niche Cell-Cell Interactions. *Cell Stem Cell* **2008**, *3*, 289–300. [CrossRef]
28. Robertson, N.G.; Lu, L.; Heller, S.; Merchant, S.N.; Eavey, R.D.; McKenna, M.; Nadol, J.B.; Miyamoto, R.T.; Linthicum, F.H.; Neto, J.F.L.; et al. Mutations in a novel cochlear gene cause DFNA9, a human nonsyndromic deafness with vestibular dysfunction. *Nat. Genet.* **1998**, *20*, 299–303. [CrossRef]
29. Poltorak, A.; He, X.; Smirnova, I.; Liu, M.-Y.; Van Huffel, C.; Du, X.; Birdwell, D.; Alejos, E.; Silva, M.; Galanos, C.; et al. Defective LPS Signaling in C3H/HeJ and C57BL/10ScCr Mice: Mutations in Tlr4 Gene. *Science* **1998**, *282*, 2085–2088. [CrossRef]
30. Jung, J.; Yoo, J.E.; Choe, Y.H.; Park, S.C.; Lee, H.J.; Lee, H.J.; Noh, B.; Kim, S.H.; Kang, G.-Y.; Lee, K.-M.; et al. Cleaved Cochlin Sequesters *Pseudomonas aeruginosa* and Activates Innate Immunity in the Inner Ear. *Cell Host Microbe* **2019**, *25*, 513–525.e6. [CrossRef]

31. Pickard, J. Physiology and Pathophysiology of the Cerebrospinal Fluid. *J. Neurol. Neurosurg. Psychiatry* **1988**, *51*, 469–470. [CrossRef]
32. Cui, J.; Shipley, F.B.; Shannon, M.L.; Alturkistani, O.; Dani, N.; Webb, M.D.; Sugden, A.U.; Andermann, M.L.; Lehtinen, M.K. Inflammation of the Embryonic Choroid Plexus Barrier following Maternal Immune Activation. *Dev. Cell* **2020**, *55*, 617–628.e6. [CrossRef]
33. Ozaki, K.; Kato, D.; Ikegami, A.; Hashimoto, A.; Sugio, S.; Guo, Z.; Shibushita, M.; Tatematsu, T.; Haruwaka, K.; Moorhouse, A.J.; et al. Maternal immune activation induces sustained changes in fetal microglia motility. *Sci. Rep.* **2020**, *10*, 1–19. [CrossRef] [PubMed]
34. Nagashima, F.; Suzuki, I.K.; Shitamukai, A.; Sakaguchi, H.; Iwashita, M.; Kobayashi, T.; Toné, S.; Toida, K.; Vanderhaeghen, P.; Kosodo, Y. Novel and Robust Transplantation Reveals the Acquisition of Polarized Processes by Cortical Cells Derived from Mouse and Human Pluripotent Stem Cells. *Stem Cells Dev.* **2014**, *23*, 2129–2142. [CrossRef] [PubMed]
35. Clegg, D.O.; Mullick, L.H.; Wingerd, K.L.; Lin, H.; Atienza, J.W.; Bradshaw, A.D.; Gervin, D.B.; Cann, G.M. Adhesive events in retinal development and function: The role of integrin receptors. In *Chemistry and Biology of Pteridines and Folates*; Springer Science and Business Media LLC: Berlin/Heidelberg, Germany, 2000; Volume 31, pp. 141–156.
36. Zhao, X.; Das, A.V.; Soto-Leon, F.; Ahmad, I. Growth factor-responsive progenitors in the postnatal mammalian retina. *Dev. Dyn.* **2005**, *232*, 349–358. [CrossRef] [PubMed]
37. Weiss, S.; Dunne, C.; Hewson, J.; Wohl, C.; Wheatley, M.; Peterson, A.C.; Reynolds, B.A. Multipotent CNS Stem Cells Are Present in the Adult Mammalian Spinal Cord and Ventricular Neuroaxis. *J. Neurosci.* **1996**, *16*, 7599–7609. [CrossRef] [PubMed]
38. Sabourin, J.-C.; Ackema, K.B.; Ohayon, D.; Guichet, P.-O.; Perrin, F.E.; Garcès, A.; Ripoll, C.; Charitá, J.; Simonneau, L.; Kettenmann, H.; et al. A Mesenchymal-Like ZEB1+Niche Harbors Dorsal Radial Glial Fibrillary Acidic Protein-Positive Stem Cells in the Spinal Cord. *Stem Cells* **2009**, *27*, 2722–2733. [CrossRef] [PubMed]
39. Acharjee, U.K.; Felemban, A.A.; Riyadh, A.M.; Ohta, K. Regulation of the neural niche by the soluble molecule Akhirin. *Dev. Growth Differ.* **2016**, *58*, 463–468. [CrossRef]
40. Wintzer, M.E.; Boehringer, R.; Polygalov, D.; McHugh, T.J. The Hippocampal CA2 Ensemble Is Sensitive to Contextual Change. *J. Neurosci.* **2014**, *34*, 3056–3066. [CrossRef]
41. Hitti, F.L.; Siegelbaum, S.A. The hippocampal CA2 region is essential for social memory. *Nature* **2014**, *508*, 88–92. [CrossRef] [PubMed]
42. MacDonald, C.J.; Tonegawa, S. Crucial role for CA2 inputs in the sequential organization of CA1 time cells supporting memory. *Proc. Natl. Acad. Sci. USA* **2021**, *118*. [CrossRef]
43. McAllister, T.W. Neurobiological consequences of traumatic brain injury. *Dialogues Clin. Neurosci.* **2011**, *13*, 287. [CrossRef] [PubMed]
44. Vidovic, D.; Harris, L.; Harvey, T.J.; Heng, Y.H.E.; Smith, A.G.; Osinski, J.; Hughes, J.; Thomas, P.; Gronostajski, R.M.; Bailey, T.L.; et al. Expansion of the lateral ventricles and ependymal deficits underlie the hydrocephalus evident in mice lacking the transcription factor NFIX. *Brain Res.* **2015**, *1616*, 71–87. [CrossRef] [PubMed]
45. Park, R.; Moon, U.Y.; Park, J.Y.; Hughes, L.J.; Johnson, R.L.; Cho, S.-H.; Kim, S. Yap is required for ependymal integrity and is suppressed in LPA-induced hydrocephalus. *Nat. Commun.* **2016**, *7*, 10329. [CrossRef] [PubMed]



Review

# Morphological and Functional Changes of Roof Plate Cells in Spinal Cord Development

Takuma Shinozuka <sup>1,2,\*</sup>  and Shinji Takada <sup>1,2,3,\*</sup>

<sup>1</sup> Exploratory Research Center on Life and Living Systems, National Institutes of Natural Sciences, 5-1 Higashiyama, Myodaiji, Aichi, Okazaki 444-8787, Japan

<sup>2</sup> National Institute for Basic Biology, National Institutes of Natural Sciences, 5-1 Higashiyama, Myodaiji, Aichi, Okazaki 444-8787, Japan

<sup>3</sup> Department of Basic Biology, School of Life Science, The Graduate University for Advanced Studies (SOKENDAI), 5-1 Higashiyama, Myodaiji, Aichi, Okazaki 444-8787, Japan

\* Correspondence: shinozuk@nibb.ac.jp (T.S.); stakada@nibb.ac.jp (S.T.)

**Abstract:** The most dorsal region, or roof plate, is the dorsal organizing center of developing spinal cord. This region is also involved in development of neural crest cells, which are the source of migratory neural crest cells. During early development of the spinal cord, roof plate cells secrete signaling molecules, such as Wnt and BMP family proteins, which regulate development of neural crest cells and dorsal spinal cord. After the dorso-ventral pattern is established, spinal cord dynamically changes its morphology. With this morphological transformation, the lumen of the spinal cord gradually shrinks to form the central canal, a cavity filled with cerebrospinal fluid that is connected to the ventricular system of the brain. The dorsal half of the spinal cord is separated by a glial structure called the dorsal (or posterior) median septum. However, underlying mechanisms of such morphological transformation are just beginning to be understood. Recent studies reveal that roof plate cells dramatically stretch along the dorso-ventral axis, accompanied by reduction of the spinal cord lumen. During this stretching process, the tips of roof plate cells maintain contact with cells surrounding the shrinking lumen, eventually exposed to the inner surface of the central canal. Interestingly, Wnt expression remains in stretched roof plate cells and activates Wnt/ $\beta$ -catenin signaling in ependymal cells surrounding the central canal. Wnt/ $\beta$ -catenin signaling in ependymal cells promotes proliferation of neural progenitor and stem cells in embryonic and adult spinal cord. In this review, we focus on the role of the roof plate, especially that of Wnt ligands secreted by roof plate cells, in morphological changes occurring in the spinal cord.

**Citation:** Shinozuka, T.; Takada, S. Morphological and Functional Changes of Roof Plate Cells in Spinal Cord Development. *J. Dev. Biol.* **2021**, *9*, 30. <https://doi.org/10.3390/jdb9030030>

Academic Editors: Tsutomu Nohno and Hideyo Ohuchi

Received: 5 July 2021

Accepted: 28 July 2021

Published: 30 July 2021

**Keywords:** Wnt; roof plate; spinal cord; morphogenesis; central canal; dorsal collapse; dorsal median septum; neural crest

**Publisher's Note:** MDPI stays neutral with regard to jurisdictional claims in published maps and institutional affiliations.



**Copyright:** © 2021 by the authors. Licensee MDPI, Basel, Switzerland. This article is an open access article distributed under the terms and conditions of the Creative Commons Attribution (CC BY) license (<https://creativecommons.org/licenses/by/4.0/>).

## 1. Roof Plate Functions in the Early Developmental Stage of Spinal Cord

### 1.1. Generation of Trunk Neural Crest Cells

In the beginning of neural development, the neural plate gradually invaginates and its lateral edges are transformed into the neural fold. The appearance of the neural fold is probably the first morphological indication of the dorsal region of neural tissues. Then, the tips of the neural fold fuse, resulting in formation of the neural tube, which develops into the brain in the head and the spinal cord in the trunk. In the mouse, anterior neural tube is generated by this process, called primary neurulation (Figure 1). On the other hand, the posterior neural tube is formed by a process called secondary neurogenesis, in which the neural tube is formed from precursors in the tail bud, followed by condensation of the mesenchyme and subsequent epithelialization [1]. After these processes, neuroepithelial cells adjacent to the lumen proliferate rapidly and differentiate into several distinct types of neuronal and glial cells. Roof plate cells are located in the most dorsal part of developing



spinal cord and serve as the organizing center for surrounding neuroepithelial cells, promoting their proliferation and specification [2]. Prior to functioning as an organizing center, these cells give rise to neural crest cells, which migrate to many different tissues, where they give rise to neurons and glial cells of the sensory, sympathetic, and parasympathetic nervous systems, pigment-containing cells of the epidermis, and chromaffin cells of the adrenal gland [3–6]. Thus, cells in the roof plate, have markedly different roles and their behaviors are dynamic in early embryonic stages.

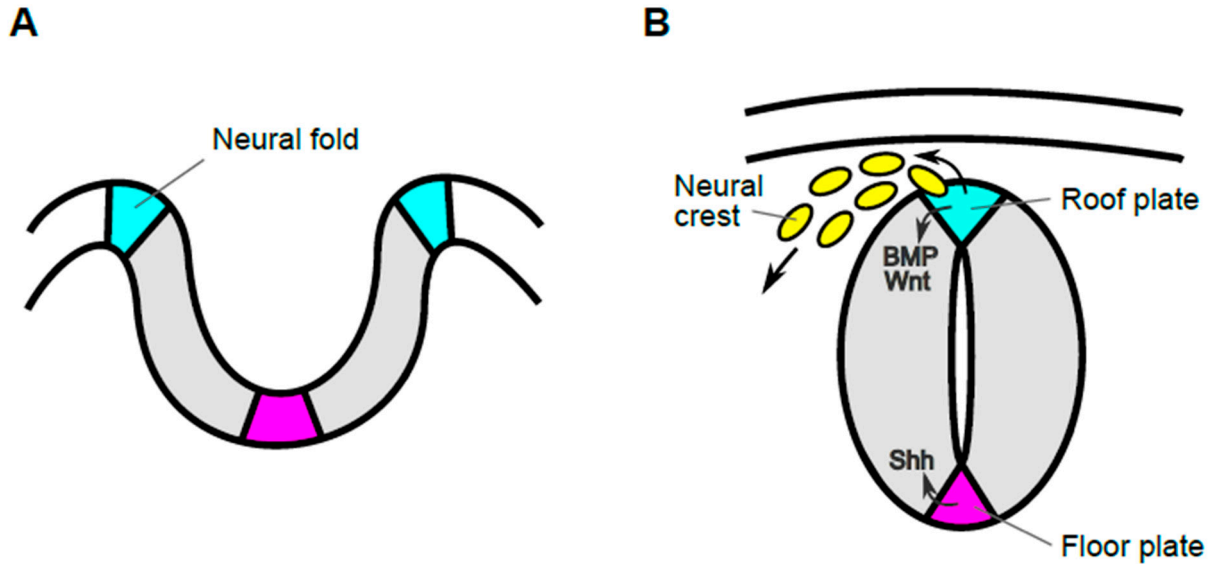


**Figure 1.** Transition in morphology of neural tissue and functions of cells in the most dorsal region during early developmental stages. Schematic images of transverse sections of developing spinal cord before (A) and after (B) closure of the neural tube during mouse development. The edge of the neural plate elevates and becomes the neural fold (cyan), from which neural crest cells are generated (A). Then, the lateral tips of the neural fold fuse, generating the neural tube (B). Cells in the most dorsal region of the neural tube, or roof plate (cyan), act as progenitors of migrating neural crest cells (yellow) and also as the organizing center for dorsal neuroepithelial cells. Roof plate cells secrete signaling molecules such as Wnt and BMP, which govern development of both neural crest and dorsal neuroepithelial cells. By contrast, cells in the most ventral region, the floor plate (magenta), act as the ventral organizer, by producing Shh.

During development of the neural tube, premigratory neural crest cells first exist in the neural fold and undergo delamination and epithelial-mesenchymal transition to become migratory neural crest cells [7]. However, the timing and mechanism of fate determination in these neural crest cells remains controversial. Lineage tracing analysis using *R26R-Confetti* mice revealed that the vast majority of individual premigratory and even migratory neural crest cells are multipotent. Furthermore, in some clones with labeled progeny cells among neural crest derivatives, labeled progeny cells are retained in the dorsal neural tube, suggesting an asymmetric cell division of premigratory neural crest cells in the dorsal neural tube [6]. By contrast, lineage tracing analysis using avian embryos after electroporation with GFP reporter showed that pre-migratory neural crest cells generate progeny in single, rather than multiple derivatives, in most cases where delaminated neural crest cells are labeled. In these cases, no labeled cells remained in the neural tube [8]. This result with avian embryos suggests that premigratory neural crest cells are a distinct population from cells that remain in the neural tube, such as roof plate cells, which act as the organizing center. In addition, this transition from neural crest to roof plate accompanied by loss of responsiveness to BMP signaling in dorsal spinal cord [8–10]. These discrepancies may be due to differences in labeling techniques, in the stage and location of labeling, or in mechanisms of lineage segregation between mammalian and avian systems.

During development of neural crest cells, cells in the most dorsal region of the spinal cord produce secreted ligands such as BMP and Wnt [2,11,12] (Figure 1B). Several lines of evidence indicate that Wnt ligands, which activate Wnt/ $\beta$ -catenin signaling, are required for generation of neural crest cells. In the spinal cord of mouse embryos, two Wnt ligands, *Wnt1* and *Wnt3a*, are specifically expressed in roof plate cells [13–15]. These Wnt ligands activate a common signaling pathway, the Wnt/ $\beta$ -catenin pathway, and are functionally redundant in the dorsal spinal cord. Thus, neither *Wnt1* nor *Wnt3a* single KO mutants show any obvious defects in dorsal spinal cord development, although *Wnt1* KO mutant impairs the development of midbrain and cerebellum and *Wnt3a* KO mutant exhibits severe truncation of axis elongation [14,16–18]. On the other hand, *Wnt1* and *Wnt3a* double-mutant embryos exhibit a reduction of neural crest cell number and a marked deficiency of neural crest derivatives [19]. Similarly, Wnt/ $\beta$ -catenin signaling can induce and is required for neural crest formation in other species [20–24].

In addition to formation of neural crest cells, Wnt/ $\beta$ -catenin signaling also promotes segregation of sub-lineages of neural crest cells [25–29]. For instance, conditional loss of function of  $\beta$ -catenin in the mouse roof plate reduces melanocytes and *Ngn2*-positive sensory lineage cells, resulting in impaired formation of neurons and glial cells in dorsal root ganglia (DRG) [26]. On the other hand, studies in which  $\beta$ -catenin is activated at different time points in neural crest differentiation suggest the importance of this signaling in determining the fate of the neural crest sub-lineage [27,29]. In zebrafish, studies of gain- and loss-of-function of Wnt/ $\beta$ -catenin signaling in pre-migratory cranial neural crest cells also indicate the importance of this signaling in determining the fate of the neural crest sub-lineage [25]. Furthermore, in addition to Wnt/ $\beta$ -catenin signaling, ligands of the BMP family are also involved in fate decision of neural crest cells. For instance, late emigrating neural crest cells in the roof plate are restricted to a sensory fate by *Gdf7* [30], and BMP2 antagonizes sensory specification induced by Wnt signaling [31].

### 1.2. Specification of Dorsal Interneurons

Direct evidence showing the requirement for roof plate cells in specification of dorsal neuroepithelial cells comes from genetic ablation of roof plate cells with *Gdf7-DTA*. Progenitors of dorsal interneurons are subclassified as dI1 to dI6, in dorsal-to-ventral order in developing spinal cord [32]. This ablation causes loss of progenitors of dorsal interneurons dI1–3 and compensatory occupation of a dorsal position by dI4–6 [33]. This specification, as well as proliferation of dorsal neuroepithelial cells, is regulated by roof plate-derived Wnt and BMP family proteins. For instance, *Wnt1* and *Wnt3a* double-mutant embryos exhibit impaired proliferation and specification of cells in the dorsal spinal cord [34]. A similar phenotype is also observed in mutant embryos in which components of the Wnt/ $\beta$ -catenin pathway, including *Wntless* and  *$\beta$ -catenin*, are impaired [35,36]. In addition, activation of Wnt/ $\beta$ -catenin signaling in developing spinal cord indicates that this signaling can regulate specification and proliferation of neuroepithelial cells [36–38]. In terms of Wnt-mediated proliferation, it has been proposed that several Wnt ligands expressed in the dorsal spinal cord generate a proliferation gradient along the dorso-ventral axis [39].

BMP family proteins, including BMP4, BMP6, BMP7, and *Gdf7*, are also expressed in the surface ectoderm and the dorsal spinal cord and are involved in differentiation of dorsal interneurons [40–44]. Manipulation of BMP signaling can promote differentiation of dorsal interneurons in vitro [45,46]. Genetic analyses with mutant embryos showed that *Gdf7* is required in formation of dI1 interneurons [42] and that *Bmp7* is similarly essential for several subtypes of dorsal interneurons [47]. In contrast, inhibitory Smad6 and Smad7 are expressed in the neural tube, restricting the action of BMP signaling in the dorsal neural tube [48]. *Bmp7* and *Gdf7* are also required for dI1 axon growth [49]. Since activation of Wnt/ $\beta$ -catenin signaling in roof plate induces expansion of BMP signaling activity in dorsal spinal cord [50], combinatorial Wnt and BMP signaling appears to regulate dorsal interneuron specification and proliferation. Moreover, recent study revealed that Notch signaling in dorsal neural tube is also required for roof plate and dI1 formation. Loss

of Notch function causes missing of roof plate and *dl1* with a compensatory expansion of *dl2* [51]. Taken together, there are several lines of evidence to show that signaling molecules secreted from roof plate cells are critical in neural crest formation and interneuron specification. On the other hand, there are few studies examining the role of roof plate-derived ligands in later developmental stages, as discussed below.

## 2. Morphological Transformation of the Spinal Cord and Central Canal Formation in Mouse Development

### 2.1. Morphological Transformation of the Spinal Cord

During development of spinal cord, its size and morphology change dramatically. Neuroepithelial cells proliferate and give rise to migrating cells that accumulate around the original layer of neuroepithelial, or neuroprogenitor, cells. This accumulation results in formation of the mantle zone and the layer of neuroprogenitor cells remaining along the lumen, which is now called the ventricular layer. Cells in the mantle zone differentiate into neurons and glia, and these neurons are interconnected and extend their axons to the lateral region of the spinal cord, known as the marginal zone [11]. The mantle zone, which will form the gray matter of the spinal cord, gradually becomes a butterfly-shaped structure, surrounded by the marginal zone, which will form the white matter (Figure 2C). The spinal cord, as well as the brain, is surrounded by three layers of meninges, the pia mater, the arachnoid mater, and the dura mater. As the spinal cord develops, all three layers are generated from a mesenchymal sheath on the surface of the developing spinal cord, called the primary meninx [52].

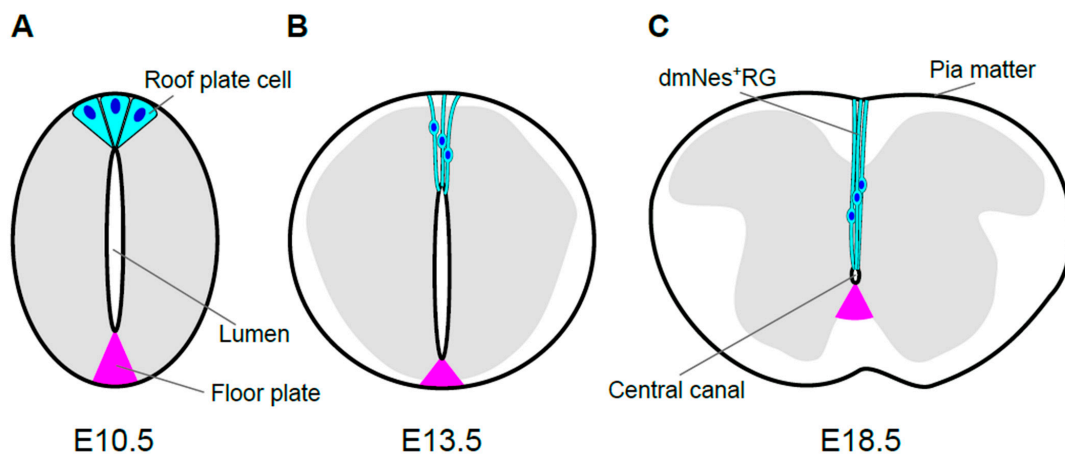


**Figure 2.** Morphological transformation of the mouse spinal cord. Schematic images of spinal cord morphology and roof plate shape are shown at E10.5 (A), E13.5 (B), and E18.5 (C) during mouse development. The gray matter of the spinal cord is shown in gray. Roof plate cells, or their descendants, and their nuclei are shown in cyan and blue, respectively. The size and morphology of spinal cord change dramatically during development. In accordance with these changes, morphology of roof plate cells also transforms. In mouse embryos, the apical sides of roof plate cells gradually constrict, such that roof plate cells assume a wedge-shaped form at E10.5 (A). Then, the lumen of the spinal cord shrinks gradually. The reduction of lumen size is caused by gradual attrition of neuroepithelial cells adjacent to roof plate cells. As a result, cell reduction from the surface of the lumen proceeds progressively in a dorsal-to-ventral manner known as dorsal collapse. Accompanying the dorsal collapse and reduction of the lumen, roof plate cells are stretched along the dorso-ventral axis and line up along the midline, resulting in morphological transformation. Compared to the dorsal side, reduction of the ventral ventricular zone and transformation of floor plate (magenta) are comparatively smaller (B). The stretched roof plate cells are also known as dorsomedial Nestin-positive radial glia (dmNes<sup>+</sup>RGs). At E18.5, the diameter of the lumen finally shrinks to roughly a few cell diameters, resulting in the central canal, a cavity filled with cerebrospinal fluid and connected to the ventricular system of the brain. Quiescent neural stem cells locate around the central canal. At this stage, roof plate cells (dmNes<sup>+</sup>RGs) are stretched, maintaining contact with the inner surface of the central canal and also with the pia mater, which covers the outer surface of the spinal cord (C).

## 2.2. Morphological Transformation of the Lumen

Contemporaneously with morphological transformation of the spinal cord, the lumen of the spinal cord, which is surrounded by the ventricular layer, gradually diminishes in size and finally becomes the central canal, a cavity filled with cerebrospinal fluid (CSF) that is connected to the ventricular system of the brain. In mouse embryos, this reduction starts on approximately embryonic day 13.5 (E13.5; Figure 2B). Prior to its reduction, the lumen extends over almost the entire dorsoventral axis of the spinal cord. The size of lumen, i.e., the dorso-ventral length of the ventricular layer, is dramatically reduced between E13.5 and E15.5. By E17.5 and E18.5, the diameter of the lumen has shrunk to roughly a few cell diameters, resulting in the central canal [53,54] (Figure 2).

The central canal is lined with the ependymal layer, which is composed of several distinct cell types, including ciliated ependymal cells, tanycytes (a subpopulation of radial glia), and CSF-contacting, neuron-like cells [55–58]. Although the functions of these cell types remain to be determined, some of them are likely responsible for homeostatic regulation of CSF in adults [59,60]. Moreover, the ependymal layer includes quiescent stem cells, which generate progeny that undergo glial fates after injury to the spinal cord [55,61,62].

Of note, at the dorsal pole of the central canal, neuron-like cells with extensive projections are observed. These cells express Nestin, and their projections extend from the apical side facing the central canal toward the superficial regions of the spinal cord, as far as the meninges [63–65]. These cells are referred to as dorsal midline Nestin<sup>(+)</sup> radial glia (dmNes<sup>+</sup>RG) [65].

## 2.3. Origin of Ependymal Layer

Lineage-tracing analyses reveal that most cells comprising the ependymal layer are from the ventral ventricular zone, especially in the subdomains called p2 and pMN [66–69]. Conditional knock-out of components of Shh signaling, including *Shh* and *Smo*, reveals that Shh signaling is required for formation of the ependymal zone [69]. By contrast, dmNes<sup>+</sup>RG cells which are derived from the roof plate and cells at the ventral pole of the ependymal layer are from the floor plate [54,70]. Thus, cells forming the ependymal layer are heterogeneous in origin and reduction of the lumen does not progress proportionally along the dorso-ventral axis.

## 2.4. Regulatory Mechanisms Governing Lumen Reduction

Reduction of lumen size is caused by gradual attrition of the neuroepithelial cell population in the ventricular zone (Figure 2). Importantly, this process is promoted by a morphological phenomenon known as dorsal collapse [54,65]. In dorsal collapse, cell reduction proceeds progressively in a dorsal-to-ventral manner in the ventricular zone. In this process, cells adjacent to the dorsal midline down-regulate apical polarity proteins and delaminate in a stepwise manner. The loss of polarity and delamination can be promoted by a secreted form of Crumbs2 produced by dmNes<sup>+</sup>RGs [65]. In addition, loss of apical polarity protein, such as *pard6γb*, is involved in this process, because loss of *pard6γb* disrupts dorsal collapse and lumen reduction in zebrafish [71,72]. Moreover, ventricular layer attrition is accompanied by reduction of cell proliferation in the ventricular layer but not apoptosis [54]. Compared to the dorsal side, reduction of the ventral ventricular zone is comparatively smaller, but apparent over time. This ventral reduction may be pronounced by migration of glial cells differentiated from neuroepithelial cells in the ventricular layer [54].

## 3. Development of Roof Plate Cells in Formation of the Central Canal

### 3.1. Formation of dmNes<sup>+</sup>RGs

As mentioned above, roof plate and floor plate cells remain at the dorsal and ventral poles of the ependymal layer, respectively. Labeling of zebrafish roof plate cells, as well as tracing of roof plate cells using mouse embryos carrying *Wnt1-creERT*, revealed that

roof plate cells are actually elongated along the dorso-ventral axis and transformed into dmNes<sup>+</sup>RGs, accompanying the reduction of the lumen [35,72]. Low-frequency labeling of roof plate cells, which enables the morphology of each cell to be distinguished, revealed that dmNes<sup>+</sup>RGs contact the surface of the ependymal layer. dmNes<sup>+</sup>RGs also maintain contact with the outer surface of the spinal cord, the pia mater. Thus, it seems probable that roof plate cells are stretched, maintaining contact with the central canal and the pia mater (Figure 2C). dmNes<sup>+</sup>RGs eventually become part of the dorsal (or posterior) median septum, a thin, dense septum dividing the dorsal side of the spinal cord [35]. In contrast, floor plate cells do not exhibit dynamic morphological changes (Figure 2). Rather, only a subset of floor plate cells is retained around the central canal, whereas other floor plate cells separate from the ependymal layer during reduction of the lumen [54].

### 3.2. Morphology and Roles of dmNes<sup>+</sup>RGs

Along the stretching of dmNes<sup>+</sup>RGs, cytoskeletal structures are well developed. Electron microscopic analysis revealed enrichment of intermediate filament structure during this process [53,73]. This is consistent with enrichment of Nestin, which is a component of intermediate filaments, and directional organization of actin filaments in this process [35,63]. In zebrafish, inhibition of Zic6 or Rock impairs the stretching morphogenesis of roof plate with disruption of the actin cytoskeleton [72,74]. Thus, these cytoskeletal structures apparently contribute to formation of the physically robust structure of the dorsal median septum.

In the dorsal median septum, dmNes<sup>+</sup>RGs seem to act as a physical and molecular barrier, preventing decussation of developing long tracts of commissural axons [75,76]. In addition, dmNes<sup>+</sup>RGs apparently serve several different functions. For instance, *dreher* (*Lmx1a*-deficient) mice, which impair roof plate formation, show that dmNes<sup>+</sup>RGs regulate growth of long-range dorsal column axons [77,78]. Furthermore, as described below, dmNes<sup>+</sup>RGs promote proliferation of ependymal cells by producing Wnt ligands [35,70]. Thus, in addition to serving as a signaling center in early spinal cord development, roof plate has additional roles in later spinal cord development [10].

## 4. Wnt Signaling in Morphological Transformation of Roof Plate Cells

### 4.1. Expression of Wnt Ligands and Activation of Wnt Signaling

As described above, *Wnt1* and *Wnt3a*, which are secreted by roof plate cells, participate in development of neural crest cells and dorsal interneurons [19,34]. Whereas expression of *Wnt1* and *Wnt3a* mRNA is detected in the roof plate of developing mouse spinal cord until E12.5 [15,79], using in situ hybridization with a digoxigenin-based probe, it had been difficult to judge whether expression of these Wnt genes is maintained after E12.5, because roof plate cells become long and thin. However, recent immunostaining analysis revealed that expression of both *Wnt1* and *Wnt3a* proteins remains in elongating roof plate cells, dmNes<sup>+</sup>RGs, after E13.5 [35]. This persistent expression was also confirmed with knock-in mouse embryos in which endogenous *Wnt3a* is replaced by *egfp-Wnt3a*. Consistent with Wnt expression in dmNes<sup>+</sup>RGs, activation of Wnt/ $\beta$ -catenin signaling is evident in dmNes<sup>+</sup>RGs [35,70].

### 4.2. Functions of Wnt Ligands Secreted by dmNes<sup>+</sup>RGs

Since most *Wnt1*- and *Wnt3a*-double mutants die before E12.5 [19], genetic studies of *Wnt1*- and *Wnt3a*-deficient mutant mouse embryos yield no information regarding their roles in later stages. Thus, the function of Wnt signaling in the morphological transformation from roof plate cell to dmNes<sup>+</sup>RG was investigated by generating roof plate-specific conditional knock-out of the *Wls/Evi/Sprinter* gene, which is specifically required for secretion of Wnt proteins [80–82]. In normal embryos, prior to elongation of the apical processes of roof plate cells, the apical surfaces of roof plate cells are constricted, causing cell shape to become wedge-like at E10.5 (Figure 2A). At E13.5, when reduction of the lumen starts, apical processes of roof plate cells begin to elongate in parallel in a dorsoventral direc-

tion. Subsequently, these processes continue to elongate along the midline, accompanying reduction of the lumen, and nuclei of these cells become aligned on the midline [35,54] (Figure 2B,C). In *Wls* cKO embryos, the apical end of each process is also attached to the dorsal pole of the central canal, but these processes are not aligned along the midline. Rather, they extend laterally, slightly away from the midline. As a result, dorso-ventral nuclear alignment is impaired in mutant embryos. In addition, the bundle of processes of dmNes<sup>+</sup>RGs appears thinner and is frequently branched in mutant embryos, although the cytoskeletons are properly oriented [35]. These data suggest that mechanical tension in roof plate cells regulated by Wnt signaling may control the coordinated rearrangement of roof plate. However, since the number of roof plate cells is slightly increased in *Wls* cKO embryos at E13.5, alternative possibility that the rearrangement of roof plate cells is disrupted by crowding of roof plate cells cannot be excluded. Thus, Wnt secreted by roof plate cells is required for the change in morphology of these cells along the midline (Figure 3B).

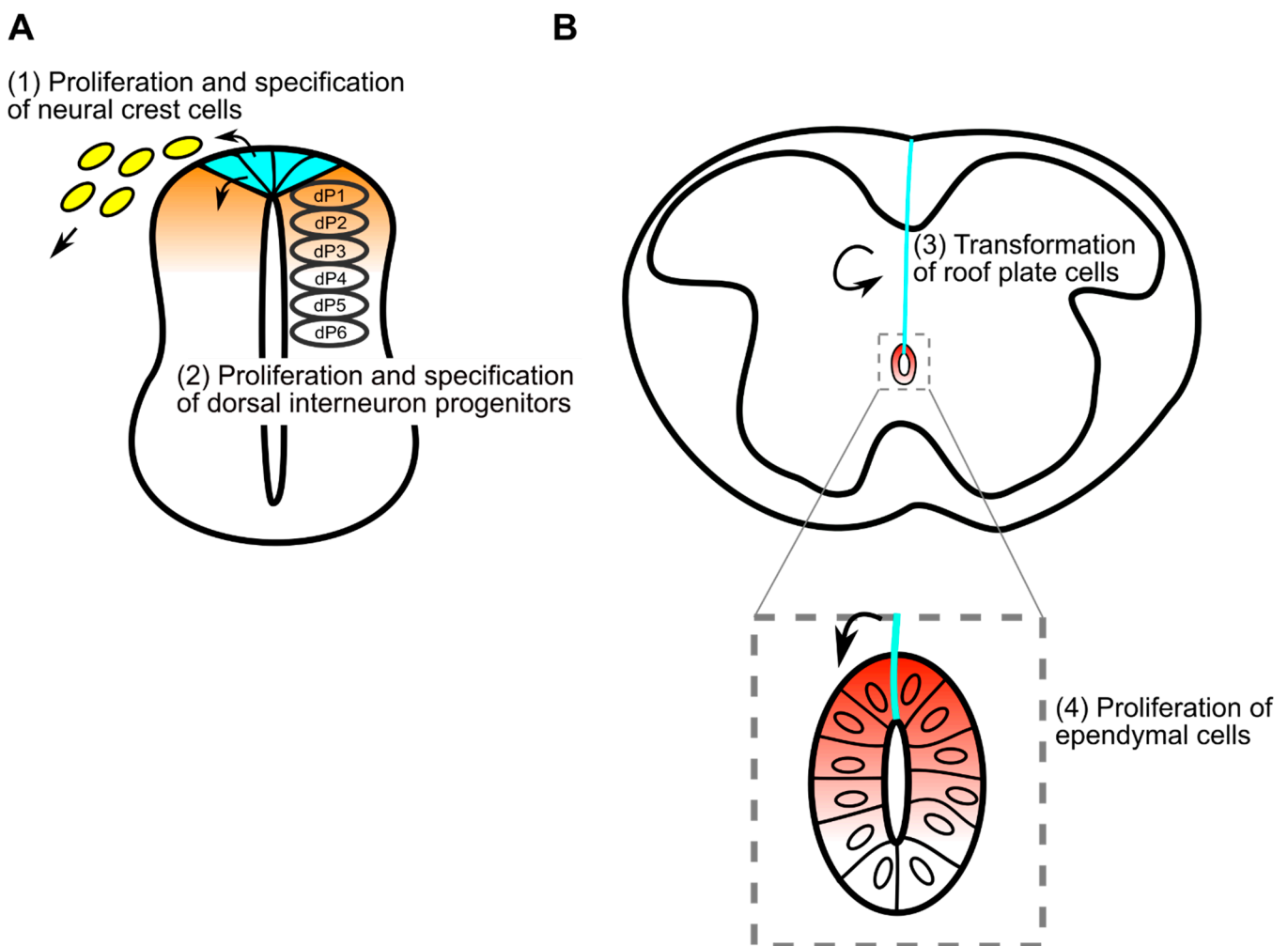


**Figure 3.** Multiple functions of Wnt ligands secreted from roof plate cells have multiple functions during spinal cord development. **(A)** Before stretching, roof plate cells exhibit a wedge-shaped form (cyan) and act as a source of neural crest cells (yellow), forming the dorsal organizing center. At this stage, Wnt signaling in roof plate regulates formation and fate determination of neural crest cells (1), as well as proliferation and specification of dorsal interneuron progenitors (2). In the dorsal spinal cord, Wnt signaling is likely to be activated in a gradual manner (orange). **(B)** After stretching, roof plate cells extend long processes (cyan) in contact with the central canal and pial surface. During this later stage, Wnt signaling in stretching roof plate cells regulates transformation of roof plate cells themselves (3) and proliferation of ependymal cells (4). In ependymal cells, Wnt signaling is likely to be activated in a gradual manner (red).

## 5. Wnt Signaling in Development of Cells Surrounding the Central Canal

### 5.1. Wnt Signaling in Ependymal Cells

In the ependymal layer surrounding the central canal, Wnt/ $\beta$ -catenin signaling is activated [35,70]. This activation depends partly on Wnt secretion from dmNes<sup>+</sup>RGs, apical ends of which face the dorsal surface of the central canal. Actually, embryos in which *Wls* function is defective, specifically in stretched dmNes<sup>+</sup>RGs, exhibit a significant reduction in Wnt-active cells among ependymal cells at E15.5 and E18.5. Since this reduction is more severe in dorsal ependymal layer zone cells, it seems plausible that Wnt proteins from dmNes<sup>+</sup>RGs are specifically required for dorsal activation of Wnt/ $\beta$ -catenin signaling [35].

On the other hand, the Gene Expression Nervous System Atlas (GENSAT) Project revealed that several Wnt ligands, including *Wnt2b*, *Wnt3*, *Wnt7a* and *Wnt8b*, are expressed in spinal cord, except dmNes<sup>+</sup>RGs at E15.5 [83]. Thus, it also seems possible that Wnt proteins produced by some other cells, other than descendants of roof plate cells, are involved in activation of Wnt signaling in ependymal cells. In addition, since it was reported that a few Wnt-positive ependymal cells originated from the roof plate, it is also possible that these cells still maintain Wnt activity in the ependymal layer [70]. Actually, expression of *Wnt1* and *Wnt3a* is detectable in the ependymal layer shortly after birth, consistent with activation of Wnt/ $\beta$ -catenin signaling. In adults, many Wnt ligands, including *Wnt1*, *Wnt3a*, *Wnt5a* and *Wnt11*, are expressed in ependymal cells and expression of *Axin2*, a downstream target of Wnt/ $\beta$ -catenin signaling, is detected, indicating activation of Wnt/ $\beta$ -catenin signaling in these cells [70].

### 5.2. Proliferation of Ependymal Cells

In the spinal cord, a small number of ependymal cells constitutively proliferate [84], and these cells are concentrated dorsally [56]. Since Wnt/ $\beta$ -catenin regulates proliferation of neural progenitor/stem cells in the brain [85–87], it seems probable that this signaling is also involved in regulation of progenitor/stem cells in the spinal cord. A recent study showed that Wnt signaling actually appears to be involved in promoting proliferation of ependymal cells [35,70]. At E18.5, *Wls* cKO mutant embryos exhibited significant decreases in the frequency of Ki67-positive proliferating cells in the ependymal layer. Furthermore, this defect is more severe in the dorsal half, suggesting that Wnt secretion by dmNes<sup>+</sup>RGs is required for normal proliferation of ependymal cells in embryos [35] (Figure 3B).

### 5.3. Adult Spinal Cord

In adult mice, neurogenesis hardly occurs in the spinal cord. However, after injury to the spinal cord, ependymal cells proliferate and generate progeny that undergo multiple fates, suggesting that ependymal cells exhibit latent neural stem cell properties [55,61]. This injury-induced proliferation of ependymal cells is suppressed in *Wls* cKO mice, and as in embryos, cells in the dorsal half of the ependymal layer exhibit more severe defects [35]. Thus, Wnt secretion by roof plate cells is also required for proliferation of ependymal cells after injury to the spinal cord.

Moreover, secretion of Wnt and expression of  $\beta$ -catenin in ependymal cells is required for proliferation of ependymal cells in postnatal and adult mice. Disruption of  $\beta$ -catenin or *Wls* in *Axin2*-expressing ependymal cells in adult mice significantly reduces the frequency of Ki67-positive proliferating cells in the ependymal layer [70]. Thus, activation of Wnt/ $\beta$ -catenin signaling and secretion of Wnt ligands is required for proliferation of ependymal cells in adult mouse spinal cord.

## 6. Conclusions and Future Perspectives

In conclusion, in early development of the spinal cord, the most dorsal cells act as a source of neural crest cells and constitute the dorsal organizing center, the roof plate, that regulates interneuron specification and proliferation. These functions are regulated by Wnt signaling in roof plate (Figure 3A). After neural specification, roof plate cells transform to dmNes<sup>+</sup>RGs, controlled by Wnt/ $\beta$ -catenin signaling. Moreover, Wnt ligands

are still expressed in stretched roof plate cells and activate Wnt/ $\beta$ -catenin signaling in the ependymal layer (Figure 3B). Activation of Wnt/ $\beta$ -catenin signaling in ependymal cells promotes proliferation of neural progenitor and stem cells in embryonic and adult spinal cord. Thus, during spinal cord development, roof plate cells are a source of Wnt ligands and activate Wnt/ $\beta$ -catenin in themselves, as well as in surrounding cells that dramatically change morphology and function.

Despite the function of roof plate cells in each stage of spinal cord development, regulatory mechanism of morphological change of roof plate cells by Wnt signaling still remain unclear. An interesting question for future studies is whether roof plate cells elongate their processes or are pulled by surrounding cells during transformation of roof plate cells. Given that the cytoskeleton regulates transformation of roof plate cells, a remaining challenge is to understand the mechanism by which Wnt signaling controls the cytoskeleton. In general, *Wnt1* and *Wnt3a* act as ligands to activate Wnt/ $\beta$ -catenin signaling, which directly regulates transcription but not cytoskeletal reorganization. Thus, understanding of the regulatory mechanism of roof plate transformation may provide a new insight into the Wnt signaling pathway in cell biology.

In the adult spinal cord, Wnt/ $\beta$ -catenin signaling promotes cell proliferation in the ependymal layer in normal condition and after spinal cord injury. Pool of quiescent neural progenitor and stem cells in ependymal layer contribute to the regeneration in response to spinal cord injury. However, it remains unclear which type of the cells proliferate in ependymal layer in a Wnt/ $\beta$ -catenin signaling dependent manner and contribute to the regeneration after spinal cord injury. Elucidating the mechanism of cell proliferation and differentiation in the ependymal layer regulated by Wnt/ $\beta$ -catenin signaling may help to understand the mechanism of regeneration after spinal cord injury.

**Author Contributions:** T.S. and S.T. contributed to the manuscript. Both authors have read and agreed to the published version of the manuscript.

**Funding:** This work was supported in part by a Grant-in-Aid for Scientific Research from the Japan Society for the Promotion of Science (JSPS) to T.S. (20K15809) and S.T. (17H05782, 18H02454, 19H04797).

**Institutional Review Board Statement:** Not applicable.

**Informed Consent Statement:** Not applicable.

**Data Availability Statement:** Not applicable.

**Acknowledgments:** We thank all members of S.T.'s laboratory for their helpful discussions.

**Conflicts of Interest:** The authors declare no conflict of interest.

## References

1. Copp, A.J.; Greene, N.D.E.; Murdoch, J.N. The Genetic Basis of Mammalian Neurulation. *Nat. Rev. Genet.* **2003**, *4*, 784–793. [CrossRef]
2. Chizhikov, V.V.; Millen, K.J. Mechanisms of Roof Plate Formation in the Vertebrate CNS. *Nat. Rev. Neurosci.* **2004**, *5*, 808–812. [CrossRef] [PubMed]
3. Serbedzija, G.N.; Fraser, S.E.; Bronner-Fraser, M. Pathways of Trunk Neural Crest Cell Migration in the Mouse Embryo as Revealed by Vital Dye Labelling. *Development* **1990**, *108*, 605–612. [CrossRef] [PubMed]
4. Serbedzija, G.N.; Bronner-Fraser, M.; Fraser, S.E. Developmental Potential of Trunk Neural Crest Cells in the Mouse. *Development* **1994**, *120*, 1709–1718. [CrossRef] [PubMed]
5. Wilson, Y.M.; Richards, K.L.; Ford-Perriss, M.L.; Panthier, J.-J.; Murphy, M. Neural Crest Cell Lineage Segregation in the Mouse Neural Tube. *Development* **2004**, *131*, 6153–6162. [CrossRef] [PubMed]
6. Baggiolini, A.; Varum, S.; Mateos, J.M.; Bettosini, D.; John, N.; Bonalli, M.; Ziegler, U.; Dimou, L.; Clevers, H.; Furrer, R.; et al. Premigratory and Migratory Neural Crest Cells Are Multipotent In Vivo. *Cell Stem Cell* **2015**, *16*, 314–322. [CrossRef]
7. Martik, M.L.; Bronner, M.E. Regulatory Logic Underlying Diversification of the Neural Crest. *Trends Genet.* **2017**, *33*, 715–727. [CrossRef]
8. Krispin, S.; Nitzan, E.; Kassem, Y.; Kalcheim, C. Evidence for a Dynamic Spatiotemporal Fate Map and Early Fate Restrictions of Premigratory Avian Neural Crest. *Development* **2010**, *137*, 585–595. [CrossRef]



9. Nitzan, E.; Avraham, O.; Kahane, N.; Ofek, S.; Kumar, D.; Kalcheim, C. Dynamics of BMP and Hes1/Hairy1 Signaling in the Dorsal Neural Tube Underlies the Transition from Neural Crest to Definitive Roof Plate. *BMC Biol.* **2016**, *14*, 23. [CrossRef]
10. Rekler, D.; Kalcheim, C. From Neural Crest to Definitive Roof Plate: The Dynamic Behavior of the Dorsal Neural Tube. *Int. J. Mol. Sci.* **2021**, *22*, 3911. [CrossRef]
11. Caspary, T.; Anderson, K.V. Patterning Cell Types in the Dorsal Spinal Cord: What the Mouse Mutants Say. *Nat. Rev. Neurosci.* **2003**, *4*, 289–297. [CrossRef] [PubMed]
12. Chizhikov, V.V.; Millen, K.J. Roof Plate-Dependent Patterning of the Vertebrate Dorsal Central Nervous System. *Dev. Biol.* **2005**, *277*, 287–295. [CrossRef] [PubMed]
13. Wilkinson, D.G.; Bailes, J.A.; McMahon, A.P. Expression of the Proto-Oncogene Int-1 Is Restricted to Specific Neural Cells in the Developing Mouse Embryo. *Cell* **1987**, *50*, 79–88. [CrossRef]
14. McMahon, A.P.; Joyner, A.L.; Bradley, A.; McMahon, J.A. The Midbrain-Hindbrain Phenotype of Wnt-1-/Wnt-1- Mice Results from Stepwise Deletion of Engrailed-Expressing Cells by 9.5 Days Postcoitum. *Cell* **1992**, *69*, 581–595. [CrossRef]
15. Parr, B.A.; Shea, M.J.; Vassileva, G.; McMahon, A.P. Mouse Wnt Genes Exhibit Discrete Domains of Expression in the Early Embryonic CNS and Limb Buds. *Development* **1993**, *119*, 247–261. [CrossRef]
16. McMahon, A.P.; Bradley, A. The Wnt-1 (Int-1) Proto-Oncogene Is Required for Development of a Large Region of the Mouse Brain. *Cell* **1990**, *62*, 1073–1085. [CrossRef]
17. Thomas, K.R.; Capocchi, M.R. Targeted Disruption of the Murine Int-1 Proto-Oncogene Resulting in Severe Abnormalities in Midbrain and Cerebellar Development. *Nature* **1990**, *346*, 847–850. [CrossRef]
18. Takada, S.; Stark, K.L.; Shea, M.J.; Vassileva, G.; McMahon, J.A.; McMahon, A.P. Wnt-3a Regulates Somite and Tailbud Formation in the Mouse Embryo. *Genes. Dev.* **1994**, *8*, 174–189. [CrossRef]
19. Ikeya, M.; Lee, S.M.K.; Johnson, J.E.; McMahon, A.P.; Takada, S. Wnt Signalling Required for Expansion of Neural Crest and CNS Progenitors. *Nature* **1997**, *389*, 966–970. [CrossRef]
20. LaBonne, C.; Bronner-Fraser, M. Neural Crest Induction in Xenopus: Evidence for a Two-Signal Model. *Development* **1998**, *125*, 2403–2414. [CrossRef]
21. Deardorff, M.A.; Tan, C.; Saint-Jeannet, J.P.; Klein, P.S. A Role for Frizzled 3 in Neural Crest Development. *Development* **2001**, *128*, 3655–3663. [CrossRef]
22. García-Castro, M.I.; Marcelle, C.; Bronner-Fraser, M. Ectodermal Wnt Function as a Neural Crest Inducer. *Science* **2002**, *297*, 848–851.
23. Wu, J.; Yang, J.; Klein, P.S. Neural Crest Induction by the Canonical Wnt Pathway Can Be Dissociated from Anterior–Posterior Neural Patterning in Xenopus. *Dev. Biol.* **2005**, *279*, 220–232. [CrossRef]
24. Hassler, C.; Cruciat, C.-M.; Huang, Y.-L.; Kuriyama, S.; Mayor, R.; Niehrs, C. Kremen Is Required for Neural Crest Induction in Xenopus and Promotes LRP6-Mediated Wnt Signaling. *Development* **2007**, *134*, 4255–4263. [CrossRef]
25. Dorsky, R.I.; Moon, R.T.; Raible, D.W. Control of Neural Crest Cell Fate by the Wnt Signalling Pathway. *Nature* **1998**, *396*, 370–373. [CrossRef] [PubMed]
26. Hari, L.; Brault, V.; Kléber, M.; Lee, H.-Y.; Ille, F.; Leimeroth, R.; Paratore, C.; Suter, U.; Kemler, R.; Sommer, L. Lineage-Specific Requirements of Beta-Catenin in Neural Crest Development. *J. Cell Biol.* **2002**, *159*, 867–880. [CrossRef] [PubMed]
27. Lee, H.-Y.; Kléber, M.; Hari, L.; Brault, V.; Suter, U.; Taketo, M.M.; Kemler, R.; Sommer, L. Instructive Role of Wnt/Beta-Catenin in Sensory Fate Specification in Neural Crest Stem Cells. *Science* **2004**, *303*, 1020–1023. [CrossRef]
28. Sommer, L. Generation of Melanocytes from Neural Crest Cells: Generation of Melanocytes from Neural Crest Cells. *Pigment Cell Melanoma Res.* **2011**, *24*, 411–421. [CrossRef]
29. Hari, L.; Miescher, I.; Shakhova, O.; Suter, U.; Chin, L.; Taketo, M.; Richardson, W.D.; Kessar, N.; Sommer, L. Temporal Control of Neural Crest Lineage Generation by Wnt/ $\beta$ -Catenin Signaling. *Development* **2012**, *139*, 2107–2117. [CrossRef] [PubMed]
30. Lo, L.; Dormand, E.L.; Anderson, D.J. Late-Emigrating Neural Crest Cells in the Roof Plate Are Restricted to a Sensory Fate by GDF7. *Proc. Natl. Acad. Sci. USA* **2005**, *102*, 7192–7197. [CrossRef]
31. Kléber, M.; Lee, H.-Y.; Wurdak, H.; Buchstaller, J.; Riccomagno, M.M.; Ittner, L.M.; Suter, U.; Epstein, D.J.; Sommer, L. Neural Crest Stem Cell Maintenance by Combinatorial Wnt and BMP Signaling. *J. Cell Biol.* **2005**, *169*, 309–320. [CrossRef] [PubMed]
32. Helms, A.W.; Johnson, J.E. Specification of Dorsal Spinal Cord Interneurons. *Curr. Opin. Neurobiol.* **2003**, *13*, 42–49. [CrossRef]
33. Lee, K.J.; Dietrich, P.; Jessell, T.M. Genetic Ablation Reveals That the Roof Plate Is Essential for Dorsal Interneuron Specification. *Nature* **2000**, *403*, 734–740. [CrossRef]
34. Muroyama, Y.; Fujihara, M.; Ikeya, M.; Kondoh, H.; Takada, S. Wnt Signaling Plays an Essential Role in Neuronal Specification of the Dorsal Spinal Cord. *Genes Dev.* **2002**, *16*, 548–553. [CrossRef]
35. Shinozuka, T.; Takada, R.; Yoshida, S.; Yonemura, S.; Takada, S. Wnt Produced by Stretched Roof-Plate Cells Is Required for the Promotion of Cell Proliferation around the Central Canal of the Spinal Cord. *Development* **2019**, *146*, dev159343. [CrossRef]
36. Zechner, D.; Müller, T.; Wende, H.; Walther, I.; Taketo, M.M.; Crenshaw, E.B.; Treier, M.; Birchmeier, W.; Birchmeier, C. Bmp and Wnt/ $\beta$ -Catenin Signals Control Expression of the Transcription Factor Olig3 and the Specification of Spinal Cord Neurons. *Dev. Biol.* **2007**, *303*, 181–190. [CrossRef]
37. Dickinson, M.E.; Krumlauf, R.; McMahon, A.P. Evidence for a Mitogenic Effect of Wnt-1 in the Developing Mammalian Central Nervous System. *Development* **1994**, *120*, 1453–1471. [CrossRef] [PubMed]

38. Grigoryan, T.; Wend, P.; Klaus, A.; Birchmeier, W. Deciphering the Function of Canonical Wnt Signals in Development and Disease: Conditional Loss- and Gain-of-Function Mutations of Beta-Catenin in Mice. *Genes Dev.* **2008**, *22*, 2308–2341. [CrossRef]
39. Megason, S.G.; McMahon, A.P. A Mitogen Gradient of Dorsal Midline Wnts Organizes Growth in the CNS. *Development* **2002**, *129*, 2087–2098. [CrossRef] [PubMed]
40. Winnier, G.; Blessing, M.; Labosky, P.A.; Hogan, B.L. Bone Morphogenetic Protein-4 Is Required for Mesoderm Formation and Patterning in the Mouse. *Genes Dev.* **1995**, *9*, 2105–2116. [CrossRef] [PubMed]
41. Dudley, A.T.; Robertson, E.J. Overlapping Expression Domains of Bone Morphogenetic Protein Family Members Potentially Account for Limited Tissue Defects in BMP7 Deficient Embryos. *Dev. Dyn.* **1997**, *208*, 349–362. [CrossRef]
42. Lee, K.J.; Mendelsohn, M.; Jessell, T.M. Neuronal Patterning by BMPs: A Requirement for GDF7 in the Generation of a Discrete Class of Commissural Interneurons in the Mouse Spinal Cord. *Genes Dev.* **1998**, *12*, 3394–3407. [CrossRef]
43. Hu, Q.; Ueno, N.; Behringer, R.R. Restriction of BMP4 Activity Domains in the Developing Neural Tube of the Mouse Embryo. *EMBO Rep.* **2004**, *5*, 734–739. [CrossRef] [PubMed]
44. Le Dréau, G.; Martí, E. The Multiple Activities of BMPs during Spinal Cord Development. *Cell. Mol. Life Sci.* **2013**, *70*, 4293–4305. [CrossRef]
45. Liem, K.F.; Tremml, G.; Roelink, H.; Jessell, T.M. Dorsal Differentiation of Neural Plate Cells Induced by BMP-Mediated Signals from Epidermal Ectoderm. *Cell* **1995**, *82*, 969–979. [CrossRef]
46. Liem, K.F.; Tremml, G.; Jessell, T.M. A Role for the Roof Plate and Its Resident TGFbeta-Related Proteins in Neuronal Patterning in the Dorsal Spinal Cord. *Cell* **1997**, *91*, 127–138. [CrossRef]
47. Le Dréau, G.; Garcia-Campmany, L.; Rabadán, M.A.; Ferronha, T.; Tozer, S.; Briscoe, J.; Martí, E. Canonical BMP7 Activity Is Required for the Generation of Discrete Neuronal Populations in the Dorsal Spinal Cord. *Development* **2012**, *139*, 259–268. [CrossRef]
48. Hazen, V.M.; Phan, K.D.; Hudiburgh, S.; Butler, S.J. Inhibitory Smads Differentially Regulate Cell Fate Specification and Axon Dynamics in the Dorsal Spinal Cord. *Dev. Biol.* **2011**, *356*, 566–575. [CrossRef]
49. Butler, S.J.; Dodd, J. A Role for BMP Heterodimers in Roof Plate-Mediated Repulsion of Commissural Axons. *Neuron* **2003**, *38*, 389–401. [CrossRef]
50. Ille, F.; Atanasoski, S.; Falk, S.; Ittner, L.M.; Märki, D.; Büchmann-Møller, S.; Wurdak, H.; Suter, U.; Taketo, M.M.; Sommer, L. Wnt/BMP Signal Integration Regulates the Balance between Proliferation and Differentiation of Neuroepithelial Cells in the Dorsal Spinal Cord. *Dev. Biol.* **2007**, *304*, 394–408. [CrossRef]
51. Ofek, S.; Wiszniak, S.; Kagan, S.; Tondl, M.; Schwarz, Q.; Kalcheim, C. Notch Signaling Is a Critical Initiator of Roof Plate Formation as Revealed by the Use of RNA Profiling of the Dorsal Neural Tube. *BMC Biol.* **2021**, *19*, 84. [CrossRef] [PubMed]
52. Dasgupta, K.; Jeong, J. Developmental Biology of the Meninges. *Genesis* **2019**, *57*, e23288. [CrossRef] [PubMed]
53. Sturrock, R.R. An Electron Microscopic Study of the Development of the Ependyma of the Central Canal of the Mouse Spinal Cord. *J. Anat.* **1981**, *132*, 119–136.
54. Cañizares, M.A.; Albors, A.R.; Singer, G.; Suttie, N.; Gorkic, M.; Felts, P.; Storey, K.G. Multiple Steps Characterise Ventricular Layer Attrition to Form the Ependymal Cell Lining of the Adult Mouse Spinal Cord Central Canal. *J. Anat.* **2020**, *236*, 334–350. [CrossRef] [PubMed]
55. Meletis, K.; Barnabé-Heider, F.; Carlén, M.; Evergren, E.; Tomilin, N.; Shupliakov, O.; Frisén, J. Spinal Cord Injury Reveals Multilineage Differentiation of Ependymal Cells. *PLoS Biol.* **2008**, *6*, e182. [CrossRef] [PubMed]
56. Hamilton, L.K.; Truong, M.K.V.; Bednarczyk, M.R.; Aumont, A.; Fernandes, K.J.L. Cellular Organization of the Central Canal Ependymal Zone, a Niche of Latent Neural Stem Cells in the Adult Mammalian Spinal Cord. *Neuroscience* **2009**, *164*, 1044–1056. [CrossRef] [PubMed]
57. Sabourin, J.-C.; Ackema, K.B.; Ohayon, D.; Guichet, P.-O.; Perrin, F.E.; Garces, A.; Ripoll, C.; Charité, J.; Simonneau, L.; Kettenmann, H.; et al. A Mesenchymal-like ZEB1(+) Niche Harbors Dorsal Radial Glial Fibrillary Acidic Protein-Positive Stem Cells in the Spinal Cord. *Stem Cells* **2009**, *27*, 2722–2733. [CrossRef] [PubMed]
58. Hugnot, J.P.; Franzen, R. The Spinal Cord Ependymal Region: A Stem Cell Niche in the Caudal Central Nervous System. *Front. Biosci.* **2011**, *16*, 1044–1059. [CrossRef] [PubMed]
59. Del Bigio, M.R. The Ependyma: A Protective Barrier between Brain and Cerebrospinal Fluid. *Glia* **1995**, *14*, 1–13. [CrossRef] [PubMed]
60. Bruni, J.E. Ependymal Development, Proliferation, and Functions: A Review. *Microsc. Res. Tech.* **1998**, *41*, 2–13. [CrossRef]
61. Johansson, C.B.; Momma, S.; Clarke, D.L.; Risling, M.; Lendahl, U.; Frisén, J. Identification of a Neural Stem Cell in the Adult Mammalian Central Nervous System. *Cell* **1999**, *96*, 25–34. [CrossRef]
62. Shechter, R.; Ziv, Y.; Schwartz, M. New GABAergic Interneurons Supported by Myelin-Specific T Cells Are Formed in Intact Adult Spinal Cord. *Stem Cells* **2007**, *25*, 2277–2282. [CrossRef]
63. Sevc, J.; Daxnerová, Z.; Miklosová, M. Role of Radial Glia in Transformation of the Primitive Lumen to the Central Canal in the Developing Rat Spinal Cord. *Cell Mol. Neurobiol.* **2009**, *29*, 927–936. [CrossRef] [PubMed]
64. Ghazale, H.; Ripoll, C.; Leventoux, N.; Jacob, L.; Azar, S.; Mamaeva, D.; Glasson, Y.; Calvo, C.-F.; Thomas, J.-L.; Meneceur, S.; et al. RNA Profiling of the Human and Mouse Spinal Cord Stem Cell Niches Reveals an Embryonic-like Regionalization with MSX1+ Roof-Plate-Derived Cells. *Stem Cell Rep.* **2019**, *12*, 1159–1177. [CrossRef] [PubMed]

65. Tait, C.M.; Chinnaiya, K.; Manning, E.; Murtaza, M.; Ashton, J.-P.; Furley, N.; Hill, C.J.; Alves, C.H.; Wijnholds, J.; Erdmann, K.S.; et al. Crumbs2 Mediates Ventricular Layer Remodelling to Form the Spinal Cord Central Canal. *PLoS Biol.* **2020**, *18*, e3000470. [CrossRef] [PubMed]
66. Leber, S.M.; Breedlove, S.M.; Sanes, J.R. Lineage, Arrangement, and Death of Clonally Related Motoneurons in Chick Spinal Cord. *J. Neurosci.* **1990**, *10*, 2451–2462. [CrossRef]
67. Fu, H.; Qi, Y.; Tan, M.; Cai, J.; Hu, X.; Liu, Z.; Jensen, J.; Qiu, M. Molecular Mapping of the Origin of Postnatal Spinal Cord Ependymal Cells: Evidence That Adult Ependymal Cells Are Derived from Nkx6.1+ Ventral Neural Progenitor Cells. *J. Comp. Neurol.* **2003**, *456*, 237–244. [CrossRef]
68. Masahira, N.; Takebayashi, H.; Ono, K.; Watanabe, K.; Ding, L.; Furusho, M.; Ogawa, Y.; Nabeshima, Y.; Alvarez-Buylla, A.; Shimizu, K.; et al. Olig2-Positive Progenitors in the Embryonic Spinal Cord Give Rise Not Only to Motoneurons and Oligodendrocytes, but Also to a Subset of Astrocytes and Ependymal Cells. *Dev. Biol.* **2006**, *293*, 358–369. [CrossRef]
69. Yu, K.; McGlynn, S.; Matisse, M.P. Floor Plate-Derived Sonic Hedgehog Regulates Glial and Ependymal Cell Fates in the Developing Spinal Cord. *Development* **2013**, *140*, 1594–1604. [CrossRef]
70. Xing, L.; Anbarchian, T.; Tsai, J.M.; Plant, G.W.; Nusse, R. Wnt/ $\beta$ -Catenin Signaling Regulates Ependymal Cell Development and Adult Homeostasis. *Proc. Natl. Acad. Sci. USA* **2018**, *115*, E5954–E5962. [CrossRef]
71. Munson, C.; Huisken, J.; Bit-Avragim, N.; Kuo, T.; Dong, P.D.; Ober, E.A.; Verkade, H.; Abdelilah-Seyfried, S.; Stainier, D.Y.R. Regulation of Neurocoel Morphogenesis by *Pard6y*b. *Dev. Biol.* **2008**, *324*, 41–54. [CrossRef] [PubMed]
72. Kondrychyn, L.; Teh, C.; Sin, M.; Korzh, V. Stretching Morphogenesis of the Roof Plate and Formation of the Central Canal. *PLoS ONE* **2013**, *8*, e56219. [CrossRef]
73. Böhme, G. Formation of the Central Canal and Dorsal Glial Septum in the Spinal Cord of the Domestic Cat. *J. Anat.* **1988**, *159*, 37–47.
74. Korzh, V. Stretching Cell Morphogenesis during Late Neurulation and Mild Neural Tube Defects. *Dev. Growth Differ.* **2014**, *56*, 425–433. [CrossRef] [PubMed]
75. Snow, D.M.; Steindler, D.A.; Silver, J. Molecular and Cellular Characterization of the Glial Roof Plate of the Spinal Cord and Optic Tectum: A Possible Role for a Proteoglycan in the Development of an Axon Barrier. *Dev. Biol.* **1990**, *138*, 359–376. [CrossRef]
76. Sarnat, H.B. Role of Human Fetal Ependyma. *Pediatr. Neurol.* **1992**, *8*, 163–178. [CrossRef]
77. Millonig, J.H.; Millen, K.J.; Hatten, M.E. The Mouse Dreher Gene *Lmx1a* Controls Formation of the Roof Plate in the Vertebrate CNS. *Nature* **2000**, *403*, 764–769. [CrossRef] [PubMed]
78. Kridsada, K.; Niu, J.; Haldipur, P.; Wang, Z.; Ding, L.; Li, J.J.; Lindgren, A.G.; Herrera, E.; Thomas, G.M.; Chizhikov, V.V.; et al. Roof Plate-Derived Radial Glial-like Cells Support Developmental Growth of Rapidly Adapting Mechanoreceptor Ascending Axons. *Cell Rep.* **2018**, *23*, 2928–2941. [CrossRef]
79. Shimizu, T.; Kagawa, T.; Wada, T.; Muroyama, Y.; Takada, S.; Ikenaka, K. Wnt Signaling Controls the Timing of Oligodendrocyte Development in the Spinal Cord. *Dev. Biol.* **2005**, *282*, 397–410. [CrossRef] [PubMed]
80. Bänziger, C.; Soldini, D.; Schütt, C.; Zipperlen, P.; Hausmann, G.; Basler, K. Wntless, a Conserved Membrane Protein Dedicated to the Secretion of Wnt Proteins from Signaling Cells. *Cell* **2006**, *125*, 509–522. [CrossRef]
81. Bartscherer, K.; Pelte, N.; Ingelfinger, D.; Boutros, M. Secretion of Wnt Ligands Requires Evi, a Conserved Transmembrane Protein. *Cell* **2006**, *125*, 523–533. [CrossRef] [PubMed]
82. Goodman, R.M.; Thombre, S.; Firtina, Z.; Gray, D.; Betts, D.; Roebuck, J.; Spana, E.P.; Selva, E.M. Sprinter: A Novel Transmembrane Protein Required for Wg Secretion and Signaling. *Development* **2006**, *133*, 4901–4911. [CrossRef] [PubMed]
83. GENSAT Brain Atlas of Gene Expression in EGFP Transgenic Mice. Available online: <http://www.gensat.org/index.html> (accessed on 29 July 2021).
84. Horner, P.J.; Power, A.E.; Kempermann, G.; Kuhn, H.G.; Palmer, T.D.; Winkler, J.; Thal, L.J.; Gage, F.H. Proliferation and Differentiation of Progenitor Cells Throughout the Intact Adult Rat Spinal Cord. *J. Neurosci.* **2000**, *20*, 2218–2228. [CrossRef] [PubMed]
85. Lie, D.-C.; Colamarino, S.A.; Song, H.-J.; Désiré, L.; Mira, H.; Consiglio, A.; Lein, E.S.; Jessberger, S.; Lansford, H.; Dearie, A.R.; et al. Wnt Signalling Regulates Adult Hippocampal Neurogenesis. *Nature* **2005**, *437*, 1370–1375. [CrossRef]
86. Adachi, K.; Mirzadeh, Z.; Sakaguchi, M.; Yamashita, T.; Nikolcheva, T.; Gotoh, Y.; Peltz, G.; Gong, L.; Kawase, T.; Alvarez-Buylla, A.; et al.  $\beta$ -Catenin Signaling Promotes Proliferation of Progenitor Cells in the Adult Mouse Subventricular Zone. *Stem Cells* **2007**, *25*, 2827–2836. [CrossRef]
87. Varela-Nallar, L.; Inestrosa, N.C. Wnt Signaling in the Regulation of Adult Hippocampal Neurogenesis. *Front. Cell. Neurosci.* **2013**, *7*, 100. [CrossRef] [PubMed]

Review

# Craniofacial Phenotypes and Genetics of DiGeorge Syndrome

Noriko Funato 

Department of Signal Gene Regulation, Advanced Therapeutic Sciences, Medical and Dental Sciences, Graduate School of Medical and Dental Sciences, Tokyo Medical and Dental University (TMDU), Tokyo 113-8510, Japan; noriko-funato@umin.ac.jp

**Abstract:** The 22q11.2 deletion is one of the most common genetic microdeletions, affecting approximately 1 in 4000 live births in humans. A 1.5 to 2.5 Mb hemizygous deletion of chromosome 22q11.2 causes DiGeorge syndrome (DGS) and velocardiofacial syndrome (VCFS). DGS/VCFS are associated with prevalent cardiac malformations, thymic and parathyroid hypoplasia, and craniofacial defects. Patients with DGS/VCFS manifest craniofacial anomalies involving the cranium, cranial base, jaws, pharyngeal muscles, ear-nose-throat, palate, teeth, and cervical spine. Most craniofacial phenotypes of DGS/VCFS are caused by proximal 1.5 Mb microdeletions, resulting in a hemizygosity of coding genes, microRNAs, and long noncoding RNAs. *TBX1*, located on chromosome 22q11.21, encodes a T-box transcription factor and is a candidate gene for DGS/VCFS. *TBX1* regulates the fate of progenitor cells in the cranial and pharyngeal apparatus during embryogenesis. *Tbx1*-null mice exhibit the most clinical features of DGS/VCFS, including craniofacial phenotypes. Despite the frequency of DGS/VCFS, there has been a limited review of the craniofacial phenotypes of DGS/VCFS. This review focuses on these phenotypes and summarizes the current understanding of the genetic factors that impact DGS/VCFS-related phenotypes. We also review DGS/VCFS mouse models that have been designed to better understand the pathogenic processes of DGS/VCFS.

**Keywords:** 22q11.2 deletion syndrome; DiGeorge syndrome; velocardiofacial syndrome; cleft palate; skull base; cleidocranial dysplasia; hyoid bone; teeth abnormalities

**Citation:** Funato, N. Craniofacial Phenotypes and Genetics of DiGeorge Syndrome. *J. Dev. Biol.* **2022**, *10*, 18. <https://doi.org/10.3390/jdb10020018>

Academic Editors: Hideyo Ohuchi and Tsutomu Nohno

Received: 21 April 2022

Accepted: 11 May 2022

Published: 13 May 2022

**Publisher's Note:** MDPI stays neutral with regard to jurisdictional claims in published maps and institutional affiliations.



**Copyright:** © 2022 by the author. Licensee MDPI, Basel, Switzerland. This article is an open access article distributed under the terms and conditions of the Creative Commons Attribution (CC BY) license (<https://creativecommons.org/licenses/by/4.0/>).

## 1. Introduction

The 22q11.2 deletion syndrome is one of the most common chromosomal microdeletions, affecting approximately 1 in 4000 live births in humans [1]. A 1.5 to 2.5 Mb hemizygous deletion of chromosome 22q11.2 causes DiGeorge syndrome (DGS; OMIM #188400) and velocardiofacial syndrome (VCFS or Shprintzen VCF syndrome; OMIM #192430) [2]. DGS/VCFS appears to be a genomic disorder distinct from 22q11.2 distal deletion syndrome (OMIM #611867). The clinical phenotype of DGS/VCFS is a complex and variable congenital disability, including cardiovascular defects, thymic hypoplasia, parathyroid hypoplasia, and craniofacial malformations [3]. Craniofacial malformations occur in approximately 60% of patients with DGS/VCFS [4].

*TBX1*, located on chromosome 22q11.21, encodes a T-box transcription factor and is considered a candidate gene for DGS/VCFS since mutations in *TBX1* have been found in patients with DGS/VCFS [5]. Heterozygous *Tbx1*-mutant (*Tbx1*<sup>+/-</sup>) mice exhibit DGS/VCFS-related cardiovascular, parathyroid, and thymic phenotypes, suggesting that *TBX1* dosage is critical for cardiovascular, parathyroid and thymic development [6–9]. *Tbx1*-null mice exhibit the most clinical features of DGS/VCFS, including craniofacial phenotypes, while *Tbx1*<sup>+/-</sup> mice exhibit no significant craniofacial phenotypes [6–10].

There have been some excellent reviews on genetics and cardiovascular anomalies of DGS/VCFS [3,11–13]. However, information on the craniofacial anomalies of DGS/VCFS is limited. This review focuses on these phenotypes and summarizes the current understanding of the genetic factors that impact DGS/VCFS-related phenotypes. We also review

DGS/VCFS mouse models that have been designed to better understand the pathogenic processes of DGS/VCFS.

## 2. Craniofacial Phenotypes of Patients with DGS/VCFS

Patients with DGS/VCFS manifest craniofacial anomalies involving the cranium, cranial base, jaws, pharyngeal muscles, ear-nose-throat, palate, teeth, and cervical spine (Figure S1, Tables 1 and 2). Frequently observed craniofacial phenotypes include velopharyngeal insufficiency (27–92%), enamel hypomineralization (39–41%), hearing loss (33–39%), platybasia (50–91%), and cervical spine anomalies (75%) (Table 1). Delayed development of the hyoid bone has also been reported [14,15].

**Table 1.** Craniofacial anomalies in patients with DGS/VCFS.

Phenotypes	Features	Frequency
Palatal anomalies	Overt cleft palate	7–11%
	Submucous cleft palate	5–23%
	Bifid uvula	5–10%
	Velopharyngeal insufficiency	27–92%
Dental anomalies	Tooth agenesis	15%
	Hypoplasia of primary teeth	32%
	Hypoplasia of permanent teeth	10%
	Enamel hypomineralization of primary teeth	39%
	Enamel hypomineralization of permanent teeth	41%
Ear-nose-throat abnormalities	Hearing loss	33–39%
	Otitis media with effusion	2%
	Tracheomalacia/laryngomalacia	2%
	Laryngeal web	1%
Ocular abnormalities	Hooding of the upper lid	41%
	Ptosis	9%
	Hooding of the lower lid	6%
	Epicanthal folds	3%
	Distichiasis	3%
Cranial base anomalies	Platybasia	50–91%
	Basilar impression	3%
Cervical spine anomalies	Atlas (C1) anomalies	75%
	Axis (C2) anomalies	59%
	Fusion of C2–C3	34%

Data were summarized from the following references: [16–22].

**Table 2.** Craniofacial and skeletal phenotypes of DGS/VCFS and *Tbx1*-null mice.

	DGS/VCFS	<i>Tbx1</i> -Null Mice	
Cranium	Dolichocephaly	Small cranium	
	Abnormal skull morphology	Hypoplastic parietal bone	
	Malar flattening	Hypoplastic interparietal bone	
	Long face		Unfused cranial sutures between frontal and parietal bones
			Temporal bone hypoplasia
			Absent zygomatic arch
		Abnormal zygomatic arch morphology	
Cranial Base	Platybasia	Abnormal fusion of the basioccipital and basisphenoid bones	
	Basilar impression	Abnormal presphenoid bone morphology	
		Abnormal basioccipital bone morphology	
Palate	Cleft palate	Cleft palate	
	Submucous cleft palate	Submucous cleft palate	
	Bifid uvula	Bifid uvula	
	Highly arched palate		
	Velopharyngeal insufficiency		

**Table 2.** *Cont.*

	DGS/VCFS	<i>Tbx1</i> -Null Mice
Mandible	Retrognathia Short mandible Micrognathia	Absent mandibular coronoid process Short mandible Micrognathia
Teeth	Enamel hypoplasia Single central incisor Small teeth Abnormality of the dentition Carious teeth	Abnormal upper incisor morphology Absent upper incisors
Muscles	Pharyngeal hypotonia	Absent masseter muscle Absent pterygoid muscle Absent temporalis muscle
Eyes	Hypertelorism/telecanthus Downslanted palpebral fissures Proptosis Strabismus Abnormal eyelid morphology Epicanthus Microphthalmia	Hypertelorism
External Ears	Small earlobe Low-set ears Abnormally folded pinna Preauricular pit	Ear lobe hypoplasia Lowered ear position Abnormal ear shape Absent outer ear Anotia
Middle and Inner Ears	Chronic otitis media Conductive hearing loss Sensorineural hearing loss Auditory canal stenosis Pulsatile tympanic membrane Thickened tympanic membrane Tympanic membrane retraction	Abnormal middle ear ossicle morphology Absent middle ear ossicles Abnormal stapes morphology Abnormal incus morphology Abnormal malleus morphology Absent stapes Abnormal external auditory canal morphology Decreased tympanic ring size
Nose	Prominent nasal bridge Abnormal nasal morphology Underdeveloped nasal alae Choanal atresia	Short snout
Throat	Abnormal thorax morphology Abnormality of the pharynx	Small thyroid cartilage Small cricoid cartilage Abnormal thyroid cartilage morphology Pharynx hypoplasia
Hyoid bones	Delayed development of the hyoid bone Invisible hyoid ossification center	Hyoid bone hypoplasia Abnormal hyoid bone morphology
Cervical spine	Dysmorphic C1 Anterior arch cleft of C1 Open posterior arch C1 Fusion of C1–C2 Fusion of C2–C3 Upswept C2 lamina Platyspondyly	Abnormal cervical atlas (C1) morphology Absent arcus anterior of C1
Others		Short clavicle
References	[14–28]	[6–10,29–36]

Data were summarized from the following references [6–10,14–36], OMIM (<https://www.omim.org> accessed on 3 August 2021) and the Monarch Initiative (<https://monarchinitiative.org> accessed on 3 August 2021).

In addition to morphological anomalies, infants and young children with DGS/VCFS often exhibit a high prevalence of functional difficulties in feeding and speech/language associated with cleft palate, laryngeal anomalies, and velopharyngeal dysfunction [37]. Even after cleft palate closure, children with DGS/VCFS sometimes present communication disorders related to speech-language problems, such as articulation disorders of speech sounds and vocal disorders [37]. They exhibit slower language acquisition than those with other disorders that may be associated with abnormal muscle development.

### 3. Genetics of DGS/VCFS

DGS/VCFS is caused by a 1.5 to 2.5 Mb hemizygous deletion of chromosome 22q11.2 (Figure 1). Chromosomal microdeletions at 10p14-p13 (the *DGS2* locus) in patients with DGS/VCFS phenotypes are defined as the DGS/VCFS complex 2. In this review, we focus on the 22q11.2 locus, its associated genes, and miRNAs.

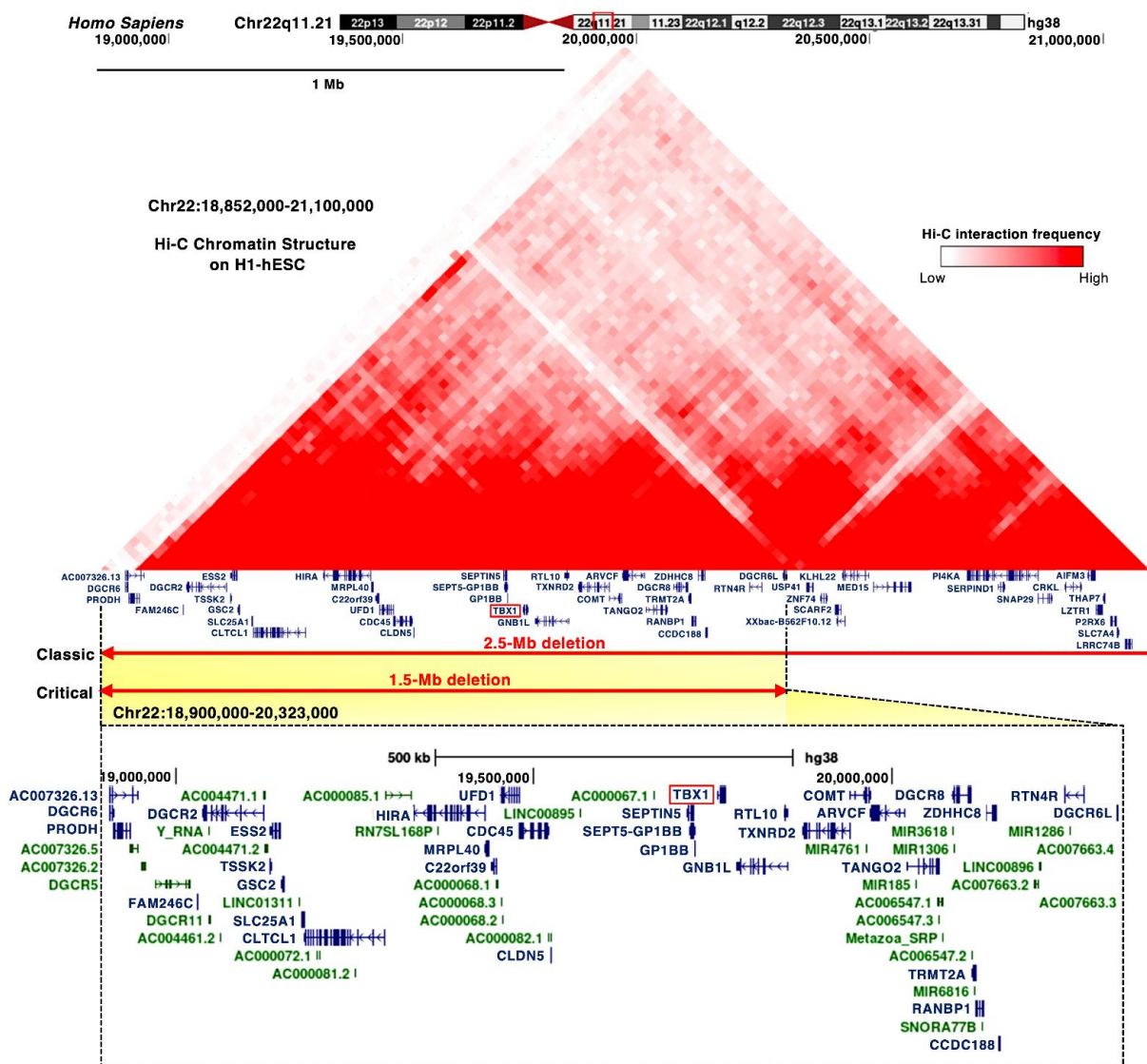


**Figure 1.** Proximal deletions of chromosome 22q11.2 are responsible for the clinical features of DGS/VCFS. Snapshot of the UCSC Genome Browser (<http://genome.ucsc.edu> accessed on 3 August 2021) in the hg38 assembly showing the genomic context in the proximal deletions of chromosome 22q11.2. Top, the 25 kb resolution Hi-C data in H1 human embryonic stem cell line (H1-hESC). Bottom, the coding (blue) and noncoding RNAs (green), including miRNAs and long noncoding RNAs, are shown.

Most of the chromosomal deletions of the 22q11.2 locus are de novo, but inherited deletions of the 22q11.2 locus have been reported in 6–28% of patients as autosomal dominant [16,17]. The majority of clinical phenotypes of DGS/VCFS are caused by proximal 1.5 Mb microdeletions [3,22], resulting in a hemizyosity of approximately 30 coding genes, including *DGCR6*, *PRODH*, *DGCR2*, *ESS2*, *TSSK2*, *GSC2*, *FAM246C*, *SLC25A1*, *CLTCL1*, *UFD1*, *HIRA*, *CDC45*, *MRPL40*, *C22orf39*, *CLDN5*, *TBX1*, *SEPTIN5*, *SEPT5-GP1BB*, *GP1BB*, *GNB1L*, *RTL10*, *TXNRD2*, *COMT*, *ARVCF*, *TANGO2*, *TRMT2A*, *RANBP1*, *CCDC188*, *DGCR8*, *ZDHHC8*, *RTN4R*, *DGCR6L*, and *C007326*, as well as microRNAs (miRNAs) and long noncoding RNAs (Figures 1 and S2A). The Hi-C chromatin structure of the 1.5 Mb region indicates interactions between these loci and their neighboring regions (Figure 1).

### 3.1. *TBX1* Gene

The proximal deletion of 1.5 Mb on the 22q11.2 locus includes *TBX1* (Figure 1). *TBX1* is considered a candidate gene of DGS/VCFS because haploinsufficiency of *TBX1* leads to the typical phenotypes of DGS/VCFS, conotruncal anomaly face syndrome (OMIM #217095), and tetralogy of Fallot (OMIM #187500) (Table 3). Identical mutations in *TBX1* present among patients resulted in distinct phenotypes, suggesting that genetic and epigenetic changes or environmental factors are involved in the clinical phenotypes [5]. The coding variants in the T-box and C-terminal domains of *TBX1* showed high combined annotation-dependent depletion (CADD) scores (Table S1); however, further investigation is required to confirm that the variants cause DGS/VCFS and how they impact the phenotypes.

**Table 3.** DGS/VCFS-associated variants of *TBX1*.

Mutation	Domain	Condition	Craniofacial Anomalies	References
c.89_284del	N-terminal	DiGeorge syndrome	Yes	ClinVar Variant: 971780
c.199_224del	N-terminal	DiGeorge syndrome	Yes	ClinVar Variant: 949172
c.292A>T	N-terminal	DiGeorge syndrome	Yes	ClinVar Variant: 526036
c.385G>A	T-box	Tetralogy of Fallot	No	ClinVar Variant: 488618
c.443T>A (F148Y)	T-box	Conotruncal anomaly face syndrome	Yes	[5]
		DiGeorge syndrome		
c.503T>C	T-box	Velocardiofacial syndrome (Shprintzen syndrome)	Yes	ClinVar Variant: 973222
		Tetralogy of Fallot		
c.569C > A (P190Q)	T-box	Congenital heart defects	No	[38]
c.582C>G (H194Q)	T-box	Velocardiofacial syndrome	Yes	[39]
c.928G>A (G310S)	C-terminal	DiGeorge syndrome	Yes	[5]
c.967_977dup AACCCCGTGGC	C-terminal	Thymic hypoplasia	No	[40]
		Postaxial polydactyly of the right fifth toe		
		Hypoparathyroidism and hypocalcemia		
c.1158_1159delinsT	C-terminal	Facial asymmetry	Yes	[41]
		Deafness		
c.1223delC	C-terminal	Conotruncal anomaly face syndrome	Yes	[5]
		Velocardiofacial syndrome		
c.1253delA	C-terminal	DiGeorge syndrome	Yes	[42]
c.1320-1342del23bp	C-terminal	Velocardiofacial syndrome	Yes/No	[43]
		Tetralogy of Fallot		
		Scoliosis		
c.1399-1428dup30	C-terminal	Facial asymmetry	Yes	[44]
		Upslanting palpebral fissures		
		Absent pulmonary valve		
		Isolated left pulmonary artery		

ClinVar (<https://www.ncbi.nlm.nih.gov/clinvar> accessed on 3 August 2021).

### 3.2. *DiGeorge Syndrome Critical Region (DGCR)*

*DGCR8*, *DGCR6*, and *DGCR6L* map to the commonly deleted 1.5 Mb region in DGS/VCFS (Figure 1). *DGCR8* is a nuclear miRNA-binding protein required for miRNA



biogenesis. Dgcr8 haploinsufficiency in mice reduces the expression of miRNAs in the brain [45]. DGCR6 and DGCR6L genes encode a protein with a sequence similar to the *Drosophila* gonadal [46] (Figure S2B). In a chicken model, targeting DGCR6 function resulted in a vascular phenotype [47]. Attenuation of DGCR6 affects the expression of three genes localized within the 1.5 Mb region, upregulating the expression of TBX1 and UFD1 and reducing the expression of HIRA in the heart and pharyngeal arches of the chicken embryos [47]. Thus, the haploinsufficiency of DGCR8 or DGCR6 may be linked to DGS/VCFS phenotypes when targeting DGS/VCFS-related genes and miRNAs.

### 3.3. MicroRNAs

The deleted 1.5 Mb on the 22q11.2 locus includes several miRNAs, such as miR-185, miR-4716, miR-3618, miR-1286, miR-1306, and miR-6816 (Figure 1). The TargetScan miRNA target prediction program (<http://www.targetscan.org> accessed on 3 August 2021) identified that the 3' UTR of *TBX1* includes conserved sites for miR-183-5p, miR-96-5p, miR-1271-5p, miR-182-5p, miR-144-3p, miR-139-5p, miR-101-3p, and miR-451. Two miRNAs were confirmed to target the 3' UTR of *TBX1*. miR-96-5p represses *Tbx1* expression and, in turn, TBX1 suppresses the promoter activity and expression of miR-96 [48]. miR-451a, a tumor suppressor, also directly targets *TBX1* [49]. The expression of this gene is upregulated in cutaneous basal cell carcinoma, inversely to miR-451a [49]. miR-17-92 fine-tunes the expression of *Tbx1* in craniofacial development, suggesting miR-17-92 as a candidate genetic modifier for *Tbx1* [50]. Thus, miRNAs both inside and outside the 22q11.2 locus may influence the severity of the clinical phenotypes of DGS/VCFS.

## 4. Craniofacial Phenotypes of DGS/VCFS Mouse Models

Mouse models with DGS/VCFS help identify additional candidate genes or modifier genes that influence the penetrance and/or severity of DGS/VCFS-related phenotypes. According to the mouse genome informatics (MGI) database (<http://www.informatics.jax.org> accessed on 3 August 2021), DGS/VCFS-related anomalies concerning *Tbx1*, *Chrd*, *Tgfb2*, *Vegfa*, *Fgf8*, *Crkl*, *Aldh1a2/Raldh2*, *Hoxa3*, *Kat6a/Moz/Myst3*, *Dicer1*, *Plxnd1*, *Dock1*, *Ndst1*, *Prickle1*, *Trappc10*, *Zfp366*, and *Foxn1* have been reported in genetically altered mice (Tables 4 and S2). When these genes were analyzed according to biological process, “heart morphogenesis” and “cranial skeletal system development” were enriched (Table S3). Our enrichment analysis using ToppCluster [51] indicated that genes associated with DGS/VCFS phenotypes in mice are specifically enriched in the morphogenesis of craniofacial tissues and heart (Figure 2A). Interestingly, among these genes, only *Tbx1* and *Chrd* were specifically enriched in the morphogenesis of cricoid and thyroid cartilages (Figure 2A). Genes associated with DGS/VCFS phenotypes in mice also indicated that DGS/VCFS-related phenotypes involve the interaction of several signaling pathways, including bone morphogenetic protein (BMP), transforming growth factor (TGF) $\beta$ , vascular endothelial growth factor (VEGF), fibroblast growth factor (FGF), and retinoic acid signaling pathways (Figure 2B). Genes involved in the genetic pathway of *Tbx1* are likely to induce phenotypes similar to *Tbx1*-null mice (Figure 2B, Tables 4 and S2). These are described below.



#### 4.1. *Tbx1*

Craniofacial structures with DGS/VCFS phenotypes are derivatives of the head mesenchyme and the first and second pharyngeal arches [62]. *Tbx1* is expressed in the mesoderm, ectoderm, and endoderm of the pharyngeal apparatus and head mesenchyme between embryonic day (E)9.5 and E11.5 in mice [62,63]. At E12.5, *Tbx1* is expressed in the oral epithelium, the myogenic core of the tongue, incisor tooth buds, pharyngeal muscles, and otic vesicle epithelium [63,64]. *Tbx1*-null mice exhibit the most clinical features of DGS/VCFS, while *Tbx1*<sup>+/-</sup> mice exhibit no significant craniofacial phenotypes (Tables 2, 5 and S2). Information about ocular phenotypes in *Tbx1*-mutant mice is limited (Table 2), although these anomalies in patients with DGS/VCFS have been reported [16,17]. The Cre/loxP system has been used with *Tbx1* conditional knockout mice to examine the tissue-specific function of TBX1 in craniofacial development (Table 5).

**Table 5.** Selected craniofacial phenotypes of *Tbx1*-mutant neonates.

<i>Tbx1</i> -Mutant Mice		Craniofacial Phenotypes					
Mutation Type	Tissue/Cell	Cranium	Cranial Base	Palate	Mandible	Hyoid Bone	Cervical Spine
<i>Tbx1</i> <sup>+/-</sup>	Entire body	Normal	Normal	Normal	Normal	Normal	Normal
<i>Tbx1</i> -null	Entire body	Abnormal	Abnormal	CP	Hypoplastic	Hypoplastic	Abnormal
Deletion ( <i>Foxg1-Cre</i> )	Pharyngeal tissues *	Abnormal	Abnormal	CP	Hypoplastic	Hypoplastic	NA
Deletion ( <i>KRT14-Cre</i> )	Epithelium	Normal	Normal	Anterior CP	Normal	Normal	Normal
Deletion ( <i>Mesp1-Cre</i> )	Mesoderm	Abnormal	Abnormal	NA	Hypoplastic	Hypoplastic	Abnormal
Deletion ( <i>Twist2-Cre</i> )	Osteochondral progenitors	Abnormal	Abnormal	Normal	Normal	Hypoplastic	Abnormal
Deletion ( <i>Wnt1-Cre</i> )	Neural crest	Normal	Normal	Normal	Normal	Hypoplastic	Normal

Data were summarized from the following references: [30,31,34–36,65,66]. \* pharyngeal pouches, otic and optic vesicles [30,31]; \* pharyngeal endoderm, ectoderm, and mesoderm [65]; CP, cleft palate; NA, not available.

##### 4.1.1. Cleft Palate

During palatogenesis, the palatal shelves develop bilaterally from the internal parts of the maxillary prominences and fuse above the tongue to form an intact oral cavity roof [67,68]. Because the palate consists of a bone-lined hard palate and a bone-free soft palate, cleft palate phenotypes include incomplete and submucosal cleft palates [67,68]. Ablation of *Tbx1*, which is expressed in the epithelium of the palatal shelves, results in abnormal intraoral epithelial fusions between the palatal shelves and the mandible, resulting in various degrees of the cleft palate phenotype (complete, incomplete, and submucosal cleft palate) [30,34,69]. Expression of *Pax9*, whose mutations lead to cleft palate and tooth agenesis [70], is downregulated in the palatal shelves and pharyngeal region of *Tbx1*-null embryos [34,71]. In *Tbx1*-null palatal shelves, muscle- and bone-related genes are downregulated, whereas neuron- and collagen biosynthesis-related genes are upregulated [72].

##### 4.1.2. Abnormalities in Craniofacial Bones

*Tbx1*-null mice display craniofacial bone abnormalities, including persistently open fontanelles, micrognathia, a short clavicle, a hypoplastic zygomatic arch, and the absence of the hyoid bone (Tables 2 and S2). Conditional deletion of *Tbx1* in the mesoderm or osteochondral progenitors recapitulates the calvarial and mandibular phenotypes of *Tbx1*-null mice [35,66], suggesting that *Tbx1* is required for morphogenesis and ossification of craniofacial bones. Although *Tbx1* expression has not been reported in the neural crest, conditional deletion of *Tbx1* here results in a hypoplastic hyoid bone [35] (Tables 2 and 5). These results indicate that *Tbx1* is required for the morphogenesis and ossification of mesoderm- and neural crest-derived membranous bones, although malformations observed in most neural crest-derived bones of *Tbx1*-null mice are secondary defects induced by non-neural crest

cells [35,66]. Interestingly, abnormalities in membranous bones observed in *Tbx1*-null mice are similar to those of cleidocranial dysplasia (OMIM #119600 and #216330) in humans, exhibiting hypoplastic membranous bones, including abnormal neurocranial morphology, a short clavicle, a hypoplastic zygomatic arch, and hyoid bone [73–75]. Cleidocranial dysplasia (OMIM #119600) is caused by heterozygous mutations in *RUNX2*, which encodes a master transcription factor for osteoblast differentiation [74,75]. Since ablation of *Tbx1* affects *Runx2* expression in calvarial bones, and TBX1 overexpression induces *Runx2* expression in vitro [35], TBX1 may act upstream of *Runx2* by maintaining cell populations that express *Runx2* at the onset of bone development. In addition, TBX1 could be a candidate gene for recessive inheritance of cleidocranial dysplasia (OMIM #216330).

#### 4.1.3. Abnormalities in the Cranial Base and Cervical Spine

The spheno-occipital synchondrosis (SOS) in the cranial base is a vital growth center for the skull (reviewed in [76]). TBX1 is expressed in the mesoderm-derived cartilage primordium of the SOS and basioccipital bones, and *Tbx1* deletion in the mesoderm induces malformed basioccipital bones and precocious ossified SOS. This indicates that *Tbx1* is an essential regulator of chondrocyte differentiation and subsequent ossification at the SOS [36]. TBX1 inhibits the transcriptional activity of RUNX2 in vitro as well as the expression of RUNX2 target genes in SOS [36]. *Tbx1*-null mice also exhibit endochondral bone abnormalities in the atlas, axis, and xiphoid process [6,35]. There is potential to examine the phenotypes of cranial synchondroses in DGS/VCFS patients, as abnormalities in the SOS and basioccipital bones may induce cranial phenotypes of DGS/VCFS, such as dolichocephaly, basilar impression, and platybasia.

#### 4.1.4. Dental Anomalies

Dental abnormalities (single central incisors, enamel hypoplasia, and small teeth) have been reported in many patients [18,28]. Accordingly, in approximately 30% of *Tbx1*-null mice, the upper incisors are absent [6]. *Tbx1* is expressed in the cervical loops, which contain the dental stem cell niche in mice. The cervical loop region of the incisor is either severely reduced or completely absent in *Tbx1*-null mice, and cultured incisors of *Tbx1*-null mice are hypoplastic and lack enamel [77]. Ablation of *Tbx1* in the epithelium results in smaller teeth than in the wild type, suggesting that TBX1 regulates the proliferation of dental progenitor cells [48].

#### 4.1.5. Muscle Hypotonia

Branchiomeric muscles are derived from the mesoderm of the pharyngeal arch. In *Tbx1*-null and *Tbx1*<sup>fllox/-</sup>;*Mesp1-Cre* embryos, the masseter, pterygoid, and temporalis muscles are intermittently absent [78,79]. Accordingly, muscle-related genes are also downregulated in *Tbx1*-null palatal shelves [72]. *Tbx1* acts upstream of critical transcription factors to form branchiomeric muscles. These include LIM homeobox protein 2 (*Lhx2*), transcription factor 21 (*Tcf21/capsulin*), musculin (*Msc*), myogenic factor 5 (*Myf5*), myogenic differentiation 1 (*Myod1*), myocyte enhancer factor 2C (*Mef2c*), and GATA binding protein 4 (*Gata4*) [79–82]. *Tbx1* is in the downstream genetic pathways of *Tcf21*, paired-like homeodomain transcription factor 2 (*Pitx2*), and ISL LIM homeobox 1 (*Isl1*) [80,83,84]. Thus, TBX1 regulates the pattern and development of branchiomeric muscles through the transcriptional regulation of myogenic genes.

#### 4.2. Chordin (*Chrd*) and Transforming Growth Factor, Beta Receptor II (*Tgfbr2*)

Mice lacking the *Chrd* gene encoding chordin, an antagonist of bone morphogenetic proteins (BMPs), exhibit recapitulating phenotypes in *Tbx1*-null mice [32,52] (Table S2). *Chrd*-null neonates exhibit most craniofacial phenotypes in the cranium, cranial base, maxilla, mandible, ears, and hyoid bone (Table S2). Both *Tbx1* and *Fgf8* were reduced in the endoderm of *Chrd*-null mice, indicating that *Chrd* acts upstream of *Tbx1* and *Fgf8* [52]. *Tbx1* acts upstream of SMAD family member 7 (*Smad7*), an inhibitory Smad within the

BMP/TGF $\beta$  pathway, to regulate vascular smooth muscle and extracellular matrix investment of the fourth arch artery [85]. Conditional deletion of *Tgfbr2*, which encodes TGF $\beta$  receptor 2, in the neural crest resulted in DGS/VCFS-related cardiovascular defects [53]. These findings suggest a potential role of BMP/TGF $\beta$  signaling in the pathogenesis of DGS/VCFS.

#### 4.3. Vascular Endothelial Growth Factor A (*Vegfa*)

VEGFA is an essential cytokine in angiogenesis and vascular development during embryogenesis [86]. *Vegfa*-null neonates exhibit a few aspects of DGS/VCFS-related craniofacial anomalies, including unfused cranial sutures, absent incisors, and short mandibles, as well as cardiovascular abnormalities [54] (Table S2). The deletion of *Vegfa* in mice reduces *Tbx1* expression, and the knockdown of *vegfa/vegfa* levels in zebrafish enhances the pharyngeal arch malformations induced by *tbx1* knockdown [54]. In humans, low expression of the VEGFA haplotype increases the risk of a cardiac phenotype of DGS/VCFS, indicating that expression levels of VEGFA affect the severity of DGS/VCFS phenotypes [87]. These results suggest that VEGFA modifies DGS/VCFS-related phenotypes by regulating *TBX1* expression.

#### 4.4. Fibroblast Growth Factor 8 (*Fgf8*) and FGF Receptor 2 (*Fgfr2*)

Ablation of *Fgf8* induces craniofacial, cardiovascular, thymic, and parathyroid phenotypes [55,88]. *Fgf8*-null neonates exhibit a few aspects of DGS/VCFS-related craniofacial anomalies, including cleft palate and abnormal outer ear morphology [55,88] (Table S2). *Fgf8*<sup>+/-</sup>;*Tbx1*<sup>+/-</sup> double heterozygous embryos show an increased penetrance of cardiovascular defects compared with *Tbx1*-heterozygous embryos [89]. Tissue-specific deletion of *Fgf8* in *Tbx1*-expressing domains results in cardiovascular anomalies [90]. *TBX1* activates the *Fgf8* enhancer during cardiac development [9]. Deletion of the *Fgfr2* gene that encodes FGF receptor 2 decreases *Tbx1* expression in the dental epithelium, indicating a genetic link between FGF signaling and *Tbx1* in tooth development [91]. In addition, a *Tbx1-Six1/Eya1-Fgf8* genetic pathway is crucial for craniofacial morphogenesis [92,93]. These findings demonstrate that the FGF pathway and *Tbx1* interact genetically during pharyngeal arch development.

#### 4.5. CRK like Proto-Oncogene, Adaptor Protein (*Crkl*)

*CRKL* maps to the 2.5 Mb region commonly deleted in DGS/VCFS (Figure 1). Variants in a predicted enhancer of *CRKL* are significantly associated with the risk of congenital heart defects in DGS/VCFS [94]. Approximately 12% of *Crkl*-null mice show mild cranial bone defects, such as small cranium and poor membranous ossification of the nasal bones [56]. Compound heterozygosity of *Crkl* and *Tbx1* in mice has revealed that *Crkl* deletion enhances DGS/VCFS-related abnormalities compared with *Tbx1*-heterozygous embryos [56], suggesting that *Tbx1* and *Crkl* genes act in the same genetic pathway. *CRKL* encodes an adaptor protein that promotes the intracellular response of FGF signaling. *Crkl*<sup>+/-</sup>;*Fgf8*<sup>+/-</sup> double heterozygous mice showed DGS/VCFS-related defects [95]. Thus, *CRKL* mutations cause or modify DGS/VCFS-related phenotypes and/or penetrance as a contiguous gene syndrome.

#### 4.6. Aldehyde Dehydrogenase Family 1, Subfamily A2 (*Aldh1a2/Raldh2*)

Retinoic acid (RA), an active vitamin A derivative, is essential for various developmental processes in vertebrates. High levels of RA act as morphogens that cause phenocopies of DGS/VCFS by downregulating *Tbx1* expression in the pharyngeal apparatus [96,97]. RA levels are balanced by the RA-synthesizing enzyme aldehyde dehydrogenase (ALDH) and the Cyp26 RA-catabolizing enzyme [98,99]. Mouse embryos hypomorphic for *Aldh1a2/Raldh2* display DGS/VCFS-related cardiovascular, thymic, and parathyroid malformations [57]. Haploinsufficiency of *Aldh1a2/Raldh2* results in reduced embryonic synthesis of RA, increased levels of *Tbx1*, and accelerated recovery from ar-

terial growth delay in *Tbx1*-heterozygous mice [100]. An inhibitor of the Cyp26 enzyme induces a phenocopy of DGS/VCFS in chick embryos [101]. In *Tbx1*-null mice, upregulated expression of *Aldh1a2/Raldh2* and downregulated expression of *Cyp26a1* have been observed [71].

Further interactions occur between RA signaling, *Crkl*, and *Tbx1*. The penetrance of thymic hypoplasia is reduced in *Crkl<sup>+/-</sup>;Tbx1<sup>+/-</sup>;Aldh1a2<sup>+/-</sup>* triple heterozygous embryos compared to *Crkl<sup>+/-</sup>;Tbx1<sup>+/-</sup>* mutants, suggesting that reducing the amount of RA may rescue the DGS/VCFS-related phenotype [102]. Thus, the levels of RA in embryogenesis could contribute to the phenotypic variability of DGS/VCFS.

#### 4.7. Homeobox A3 (*Hoxa3*)

RA exposure increases the expression of *Hoxa3*, a gene which encodes a homeobox transcription factor, in the neural tube and pharyngeal apparatus [103]. Interestingly, *Hoxa3*-null neonates show some aspects of the abnormalities of DGS/VCFS [58,104] (Table S2). Thus, *HOXA3* may be a genetic modifier of DGS/VCFS-related abnormalities.

#### 4.8. *Kat6a/Moz/Myst3* (Lysine Acetyltransferase 6A) and Epigenetic Modifiers

Homozygous mutation of *Kat6a/Moz/Myst3*, which encodes a histone acetyltransferase, leads to cardiovascular defects seen in DGS/VCFS and reduces *Tbx1* expression [59]. Treatment of pregnant mice with a histone demethylase inhibitor reportedly increased the methylation levels of histone H3 lysine K4 (H3K4) and partially rescued the cardiovascular phenotypes of *Tbx1*-heterozygous mice [105]. TBX1 regulates genes transcribed at a low level by recruiting lysine methyltransferase (KMT2C) and controlling monomethylation of H3K4 (H3K4me1) enrichment on chromatin [105]. In addition, TBX1 transcriptionally targets *Wnt5a* by interacting with SMARCD1/BAF60a, a component of the SWI/SNF-like BAF chromatin remodeling complex, along with the H3K4 monomethyltransferase SETD7 [106]. Microduplication in *KANSL1*, which encodes a member of the histone acetyltransferase complex, is associated with heart anomalies in individuals with DGS/VCFS [107]. In T cells of patients with DGS/VCFS, the status of transcriptional activation (H3K4me3 and H3K27ac) is globally increased [108]. Thus, epigenetic changes are involved in DGS/VCFS-related phenotypes.

#### 4.9. Sonic Hedgehog (*Shh*)

*Shh* encodes an SHH signaling molecule. In humans, *SHH* mutations lead to holoprosencephaly 3 (OMIM #142945), microphthalmia with coloboma (OMIM #611638), and single median maxillary central incisor (OMIM #147250). *Shh*-null embryos exhibit conotruncal and pharyngeal arch artery defects similar to those observed in DGS/VCFS and *Tbx1*-null embryos [109]. *Tbx1* expression is reduced in *Shh*-null embryos, and ectopic expression of *Shh* can result in the upregulation of *Tbx1*, suggesting that *Shh* is a possible modifier for DGS/VCFS [62,110]. *Shh* is also required for the expression of the Fox family of transcription factor genes, forkhead box A2 (*Foxa2*) and forkhead box C2 (*Foxc2*), in the head mesenchyme and the pharyngeal endoderm [62]. FOXA2 and FOXC2 bind to regulatory regions in the mouse and human *TBX1* loci [111].

#### 4.10. Paired-like Homeodomain Transcription Factor 2 (*Pitx2*)

*Pitx2* gene encodes a bicoid-like homeodomain transcription factor. *Pitx2*-null mice show craniofacial defects, such as the arrest of tooth development, abnormal morphology of maxilla and mandible, and cleft palate. In humans, *PITX2* mutations lead to Axenfeld–Rieger syndrome, type 1 (OMIM #180500). Patients with Axenfeld–Rieger syndrome manifest dental and craniofacial anomalies involving the maxilla, mandible, and cranial base [112]. Both *Tbx1* and *Pitx2* are expressed in the early dental epithelium, oral epithelium, and secondary heart field [64,113,114]. *Tbx1<sup>+/-</sup>;Pitx2<sup>+/-</sup>* double heterozygous embryos exhibit increased penetrance of an extra premolar-like tooth [115] and DGS/VCFS-related cardiovascular anomalies [114]. TBX1 directly activates the *Pitx2c* enhancer through

the synergistic action of the homeobox-containing transcription factor NK2 homeobox 5 (NKX2-5) [114]. TBX1 also interacts with PITX2 and represses PITX2 transcriptional activity [48,115]. Thus, *PITX2* may be a genetic modifier of DGS/VCFS-related abnormalities.

## 5. Discussion

The penetrance and severity of congenital anomalies are related to genetic and environmental factors. Recent studies have revealed the function of TBX1 and modifiers that impact the severity and penetrance of DGS/VCFS. Studies of DGS/VCFS mouse models have provided insights into signaling pathways and genes that interact with TBX1 and/or affect the DGS/VCFS phenotypes. In addition, mouse models with DGS/VCFS may help us to identify additional DGS/VCFS-related phenotypes. For example, there is potential to examine the phenotypes of cranial synchondroses, cranium, zygomatic arches, and pharyngeal muscles in DGS/VCFS patients. We also noted that information about ocular phenotypes in *Tbx1*-mutant mice is limited, although these anomalies in patients with DGS/VCFS have been reported [16,17]. Crosstalk with key embryonic signals, especially BMP, TGF $\beta$ , VEGFA, FGF, RA, and SHH, critically regulates DGS/VCFS-related pharyngeal development. Genes involved in these signaling pathways may modify the phenotypic spectrum of DGS/VCFS. Given the broad spectrum of DGS/VCFS disease phenotypes, other genes essential to craniofacial development could modify the phenotypic spectrum. Genetically engineered mice are useful for studying disease phenotypes; however, ablation of essential genes involved in cardiovascular development may cause early embryonic lethality, which would prevent observation of craniofacial phenotypes. For example, ablation of *Ufd1*, whose human ortholog has been mapped to the 1.5 Mb region, causes early embryonic lethality before organogenesis in mice [116]. It is also essential to identify novel proteins that interact with TBX1 and examine whether interacting partners may influence the phenotypes of mouse models.

## 6. Conclusions

Studies of *Tbx1*-mutant mice have provided insights into the underlying pathogenesis of DGS/VCFS and the knowledge to diagnose patients with DGS/VCFS. Genes, miRNAs, and epigenetics could change *Tbx1* expression. Polymorphisms, variations, and mutations in *TBX1* may induce the penetrance and severity of DGS/VCFS-like craniofacial phenotypes. The molecular basis of the variant sequence of *TBX1* will further define how *TBX1* contributes to the craniofacial and other phenotypes of DGS/VCFS. Since interactions with TBX1 and other molecules in transcriptional complexes or chromatin remodeling are crucial for TBX1 function, identifying and understanding these genetic and epigenetic modifiers individually for each patient may direct therapeutics to minimize the severity.

**Supplementary Materials:** The following are available online at <https://www.mdpi.com/article/10.3390/jdb10020018/s1>, Figure S1: Craniofacial and skeletal phenotypes of DGS/VCFS. Figure S2: Human genes in the proximal deletion of 1.5 Mb on the 22q11.2 locus. Table S1: Craniofacial and skeletal phenotypes of DGS/VCFS and *Tbx1*-null mice. Table S2: Craniofacial and skeletal phenotypes in mouse models of DGS/VCFS. Table S3: Classification of mouse genes associated with DGS/VCFS.

**Author Contributions:** N.F. contributed to the conceptual idea, performed the database searches, analyzed the data, and wrote the manuscript. All authors have read and agreed to the published version of the manuscript.

**Funding:** This work was supported by the Japan Society for the Promotion of Science (JSPS) KAKENHI [20K09901].

**Institutional Review Board Statement:** Not applicable.

**Informed Consent Statement:** Not applicable.

**Acknowledgments:** We would like to thank Hiroshi Kurosaka, Cedric Boeckx, and Mizuki Funato for a critical reading of the manuscript.

**Conflicts of Interest:** The author declares no conflict of interest.

## References

1. Tézenas Du Montcel, S.; Mendizabai, H.; Aymé, S.; Lévy, A.; Philip, N. Prevalence of 22q11 microdeletion. *J. Med. Genet.* **1996**, *33*, 719. [CrossRef] [PubMed]
2. Lopez-Rivera, E.; Liu, Y.P.; Verbitsky, M.; Anderson, B.R.; Capone, V.P.; Otto, E.A.; Yan, Z.; Mitrotti, A.; Martino, J.; Steers, N.J.; et al. Genetic Drivers of Kidney Defects in the DiGeorge Syndrome. *N. Engl. J. Med.* **2017**, *376*, 742–754. [CrossRef] [PubMed]
3. Du, Q.; de la Morena, M.T.; van Oers, N.S.C. The Genetics and Epigenetics of 22q11.2 Deletion Syndrome. *Front. Genet.* **2019**, *10*, 1365. [CrossRef] [PubMed]
4. Gorlin, R.J.; Cohen, M.M., Jr.; Hennekam, R.C.M. *Syndromes of the Head and the Neck*; Oxford University Press: New York, NY, USA, 2001; pp. 850–853.
5. Yagi, H.; Furutani, Y.; Hamada, H.; Sasaki, T.; Asakawa, S.; Minoshima, S.; Ichida, F.; Joo, K.; Kimura, M.; Imamura, S.; et al. Role of TBX1 in human del22q11.2 syndrome. *Lancet* **2003**, *362*, 1366–1373. [CrossRef]
6. Jerome, L.A.; Papaioannou, V.E. DiGeorge syndrome phenotype in mice mutant for the T-box gene, Tbx1. *Nat. Genet.* **2001**, *27*, 286–291. [CrossRef]
7. Lindsay, E.A.; Vitelli, F.; Su, H.; Morishima, M.; Huynh, T.; Pramparo, T.; Jurecic, V.; Ogunrinu, G.; Sutherland, H.F.; Scambler, P.J.; et al. Tbx1 haploinsufficiency in the DiGeorge syndrome region causes aortic arch defects in mice. *Nature* **2001**, *410*, 97–101. [CrossRef]
8. Merscher, S.; Funke, B.; Epstein, J.A.; Heyer, J.; Puech, A.; Lu, M.M.; Xavier, R.J.; Demay, M.B.; Russell, R.G.; Factor, S.; et al. TBX1 is responsible for cardiovascular defects in velo-cardio-facial/DiGeorge syndrome. *Cell* **2001**, *104*, 619–629. [CrossRef]
9. Hu, T.; Yamagishi, H.; Maeda, J.; McAnally, J.; Yamagishi, C.; Srivastava, D. Tbx1 regulates fibroblast growth factors in the anterior heart field through a reinforcing autoregulatory loop involving forkhead transcription factors. *Development* **2004**, *131*, 5491–5502. [CrossRef]
10. Liao, J.; Kochilas, L.; Nowotschin, S.; Arnold, J.S.; Aggarwal, V.S.; Epstein, J.A.; Brown, M.C.; Adams, J.; Morrow, B.E. Full spectrum of malformations in velo-cardio-facial syndrome/DiGeorge syndrome mouse models by altering Tbx1 dosage. *Hum. Mol. Genet.* **2004**, *13*, 1577–1585. [CrossRef]
11. Baldini, A. Dissecting contiguous gene defects: TBX1. *Curr. Opin. Genet. Dev.* **2005**, *15*, 279–284. [CrossRef]
12. Aggarwal, V.S.; Morrow, B.E. Genetic modifiers of the physical malformations in velo-cardio-facial syndrome/DiGeorge syndrome. *Dev. Disabil. Res. Rev.* **2008**, *14*, 19–25. [CrossRef] [PubMed]
13. Papangelis, I.; Scambler, P. The 22q11 deletion: DiGeorge and velocardiofacial syndromes and the role of TBX1. *Wiley Interdiscip. Rev. Dev. Biol.* **2013**, *2*, 393–403. [CrossRef] [PubMed]
14. Heliövaara, A.; Ranta, R.; Rautio, J. Pharyngeal morphology in children with submucous cleft palate with and without surgery. *Eur. Arch. Oto-Rhino-Laryngol. Head Neck* **2005**, *262*, 534–538. [CrossRef] [PubMed]
15. Heliövaara, A.; Hurmerinta, K. Craniofacial cephalometric morphology in children with CATCH 22 syndrome. *Orthod. Craniofac. Res.* **2006**, *9*, 186–192. [CrossRef]
16. Ryan, A.K.; Goodship, J.A.; Wilson, D.I.; Philip, N.; Levy, A.; Seidel, H.; Schuffenhauer, S.; Oechsler, H.; Belohradsky, B.; Prieur, M.; et al. Spectrum of clinical features associated with interstitial chromosome 22q11 deletions: A European collaborative study. *J. Med. Genet.* **1997**, *34*, 798–804. [CrossRef]
17. McDonald-McGinn, D.M.; Kirschner, R.; Goldmuntz, E.; Sullivan, K.; Eicher, P.; Gerdes, M.; Moss, E.; Solot, C.; Wang, P.; Jacobs, I.; et al. The Philadelphia story: The 22q11.2 deletion: Report on 250 patients. *Genet. Couns.* **1999**, *10*, 11–24.
18. Klingberg, G.; Oskarsdóttir, S.; Johannesson, E.L.; Norén, J.G. Oral manifestations in 22q11 deletion syndrome. *Int. J. Paediatr. Dent.* **2002**, *12*, 14–23.
19. Ricchetti, E.T.; States, L.; Hosalkar, H.S.; Tamai, J.; Maisenbacher, M.; McDonald-McGinn, D.M.; Zackai, E.H.; Drummond, D.S. Radiographic study of the upper cervical spine in the 22q11.2 deletion syndrome. *J. Bone Joint Surg. Am.* **2004**, *86*, 1751–1760. [CrossRef]
20. Herman, S.B.; Guo, T.; McGinn, D.M.M.; Bolsa, A.; Shanske, A.L.; Bassett, A.S.; Chow, E.W.C.; Bowser, M.; Sheridan, M.; Beemer, F.; et al. Overt cleft palate phenotype and TBX1 genotype correlations in velo-cardio-facial/DiGeorge/22q11.2 deletion syndrome patients. *Am. J. Med. Genet. A* **2012**, *158A*, 2781–2787. [CrossRef]
21. Hamidi, M.; Nabi, S.; Husein, M.; Mohamed, M.E.; Tay, K.Y.; McKillop, S. Cervical spine abnormalities in 22q11.2 deletion syndrome. *Cleft Palate-Craniofacial J.* **2014**, *51*, 230–233. [CrossRef]
22. Jackson, O.; Crowley, T.B.; Sharkus, R.; Smith, R.; Jeong, S.; Solot, C.; McDonald-McGinn, D. Palatal evaluation and treatment in 22q11.2 deletion syndrome. *Am. J. Med. Genet. Part A* **2019**, *179*, 1184–1195. [CrossRef] [PubMed]
23. Bassett, A.S.; Chow, E.W.C.; Husted, J.; Weksberg, R.; Caluseriu, O.; Webb, G.D.; Gatzoulis, M.A. Clinical features of 78 adults with 22q11 Deletion Syndrome. *Am. J. Med. Genet. A* **2005**, *138*, 307–313. [CrossRef] [PubMed]
24. Loos, E.; Verhaert, N.; Willaert, A.; Devriendt, K.; Swillen, A.; Hermans, R.; Op de Beeck, K.; Hens, G. Malformations of the middle and inner ear on CT imaging in 22q11 deletion syndrome. *Am. J. Med. Genet. Part A* **2016**, *170*, 2975–2983. [CrossRef] [PubMed]
25. Verheij, E.; Kist, A.L.; Mink van der Molen, A.B.; Stegeman, I.; van Zanten, G.A.; Grolman, W.; Thomeer, H.G.X.M. Otologic and audiological findings in 22q11.2 deletion syndrome. *Eur. Arch. Oto-Rhino-Laryngol. Head Neck* **2017**, *274*, 765–771. [CrossRef]



26. Ford, L.C.; Sulprizio, S.L.; Rasgon, B.M. Otolaryngological manifestations of velocardiofacial syndrome: A retrospective review of 35 patients. *Laryngoscope* **2000**, *110*, 362–367. [CrossRef]
27. Kobrynski, L.J.; Sullivan, K.E. Velocardiofacial syndrome, DiGeorge syndrome: The chromosome 22q11.2 deletion syndromes. *Lancet* **2007**, *370*, 1443–1452. [CrossRef]
28. Oberoi, S.; Vargervik, K. Velocardiofacial syndrome with single central incisor. *Am. J. Med. Genet. A* **2005**, *132A*, 194–197. [CrossRef]
29. Zhang, Z.; Huynh, T.; Baldini, A. Mesodermal expression of Tbx1 is necessary and sufficient for pharyngeal arch and cardiac outflow tract development. *Development* **2006**, *133*, 3587–3595. [CrossRef]
30. Arnold, J.S.; Werling, U.; Braunstein, E.M.; Liao, J.; Nowotschin, S.; Edelmann, W.; Hebert, J.M.; Morrow, B.E. Inactivation of Tbx1 in the pharyngeal endoderm results in 22q11DS malformations. *Development* **2006**, *133*, 977–987. [CrossRef]
31. Arnold, J.S.; Braunstein, E.M.; Ohyama, T.; Groves, A.K.; Adams, J.C.; Brown, M.C.; Morrow, B.E. Tissue-specific roles of Tbx1 in the development of the outer, middle and inner ear, defective in 22q11DS patients. *Hum. Mol. Genet.* **2006**, *15*, 1629–1639. [CrossRef]
32. Choi, M.; Klingensmith, J. Chordin is a modifier of tbx1 for the craniofacial malformations of 22q11 deletion syndrome phenotypes in mouse. *PLoS Genet.* **2009**, *5*, e1000395. [CrossRef] [PubMed]
33. Moraes, F.; Novoa, A.; Jerome-Majewska, L.A.; Papaioannou, V.E.; Mallo, M. Tbx1 is required for proper neural crest migration and to stabilize spatial patterns during middle and inner ear development. *Mech. Dev.* **2005**, *122*, 199–212. [CrossRef] [PubMed]
34. Funato, N.; Nakamura, M.; Richardson, J.A.; Srivastava, D.; Yanagisawa, H. Tbx1 regulates oral epithelial adhesion and palatal development. *Hum. Mol. Genet.* **2012**, *21*, 2524–2537. [CrossRef] [PubMed]
35. Funato, N.; Nakamura, M.; Richardson, J.A.; Srivastava, D.; Yanagisawa, H. Loss of Tbx1 induces bone phenotypes similar to cleidocranial dysplasia. *Hum. Mol. Genet.* **2015**, *24*, 424–435. [CrossRef] [PubMed]
36. Funato, N.; Srivastava, D.; Shibata, S.; Yanagisawa, H. TBX1 Regulates Chondrocyte Maturation in the Spheno-occipital Synchronosis. *J. Dent. Res.* **2020**, *99*, 1182–1191. [CrossRef]
37. Solot, C.B.; Sell, D.; Mayne, A.; Baylis, A.L.; Persson, C.; Jackson, O.; McDonald-McGinn, D.M. Speech-Language Disorders in 22q11.2 Deletion Syndrome: Best Practices for Diagnosis and Management. *Am. J. Speech-Lang. Pathol.* **2019**, *28*, 984–999. [CrossRef]
38. Jaouadi, A.; Tabebi, M.; Abdelhedi, F.; Abid, D.; Kamoun, F.; Chabchoub, I.; Maatoug, S.; Doukali, H.; Belghuith, N.; Ksentini, M.A.; et al. A novel TBX1 missense mutation in patients with syndromic congenital heart defects. *Biochem. Biophys. Res. Commun.* **2018**, *499*, 563–569. [CrossRef]
39. Zweier, C.; Sticht, H.; Aydin-Yaylagül, I.; Campbell, C.E.; Rauch, A. Human TBX1 Missense Mutations Cause Gain of Function Resulting in the Same Phenotype as 22q11.2 Deletions. *Am. J. Hum. Genet.* **2007**, *80*, 510–517. [CrossRef]
40. Hasegawa, K.; Tanaka, H.; Higuchi, Y.; Hayashi, Y.; Kobayashi, K.; Tsukahara, H. Novel heterozygous mutation in TBX1 in an infant with hypocalcemic seizures. *Clin. Pediatr. Endocrinol.* **2018**, *27*, 159–164. [CrossRef]
41. Alghamdi, M.; Al Khalifah, R.; Al Homyani, D.K.; Alkhamis, W.H.; Arold, S.T.; Ekhzaimy, A.; El-Wetidy, M.; Kashour, T.; Halwani, R. A novel TBX1 variant causing hypoparathyroidism and deafness. *J. Endocr. Soc.* **2020**, *4*, bvz028. [CrossRef]
42. Ogata, T.; Niihori, T.; Tanaka, N.; Kawai, M.; Nagashima, T.; Funayama, R.; Nakayama, K.; Nakashima, S.; Kato, F.; Fukami, M.; et al. TBX1 mutation identified by exome sequencing in a Japanese family with 22q11.2 deletion syndrome-like craniofacial features and hypocalcemia. *PLoS ONE* **2014**, *9*, e91598. [CrossRef] [PubMed]
43. Paylor, R.; Glaser, B.; Mupo, A.; Ataliotis, P.; Spencer, C.; Sobotka, A.; Sparks, C.; Choi, C.H.; Oghalai, J.; Curran, S.; et al. Tbx1 haploinsufficiency is linked to behavioral disorders in mice and humans: Implications for 22q11 deletion syndrome. *Proc. Natl. Acad. Sci. USA* **2006**, *103*, 7729–7734. [CrossRef] [PubMed]
44. Rauch, R.; Hofbeck, M.; Zweier, C.; Koch, A.; Zink, S.; Trautmann, U.; Hoyer, J.; Kaulitz, R.; Singer, H.; Rauch, A. Comprehensive genotype-phenotype analysis in 230 patients with tetralogy of Fallot. *J. Med. Genet.* **2010**, *47*, 321–331. [CrossRef] [PubMed]
45. Stark, K.L.; Xu, B.; Bagchi, A.; Lai, W.-S.; Liu, H.; Hsu, R.; Wan, X.; Pavlidis, P.; Mills, A.A.; Karayiorgou, M.; et al. Altered brain microRNA biogenesis contributes to phenotypic deficits in a 22q11-deletion mouse model. *Nat. Genet.* **2008**, *40*, 751–760. [CrossRef]
46. Edelmann, L.; Stankiewicz, P.; Spiteri, E.; Pandita, R.K.; Shaffer, L.; Lupski, J.R.; Morrow, B.E.; Lupski, J. Two functional copies of the DGCR6 gene are present on human chromosome 22q11 due to a duplication of an ancestral locus. *Genome Res.* **2001**, *11*, 208–217. [CrossRef]
47. Hierck, B.P.; Molin, D.G.M.; Boot, M.J.; Poelmann, R.E.; Gittenberger-De Groot, A.C. A chicken model for DGCR6 as a modifier gene in the DiGeorge critical region. *Pediatr. Res.* **2004**, *56*, 440–448. [CrossRef]
48. Gao, S.; Moreno, M.; Eliason, S.; Cao, H.; Li, X.; Yu, W.; Bidlack, F.B.; Margolis, H.C.; Baldini, A.; Amendt, B.A. TBX1 protein interactions and microRNA-96-5p regulation controls cell proliferation during craniofacial and dental development: Implications for 22q11.2 deletion syndrome. *Hum. Mol. Genet.* **2015**, *24*, 2330–2348. [CrossRef]
49. Sun, H.; Jiang, P. MicroRNA-451a acts as tumor suppressor in cutaneous basal cell carcinoma. *Mol. Genet. Genom. Med.* **2018**, *6*, 1001–1009. [CrossRef]
50. Wang, J.; Bai, Y.; Li, H.; Greene, S.B.; Klysik, E.; Yu, W.; Schwartz, R.J.; Williams, T.J.; Martin, J.F. MicroRNA-17-92, a direct Ap-2alpha transcriptional target, modulates T-box factor activity in orofacial clefting. *PLoS Genet.* **2013**, *9*, e1003785. [CrossRef]

51. Kaimal, V.; Bardes, E.E.; Tabar, S.C.; Jegga, A.G.; Aronow, B.J. ToppCluster: A multiple gene list feature analyzer for comparative enrichment clustering and network-based dissection of biological systems. *Nucleic Acids Res.* **2010**, *38*, W96–102. [CrossRef]
52. Bachiller, D.; Klingensmith, J.; Shneyder, N.; Tran, U.; Anderson, R.; Rossant, J.; De Robertis, E.M. The role of chordin/Bmp signals in mammalian pharyngeal development and DiGeorge syndrome. *Development* **2003**, *130*, 3567–3578. [CrossRef] [PubMed]
53. Wurdak, H.; Ittner, L.M.; Lang, K.S.; Leveen, P.; Suter, U.; Fischer, J.A.; Karlsson, S.; Born, W.; Sommer, L. Inactivation of TGF $\beta$  signaling in neural crest stem cells leads to multiple defects reminiscent of DiGeorge syndrome. *Genes Dev.* **2005**, *19*, 530–535. [CrossRef] [PubMed]
54. Stalmans, I.; Lambrechts, D.; De Smet, F.; Jansen, S.; Wang, J.; Maity, S.; Kneer, P.; von der Ohe, M.; Swillen, A.; Maes, C.; et al. VEGF: A modifier of the del22q11 (DiGeorge) syndrome? *Nat. Med.* **2003**, *9*, 173–182. [CrossRef] [PubMed]
55. Abu-Issa, R.; Smyth, G.; Smoak, I.; Yamamura, K.; Meyers, E.N. Fgf8 is required for pharyngeal arch and cardiovascular development in the mouse. *Development* **2002**, *129*, 4613–4625. [CrossRef]
56. Guris, D.L.; Fantès, J.; Tara, D.; Druker, B.J.; Imamoto, A. Mice lacking the homologue of the human 22q11.2 gene CRLK phenocopy neurocristopathies of DiGeorge syndrome. *Nat. Genet.* **2001**, *27*, 293–298. [CrossRef]
57. Vermot, J.; Niederreither, K.; Garnier, J.M.; Chambon, P.; Dollé, P. Decreased embryonic retinoic acid synthesis results in a DiGeorge syndrome phenotype in newborn mice. *Proc. Natl. Acad. Sci. USA* **2003**, *100*, 1763–1768. [CrossRef]
58. Chisaka, O.; Capecchi, M.R. Regionally restricted developmental defects resulting from targeted disruption of the mouse homeobox gene *hox-1.5*. *Nature* **1991**, *350*, 473–479. [CrossRef]
59. Voss, A.K.; Vanyai, H.K.; Collin, C.; Dixon, M.P.; McLennan, T.J.; Sheikh, B.N.; Scambler, P.; Thomas, T. MOZ Regulates the Tbx1 Locus, and Moz Mutation Partially Phenocopies DiGeorge Syndrome. *Dev. Cell* **2012**, *23*, 652–663. [CrossRef]
60. Sheehy, N.T.; Cordes, K.R.; White, M.P.; Ivey, K.N.; Srivastava, D. The neural crest-enriched microRNA miR-452 regulates epithelial-mesenchymal signaling in the first pharyngeal arch. *Development* **2010**, *137*, 4307–4316. [CrossRef]
61. Gershwin, M.E. DiGeorge syndrome: Congenital thymic hypoplasia. Animal model: Congenitally athymic (nude) mouse. *Am. J. Pathol.* **1977**, *89*, 809–812.
62. Yamagishi, H.; Maeda, J.; Hu, T.; McAnally, J.; Conway, S.J.; Kume, T.; Meyers, E.N.; Yamagishi, C.; Srivastava, D. Tbx1 is regulated by tissue-specific forkhead proteins through a common Sonic hedgehog-responsive enhancer. *Genes Dev.* **2003**, *17*, 269–281. [CrossRef] [PubMed]
63. Chapman, D.L.; Garvey, N.; Hancock, S.; Alexiou, M.; Agulnik, S.I.; Gibson-Brown, J.J.; Cebra-Thomas, J.; Bollag, R.J.; Silver, L.M.; Papaioannou, V.E. Expression of the T-box family genes, Tbx1–Tbx5, during early mouse development. *Dev. Dyn.* **1996**, *206*, 379–390. [CrossRef]
64. Zoupa, M.; Seppala, M.; Mitsiadis, T.; Cobourne, M.T. Tbx1 is expressed at multiple sites of epithelial-mesenchymal interaction during early development of the facial complex. *Int. J. Dev. Biol.* **2006**, *50*, 504–510. [CrossRef] [PubMed]
65. Zhang, Z.; Cerrato, F.; Xu, H.; Vitelli, F.; Morishima, M.; Vincentz, J.; Furuta, Y.; Ma, L.; Martin, J.F.; Baldini, A.; et al. Tbx1 expression in pharyngeal epithelia is necessary for pharyngeal arch artery development. *Development* **2005**, *132*, 5307–5315. [CrossRef]
66. Aggarwal, V.S.; Carpenter, C.; Freyer, L.; Liao, J.; Petti, M.; Morrow, B.E. Mesodermal Tbx1 is required for patterning the proximal mandible in mice. *Dev. Biol.* **2010**, *344*, 669–681. [CrossRef]
67. Bush, J.O.; Jiang, R. Palatogenesis: Morphogenetic and molecular mechanisms of secondary palate development. *Development* **2012**, *139*, 828. [CrossRef]
68. Funato, N. Molecular basis of cleft palates in mice. *World J. Biol. Chem.* **2015**, *6*, 121. [CrossRef]
69. Goudy, S.; Law, A.; Sanchez, G.; Baldwin, H.S.; Brown, C. Tbx1 is necessary for palatal elongation and elevation. *Mech. Dev.* **2010**, *127*, 292–300. [CrossRef]
70. Peters, H.; Neubuser, A.; Kratochwil, K.; Balling, R. Pax9-deficient mice lack pharyngeal pouch derivatives and teeth and exhibit craniofacial and limb abnormalities. *Genes Dev.* **1998**, *12*, 2735–2747. [CrossRef]
71. Ivins, S.; Van Beuren, K.L.; Roberts, C.; James, C.; Lindsay, E.; Baldini, A.; Ataliotis, P.; Scambler, P.J. Microarray analysis detects differentially expressed genes in the pharyngeal region of mice lacking Tbx1. *Dev. Biol.* **2005**, *285*, 554–569. [CrossRef]
72. Funato, N.; Yanagisawa, H. Deletion of the T-box transcription factor gene, Tbx1, in mice induces differential expression of genes associated with cleft palate in humans. *Arch. Oral Biol.* **2018**, *95*, 149–155. [CrossRef] [PubMed]
73. Komori, T.; Yagi, H.; Nomura, S.; Yamaguchi, A.; Sasaki, K.; Deguchi, K.; Shimizu, Y.; Bronson, R.T.; Gao, Y.H.; Inada, M.; et al. Targeted disruption of Cbfa1 results in a complete lack of bone formation owing to maturational arrest of osteoblasts. *Cell* **1997**, *89*, 755–764. [CrossRef]
74. Otto, F.; Thornell, A.P.; Crompton, T.; Denzel, A.; Gilmour, K.C.; Rosewell, I.R.; Stamp, G.W.; Beddington, R.S.; Mundlos, S.; Olsen, B.R.; et al. Cbfa1, a candidate gene for cleidocranial dysplasia syndrome, is essential for osteoblast differentiation and bone development. *Cell* **1997**, *89*, 765–771. [CrossRef]
75. Mundlos, S.; Otto, F.; Mundlos, C.; Mulliken, J.B.; Aylsworth, A.S.; Albright, S.; Lindhout, D.; Cole, W.G.; Henn, W.; Knoll, J.H.; et al. Mutations involving the transcription factor CBFA1 cause cleidocranial dysplasia. *Cell* **1997**, *89*, 773–779. [CrossRef]
76. Funato, N. New Insights Into Cranial Synchronosis Development: A Mini Review. *Front. Cell Dev. Biol.* **2020**, *8*, 706. [CrossRef]
77. Catón, J.; Luder, H.U.; Zoupa, M.; Bradman, M.; Bluteau, G.; Tucker, A.S.; Klein, O.; Mitsiadis, T.A. Enamel-free teeth: Tbx1 deletion affects amelogenesis in rodent incisors. *Dev. Biol.* **2009**, *328*, 493–505. [CrossRef]

78. Kelly, R.G.; Jerome-Majewska, L.A.; Papaioannou, V.E. The del22q11.2 candidate gene Tbx1 regulates branchiomic myogenesis. *Hum. Mol. Genet.* **2004**, *13*, 2829–2840. [CrossRef]
79. Kong, P.; Racedo, S.E.; Macchiarulo, S.; Hu, Z.; Carpenter, C.; Guo, T.; Wang, T.; Zheng, D.; Morrow, B.E. Tbx1 is required autonomously for cell survival and fate in the pharyngeal core mesoderm to form the muscles of mastication. *Hum. Mol. Genet.* **2014**, *23*, 4215–4231. [CrossRef]
80. Harel, I.; Maezawa, Y.; Avraham, R.; Rinon, A.; Ma, H.Y.; Cross, J.W.; Leviatan, N.; Hegesh, J.; Roy, A.; Jacob-Hirsch, J.; et al. Pharyngeal mesoderm regulatory network controls cardiac and head muscle morphogenesis. *Proc. Natl. Acad. Sci. USA.* **2012**, *109*, 18839–18844. [CrossRef]
81. Grifone, R.; Jarry, T.; Dandonneau, M.; Grenier, J.; Duprez, D.; Kelly, R.G. Properties of branchiomic and somite-derived muscle development in Tbx1 mutant embryos. *Dev. Dyn.* **2008**, *237*, 3071–3078. [CrossRef]
82. Pane, L.S.; Zhang, Z.; Ferrentino, R.; Huynh, T.; Cuttillo, L.; Baldini, A. Tbx1 is a negative modulator of Mef2c. *Hum. Mol. Genet.* **2012**, *21*, 2485–2496. [CrossRef] [PubMed]
83. Dong, F.; Sun, X.; Liu, W.; Ai, D.; Klysiak, E.; Lu, M.F.; Hadley, J.; Antoni, L.; Chen, L.; Baldini, A.; et al. Pitx2 promotes development of splanchnic mesoderm-derived branchiomic muscle. *Development* **2006**, *133*, 4891–4899. [CrossRef] [PubMed]
84. Shih, H.P.; Gross, M.K.; Kioussi, C. Cranial muscle defects of Pitx2 mutants result from specification defects in the first branchial arch. *Proc. Natl. Acad. Sci. USA* **2007**, *104*, 5907–5912. [CrossRef] [PubMed]
85. Papangeli, I.; Scambler, P.J. Tbx1 genetically interacts with the transforming growth factor- $\beta$ /bone morphogenetic protein inhibitor Smad7 during great vessel remodeling. *Circ. Res.* **2013**, *112*, 90–102. [CrossRef]
86. Vieira, J.M.; Ruhrberg, C.; Schwarz, Q. VEGF receptor signaling in vertebrate development. *Organogenesis* **2010**, *6*, 97–106. [CrossRef]
87. Lambrechts, D.; Devriendt, K.; Driscoll, D.A.; Goldmuntz, E.; Gewillig, M.; Vlietinck, R.; Collen, D.; Carmeliet, P. Low expression VEGF haplotype increases the risk for tetralogy of Fallot: A family based association study. *J. Med. Genet.* **2005**, *42*, 519–522. [CrossRef]
88. Frank, D.U.; Fotheringham, L.K.; Brewer, J.A.; Muglia, L.J.; Tristani-Firouzi, M.; Capecchi, M.R.; Moon, A.M. An Fgf8 mouse mutant phenocopies human 22q11 deletion syndrome. *Development* **2002**, *129*, 4591–4603. [CrossRef]
89. Vitelli, F.; Taddei, I.; Morishima, M.; Meyers, E.N.; Lindsay, E.A.; Baldini, A. A genetic link between Tbx1 and fibroblast growth factor signaling. *Development* **2002**, *129*, 4605–4611. [CrossRef]
90. Brown, C.B.; Wenning, J.M.; Lu, M.M.; Epstein, D.J.; Meyers, E.N.; Epstein, J.A. Cre-mediated excision of Fgf8 in the Tbx1 expression domain reveals a critical role for Fgf8 in cardiovascular development in the mouse. *Dev. Biol.* **2004**, *267*, 190–202. [CrossRef]
91. Mitsiadis, T.A.; Tucker, A.S.; De Bari, C.; Cobourne, M.T.; Rice, D.P.C. A regulatory relationship between Tbx1 and FGF signaling during tooth morphogenesis and ameloblast lineage determination. *Dev. Biol.* **2008**, *320*, 39–48. [CrossRef]
92. Lin, C.-Y.; Chen, W.-T.; Lee, H.-C.; Yang, P.-H.; Yang, H.-J.; Tsai, H.-J. The transcription factor Six1a plays an essential role in the craniofacial myogenesis of zebrafish. *Dev. Biol.* **2009**, *331*, 152–166. [CrossRef] [PubMed]
93. Guo, C.; Sun, Y.; Zhou, B.; Adam, R.M.; Li, X.; Pu, W.T.; Morrow, B.E.; Moon, A.; Li, X. A Tbx1-Six1/Eya1-Fgf8 genetic pathway controls mammalian cardiovascular and craniofacial morphogenesis. *J. Clin. Investig.* **2011**, *121*, 1585–1595. [CrossRef] [PubMed]
94. Zhao, Y.; Diacou, A.; Johnston, H.R.; Musfee, F.I.; McDonald-McGinn, D.M.; McGinn, D.; Crowley, T.B.; Repetto, G.M.; Swillen, A.; Breckpot, J.; et al. Complete Sequence of the 22q11.2 Allele in 1,053 Subjects with 22q11.2 Deletion Syndrome Reveals Modifiers of Conotruncal Heart Defects. *Am. J. Hum. Genet.* **2020**, *106*, 26–40. [CrossRef] [PubMed]
95. Moon, A.M.; Guris, D.L.; Seo, J.H.; Li, L.; Hammond, J.; Talbot, A.; Imamoto, A. Crkl deficiency disrupts Fgf8 signaling in a mouse model of 22q11 deletion syndromes. *Dev. Cell* **2006**, *10*, 71–80. [CrossRef] [PubMed]
96. Rosa, F.W.; Wilk, A.L.; Kelsey, F.O. Teratogen update: Vitamin A congeners. *Teratology* **1986**, *33*, 355–364. [CrossRef] [PubMed]
97. Roberts, C.; Ivins, S.M.; James, C.T.; Scambler, P.J. Retinoic acid down-regulates Tbx1 expression in vivo and in vitro. *Dev. Dyn.* **2005**, *232*, 928–938. [CrossRef] [PubMed]
98. Wendling, O.; Dennefeld, C.; Chambon, P.; Mark, M. Retinoid signaling is essential for patterning the endoderm of the third and fourth pharyngeal arches. *Development* **2000**, *127*, 1553–1562. [CrossRef]
99. Niederreither, K.; Vermot, J.; Le Roux, I.; Schuhbaur, B.; Chambon, P.; Dollé, P. The regional pattern of retinoic acid synthesis by RALDH2 is essential for the development of posterior pharyngeal arches and the enteric nervous system. *Development* **2003**, *130*, 2525–2534. [CrossRef]
100. Ryckebüsch, L.; Bertrand, N.; Mesbah, K.; Bajolle, F.; Niederreither, K.; Kelly, R.G.; Zaffran, S. Decreased levels of embryonic retinoic acid synthesis accelerate recovery from arterial growth delay in a mouse model of DiGeorge syndrome. *Circ. Res.* **2010**, *106*, 686–694. [CrossRef]
101. Roberts, C.; Ivins, S.; Cook, A.C.; Baldini, A.; Scambler, P.J. Cyp26 genes a1, b1 and c1 are down-regulated in Tbx1 null mice and inhibition of Cyp26 enzyme function produces a phenocopy of DiGeorge Syndrome in the chick. *Hum. Mol. Genet.* **2006**, *15*, 3394–3410. [CrossRef]
102. Guris, D.L.; Duester, G.; Papaioannou, V.E.; Imamoto, A. Dose-dependent interaction of Tbx1 and Crkl and locally aberrant RA signaling in a model of del22q11 syndrome. *Dev. Cell* **2006**, *10*, 81–92. [CrossRef] [PubMed]

103. Mulder, G.B.; Manley, N.; Maggio-Price, L. Retinoic acid-induced thymic abnormalities in the mouse are associated with altered pharyngeal morphology, thymocyte maturation defects, and altered expression of *Hoxa3* and *Pax1*. *Teratology* **1998**, *58*, 263–275. [CrossRef]
104. Chen, L.; Zhao, P.; Wells, L.; Amemiya, C.T.; Condie, B.G.; Manley, N.R. Mouse and zebrafish *Hoxa3* orthologues have nonequivalent in vivo protein function. *Proc. Natl. Acad. Sci. USA* **2010**, *107*, 10555–10560. [CrossRef] [PubMed]
105. Fulcoli, F.G.; Franzese, M.; Liu, X.; Zhang, Z.; Angelini, C.; Baldini, A. Rebalancing gene haploinsufficiency in vivo by targeting chromatin. *Nat. Commun.* **2016**, *7*, 11688. [CrossRef] [PubMed]
106. Chen, L.; Fulcoli, F.G.; Ferrentino, R.; Martucciello, S.; Illingworth, E.A.; Baldini, A. Transcriptional control in cardiac progenitors: *Tbx1* interacts with the BAF chromatin remodeling complex and regulates *Wnt5a*. *PLoS Genet.* **2012**, *8*, e1002571. [CrossRef]
107. León, L.E.; Benavides, F.; Espinoza, K.; Vial, C.; Alvarez, P.; Palomares, M.; Lay-Son, G.; Miranda, M.; Repetto, G.M. Partial microduplication in the histone acetyltransferase complex member *KANSL1* is associated with congenital heart defects in 22q11.2 microdeletion syndrome patients. *Sci. Rep.* **2017**, *7*, 1795. [CrossRef]
108. Zhang, Z.; Shi, L.; Song, L.; Maurer, K.; Zhao, X.; Zackai, E.H.; McGinn, D.E.; Crowley, T.B.; McGinn, D.M.M.; Sullivan, K.E. Chromatin Modifications in 22q11.2 Deletion Syndrome. *J. Clin. Immunol.* **2021**, *41*, 1853–1864. [CrossRef]
109. Washington Smoak, I.; Byrd, N.A.; Abu-Issa, R.; Goddeeris, M.M.; Anderson, R.; Morris, J.; Yamamura, K.; Klingensmith, J.; Meyers, E.N. Sonic hedgehog is required for cardiac outflow tract and neural crest cell development. *Dev. Biol.* **2005**, *283*, 357–372. [CrossRef]
110. Garg, V.; Yamagishi, C.; Hu, T.; Kathiriyai, I.S.; Yamagishi, H.; Srivastava, D. *Tbx1*, a DiGeorge syndrome candidate gene, is regulated by sonic hedgehog during pharyngeal arch development. *Dev. Biol.* **2001**, *235*, 62–73. [CrossRef]
111. Kou, I.; Otomo, N.; Takeda, K.; Momozawa, Y.; Lu, H.-F.; Kubo, M.; Kamatani, Y.; Ogura, Y.; Takahashi, Y.; Nakajima, M.; et al. Genome-wide association study identifies 14 previously unreported susceptibility loci for adolescent idiopathic scoliosis in Japanese. *Nat. Commun.* **2019**, *10*, 3685. [CrossRef]
112. Brooks, J.K.; Coccaro, P.J.; Zarbin, M.A. The Rieger anomaly concomitant with multiple dental, craniofacial, and somatic midline anomalies and short stature. *Oral Surg. Oral Med. Oral Pathol.* **1989**, *68*, 717–724. [CrossRef]
113. Mucchielli, M.L.; Mitsiadis, T.A.; Raffo, S.; Brunet, J.F.; Proust, J.P.; Goridis, C. Mouse *Otlx2*/RIEG expression in the odontogenic epithelium precedes tooth initiation and requires mesenchyme-derived signals for its maintenance. *Dev. Biol.* **1997**, *189*, 275–284. [CrossRef] [PubMed]
114. Nowotschin, S.; Liao, J.; Gage, P.J.; Epstein, J.A.; Campione, M.; Morrow, B.E. *Tbx1* affects asymmetric cardiac morphogenesis by regulating *Pitx2* in the secondary heart field. *Development* **2006**, *133*, 1565–1573. [CrossRef] [PubMed]
115. Cao, H.; Florez, S.; Amen, M.; Huynh, T.; Skobe, Z.; Baldini, A.; Amendt, B.A. *Tbx1* regulates progenitor cell proliferation in the dental epithelium by modulating *Pitx2* activation of p21. *Dev. Biol.* **2010**, *347*, 289–300. [CrossRef]
116. Lindsay, E.A.; Botta, A.; Jurecic, V.; Carattini-Rivera, S.; Cheah, Y.C.; Rosenblatt, H.M.; Bradley, A.; Baldini, A. Congenital heart disease in mice deficient for the DiGeorge syndrome region. *Nature* **1999**, *401*, 379–383. [CrossRef]



Review

# A Review of Delayed Delivery Models and the Analysis Method in Mice

Hiroschi Yomogita <sup>1,2</sup> , Naoyuki Miyasaka <sup>1</sup> and Masami Kanai-Azuma <sup>2,\*</sup>

<sup>1</sup> Department of Perinatal and Women's Medicine, Tokyo Medical and Dental University, Tokyo 113-8510, Japan; yomocrm@tmd.ac.jp (H.Y.); n.miyasaka.gyne@tmd.ac.jp (N.M.)

<sup>2</sup> Center for Experimental Animals, Tokyo Medical and Dental University, Tokyo 113-8510, Japan

\* Correspondence: mkanai.arc@tmd.ac.jp; Tel.: +813-3813-6111

**Abstract:** In humans, the incidence of post-term delivery is 1–10%. Post-term delivery significantly increases the risk of cesarean section or neonatal intensive care unit (NICU) admission. Despite these serious challenges, the cause of prolonged delivery remains unclear. Several common factors of delayed parturition between mice and humans will help elucidate the mechanisms of pregnancy and labor. At present, gene modification techniques are rapidly developing; however, there are limited reviews available describing the mouse phenotype analysis as a human model for post-term delivery. We classified the delayed-labor mice into nine types according to their causes. In mice, progesterone (P<sub>4</sub>) maintains pregnancy, and the most common cause of delayed labor is luteolysis failure. Other contributing factors include humoral molecules in the fetus/placenta, uterine contractile dysfunction, poor cervical ripening, and delayed implantation. The etiology of delayed parturition is overexpression of the pregnancy maintenance mechanism or suppression of the labor induction mechanism. Here, we describe how to investigate their causes using mouse genetic analysis. In addition, we generated a list to identify the causes. Our review will help understand the findings obtained using the mouse model, providing a foundation for conducting more systematic research on delayed delivery.

**Citation:** Yomogita, H.; Miyasaka, N.; Kanai-Azuma, M. A Review of Delayed Delivery Models and the Analysis Method in Mice. *J. Dev. Biol.* **2022**, *10*, 20. <https://doi.org/10.3390/jdb10020020>

Academic Editors: Tsutomu Nohno, Hideyo Ohuchi and Simon J. Conway

Received: 7 April 2022

Accepted: 17 May 2022

Published: 20 May 2022

**Publisher's Note:** MDPI stays neutral with regard to jurisdictional claims in published maps and institutional affiliations.



**Copyright:** © 2022 by the authors. Licensee MDPI, Basel, Switzerland. This article is an open access article distributed under the terms and conditions of the Creative Commons Attribution (CC BY) license (<https://creativecommons.org/licenses/by/4.0/>).

**Keywords:** prolonged delivery; delayed delivery; progesterone; luteolysis

## 1. Introduction

Placental–fetal–maternal close signal interactions are essential for pregnancy and labor. Imbalances between these factors cause abnormalities during the gestation period. Recently, several mice with delayed labor have been reported due to abnormal development of the fetus and placenta. In humans, the incidence of post-term delivery is 1–10% [1]. Post-term delivery significantly increases the risk of cesarean section or neonatal intensive care unit (NICU) admission. Despite these serious challenges, the cause of prolonged delivery remains unclear. Primates have similar-evolved villous placentas. In many studies, mouse pregnancy has been used as a model of human pregnancy. At present, gene modification techniques are rapidly developing; however, there are limited reviews to describe mouse phenotype analysis as a human model for post-term delivery. To elucidate, the effects of fetal and placental developmental abnormalities on delayed labor, we reviewed genetically modified mice that cause delayed labor. We reviewed the causes of delayed births and investigated them using mouse genetic analysis.

## 2. Normal Progression of Pregnancy and Labor Onset in Mice

Parturition is divided into two phases, pregnancy and labor, which correlate with changes in the cervix and myometrium (Figure 1). The cervix, a cylindrical tissue, is the lower part of the uterus and is used as the birth canal. During pregnancy, the cervix is firm and closed. It protects the fetus from microorganisms and acts as a barrier between

intrauterine and extrauterine conditions. The cervix gradually softens as pregnancy progresses. The uterine myometrium is quiescent and does not respond to natural stimuli. In the labor phase, the cervix is soft and elastic, which is referred to as ‘cervical ripening’. Cervical ripening is caused by the decomposition of collagen and glycosaminoglycans (the main material of the cervix). The uterine myometrium contracts collaboratively and provides sufficient pressure to eliminate the fetus and placenta. Cervical ripening and uterine contractions are essential delivery processes, hence if either is missing, labor does not progress. The pregnancy-maintenance mechanism suppresses cervical ripening and uterine contractions. In the labor phase, the pregnancy-maintenance mechanism weakens, while the labor-induction mechanism is strengthened. Therefore, cervical ripening and uterine contractions occur. To deliver at term, the two mechanisms must switch at the right time. Delayed delivery occurs when the pregnancy-maintenance mechanism is excessively long or when the labor-induction mechanism is weak. A proper balance between the two systems is essential for normal pregnancy and delivery.

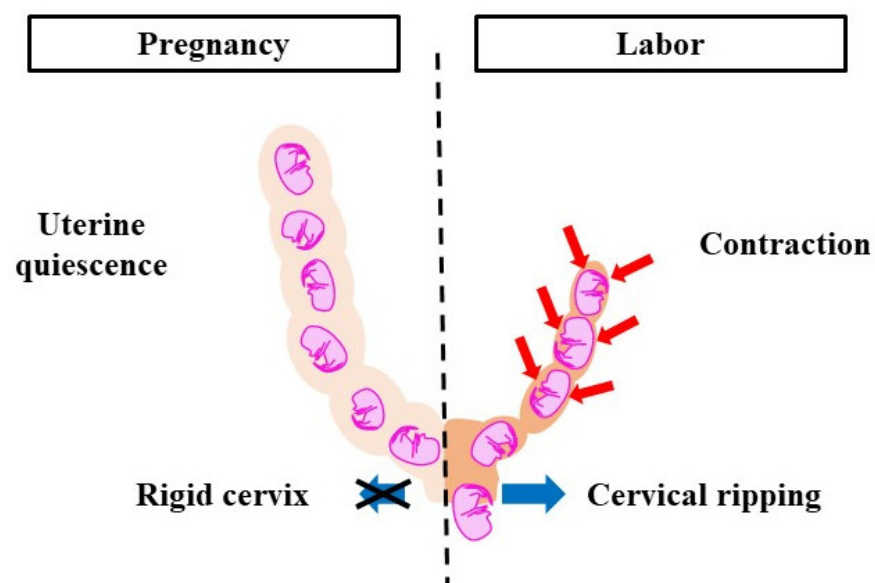


**Figure 1.** Pregnancy-maintenance mechanism and labor-induction mechanism. During pregnancy, uterine contractions do not occur and the cervical canal is immature. During labor, uterine contractions are activated and cervical ripening is promoted. To deliver at term, the pregnancy-maintenance mechanism and labor-induction mechanism need to work at the right time. Red arrows: contraction, blue arrows: cervical dilation.

### 3. Factors of Pregnancy Maintenance and Labor Induction

In rodents, progesterone ( $P_4$ ) has the strongest pregnancy-maintenance effect.  $P_4$  is secreted by the corpus luteum in pregnant mice, and suppresses labor-induction substances, such as prostaglandins (PGs) and oxytocin receptor (OTR). At 18.5 days post coitum (dpc), serum  $P_4$  declines rapidly because of luteolysis and  $P_4$  withdrawal increases the levels of the labor-inducing substances (Figure 2).

Other substances that maintain pregnancy include relaxin and placental lactogen (PL), a part of the PRL family, which can maintain the corpus luteum. Human placental lactogen (hPL) does not maintain pregnancy. In contrast, mouse placental lactogen 1 (mPL1) and mouse placental lactogen 2 (mPL2) prevent luteolysis.

Labor-inducing substances include oxytocin,  $PGE_2$  (prostaglandin E2),  $PGF2\alpha$  (prostaglandin F2 $\alpha$ ), their receptors, and connexin (Cx). These are collectively referred to as contractile-associated proteins (CAPS).

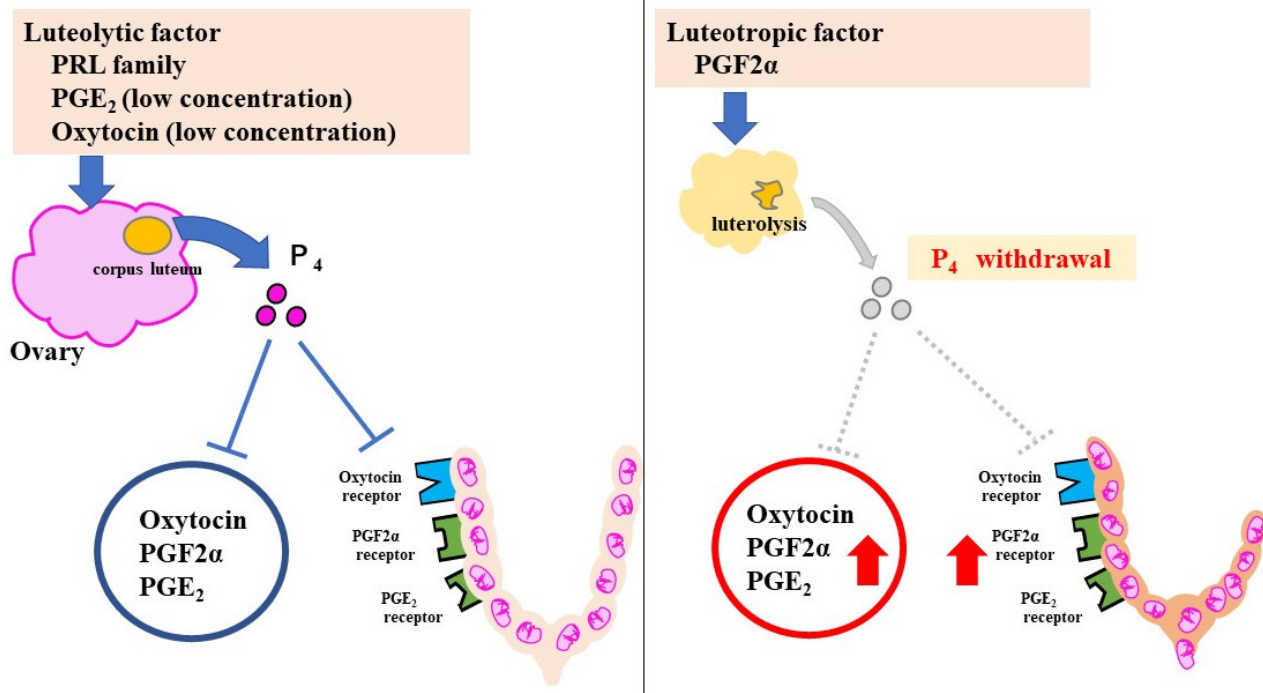


**Figure 2.** Pregnancy-maintenance and parturition mechanisms in mice. The luteolytic factor maintains the corpus luteum during pregnancy.  $P_4$  suppresses CAPS. Luteolysis at 18.5 dpc causes a sharp decrease in  $P_4$ . With an increase in CAPS, uterine contractions and cervical ripening progress rapidly. The red Arrows indicate increased effect.

Oxytocin, a hormone secreted by the pituitary gland, has a uterine contraction effect and is used as a labor-inducing agent in humans; however, *oxytocin* knockout (*OT* KO) mice can normally deliver [2]. Oxytocin is not essential for delivery. In oxytocin-administration experiments in *OT* KO mice, low concentrations of oxytocin maintained the corpus luteum and caused delayed labor and high concentrations of oxytocin enhanced uterine contractions and caused preterm delivery [3]. It is, therefore, difficult to elucidate the mechanism of labor since these molecules show different functions depending on the site and timing.

PG is a bioactive lipid produced from free arachidonic acid. PG is produced by phospholipase A (PLA) 2 and Cox; Cox1 and Cox2 are rate-limiting enzymes. There are various types of PG, such as D2, E2, F2 $\alpha$ , and G12, all of which have a different function.  $PGF2\alpha$  and  $PGE_2$  are used as labor-inducing agents in humans.

$PGF2\alpha$  also has a luteolytic effect in mice.  $PGE_2$  has a cervical-ripening effect and causes weak uterine contractions. However,  $PGE_2$  may also have an indirect luteotropic effect [4]. Since PG has a short half-life and acts locally around the secretory site, it is characterized by different functions depending on the site of action.

Cx is a protein that forms gap junctions, which are cell–cell conjugations. Gap junctions play a role in the exchange of calcium ions between cells. When Cx43 is abundantly expressed in the myometrium, gap junctions also increase. Gap junctions are important for cooperative uterine contractions.

#### 4. Classification by Cause of Labor Delay

We searched the literature published between 1970 and 2022 and classified 26 mice according to the cause of delayed labor (Table 1).



**Table 1.** Classification of genetically modified mice that exhibit delayed delivery (official name: abbreviation). We searched the literature published between 1970 and 2020, and classified the 26 mice according to the cause of delayed labor.

1. Failure of luteolysis <i>Prostaglandin F Receptor</i> knockout mouse: <i>Fp</i> KO [5,6] <i>Cyclooxygenase-1</i> -deficient mouse: <i>Cox1</i> KO [7] <i>20<math>\alpha</math> hydroxysteroid dehydrogenase</i> -deficient mice: <i>20<math>\alpha</math> Hsd</i> KO [8] <i>G<math>\alpha_q</math><sup>fl/fl</sup>;G<math>\alpha_{11}</math><sup>-/-</sup>;Cre<sup>+</sup></i> mice: <i>Gq/11</i> cKO [9] <i>Mastermind-like domain-containing 1</i> knockout mouse: <i>Mamld1</i> KO [10]
2. Abnormalities in progesterone metabolism and receptors <i>Kruppel-like factor 9</i> knockout mouse: <i>Klf 9</i> KO [11] <i>Cytochrome p450 family 11a1</i> -overexpression mouse: <i>Cyp11a1</i> Tg [12]
3. Fetal factors <i>Surfactant protein A and D</i> double-deficient mice: <i>Sp A/D</i> dKO [13] <i>Steroid receptor coactivator 1 and 2</i> double-deficient mice: <i>Src 1/2</i> dKO [14]
4. Placental factors <i>Solute carrier organic anion transporter family member 2A1</i> knockout mouse: <i>Slco2a1</i> KO [4] <i>Sushi-ichi retrotransposon homolog 7/Leucine zipper, downregulated cancer 1</i> knockout mouse: <i>Sirh7/Ldoc1</i> KO [15] <i>Nik-related kinase</i> knockout mouse: <i>Nrk</i> KO [16]
5. Autoimmune disorder <i>Toll-like receptor 2</i> -deficient mice: <i>Tlr 2</i> KO [13] <i>Toll-like receptor 4</i> -deficient mice: <i>Tlr 4</i> KO [17] <i>Interleukin 6</i> null mutant mice: <i>Il6</i> KO [18]
6. Uterine contractile dysfunction <i>Connexin 43<sup>fl/fl</sup>:SM-CreER<sup>T2</sup></i> mice: <i>Sm-CreER<sup>T2</sup></i> KO [19] <i>Kcnn3<sup>tm1</sup>pad/Kcnn3<sup>tm1</sup>pad</i> : <i>Sk3<sup>T/T</sup></i> mice [20] <i>Anthrax toxin receptor 2</i> knockout mice: <i>Antxr 2</i> KO [21]
7. Poor cervical ripening <i>5<math>\alpha</math> reductase type 1</i> knockout mice: <i>5<math>\alpha</math>R1</i> KO [22,23] <i>TgN(hApoB)1102SY</i> line: <i>Tg/Tg</i> mouse [24] <i>Anthrax toxin receptor 2</i> knockout mice: <i>Antxr 2</i> KO [21]
8. Delayed implantation <i>Cytosolic phosphatase A2</i> mutant mouse: <i>Pla2g4a</i> KO [25–27] <i>Lysophosphatidic acid receptor 3</i> -deficient mouse: <i>LPA3</i> KO [28]
9. Unknown cause <i>Erk 1 and Erk 2</i> conditional knockout mouse: <i>Erk1/2</i> cKO [29] <i>Leptin</i> KO mouse: <i>Leptin</i> KO [30] <i>Mt mER</i> mouse [31] <i>Activin/inhibin <math>\beta</math>B subunit</i> -deficient mouse: <i>Activin/inhibin <math>\beta</math>B subunit</i> dKO [32]

#### 4.1. Failure of Luteolysis

The most common cause of delayed delivery in genetically modified mice is the absence of P<sub>4</sub> withdrawal due to the failure of luteolysis. The decrease in serum P<sub>4</sub> can be confirmed by measuring approximately 18.5 dpc. Ovariectomy and administration of RU486 (a P<sub>4</sub> antagonist) are methods to determine whether P<sub>4</sub> maintains pregnancy [5,33]. Wild-type mice are delivered within 24 h using these methods [5,33].

There are two phases in the degeneration of the corpus luteum: functional and structural degeneration. Functional degeneration is associated with P<sub>4</sub> withdrawal. The enhanced action of 20 $\alpha$ -hydroxysteroid dehydrogenase (20 $\alpha$ HSD), which inactivates P<sub>4</sub>, reduces serum P<sub>4</sub> levels. Meanwhile, in structural degeneration, apoptosis of pregnant luteal cells is enhanced, replacement of capillaries and connective tissue occurs, and the size and weight of the corpus luteum decreased rapidly. Structural degeneration can be confirmed by exenteration of the ovaries after 18.5 dpc and observing them with hematoxylin–eosin staining and/or tunnel staining.

#### 4.1.1. Prostaglandin F Receptor Knockout Mouse: *Fp* KO

One of the most famous genetically modified mice with delayed delivery is *Fp*-KO. In 1997, Sugimoto et al. produced mice to investigate the physiological function of  $\text{PGF}_2\alpha$  [5]. *Fp* KO mice that lack the prostaglandin F receptor (FP) do not deliver and absorb their fetuses in utero [5]. The  $\text{P}_4$  level of *Fp* KO mice did not decrease at 18.5 dpc [5]. *Fp* KO mice with both ovaries removed at 19.5 dpc delivered within 24 h [5]. Luteolysis failure is the cause of the delayed delivery. This report suggests that  $\text{PGF}_2$  leads to luteolysis in pregnant mice.

In *Fp* KO at 19.5 dpc, ovariectomy leads to the expression of oxytocin, OTR, and *Cox2* [6]. When *Cox2* selective inhibitor was administered to these mice, labor did not occur [6]. Labor after luteolysis is caused by COX-2-derived PGs in the myometrium [6]. In wild-type mice, *Cox2* selective inhibitor leads to prolonged delivery [34]. Conversely, in humans, *Cox2* selective inhibitors restrict uterine contractions and have been investigated as a treatment to prevent preterm delivery [35].

#### 4.1.2. *Cox1*-Deficient Mouse: *Cox1* KO

The average gestation period of *Cox1* KO mice is  $21.6 \pm 0.2$  days [7]. These mice showed no sharp  $\text{P}_4$  decline and had a luteal regression disorder [7]. *Cox1* KO in late pregnancy results in a decreased amount of  $\text{PGF}_2\alpha$  in the uterus [7]. The administration of  $\text{PGF}_2\alpha$  to mice improved delayed delivery [7]. This research suggests that the cause of delayed parturition in mice is a failure of luteolysis due to a decrease in  $\text{PGF}_2\alpha$  levels [7]. The uterine contractions of *Cox1* KO mice were the same as those of wild-type mice, but the cervix was immature [33]. The cause of delayed labor in mice may also be related to poor cervical ripening due to impaired PG production.

#### 4.1.3. $20\alpha$ Hydroxysteroid Dehydrogenase-Deficient Mice: $20\alpha$ *Hsd* KO

$20\alpha\text{HSD}$  is an enzyme that inactivates  $\text{P}_4$ .  $20\alpha$  *Hsd* KO caused delayed labor without  $\text{P}_4$  withdrawal [8]. Administration of  $\text{PGF}_2\alpha$  did not induce labor in these mice [8].  $20\alpha\text{HSD}$  is presumed to act downstream of  $\text{PGF}_2\alpha$  [8].

The expression of  $20\alpha\text{HSD}$  is controlled by various pathways (Figure 3). For example, PRL activates a transcription factor called *Stat5b* (signal transducer and activator of transcription 5 B) in the ovary [36]. Since *Stat5b* reduces the expression of  $20\alpha\text{HSD}$ , PRL has a luteotrophic function. In mice, the lack of *Stat5b* is associated with early abortion [8].

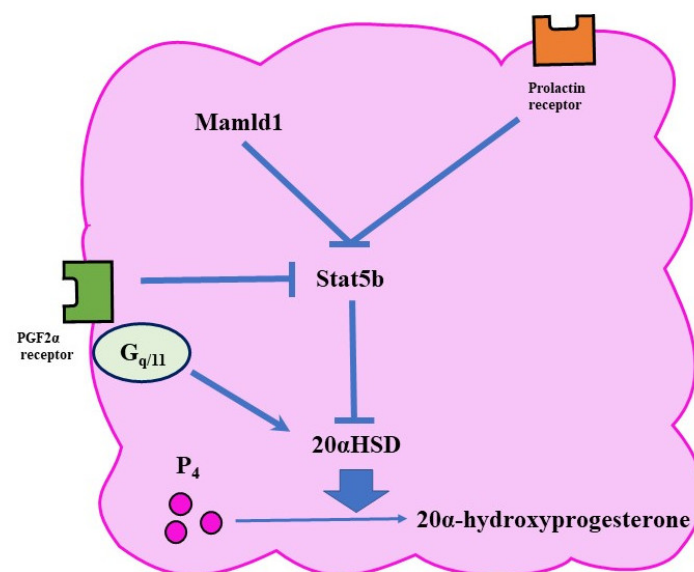


**Figure 3.** Functional luteolysis. Functional luteolysis is caused by the inactivation of  $\text{P}_4$  by  $20\alpha\text{HSD}$ . There are various pathways for regulating the expression of  $20\alpha\text{HSD}$ , such as the FP and prolactin-receptor pathways.

#### 4.1.4. $G\alpha q^{ff};G\alpha 11^{-/-};Cre+$ Mice: $Gq/11$ cKO

$G\alpha q/11$  is a G protein that binds to receptors on the surface of activated cell membranes and transmits signals to cells. It has been speculated that FP activates the PLC pathway via  $G\alpha q/11$  and activates  $20\alpha HSD$  in luteal cells [9].  $Gq/11$  cKO labor was prolonged without  $P_4$  withdrawal [9]. The mice showed decreased expression of  $Akr1c18$  (a gene encoding  $20\alpha HSD$ ) in the ovary [9]. Therefore, FP was presumed to stimulate  $Akr1c18$  expression and increase  $20\alpha HSD$  via the  $Gq/11$  phospholipase C pathway [9].

#### 4.1.5. Mastermind-Like Domain-Containing 1 Knockout Mouse: $Mamld1$ KO

$Mamld1$  is a gene that causes hypospadias in humans and its KO can delay parturition by approximately 50% [10]. In  $Mamld1$  KO,  $P_4$  withdrawal does not exist, and  $Akr1c18$  expression is decreased in the ovary [10].  $Mamld1$  suppresses  $Akr1c18$  by increasing  $Stat5$  expression [10]. Therefore, these mice suffer from functional luteal regression disorders.  $Mamld1$  is speculated to regress the corpus luteum by a different route to the FP pathway [10].

There are many regressive pathways in the corpus luteum, which are extremely complex. Further research is needed on the maintenance and disappearance of CL.

#### 4.2. Abnormalities in $P_4$ Metabolism and Receptors

The progesterone receptor (PR) has two different nuclear receptors, PRA and PRB, with different functions. PRA knockout mice are infertile, whereas PRB knockout mice suffer from mammary gland dysgenesis [37,38]. In humans, PRB suppresses  $Cx43$ ,  $Cox2$ , OTR, and  $NF\kappa\beta$  pathways and maintains pregnancy [39]. However, PRA suppresses PRB and induces labor [39].

##### 4.2.1. Kruppel-Like Factor 9 Knockout Mouse: $Klf 9$ KO

Kruppel-like factor 9 (KLF9) is a transcription factor for PRA and PRB (Figure 4). KLF9 deficiency in early pregnancy suppresses PR expression and reduces fertility [40]. The serum  $P_4$  level of  $Klf 9$  KO mice were the same as that of wild-type mice, but the gestation of  $Klf 9$  KO mice was longer than that of wild-type mice [11]. In these mice, PRB expression is presumed to increase owing to the decreased expression of PRA [11]. KLF9 is expressed in humans and decreased in patients with delayed delivery [41]. This factor may be involved in the mechanisms of pregnancy and delivery in humans [41].

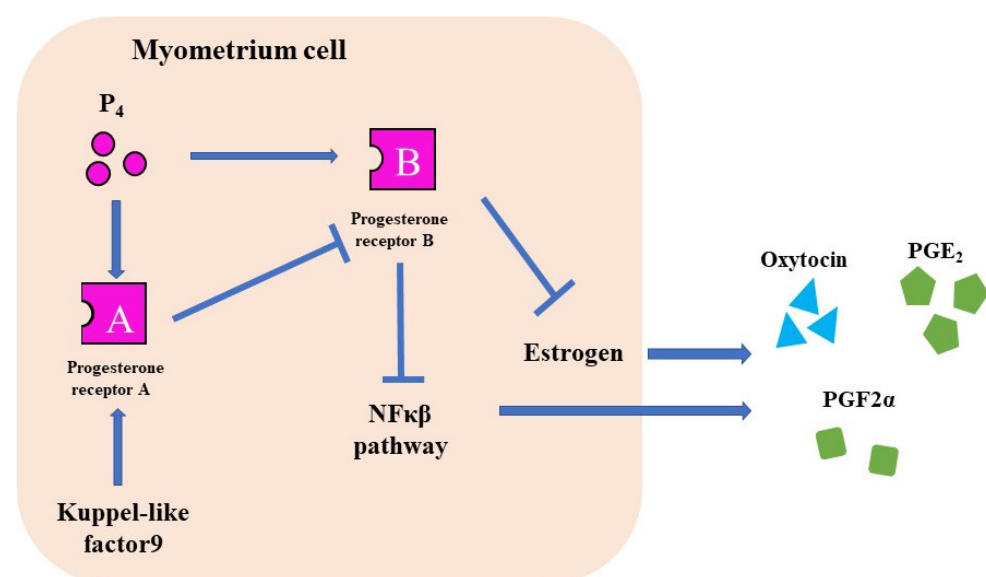


**Figure 4.** The function of  $P_4$  receptors. There are two types of PRs. PR-B suppresses CAPS and maintains pregnancy. PR-A induces labor induction by suppressing the PR-B.

In humans, the corpus luteum disappears during the second trimester of pregnancy. Therefore, P<sub>4</sub> withdrawal was not observed. The switching of progesterone receptors from PRB to PRA in late pregnancy is presumed to trigger labor induction [39,42].

#### 4.2.2. Cytochrome p450 Family 11a1-Overexpression Mouse: *Cyp11a1* Tg

*Cyp11a1* (P450scc) is an enzyme that produces P<sub>4</sub> from cholesterol. *Cyp11a1* knockout mice are fatal because of their inability to produce steroids and their underdeveloped fetal adrenal glands [43]. Chien et al., created a *Cyp11a1* Tg that overexpresses *Cyp11a1* [12]. The mice showed delayed maturation of the corpus luteum during early pregnancy, causing implantation abnormalities, placental dysplasia, and fetal development abnormalities [12]. The serum P<sub>4</sub> of *Cyp11a1* Tg mice was similar to that of wild-type mice in early pregnancy, but remained high in late pregnancy [12]. *Cyp11a1* Tg mice frequently show delayed parturition [12].

#### 4.3. Fetal Factors

In autosomal dominant inheritance, crossing genetically modified females with male wild-type mice can determine whether the cause of delayed labor is the mother or the placenta/fetus. If the cause was the mother, the mice showed delayed delivery, while this does not occur if the cause was the placenta or the fetus. This can also be examined by transplanting KO embryos into wild-type mice [16].

##### 4.3.1. Surfactant Protein A and D Double-Deficient Mice: *Sp A/D* dKO

Lung surfactant protein (Sp) is a lipoprotein produced in the lungs that assists breathing. There are four types of SP, A to D. SP-A is the most abundant and structurally similar to SP-D. SP is produced in the fetal lungs and then flows into the amniotic fluid. In humans, fetal lung maturity can be estimated by examining the SP in the amniotic fluid. SPA acts as the trigger of labor, because administration of Sp-A to the amniotic fluid of mice results in preterm birth [13]. *Sp A/D* dKO showed delayed delivery for approximately 12 h in the second and subsequent pregnancies [13]. Mice at 18.5 dpc had decreased expression of CAPS in the uterine muscle and decreased secretion of inflammatory cytokines from macrophages in the amniotic fluid [13]. The hypothesis that the Sp of the fetal lung can be the starting point for labor induction is particularly important since the fetus itself is involved in determining the time of labor.

##### 4.3.2. Steroid Receptor Coactivator 1 and 2 Double-Deficient Mice: *Src1/2* dKO

Steroid receptor coactivator 1 and 2 (*Src1/2*) (transcription factor of Sp-A) knockout mice showed prolonged delivery by 38 h [14]. These mice exhibited a reduction in Sp-A, PGF2 $\alpha$ , Cx43, and OXTR, a restricted NF- $\kappa$ B pathway, and P<sub>4</sub> withdrawal did not occur [14]. Interestingly, the higher the proportion of *Src1/2* KO fetuses, the higher the serum P<sub>4</sub> concentration in late pregnancy [14].

In these mice, platelet-activating factor (PAF) in the fetal lung and amniotic fluid was also reduced [14]. PAF is involved in several physiological events, such as platelet aggregation, inflammation, and anaphylaxis, and is produced in the fetal lung; its concentration in the amniotic fluid increases during late pregnancy [44]. Therefore, PAF was presumed to play an important role in the onset of labor and preterm delivery. Administration of PAF to *SRC-1/2* dKO increased NF- $\kappa$ B pathway activation and CAPS expression in the myometrium and improved delayed labor [14]. The results of this study suggest that PAF and SP-A may contribute to delivery.

#### 4.4. Placental Factors

When the placenta is the cause, abnormal placental development often occurs, such as in *Nrk* KO and *Sirh7/Ldoc1* KO mice [15,16]. The lentiviral vector (LV) or tetraploid chimera can determine whether the cause is the placenta or fetus. When LV is administered to mouse blastocysts, the gene is transferred only to the placenta [45]. LV rescue delayed

parturition due to placental factors. The tetraploid chimera utilizes the property that tetraploid embryonic cells contribute only to the placenta [46]. In chimeric mice established using wild-type diploid embryos and nuclear-transplanted cloned tetraploid embryos, delayed labor occurs when the cause is the placenta, but not when the cause is the fetus. In chimeras of wild-type tetraploid embryos and diploid embryos of nuclear-transplanted clones, the opposite result was observed.

#### 4.4.1. Solute Carrier Organic Anion Transporter Family Member 2A1 Knockout Mouse: *Slco2a1* KO

*Slco2a1* encodes OATP2A1, an organic anion-transporting polypeptide. OATP2A1 is a PG transporter that takes up extracellular PGs. Mating between *Slco2a1* KO mice resulted in prolonged labor in approximately 50% of mice [4], and this did not occur after mating with wild-type male mice. This suggests that the cause is fetal or placental factors, hence P<sub>4</sub> withdrawal does not occur [4]. The level of mPL2 is elevated in the placenta [4]. mPL-2 is a member of the prolactin family and is known to have a luteotropic effect. In cultured placental cells of the sponge layer (one of the layers of the placenta), PGE<sub>2</sub> enhances the secretion of mPL-2 [4]. *Slco2a1* KO maintains the corpus luteum by mPL-2 from the sponge layer of the placenta and causes delayed labor [4].

#### 4.4.2. Sushi Ichi Retrotransposon Homolog 7/Leucine Zipper, Downregulated Cancer 1 Knockout Mice: *Sirh7/Ldoc1* KO

*Sushi ichi retrotransposon homolog 7/leucine zipper (Sirh7/Ldoc1)* is a member of the long terminal repeat (LTR) retrotransposon-like gene family [15]. *Sirh7/Ldoc1* is an X-linked gene that is unique to eutherians; therefore, it is highly conserved in both mice and humans. *Sirh7/Ldoc1* KO showed a delayed delivery of approximately 1–4 days in 49% of mice due to residual P<sub>4</sub> at 18.5 dpc [15]. RU486 and ovariectomy improved prolonged delivery, suggesting that P<sub>4</sub> was the cause of prolonged delivery [15]. The mice had elevated levels of mPL1 as well as placental P<sub>4</sub> production and exhibited a delayed switch from mPL1 to mPL2 during mid-pregnancy [15]. Similar to mPL-2, mPL-1 also has a luteotropic function. MPL-1 has been proposed to be one of the causes of delayed delivery of *Sirh7/Ldoc1* KO [15]. The *Sirh7/Ldoc1* KO placenta also had an irregular boundary between the sponge and labyrinth layers.

#### 4.4.3. Nik-Related Kinase Knockout Mouse: *Nrk* KO

In 1996, *Nik-related kinase (Nrk)* was named by Kanai-Azuma et al. [47]. *Nrk* is another X-linked gene that is highly conserved in mice and humans, and its KO mice exhibit three phenotypes: overgrowth of the spongy layer of the placenta, high frequency of breast tumors, and prolonged parturition [16].

Wild-type dams with transplanted *Nrk* KO blastocysts showed delayed parturition, which suggests that the *Nrk* KO fetus or placenta is the cause of delayed delivery [16]. The P<sub>4</sub> and estrogen levels of *Nrk* KO mice were about the same as those of the wild-type at 17.5 and 19.5 dpc [16]. The report postulated that an unidentified soluble factor from the spongy layer protracts parturition [16]. However, they could not identify leading candidates.

#### 4.5. Autoimmune Disorder

Toll-like receptors (TLRs) are receptors on surface of cells such as macrophages and dendritic cells, that bind to different ligands. TLRs recognize pathogens and activate innate immunity. There are 1 to 13 types, each of which is a pattern-recognition receptor that binds to different ligands.

The model of preterm delivery of lipopolysaccharide (LPS) into mice at midgestation has been previously used. TLRs induce labor by activating the NF- $\kappa$ B pathway and increasing CAPs by recognizing inflammatory substances such as LPS [48]. Therefore, TLR is presumed to be a trigger for pathological preterm delivery due to bacterial infection. TLRs bind to non-inflammatory substances such as Sp-A and damage-associated molecular

patterns (DAMPs) emitted by stress, such as uterine stretch [49]. TLRs are also involved in the onset of normal labor.

#### 4.5.1. Toll-Like Receptor 2-Deficient Mice: *Tlr2* KO

Compared with wild-type mice, *Tlr2* KO mice showed a significant delay in the timing of labor during the first pregnancy, and a decrease in the amniotic fluid macrophages and Cx43 expression in the myometrium [13]. Sp-A/D diffuses from the fetal lung into the amniotic fluid, and binds to TLR2 in amniotic fluid macrophages [13]. Amniotic fluid macrophages secrete IL1b and IL6, which in turn activate the NF- $\kappa$ B pathway in the uterus and induce labor [13].

#### 4.5.2. Toll-Like Receptor 4-Deficient Mice: *Tlr4* KO

Since TLR4 binds to LPS and DAMPs, it is associated with both bacterial infection and aseptic preterm delivery [48,49]. The average gestation length of *Tlr4* KO mice was extended by 13 h [17]. The timing of FP, OTR, and Cx43 expression was delayed [34], and P<sub>4</sub> withdrawal did not occur [17]. Administration of a TLR4 antagonist to wild-type mice resulted in delayed delivery [17]. Therefore, TLR4 is presumed to play an important role in gestation.

#### 4.5.3. Interleukin 6 Null Mutant Mice: *Il6* KO

*Il6* KO mice delivered 24 h after wild-type mice, yet the P<sub>4</sub> level of the mice was equivalent to that of the wild-type [18]. *Il6* KO delayed the expression of FP and Cox2 in the myometrium, while administration of IL6 to *Il6* KO improved delayed delivery. IL6 is involved in the pathway after P<sub>4</sub> withdrawal and induces PG [18].

### 4.6. Uterine Contractile Dysfunction

Uterine contractile dysfunction refers to the lack of intrauterine pressure sufficient to push a fetus out of the uterus. It is caused by a weak contraction force of the uterine muscles and impairment of coordinated contractions. The intrauterine pressure should be measured directly to accurately observe labor.

There are in vitro and in vivo methods for measuring uterine contractile force. The contractile force of the removed uterine muscle can directly be measured in vitro [33]. Pure muscle contraction force can be measured, but the reproducibility of the in vivo environment is poor.

In vivo, there are two methods: surgical implantation of a pressure transducer and transvaginal insertion into the uterus. For surgical implantation, a pressure transducer is surgically implanted in the myometrium after laparotomy under anesthesia [50]. The advantage of this method is that intrauterine pressure can be continuously observed without anesthesia from pregnancy to delivery. However, special techniques are required, and the operation may cause fetal loss [50]. The transducer insertion method, which has also been used in humans, is less invasion of the dams [51]. This method had three disadvantages: limited insertion time, anesthesia was required at the time of the insertion, and the position of the inserted transducer was not identified [51].

#### 4.6.1. *Connexin 43<sup>fl/fl</sup>:Sm-CreER<sup>T2</sup>* mice: *Sm-CreER<sup>T2</sup>* KO

Delayed delivery was observed in 82% of mice [19]. Uterine contractions were not directly measured. The author reported that the cause of the abnormal delivery was insufficient contraction due to the loss of coordinated contraction of the uterine muscle [19].

#### 4.6.2. *Kcnn3<sup>tm1]pad</sup>/Kcnn3<sup>tm1]pad</sup>:Sk3<sup>T/T</sup>* mice

The small-conductance Ca<sup>2+</sup>-activated potassium channel isoform-3 (SK3 channel) is a selective potassium channel. *SK3<sup>T/T</sup>* mice overexpress SK3 channels [20]. The contractile force in these mice was attenuated in vivo [20]. Although the mechanism is unclear, the investigation showed that mice also experience abnormal labor due to weak uterine

contractions [20]. It has been reported that the SK3 channel is involved in delivery even in humans [52]. This research is expected to be applied to the treatment of preterm births.

#### 4.7. Poor Cervical Ripening

Almost 90% of the cervix is composed of an extracellular matrix, such as collagen and glycosaminoglycans. Cervical ripening is the decomposition of collagen and glycosaminoglycans during late pregnancy. In humans, cervical ripening is evaluated using pelvic examination. In mice, cervical ripening is often evaluated using pathological and biomechanical examinations. There are three pathological examinations: Masson trichrome staining (evaluation of collagen degradation), immunostaining (evaluation of neutrophils and monocytes), and Mayer's mucicarmine (evaluation of epithelial mucus volume) [22–24]. The pressure generated can be determined by mechanically dilating the removed cervix [22,24].

##### 4.7.1. *5 $\alpha$ -Reductase Type 1* Knockout Mice: *5 $\alpha$ R1* KO

*5 $\alpha$ -reductase* (*5 $\alpha$ R1*) is an enzyme involved in the production of dihydrotestosterone and the decomposition of testosterone. Thirty-three percent of *5 $\alpha$ R1* KO mice did not start delivery [23], while 25% of mothers had died [23]. These mice showed a decrease in blood  $P_4$ , but administration of RU486 improved delayed labor [23]. Uterine contractions of *5 $\alpha$ R1* KO mice were measured by surgical transducer implantation and were not different from those of wild-type mice [22]. The elasticity of the cervix decreased and pathologically, the cervix was poorly mature [22]. It has been speculated that the amount of  $P_4$  in the cervix is increased, resulting in poor cervical ripening and delayed delivery [22].

##### 4.7.2. *TgN(hApoB) 1102SY* Line: *Tg/Tg* Mouse

The *Tg/Tg* mouse is a strain that occurs by the insertion, by chance, of the human apolipoprotein B gene [24]. Mice exhibited delayed labor when the mother was a *Tg/Tg* mouse, regardless of the fetal genotype [24].  $P_4$  withdrawal was prolonged by one day compared to wild-type mice; administration of a  $P_4$  receptor antagonist (ZK98299) and ovariectomy did not improve prolonged delivery [24]. Uterine contractions were similar to those observed in wild-type mice, the cervix was not elastic, and pathological evaluation showed poor cervical ripening [24].

##### 4.7.3. *Anthrax Toxin Receptor 2* Knockout Mice: *Antxr2* KO

*Antxr2* has been postulated to be involved in the proliferation and development of the vascular endothelium, but its function is unknown. *Antxr2* KO mice exhibited a sharp drop in  $P_4$  but did not deliver [21]. The cervix was immature with no collagen degradation, while the myometrium had lost cricothyroid and longitudinal muscle cells [21]. The cause of delayed labor in the mice was poor cervical ripening and uterine contraction failure.

#### 4.8. Delayed Implantation

A common method of observing the implantation time is to inject a pigment such as Chicago blue into the tail vein 5 and 6 days after confirmation of the vaginal plug and direct observation of the implantation site [25]. If implantation is delayed, the number of fetuses changes. Delayed implantation often causes a reduction in litter size, fetal dysgenesis, and abnormal spacing.

##### 4.8.1. *Cytosolic Phosphatase A2* Mutant Mouse: *Pla2g4a* KO

Cytosolic phosphatase A2 (*Pla2g4a*) is an enzyme that produces PGs. *Pla2g4a* KO mice showed prolonged delivery, decreased fetal population, and increased stillbirth rate [26]. The number of implantations in mice increased at 6 dpc compared to that at 5 dpc [25]. The experiment suggested that the implantation period of the mice was delayed [25]. Administration of  $PGI_2$  and  $PGE_2$  to mice improved delayed implantation and prolonged delivery [27].

#### 4.8.2. *Lysophosphatidic Acid Receptor 3*-Deficient Mouse: *LPA3* KO

LPA is a lipid that has a signaling effect and is present in the ovaries, testes, and uterine muscles. There are six types of LPA receptors that have various functions in the reproductive process. Mating between *LPA3* KOs resulted in reduced litter size, delayed implantation, abnormal spacing, and prolonged delivery. In these mice, *Cox2*, *PGE<sub>2</sub>*, and *PGI<sub>2</sub>* are decreased in the uterus [28]. Administration of *PGE<sub>2</sub>* + *PGI<sub>2</sub>* to mice improved delayed implantation and prolonged parturition; similar to *Pla2g4a* KO, delayed implantation of *LPA3* KO is caused by a decrease in PGs [28].

In cattle, LPA promotes the secretion of *P<sub>4</sub>* and *PGE<sub>2</sub>* and maintains pregnancy [53]. Therefore, *LPA3* may be directly involved in prolonged parturition. It has been reported that in humans, LPA is associated with the maintenance of pregnancy and preterm birth [54]. Therefore, future studies on LPA are required.

#### 4.9. Unknown Cause

There are some mice for which the cause is unknown, such as when a delay in labor occurs by chance.

##### 4.9.1. *Erk1* and *Erk2* Conditional Knockout Mouse: *Erk1/2* cKO

Extracellular signal-regulated kinase (ERK) is an intermediate of the MAPK pathway. The MAPK pathway is involved in cell differentiation and cell division. *Erk1* KO was reproductive with no apparent abnormalities, but *Erk2* KO was fatal [55]. *Erk1/2* cKO mice showed abnormal placental development, delayed delivery on average of approximately 2.3 days, and death of offspring [29]. This may have been due to the abnormal placental development [29]. However, the cause of this phenomenon is unknown.

##### 4.9.2. *Leptin* KO Mouse: *Leptin* KO

Leptin is a hormone secreted by fat cells and the placenta and is related to the absorption of nutrients. *Leptin* KO mice were infertile because of an abnormality in the hypothalamic–pituitary system [56]. One study recovered pregnancy and childbirth by administering leptin [30]. *Leptin* KO mice that received leptin throughout gestation increased food intake and became obese compared to the mice that received leptin after that point [30]. The mice showed delayed parturition for approximately 1–3 days; the authors claimed that the cause may have been abnormal obesity [30]. However, to date, no detailed studies have been conducted.

##### 4.9.3. *MT-mER* Mouse

In 1994, Davis et al. published a study in which the estrogen receptor (ER) was forcibly expressed throughout the mouse body. These mice expressed ER in cells expressing the metallothionein-1 promoter. *MT-mER* mice showed delayed delivery for 4 days or more [31]. The *MT-mER* mouse strongly expressed ER in the gonads, but its expression in other tissues was weak. The authors concluded that the cause may have been the difference in the time and place of the ER [31]. However, there is no further description of this cause.

##### 4.9.4. *Activin/Inhibin βB Subunit*-Deficient Mouse: *Activin/Inhibin βB Subunit* dKO

Activin and inhibin are peptides produced in the gonads, pituitary gland, and placenta. The  $\beta$  subunit of activin is common to activin. Previously, activin was presumed to be a substance that induces the mesoderm. However, the *activin/inhibitor βB subunit* dKO showed morphological abnormalities only in the eyelids [32]. The mice showed mildly delayed labor of approximately half a day to a day, while in rats, the administration of activin to the pituitary gland increases blood oxytocin concentrations. Therefore, the authors concluded that a decrease in oxytocin may have been involved [32].



## 5. How to Identify the Cause of Delayed Labor in Mice

If genetically modified mice exhibit delayed labor, we recommend investigating the items presented in Table 2. This list can help to identify the cause of delayed labor more accurately and efficiently.

**Table 2.** List for finding the cause of delayed delivery. If genetically modified mice exhibit delayed labor, we recommend investigating the items.

Before pregnancy	Transplanting KO embryos into wild-type mice Tetraploid chimera Administration of LV
5.5–6.5 dpc	Delay implantation
17.5–19.5 dpc	Measurement of P <sub>4</sub> Evaluation of cervical ripening (biometric test, pathological test) Evaluation of uterine contraction (in vivo and vitro)
19.5 dpc-	HE staining and/or tunnel staining of corpus luteum Administration of RU486 Ovariectomy
After labor	Investigation of the maternal and fetal genotype with delayed labor Screening of placenta and fetus

### 5.1. Measurement of the Landing Time

Delayed implantation often results in fetal stunting and reduced litter size. Since delayed-labor mice often miscarry or absorb their fetus in utero, measurement of landing time is useful for measuring the true litter size. Some studies have reported that small litter sizes tend to delay delivery in some mouse strains [57].

### 5.2. Investigation of the Following Factors: Dam, Fetus, and Placenta

If the dam is abnormal, mice will exhibit delayed delivery, regardless of the sire genotype. If the placenta or fetus is abnormal, wild-type female transplanting KO embryos, such as *Nrk* KO, will exhibit delayed delivery (16). Investigating the expression of the target gene in the fetus and placenta is also useful to determine whether the cause is the fetus or placenta. Placental dysplasia often occurs if the placenta is the cause. In addition, the method using the above-mentioned LV vector and tetraploid chimera is also useful.

### 5.3. Presence or Absence of P<sub>4</sub> Withdrawal during Late Pregnancy

Abnormal luteolysis is the most common cause of delayed labor; examining P<sub>4</sub> at 16.5 dpc and 18.5 dpc is especially useful. Luteolysis can also be examined by observing the ovaries pathologically.

### 5.4. Evaluation of Uterine Contractions and Cervical Ripening

It is also important to assess uterine contractions and cervical ripening in late pregnancy to directly assess the status of labor. In delayed delivery, there must be an abnormality in either, or both.

### 5.5. Comparison of Wild-Type Mice

The gestation period of mice varies depending on the strain [58]. However, the variability within the strain is small [58]. Comparison with wild-type mice is necessary to accurately prove the delayed labor. In some mice strains, fetal count and gestational duration are inversely correlated [57,58]. Extension of gestation due to a decrease in the number of fetuses should also be considered.

## 6. Conclusions and Future Perspectives

The etiology of delayed parturition is overexpression of the pregnancy-maintenance mechanism or deficiency of the labor-induction mechanism. Overexpression of the pregnancy-maintenance system is attributed to the excessive secretion of humoral factors, such as P<sub>4</sub> and

PL, which have a pregnancy maintenance effect [4,33]. Suppression of the labor-induction mechanism is caused due to uterine contraction disorder and/or cervical ripening [20,21,24,59]. Understanding both mechanisms is important for elucidating the mechanisms of pregnancy and delivery.

The biggest difference between rodents and humans in pregnancy and labor is the trigger of labor. In rodents, P<sub>4</sub> withdrawal triggers labor. In contrast, in humans, P<sub>4</sub> withdrawal does not occur in late pregnancy, suggesting that the trigger for labor may be a PR subtype change [39,42]. P<sub>4</sub> administration to high-risk patients with preterm birth reduces preterm birth rates [60]. The human corpus luteum disappears at approximately 20 weeks of gestation, and P<sub>4</sub> is produced in the placenta. Luteolysis in humans does not appear to be involved in delayed labor. Mice with delayed parturition due to abnormal luteolysis may be useful to understand human early pregnancy maintenance.

Human PL, which is only one type of PL, does not affect pregnancy [61]. There are several types of mouse PLs, and mPL-1 and mPL-2 maintain the corpus luteum and pregnancy [4,15]. The functions of other PLs are unknown, and further research is required.

However, few studies have evaluated the effects of cervical ripening and uterine contractions in mice. In humans, cervical ripening is evaluated on the basis of the degree of cervical dilatation. Uterine contractions are evaluated using cardiotocography. Similarly, examining these two factors in mice will help to clarify the cause of labor disorders.

The length of the gestation period is controlled not only by the maternal signals but also by fetal and placental signals [4,13–15]. The amount of mPL changes with placental and fetal growth [4,15]. The concentration of Sp-A in amniotic fluid increases with fetal maturation and promotes labor [13]. In humans, corticotropin-releasing hormone secreted from the fetal hypothalamus promotes labor induction [42]. The mother controls these two systems by sensing fetal development.

Studies on preterm birth in humans, which has a greater effect on infants, are more abundant than those on delayed labor. However, findings from studies on delayed delivery can also be applied to the prevention and treatment of preterm births. For example, *Fp* KO and *Cox1* KO has been used to study cox-selective inhibitors [35]. P<sub>4</sub>-related delayed delivery mice such as *Klf9* KO and *Cyp11a1* Tg provide clues to the potential of P<sub>4</sub> as a treatment for preterm birth. P<sub>4</sub> has been used in the treatment of imminent preterm births in humans [60]. Delayed delivery mice due to autoimmune disorders may be associated with surrogate mothers and pregnancy due to uterine transplantation. In humans, delayed labor has a family accumulation and is likely to involve a genetic background. In the future, if the genetic background of women who are prone to delayed delivery is clarified, it may be possible to find an association with the gene related to these mice.

Elucidation of the causes of delayed parturition in humans and animals is essential to understand the mechanisms underlying pregnancy and delivery. Summarizing the causes and examination methods of delayed delivery in mice in this review will help to focus on future research and provide new insights into novel treatment strategies.

**Author Contributions:** Writing—original draft preparation, H.Y.; writing—review and editing, N.M. and M.K.-A. All authors have read and agreed to the published version of the manuscript.

**Funding:** This study was supported by Japan Society for the Promotion of Science (JSPS) KAKENHI (grant numbers 21H02387 and 18H02361).

**Institutional Review Board Statement:** Not applicable.

**Informed Consent Statement:** Not applicable.

**Acknowledgments:** The authors thank the Center for Experimental Animals, Tokyo Medical and Dental University for supporting our research. The authors also thank H. Itoh, Y. Hirate, T. Endo, and F. Ishino for their critical reading.

**Conflicts of Interest:** The authors declare no conflict of interest directly relevant to the content of this article.

## References

1. Vayssiere, C.; Haumonte, J.B.; Chantry, A.; Coatleven, F.; Debord, M.P.; Gomez, C.; le Ray, C.; Lopez, E.; Salomon, L.J.; Senat, M.V.; et al. Prolonged and post-term pregnancies: Guidelines for clinical practice from the French College of Gynecologists and Obstetricians (CNGOF). *Eur. J. Obstet. Gynecol. Reprod. Biol.* **2013**, *169*, 10–16. [CrossRef] [PubMed]
2. Nishimori, K.; Young, L.J.; Guo, Q.; Wang, Z.; Insel, T.R.; Matzuk, M.M. Oxytocin is required for nursing but is not essential for parturition or reproductive behavior. *Proc. Natl Acad. Sci. USA* **1996**, *93*, 11699–11704. [CrossRef] [PubMed]
3. Imamura, T.; Luedke, C.E.; Vogt, S.K.; Muglia, L.J. Oxytocin modulates the onset of murine parturition by competing ovarian and uterine effects. *Am. J. Physiol. Regul. Integr. Comp. Physiol.* **2000**, *279*, R1061–R1067. [CrossRef] [PubMed]
4. Inagaki, M.; Nishimura, T.; Nakanishi, T.; Shimada, H.; Noguchi, S.; Akanuma, S.I.; Tachikawa, M.; Hosoya, K.I.; Tamai, I.; Nakashima, E.; et al. Contribution of prostaglandin transporter OATP2A1/SLCO2A1 to placenta-to-maternal hormone signaling and labor induction. *iScience* **2020**, *23*, 101098. [CrossRef]
5. Sugimoto, Y.; Yamasaki, A.; Segi, E.; Tsuboi, K.; Aze, Y.; Nishimura, T.; Oida, H.; Yoshida, N.; Tanaka, T.; Katsuyama, M.; et al. Failure of parturition in mice lacking the prostaglandin F receptor. *Science* **1997**, *277*, 681–683. [CrossRef]
6. Tsuboi, K.; Iwane, A.; Nakazawa, S.; Sugimoto, Y.; Ichikawa, A. Role of prostaglandin H2 synthase 2 in murine parturition: Study on ovariectomy-induced parturition in prostaglandin F receptor-deficient mice. *Biol. Reprod.* **2003**, *69*, 195–201. [CrossRef]
7. Gross, G.A.; Imamura, T.; Luedke, C.; Vogt, S.K.; Olson, L.M.; Nelson, D.M.; Sadovsky, Y.; Muglia, L.J. Opposing actions of prostaglandins and oxytocin determine the onset of murine labor. *Proc. Natl Acad. Sci. USA* **1998**, *95*, 11875–11879. [CrossRef]
8. Piekorz, R.P.; Gingras, S.; Hoffmeyer, A.; Ihle, J.N.; Weinstein, Y. Regulation of progesterone levels during pregnancy and parturition by signal transducer and activator of transcription 5 and 20 $\alpha$ -hydroxysteroid dehydrogenase. *Mol. Endocrinol.* **2005**, *19*, 431–440. [CrossRef]
9. Mejia, R.; Waite, C.; Ascoli, M. Activation of Gq/11 in the mouse corpus luteum is required for parturition. *Mol. Endocrinol.* **2015**, *29*, 238–246. [CrossRef]
10. Miyado, M.; Miyado, K.; Katsumi, M.; Saito, K.; Nakamura, A.; Shihara, D.; Ogata, T.; Fukami, M. Parturition failure in mice lacking Mamld1. *Sci. Rep.* **2015**, *5*, 14705. [CrossRef]
11. Zeng, Z.; Velarde, M.C.; Simmen, F.A.; Simmen, R.C. Delayed parturition and altered myometrial progesterone receptor isoform A expression in mice null for Kruppel-like factor 9. *Biol. Reprod.* **2008**, *78*, 1029–1037. [CrossRef]
12. Chien, Y.; Cheng, W.C.; Wu, M.R.; Jiang, S.T.; Shen, C.K.; Chung, B.C. Misregulated progesterone secretion and impaired pregnancy in Cyp11a1 transgenic mice. *Biol. Reprod.* **2013**, *89*, 91. [CrossRef]
13. Montalbano, A.P.; Hawgood, S.; Mendelson, C.R. Mice deficient in surfactant protein A (SP-A) and SP-D or in TLR2 manifest delayed parturition and decreased expression of inflammatory and contractile genes. *Endocrinology* **2013**, *154*, 483–498. [CrossRef]
14. Gao, L.; Rabbitt, E.H.; Condon, J.C.; Renthal, N.E.; Johnston, J.M.; Mitsche, M.A.; Chambon, P.; Xu, J.; O'Malley, B.W.; Mendelson, C.R. Steroid receptor coactivators 1 and 2 mediate fetal-to-maternal signaling that initiates parturition. *J. Clin. Investig.* **2015**, *125*, 2808–2824. [CrossRef]
15. Naruse, M.; Ono, R.; Irie, M.; Nakamura, K.; Furuse, T.; Hino, T.; Oda, K.; Kashimura, M.; Yamada, I.; Wakana, S.; et al. Sirh7/Ldoc1 knockout mice exhibit placental P4 overproduction and delayed parturition. *Development* **2014**, *141*, 4763–4771. [CrossRef]
16. Denda, K.; Nakao-Wakabayashi, K.; Okamoto, N.; Kitamura, N.; Ryu, J.Y.; Tagawa, Y.I.; Ichisaka, T.; Yamanaka, S.; Komada, M. Nrk, an X-linked protein kinase in the germinal center kinase family, is required for placental development and fetoplacental induction of labor. *J. Biol. Chem.* **2011**, *286*, 28802–28810. [CrossRef]
17. Wahid, H.H.; Dorian, C.L.; Chin, P.Y.; Hutchinson, M.R.; Rice, K.C.; Olson, D.M.; Moldenhauer, L.M.; Robertson, S.A. Toll-like receptor 4 is an essential upstream regulator of on-time parturition and perinatal viability in mice. *Endocrinology* **2015**, *156*, 3828–3841. [CrossRef]
18. Robertson, S.A.; Christiaens, I.; Dorian, C.L.; Zaragoza, D.B.; Care, A.S.; Banks, A.M.; Olson, D.M. Interleukin-6 is an essential determinant of on-time parturition in the mouse. *Endocrinology* **2010**, *151*, 3996–4006. [CrossRef]
19. Döring, B.; Shynlova, O.; Tsui, P.; Eckardt, D.; Janssen-Bienhold, U.; Hofmann, F.; Feil, S.; Feil, R.; Lye, S.J.; Willecke, K. Ablation of connexin43 in uterine smooth muscle cells of the mouse causes delayed parturition. *J. Cell Sci.* **2006**, *119*, 1715–1722. [CrossRef]
20. Pierce, S.L.; Kresowik, J.D.; Lamping, K.G.; England, S.K. Overexpression of SK3 channels dampens uterine contractility to prevent preterm labor in mice. *Biol. Reprod.* **2008**, *78*, 1058–1063. [CrossRef]
21. Reeves, C.V.; Wang, X.; Charles-Horvath, P.C.; Vink, J.Y.; Borisenko, V.Y.; Young, J.A.; Kitajewski, J.K. Anthrax toxin receptor 2 functions in ECM homeostasis of the murine reproductive tract and promotes MMP activity. *PLoS ONE* **2012**, *7*, e34862. [CrossRef]
22. Mahendroo, M.S.; Porter, A.; Russell, D.W.; Word, R.A. The parturition defect in steroid 5 $\alpha$ -reductase type 1 knockout mice is due to impaired cervical ripening. *Mol. Endocrinol.* **1999**, *13*, 981–992. [CrossRef]
23. Mahendroo, M.S.; Cala, K.M.; Russell, D.W. 5 Alpha-reduced androgens play a key role in murine parturition. *Mol. Endocrinol.* **1996**, *10*, 380–392. [CrossRef]
24. Word, R.A.; Landrum, C.P.; Timmons, B.C.; Young, S.G.; Mahendroo, M.S. Transgene insertion on mouse chromosome 6 impairs function of the uterine cervix and causes failure of parturition. *Biol. Reprod.* **2005**, *73*, 1046–1056. [CrossRef]
25. Song, H.; Lim, H.; Paria, B.C.; Matsumoto, H.; Swift, L.L.; Morrow, J.; Bonventre, J.V.; Dey, S.K. Cytosolic phospholipase A2alpha is crucial [correction of A2alpha deficiency is crucial] for 'on-time' embryo implantation that directs subsequent development. *Development* **2002**, *129*, 2879–2889. [CrossRef]

26. Uozumi, N.; Kume, K.; Nagase, T.; Nakatani, N.; Ishii, S.; Tashiro, F.; Komagata, Y.; Maki, K.; Ikuta, K.; Ouchi, Y.; et al. Role of cytosolic phospholipase A2 in allergic response and parturition. *Nature* **1997**, *390*, 618–622. [CrossRef]
27. Brown, N.; Morrow, J.D.; Slaughter, J.C.; Paria, B.C.; Reese, J. Restoration of on-time embryo implantation corrects the timing of parturition in cytosolic phospholipase A2 group IVA deficient mice. *Biol. Reprod.* **2009**, *81*, 1131–1138. [CrossRef]
28. Ye, X.; Hama, K.; Contos, J.J.; Anliker, B.; Inoue, A.; Skinner, M.K.; Suzuki, H.; Amano, T.; Kennedy, G.; Arai, H.; et al. LPA3-mediated lysophosphatidic acid signalling in embryo implantation and spacing. *Nature* **2005**, *435*, 104–108. [CrossRef]
29. Brown, J.L.; Sones, J.L.; Angulo, C.N.; Abbott, K.; Miller, A.D.; Boehm, U.; Roberson, M.S. Conditional loss of ERK1 and ERK2 results in abnormal placentation and delayed parturition in the mouse. *Sci. Rep.* **2019**, *9*, 9641. [CrossRef]
30. Mounzih, K.; Qiu, J.; Ewart-Toland, A.; Chehab, F.F. Leptin is not necessary for gestation and parturition but regulates maternal nutrition via a leptin resistance state. *Endocrinology* **1998**, *139*, 5259–5262. [CrossRef]
31. Davis, V.L.; Couse, J.F.; Goulding, E.H.; Power, S.G.; Eddy, E.M.; Korach, K.S. Aberrant reproductive phenotypes evident in transgenic mice expressing the wild-type mouse estrogen receptor. *Endocrinology* **1994**, *135*, 379–386. [CrossRef] [PubMed]
32. Vassalli, A.; Matzuk, M.M.; Gardner, H.A.; Lee, K.F.; Jaenisch, R. Activin/inhibin beta B subunit gene disruption leads to defects in eyelid development and female reproduction. *Genes Dev.* **1994**, *8*, 414–427. [CrossRef] [PubMed]
33. Herington, J.L.; O'Brien, C.; Robuck, M.F.; Lei, W.; Brown, N.; Slaughter, J.C.; Paria, B.C.; Mahadevan-Jansen, A.; Reese, J. Prostaglandin-endoperoxide synthase 1 mediates the timing of parturition in mice despite unhindered uterine contractility. *Endocrinology* **2018**, *159*, 490–505. [CrossRef] [PubMed]
34. Loftin, C.D.; Trivedi, D.B.; Langenbach, R. Cyclooxygenase-1-selective inhibition prolongs gestation in mice without adverse effects on the ductus arteriosus. *J. Clin. Investig.* **2002**, *110*, 549–557. [CrossRef] [PubMed]
35. Reinebrant, H.E.; Pileggi-Castro, C.; Romero, C.L.; Santos, R.A.D.; Kumar, S.; Souza, J.P.; Flenady, V. Cyclo-oxygenase (COX) inhibitors for treating preterm labour. *Cochrane Database Syst. Rev.* **2015**, *2015*, CD001992. [CrossRef] [PubMed]
36. Bole-Feysot, C.; Goffin, V.; Edery, M.; Binart, N.; Kelly, P.A. Prolactin (PRL) and its receptor: Actions, signal transduction pathways and phenotypes observed in PRL receptor knockout mice. *Endocr. Rev.* **1998**, *19*, 225–268. [CrossRef] [PubMed]
37. Mulac-Jericevic, B.; Lydon, J.P.; DeMayo, F.J.; Conneely, O.M. Defective mammary gland morphogenesis in mice lacking the progesterone receptor B isoform. *Proc. Natl Acad. Sci. USA* **2003**, *100*, 9744–9749. [CrossRef] [PubMed]
38. Mulac-Jericevic, B.; Mullinax, R.A.; DeMayo, F.J.; Lydon, J.P.; Conneely, O.M. Subgroup of reproductive functions of progesterone mediated by progesterone receptor-B isoform. *Science* **2000**, *289*, 1751–1754. [CrossRef]
39. Nadeem, L.; Shynlova, O.; Matysiak-Zablocki, E.; Mesiano, S.; Dong, X.; Lye, S. Molecular evidence of functional progesterone withdrawal in human myometrium. *Nat. Commun.* **2016**, *7*, 11565. [CrossRef]
40. Velarde, M.C.; Geng, Y.; Eason, R.R.; Simmen, F.A.; Simmen, R.C. Null mutation of Kruppel-like factor9/basic transcription element binding protein-1 alters peri-implantation uterine development in mice. *Biol. Reprod.* **2005**, *73*, 472–481. [CrossRef]
41. Pabona, J.M.; Zhang, D.; Ginsburg, D.S.; Simmen, F.A.; Simmen, R.C. Prolonged pregnancy in women is associated with attenuated myometrial expression of progesterone receptor co-regulator Kruppel-like factor 9. *J. Clin. Endocrinol. Metab.* **2015**, *100*, 166–174. [CrossRef]
42. Vannuccini, S.; Bocchi, C.; Severi, F.M.; Challis, J.R.; Petraglia, F. Endocrinology of human parturition. *Ann. Endocrinol.* **2016**, *77*, 105–113. [CrossRef]
43. Huang, C.C.; Shih, M.C.; Hsu, N.C.; Chien, Y.; Chung, B.C. Fetal glucocorticoid synthesis is required for development of fetal adrenal medulla and hypothalamus feedback suppression. *Endocrinology* **2012**, *153*, 4749–4756. [CrossRef]
44. Toyoshima, K.; Narahara, H.; Furukawa, M.; Frenkel, R.A.; Johnston, J.M. Platelet-activating factor. Role in fetal lung development and relationship to normal and premature labor. *Clin. Perinatol.* **1995**, *22*, 263–280. [CrossRef]
45. Okada, Y.; Ueshin, Y.; Isotani, A.; Saito-Fujita, T.; Nakashima, H.; Kimura, K.; Mizoguchi, A.; Oh-Hora, M.; Mori, Y.; Ogata, M.; et al. Complementation of placental defects and embryonic lethality by trophoblast-specific lentiviral gene transfer. *Nat. Biotechnol.* **2007**, *25*, 233–237. [CrossRef]
46. Miki, H.; Wakisaka, N.; Inoue, K.; Ogonuki, N.; Mori, M.; Kim, J.M.; Ohta, A.; Ogura, A. Embryonic rather than extraembryonic tissues have more impact on the development of placental hyperplasia in cloned mice. *Placenta* **2009**, *30*, 543–546. [CrossRef]
47. Kanai-Azuma, M.; Kanai, Y.; Okamoto, M.; Hayashi, Y.; Yonekawa, H.; Yazaki, K. Nrk: A murine X-linked NIK (Nck-interacting kinase)-related kinase gene expressed in skeletal muscle. *Mech. Dev.* **1999**, *89*, 155–159. [CrossRef]
48. Doyle, S.L.; O'Neill, L.A. Toll-like receptors: From the discovery of NFκB to new insights into transcriptional regulations in innate immunity. *Biochem. Pharmacol.* **2006**, *72*, 1102–1113. [CrossRef]
49. Piccinini, A.M.; Midwood, K.S. DAMPening inflammation by modulating TLR signalling. *Mediat. Inflamm.* **2010**, *2010*, 672395. [CrossRef]
50. Rada, C.C.; Pierce, S.L.; Grotegut, C.A.; England, S.K. Intrauterine telemetry to measure mouse contractile pressure in vivo. *J. Vis. Exp.* **2015**, *98*, 52541. [CrossRef]
51. Robuck, M.F.; O'Brien, C.M.; Knapp, K.M.; Shay, S.D.; West, J.D.; Newton, J.M.; Slaughter, J.C.; Paria, B.C.; Reese, J.; Herington, J.L. Monitoring uterine contractility in mice using a transcervical intrauterine pressure catheter. *Reproduction* **2018**, *155*, 447–456. [CrossRef]
52. Mazzone, J.N.; Kaiser, R.A.; Buxton, I.L. Calcium-activated potassium channel expression in human myometrium: Effect of pregnancy. *Proc. West. Pharmacol. Soc.* **2002**, *45*, 184–186.

53. Woclawek-Potocka, I.; Komiyama, J.; Saulnier-Blache, J.S.; Brzezicka, E.; Bah, M.M.; Okuda, K.; Skarzynski, D.J. Lysophosphatic acid modulates prostaglandin secretion in the bovine uterus. *Reproduction* **2009**, *137*, 95–105. [CrossRef]
54. Tokumura, A.; Kanaya, Y.; Miyake, M.; Yamano, S.; Irahara, M.; Fukuzawa, K. Increased production of bioactive lysophosphatidic acid by serum lysophospholipase D in human pregnancy. *Biol. Reprod.* **2002**, *67*, 1386–1392. [CrossRef]
55. Saba-El-Leil, M.K.; Vella, F.D.; Vernay, B.; Voisin, L.; Chen, L.; Labrecque, N.; Ang, S.L.; Meloche, S. An essential function of the mitogen-activated protein kinase Erk2 in mouse trophoblast development. *EMBO Rep.* **2003**, *4*, 964–968. [CrossRef]
56. Barash, I.A.; Cheung, C.C.; Weigle, D.S.; Ren, H.; Kabigting, E.B.; Kuijper, J.L.; Clifton, D.K.; Steiner, R.A. Leptin is a metabolic signal to the reproductive system. *Endocrinology* **1996**, *137*, 3144–3147. [CrossRef]
57. Biggers, J.D.; Curnow, R.N.; Finn, C.A.; McLaren, A. Regulation of the gestation period in mice. *J. Reprod. Fertil.* **1963**, *6*, 125–138. [CrossRef]
58. Murray, S.A.; Morgan, J.L.; Kane, C.; Sharma, Y.; Heffner, C.S.; Lake, J.; Donahue, L.R. Mouse gestation length is genetically determined. *PLoS ONE* **2010**, *5*, e12418. [CrossRef]
59. Reaume, A.G.; de Sousa, P.A.; Kulkarni, S.; Langille, B.L.; Zhu, D.; Davies, T.C.; Juneja, S.C.; Kidder, G.M.; Rossant, J. Cardiac malformation in neonatal mice lacking connexin43. *Science* **1995**, *267*, 1831–1834. [CrossRef]
60. Romero, R.; Nicolaides, K.; Conde-Agudelo, A.; Tabor, A.; O'Brien, J.M.; Cetingoz, E.; da Fonseca, E.; Creasy, G.W.; Klein, K.; Rode, L.; et al. Vaginal progesterone in women with an asymptomatic sonographic short cervix in the midtrimester decreases preterm delivery and neonatal morbidity: A systematic review and metaanalysis of individual patient data. *Am. J. Obstet. Gynecol.* **2012**, *206*, 124.e1–124.e19. [CrossRef]
61. Ben-Jonathan, N.; Mershon, J.L.; Allen, D.L.; Steinmetz, R.W. Extrapituitary prolactin: Distribution, regulation, functions, and clinical aspects. *Endocr. Rev.* **1996**, *17*, 639–669. [CrossRef] [PubMed]

MDPI  
St. Alban-Anlage 66  
4052 Basel  
Switzerland  
Tel. +41 61 683 77 34  
Fax +41 61 302 89 18  
[www.mdpi.com](http://www.mdpi.com)

*Journal of Developmental Biology* Editorial Office

E-mail: [jdb@mdpi.com](mailto:jdb@mdpi.com)

[www.mdpi.com/journal/jdb](http://www.mdpi.com/journal/jdb)





MDPI  
St. Alban-Anlage 66  
4052 Basel  
Switzerland  
Tel: +41 61 683 77 34  
[www.mdpi.com](http://www.mdpi.com)



ISBN 978-3-0365-7360-1